Stress-Strain Models for UHPFRC and Application in Seismic Design and Retrofit of Bridges

Ismail Mohammed

A Thesis Submitted to the Faculty of Graduate Studies
in Partial Fulfillment of the Requirements
for the Degree of Master of Applied Science

Graduate Program in Civil Engineering
York University
Toronto, Ontario

January 2023

Abstract

With the advent of Ultra-High-Performance Fiber-Reinforced Concrete (UHPFRC), most shortcomings of conventional concrete are mitigated, since UHPFRC has exceptional mechanical and durability properties. The behavior of the material in tension is the most important property that need be characterized with confidence for practical implementation of UHPFRC in construction. This is often extracted through reverse inverse analysis of flexural tests – existing inverse analysis methods are fraught with great uncertainty and scatter. In this thesis, several alternative characterization methods are explored and corroborated with test results, including an inverse analysis procedure that is consistent with first principles, as well as a practical, chart-based procedure for quality control by practitioners. Apart from the direct tension response, the tension stiffening property of UHPFRC when it interacts with embedded reinforcement was also studied both experimentally and through detailed finite element simulation. Parameters of the study included the volumetric ratio of fibers, casting methodology, loading protocol and the condition of the embedded reinforcement (corroded or uncorroded). Results quantify the amount of tension stiffening that UHPFC cover can provide to reinforcement. The emphasis on tensile stress and strain capacity of UHPFRC is of interest in seismic retrofitting of existing columns through jacketing. In this work a design framework was developed to design UHPFRC jackets by setting performance objectives for the retrofitted column, strain limits for the UHPFRC material in tension and compression, and by development of a constitutive relationship for the encased concrete under the influence of confinement imparted by the jacket. The study includes an illustrative example of a bridge pier confined with two alternative UHPFRC materials of different strength, indicating the effectiveness of the proposed methodology in estimating the performance limit states of the retrofitted component.

Acknowledgements

I would like to express my sincere and deepest gratitude to my supervisor Professor S. J. Pantazopoulou for her acceptance, invaluable guidance, encouragement, and support throughout the course of my master's program. I would not have been able to accomplish this degree without her mentorship and continuous assistance that kept me going during the most challenging two years of my life. I am extremely grateful not only for all the knowledge and skills that she has imparted me with but also for helping me grow positively both at professional and personal levels.

Great appreciation goes to my supervisory committee member Professor Liam Butler for providing timely advice and valuable feedback on multiple aspects throughout this program. I am sincerely grateful to Civil Engineering Department lab technicians Riad Rajab and Kunjan Rupakheti for their high spirit and continuous assistance in the completion of my experimental work. Furthermore, I thank Ms. Sindy Mahal for her indispensable support and help in administrative matters.

I want to thank my colleagues and friends: Zoi Ralli, Nicolas El-Joukhadar, Konstantinos Tsiotsias, Farah Dameh, Syed Husain and Joey Garristo for their assistance during my experimental and analytical work. Furthermore, I thank Mario Antoun, Austin Martins, Alessandro Paglia, Peace Ikpotokin and Soumya Dash for their help.

I am highly grateful to my family, especially to my parents who believed in me and supported me with every decision I took in my life. I would not have accomplished any of my endeavors without their selfless support and encouragement at every stage of my life. Last but not the least, I am extremely thankful to the Almighty for giving me the strength and determination to pursue my desired goals.

Table of Contents

List of Tables

List of Figures

Chapter 1: Introduction

1.1 Background

A huge proportion of the existing Reinforced Concrete (RC) infrastructure across the world is at the end of their service life or facing premature structural deficiencies that require significant repairs. Reinforced concrete was once believed to be an affordable and low-maintenance material for the built infrastructure, but it now requires tremendous investment to keep them functioning safely and serve future needs of humanity. The global cost of corrosion, which is the predominant deteriorating mechanism in RC members, was estimated to be USD$2.5 trillion in an international report published by NACE (2016). Hence, the incredible cost of these repairs led to a shift in focus from traditional practices to explore advanced and sustainable materials that could be used in repair and rehabilitation works with greater serviceability and reliability. With the advent in cementitious material technologies, UHPFRC gained prominence as a potential material that could solve many problems associated with the modern infrastructure. Ultra-high performance fiber-reinforced concrete (UHPFRC) is a type of fiber reinforced concrete with superior mechanical properties and much higher durability. Its innate characteristics and superior behavior in terms of compressive and tensile strength, post-cracking ductility and durability makes it a well-suited material in the construction industry. Besides its advantages and applications in retrofitting and rehabilitation of existing RC structures such as jacketing of bridge piers, deck joints, bridge overlay etc., it is also being considered in construction of new structural members. Owing to its significant strength and mechanical properties, UHPFRC may be used to obtain reduced sizes of design cross-sections compared to other conventional concretes. This would provide increased amount of floor area and reduce self-weight in case of buildings. The fundamental design methodology of strong column-weak beam connection in a building structure is easily achievable with the use of UHPFRC in columns, thus, giving rise to a possibility of hybrid structures comprising of both RC and UHPFRC elements. Because of its increased resistance against penetration of harmful ingressive agents that cause corrosion in RC members, UHPFRC also serves as an effective and durable retrofit material in corrosive environments. Retrofits performed with UHPFRC would significantly increase the life span of a structure, besides reducing the number of repair interventions. Hence, it justifies the amount of initial cost over its life span and was also proven to be a cost-effective alternative in some cases reported by Doiron (2016).

1.2 Brief Introduction to UHPFRC

Ultra-high performance fiber-reinforced concrete, often abbreviated as UHPFRC or UHPC, is a composite material characterized by very high compressive and tensile strength, durability, and post-cracking ductility which is imparted by the discrete fiber reinforcement that provides an effective crack bridging mechanism (Figure 1- 1). Annex 8.1 of CSA S6 (2019) describes UHPFRC as "*a cementitious material with enhanced compressive strength and durability compared to high performance concretes and having a minimum compressive strength of 120 MPa*". Tensile categories of UHPFRC are classified as tension hardening or tension softening in accordance with Annex U of CSA A23.1 (2019).

Figure 1- 1: (b) Illustration of multi-cracking and fiber bridging in UHPFRC

UHPFRC is a mixture of Portland cement, fine sand, silica fume, ground quartz, fibers (commonly steel fibers), high-range water reducing admixture (superplasticizer) and water (usually, a minimal water to binder ratio is used in the range of 0.2 or less). Since its advent as reactive powder concrete in early 1980s, remarkable advancements have been made in developing the UHPFRC technology that is used in the present day. The term Ultra-High Performance Concrete (UHPC) was first coined by de Larrard & Sedran (1994) to refer to a material with an optimized particle-packing. UHPFRC has gained worldwide attention owing to its innate mechanical properties and resilient nature and has proven to be a potential construction material ever since. A precast, prestressed pedestrian bridge in Sherbrooke, Quebec was the first bridge in Canada that was constructed using UHPC back in 1997 (Blais & Couture, 1999). Apart from its most commonly used application in the field-cast connections of bridges which require less volume of concrete and eliminate the need for post-tensioning, many more novel applications have been explored in order to fully utilize the potential of this class of material. UHPFRC can be used in seismic repair of bridge piers, off-shore

structures, windmill towers, hydraulic structures, oil and gas industry utility towers, architectural components, bridge deck overlays and tunnel linings (Azmee & Shafiq, 2018). Besides superior mechanical properties, the discontinuous pore structure and practical absence of capillaries in UHPFRC makes it more durable against the ingress of contaminating agents thereby increasing the lifespan of repair and the structure on the whole. Figure 1- 2 shows several large-scale applications of UHPFRC across the world including pedestrian and road bridges, roofs and facades, and curved panels in a building. Due to the potential benefits and wide range of applications possible with UHPFRC, several commercial or proprietary mix packages have been developed by manufacturers around the world that are available in the current markets. Global market size of UHPFRC is expected to grow by 8.6% to USD $1867.3 million by 2025 which was USD$892 million in 2016 (Grand View Research, 2017).

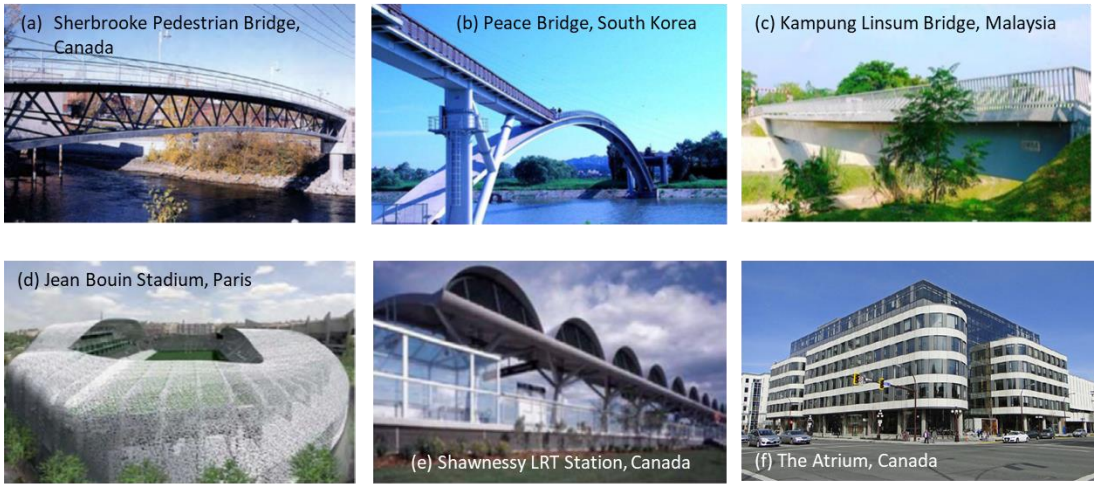

Figure 1- 2: Examples of UHPFRC applications: (a,b,c) Bridges; (d,e) Roof and facade; (f) Building (Azmee &Shafiq, 2018; Zhou et al., 2018; Yoo & Yoon, 2016)

1.3 Objectives and Scope of the Thesis

Wide scale application of UHFRC has been limited mainly due to the lack of design codes, initial cost, skilled workforce, and special mixing equipment. In the past decade, a lot of research was conducted for characterization and classification of UHPFRC often based on its tensile behavior which is one of its primary attributes. Several indirect methodologies have been proposed to estimate tensile behavior, some of which have been recommended in international standards (CSA S6, 2019; SIA 2052, 2016; AFNOR NF P18 470, 2016). However, some of the indirect methods developed were complex while others did not gather consensus of the research community due to

over simplifying assumptions or limitations. For example, the inverse analysis method recommended by Annex 8.1 of CSA S6 (2019) is applicable to specimens having clear span equal to three times the depth and was also found to possess great variability in predicting the tensile behavior of UHPFRC (Husain, 2021). Hence, the researchers are once again turning towards developing traditional direct tension tests that are feasible to implement in most laboratories around the world so as to avoid the use of complex inverse analysis methods the value of which is hampered by uncertainties. Nonetheless, the direct tension test is limited by its own complexity. The work done in this study was motivated and aimed at reducing this research gap by addressing some of the critical open issues of Annex 8 of CSA S6 (2019) regarding material characterization so as to foster the implementation of UHPFRC.

More specifically, the research presented in this thesis was aimed at providing new indirect analysis methods for estimating the tensile properties of UHPFRC, to provide stress-strain analytical model in compression calibrated with a vast experimental dataset, and to provide experimental evidence and analytical models for the tension stiffening property of this material. In addition, seismic retrofit application of UHPFRC was explored and a performance-based design framework was proposed in case of seismic retrofitting of piers through jacketing, which could significantly advance the life of critical bridge structures that require intensive and long-lasting repairs.

The main objectives of this research program are summarized as follows:

1. To develop and validate a spreadsheet-based inverse analysis methodology that is easy to use and applicable to a wide range of flexural specimens irrespective of size or fiber percentage of UHPFRC.
2. To develop and validate a Forward Analysis methodology in lieu of inverse analysis, to extract the essential tensile properties of UHPFRC such as that are useful for quality control and in design.
3. To correlate the tensile stress-strain properties obtained from direct tension tests and through various indirect testing methods including the ones proposed in this study.
4. To provide experimental data on the tension stiffening property of UHPFRC in case of uncorroded and corroded reinforcement steel.

5. To develop, correlate and validate a non-linear finite element model in order to estimate the tension stiffening behavior of UHPFRC.
6. To propose and validate an analytical uniaxial stress-strain model for the behavior of UHPFRC materials in compression and put forward design strain capacities based on the database established from UHPFRC experiments.
7. To propose a seismic retrofit performance-based design for pier jacketing application of UHPFRC in accordance with CSA S6 framework and asses its performance.

1.4 Thesis Structure

The thesis document is arranged in eight chapters. A brief introduction pertaining to each chapter is summarized as follows:

Chapter 1- Introduction: This chapter provides a brief background and introduction of UHPFRC, its structural applications, practicability and challenges hindering widespread use of this material. Scope of the research study, objectives pursued in this research, and organization of the thesis are also described in this chapter.

Chapter 2- Literature Review: This chapter provides a review on the classification of UHPFRC, mechanical properties and factors influencing the material behavior. Subsequently, experimental studies pertaining to the tension stiffening property of fiber reinforced concretes are explored. Corrosion mechanism of reinforcement steel and its effects are discussed. Furthermore, retrofit applications of UHPFRC material with an emphasis on seismic retrofit of piers through jacketing are presented. A detailed review study focused on various existing inverse analysis methods is also presented and uniaxial compression stress-strain models available for UHPFRC are reviewed.

Chapter 3- Determination of Tensile Behavior of UHPFRC: This chapter presents the experimental results carried out for UHPFRC material used in this study to obtain compressive stress-strain, modulus of Elasticity and Poisson's ratio. In addition, tests to measure splitting tensile strength, direct tension and four-point bending response are presented. The aim of this chapter was to propose an inverse analysis methodology and validate it using direct tension tests results and compare its performance with other existing inverse analysis methods. In addition, Digital Image Correlation for direct tension tests was presented.

Chapter 4- Forward Analysis Method: This chapter proposes a forward methodology to predict critical tensile stress-strain behavior of UHPFRC by using design charts developed for specific prism sizes. Results obtained from this method are compared with those of other inverse methods and direct tension tests for validation. This method is capable of removing the need of performing complex inverse analysis methods to obtain the tensile behavior.

Chapter 5- Tension Stiffening of UHPFRC: The experimental program carried out to explore the tension stiffening property of UHPFRC is presented in this chapter. Parameters of the study included fiber percentage of the mix, casting methodology and reinforcement bar condition- either corroded or uncorroded. Additionally, companion tests including flexural, compression and direct tension tests of UHPFRC were also presented.

Chapter 6- Finite Element Modeling of Tension Stiffening Behavior: This chapter includes the non-linear finite element modeling used to predict the tension stiffening behavior obtained from the experiments in the previous chapter. Two kinds of models were developed based on the geometry of reinforcement steel- 3D rebar model and 1D rebar model. Correlation between the two models and experimental results were drawn.

Chapter 7- Design of Bridge Pier Seismic Retrofit with UHPFRC: This chapter presents a pertinent framework of seismic design guidelines essential for performance-based design of UHPFRC retrofits along with a practical example of bridge pier seismic retrofit using UHPFRC jacketing. A database of compressive tests, and values of stress-strain behavior of unconfined UHPFRC is established from the experimental evidence available in the literature. Furthermore, an analytical compression stress-strain model suitable for UHPFRC was proposed based on an existing model from the high strength concrete literature along with the design strain capacities of critical points in compression.

Chapter 8- Conclusion: This chapter starts with a brief summary of the thesis followed by conclusions related to major topics of the research work presented. Lastly, challenges faced during the course of work with respect to experimental and analytical research aspects are presented and relevant recommendations for further work for the near future are proposed.

A graphical overview of the thesis' content is shown in Figure 1- 3.

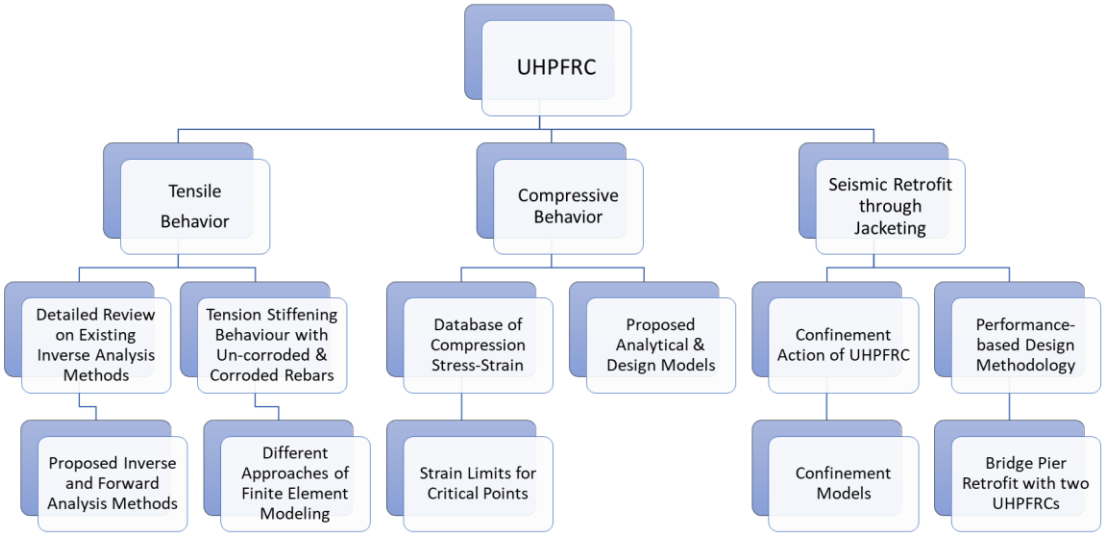

Figure 1- 3: Overview of thesis' content

Chapter 2: Literature Review

Literature review presented in this chapter begins with the classification of UHPFRC based on different international standards, followed by its mechanical properties and the factors affecting characteristic behavior of UHPFRC. Subsequently, experimental studies pertaining to the tension stiffening property of fiber reinforced concretes are explored. A review on the corrosion mechanism and its effects on reinforcement steel is presented. Furthermore, state-of-the-art retrofit methodologies of UHPFRC are discussed with an emphasis on pier jacketing retrofit applications. A detailed review on existing inverse analysis methods proposed by several researchers or standards to obtain the tensile behavior of UHPFRC is included. Lastly, existing analytical stress-strain models for uniaxial compression of UHPFRC are presented which are essential for the non-linear analysis of structural and retrofit members constructed from this material.

2.1 Classification of UHPFRC

Constituents of modern UHPFRC often include a mix of Portland cement, silica fume, fine sand, super plasticizer or high-range water reducing admixture, reinforcing fibers (generally steel), chemical admixtures and water. The difference in dosage and properties of these constituents, casting environment, fiber orientation and curing methods can result in diverse material characteristics of UHPFRC. The most common type of UHPFRC contains steel fibers and exhibits strain-hardening behavior in tension. Figure 2- 1 shows the general classification of fiber reinforced concrete (FRC) based on load-deflection response from a bending test and stress-strain response in uniaxial tension (Naaman & Reinhardt, 2006). FRC is usually identified by two types of responses in tension, namely strain-hardening and strain-softening behavior. FRC is classified as strain-hardening if it exhibits a post-cracking tensile strength higher than the tensile cracking strength. A strain-hardening behavior in tension generally follows deflection hardening response in bending. On the other hand, a strain-softening material would either have deflection hardening or deflection softening behavior in bending.

To this date, several standards on UHPFRC have been documented and published around the world. These standards help classify this type of material into various sub-categories which can be used for quality control of UHPFRC produced on-site and for design of members as adopted by their respective national standards or beyond.

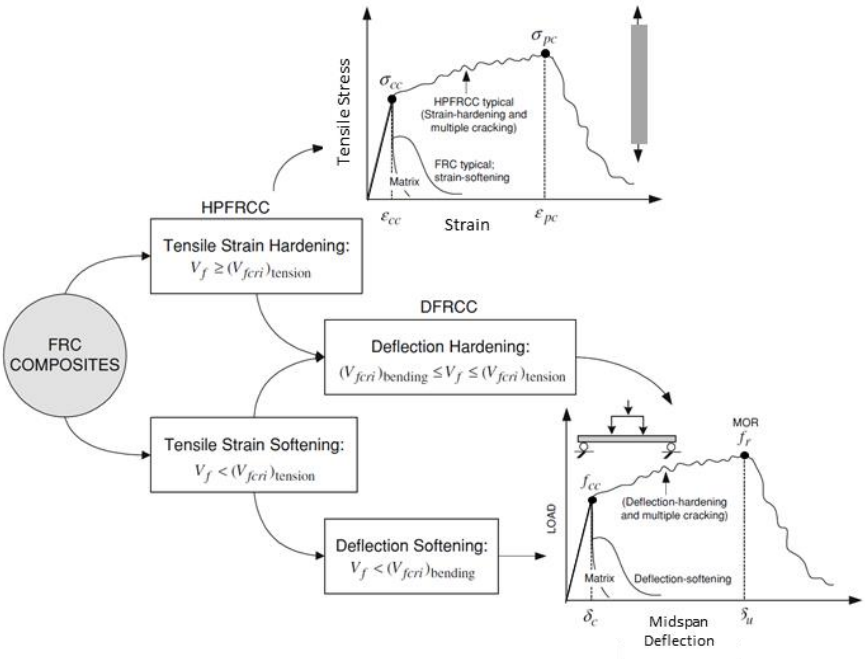

Figure 2- 1: Classification of FRC materials (adapted from Naaman & Reinhardt, 2006)

2.1.1 Classification Proposed by the Canadian Standard

Annex-U (CSA A23.1:19, 2019) provides provisions on UHPFRC material and construction aspects. The minimum compressive strength of a TN28 cylindrical specimen is required to be 120 MPa at 28 days. TN28 refers to ambient curing conditions with no thermal treatment at 23+-2 ^{o}C and at least 95% relative humidity for 28 days. With regard to compression testing, the standard recommends a cylinder size of 75 mm x150 mm and loading rate of 1.0 $\pm$ 0.1 MPa/s to be used due to high compressive strength of the UHPFRC. Annex U also classifies UHPFRC into strain-hardening and strain-softening categories based on results of direct tension tests. Strain-hardening UHPFRC should possess a minimum tensile cracking strength of 5 MPa, with a hardening ratio $(f_{t,u}/f_{t,cr})$ greater than 1.10 and a minimum ultimate tensile strain ($\varepsilon_{t,u}$) of 0.1%. Notably, tensile cracking strength of strain softening UHPFRC should be greater than 4 MPa. The standard also prescribes durability limits (DL) of DL50, DL100 and DL200 based on the results from durability tests such as abrasion loss, salt-scaling, absorption, chloride ion penetration and sulphate resistance. Annex A8.1 of the Canadian Highway Bridge Design Code (CSA S6:19, 2019) provides information on design of structural members using FRC.

2.1.2 Classification Proposed by the French Standard

AFNOR NF P18-470 (2016) is a French standard on UHPFRC-specifications, performance, production and conformity. The standard requires the minimum compressive strength of a cylindrical specimen to be 130 MPa and various classes of UHPFRC are proposed based on compressive strengths varying from 130 MPa to 250 MPa. This standard recommends testing of 110 mmx 220 mm cylinders. Type M UHPFRC (containing metallic fibers) with characteristic compressive strength greater than 150 MPa is graded as UHPFRC-S. Type M UHPFRC with characteristic compressive strength in between 130 MPa to 150 MPa is graded as UHPFRC-Z. Moreover, a loading rate ranging between 0.4 MPa/s and 0.8 MPa/s is recommended for compressive strength tests.

The characteristic value of the elasticity limit in tension (tensile cracking strength) should be at least 6MPa at 28 days. In terms of tensile behavior, UHPFRC is categorized into three groups: T1, T2 and T3, depending on ratio of the ultimate tensile strength to the cracking strength $(f_{t,u}/f_{t,cr})$. Class T1, termed as strain-softening, has the ratio lesser than 1.25 for both mean and characteristic curve. Class T2 has the ratio greater than 1.25 for the mean curve but lesser than 1.25 for the characteristic curve, termed as limited strain-hardening behavior. Class T3 corresponds to significant strain-hardening behavior for which the corresponding ratio should be >1.25 for both the mean and characteristic curves. French standard also defines limiting values for durability tests based on various exposure classes which can be referred in detail in the standard document. Moreover, design requirements pertaining to structural members constructed with UHPFRC are recommended in AFNOR NF P18-710 (2016) which is an addendum to Eurocode-2.

2.1.3 Classification Proposed by the Swiss Standard

SIA 2052 (2016) is the Swiss standard recommended for design and construction of structures with UHPFRC. This standard requires the material to possess a minimum compressive strength of 120 MPa in order to be designated as UHPFRC. It also has additional compressive strength classes as U120, U160 and U200, where the number next to U corresponds to the characteristic value of cube compressive strength of UHPFRC. It further classifies UHPFRC into three categories (U0, UA and UB) based on its direct tensile behavior. U0, UA and UB materials should have elastic tensile strength $(f_{t,cr})$ exceeding 7.0, 7.0 and 10.0 MPa, respectively. The ratio of ultimate tensile

strength to elastic tensile strength $(f_{t,u}/f_{t,cr})$ for these classes are 0.7, 1.1 and 1.2 in the same order. Moreover, it requires the ultimate tensile strain ($\varepsilon_{t,u}$) to be 1.5% and 2.0% for UA and UB classes, respectively.

2.2 Mechanical Properties of UHPFRC

2.2.1 Compression

UHPFRC achieves high compressive strength on account of its dense matrix and integrity provided by proper particle packing whereas the presence of fibers makes it more ductile in lateral strain capacity (Naeimi & Moustafa, 2021). Although addition of fibers increased the compressive strength of the material compared to the one containing no fibers, there was no significant strength enhancement for increasing fibers from 2% to 4% (El Helou, 2016; Wang et al., 2020). Graybeal (2005) observed that up to 70 MPa of compressive strength was developed in as early as 2 days. French recommendations on UHPFRC (AFGC-SETRA, 2002) proposed compression testing with a loading rate of 0.24 MPa/s to 1.7 MPa/s on account of very high compressive strength. Annex-U (CSA A23.1:19, 2019) recommended a compression test loading rate of 1 MPa/s and the same was also proposed by Graybeal & Hartmann (2003) and FHWA (Russell & Graybeal, 2013). As already noted in the previous section, the minimum compressive strength requirement for UHPFRC is 120 MPa in Annex A8.1 of CSA S6:19 (2019) and SIA 2052 (2016), whereas it is 130 MPa in AFNOR NF P18-470 (2016), and 150 MPa in FHWA (Russell & Graybeal, 2013).

2.2.2 Modulus of Elasticity

Modulus of Elasticity (MOE) is an important parameter in the design of UHPFRC structures. Annex U of the standard CSA A23.1 (2019) recommended the use of ASTM C469/C469M (2014) for determining the static modulus of elasticity and Poisson's ratio of UHPFRC. In the absence of test data, the modulus of elasticity can be estimated from a suitable empirical relationship based on the compressive strength of the material. Several relationships have been proposed for estimation of the Modulus of Elasticity of UHPFRC. Table 2- 1 summarizes a few relevant empirical relationships for MOE. Russell & Graybeal (2013) reported that the average value of MOE for commercially available UHPFRC premix in the present markets varied from 55 GPa to 59 GPa. However, Bonneau et al. (1996) reported a MOE value of about 46 GPa for non-fibered UHPC mix, which was increased to about 49 GPa with the addition of 2% fibers. A detailed review

of the existing empirical relationships for predicting the modulus of elasticity of concrete was done by Alsalman et al. (2017) who also developed an expression that reasonably predicted MOE of UHPFRC (refer to Figure 2- 2) with an error of ±10%.

Table 2- 1: Empirical relationships for MOE of UHPC (adapted from Alsalman et al., 2017)

Source	Equation	Note
Graybeal (2012)	$E_c = 4069 \cdot \sqrt{f_c'}$	$97 \leq f_c' \leq 179\ MPa$
Graybeal (2007)	$E_c = 3840 \cdot \sqrt{f_c'}$	$126 \leq f_c' \leq 193\ MPa$
Ma et al. (2004)	$E_c = 19000 \cdot (f_c'/10)^{1/3}$	UHPC without coarse aggregates, $150 \leq f_c' \leq 180\ MPa$
Ma and Schneider (2002)	$E_c = 16365 \cdot (f_c') - 34828$	$f_c' \geq 140\ MPa$
AFGC (2012)	$E_c = 9500 \cdot (f_c')^{1/3}$	Heat-cured UHPC, $f_c' \geq 140\ MPa$

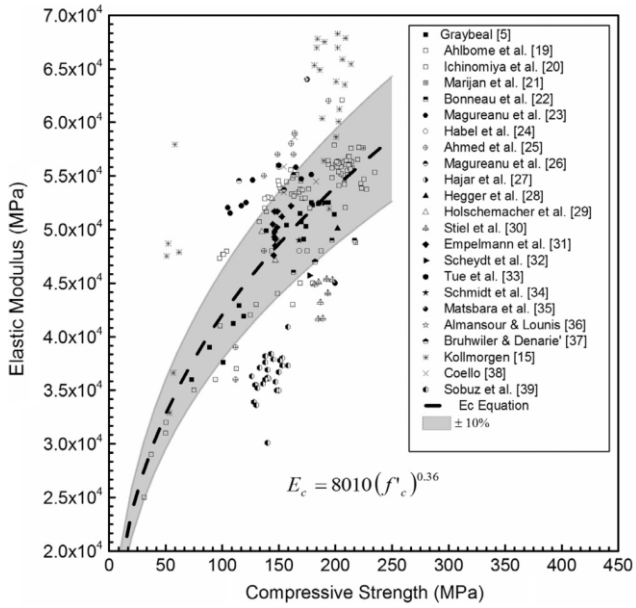

Figure 2- 2: Relation between modulus of elasticity and compressive strength (Alsalman et al., 2017)

2.2.3 Tension

The tensile strength of conventional concrete is very small and was usually neglected in the design of flexural members in the interest of simplified and conservative design. However, the tensile strength and ductility of concrete gained attention with the invention of cementitious composite materials such as ECC, HPFRC and UHPFRC. Besides ultra-high compressive strength, UHPFRC is known for its significant post-cracking tensile strength sustained up to a high tensile strain which is supported by the fiber reinforcement. Since the advent of UHPFRC, a lot of research has been conducted focused on characterization of its tensile behavior. Tensile properties of UHPFRC can be either obtained directly through direct tension tests or indirectly from flexural tests with the use of a suitable inverse analysis method (Graybeal & Baby, 2019). Several test methods and specimen geometries have been reported for conducting a direct tension test such as prismatic, dogbone, I-shaped and dumbbell specimens (Graybeal & Baby, 2013; Yang et al., 2021). Due to the high compressive strength, the bond between fibers and matrix is much improved leading to reduced length of anchorage which allows the efficient use of short fibers and enables a longer microcracking phase (López, 2017). Moreover, the use of high strength steel fibers having a high elastic modulus lead to uniaxial tensile response of UHPFRC with high cracking strength, large microcracking phase and large fracture energy. The direct tension test is the best approach to determine uniaxial tensile behavior of UHPFRC (Naaman & Reinhardt, 2006), however, it is difficult to perform direct tension tests due to several practical reasons. Imperfections in specimen, stiffness of the loading machine, boundary conditions, stress concentrations in non-uniform fiber dispersion in the specimens, shrinkage, eccentricities caused due to testing machine or the material itself are some of the challenges that occur during a direct tension test (Kanakubo, 2006; Ostergaard et al., 2005; Qian & Li, 2007).

Naaman & Reinhardt (2006) proposed a classification for strain-hardening fiber reinforced composites based on modulus of elasticity (E), ultimate tensile strength ($f_{t,u}$) and its corresponding strain ($\varepsilon_{t,u}$). Cracking strength was not included as the authors felt it does not hold significant influence on design aspects. Five different groups of strain-hardening FRC were proposed based on ultimate tensile strength, which include T-2.5, T-5, T-10, T-15 and T-20. T represents tension and the number represents the lower bound for characteristic ultimate tensile strength. Moreover, Naaman & Reinhardt (2006) proposed two more conditions for strain-hardening material: (a) the

modulus of elasticity (E) must be greater than 10,500 MPa; (b) the strain at ultimate stress should be greater than 0.005. The requirement of ultimate strain is not widely accepted as 0.5% is not easy to achieve even in most common UHPFRC's of present.

Wille et al. (2014) proposed classification of UHPFRC into four levels based on its volumetric energy absorption capacity prior to softening in uniaxial tension similar to Naaman & Reinhardt (2006). Level 1 refers to deflection-softening, level 2 corresponds to strain-softening, level 3 and 4 correspond to strain-hardening with difference in energy absorption capacity that classified level 4 to be high-energy absorbing material. In other words, level 4 was characterized by very high strain-hardening behavior. Moreover, Wille et al. (2014) idealized the uniaxial tensile response of UHPFRC into three parts as shown in Figure 2- 3. The elastic and strain-hardening response was represented by bilinear response of tensile stress vs tensile strain and the response beyond crack localization was represented by the tensile stress vs the crack opening relationship.

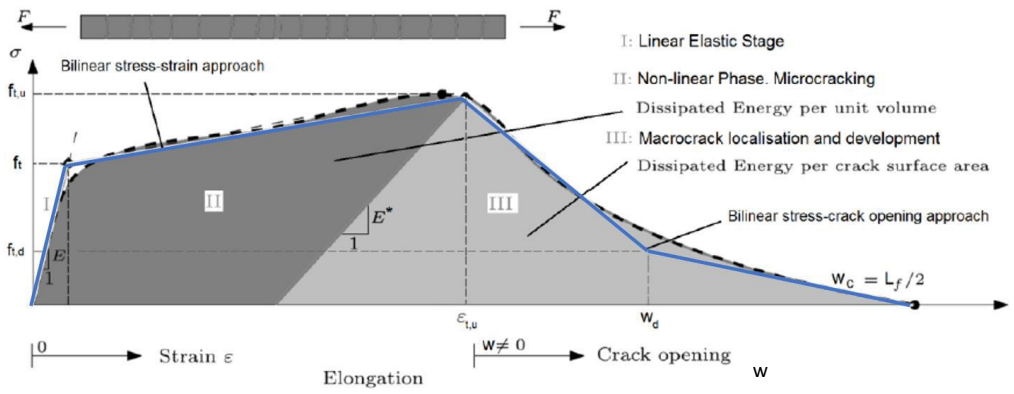

Figure 2- 3: Idealized uniaxial tensile behavior of UHPFRC proposed by Wille et al. (2014)

Minimum tensile cracking strength and ultimate strength requirements for UHPFRC, and its classification by CSA (A23.1:19, 2019), Swiss (SIA 2052, 2016) and French standards (AFNOR NF P18-470, 2016; AFNOR NF P18-710, 2016) have been mentioned earlier in Section 2.1. The Swiss standard proposed a standard dogbone specimen for conducting the uniaxial tension test of UHPFRC (Figure 2- 4). The tensile loading is applied to the specimen, bonded with 1.5 mm thick aluminum plates, through clamping action between the machine and the specimen.

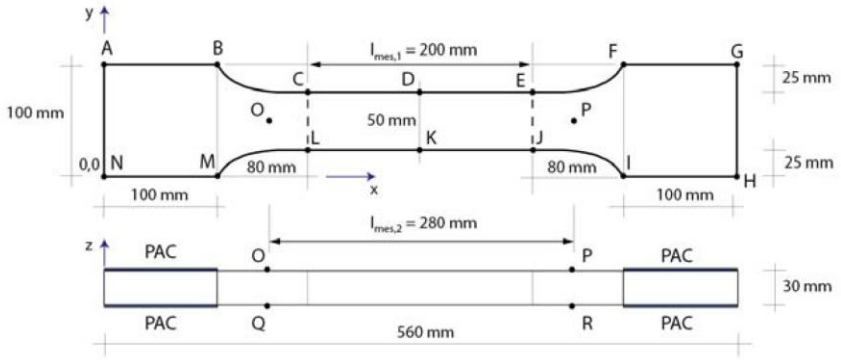

Figure 2- 4: Direct tensile test dogbone specimen proposed by SIA 2052 (2016)

Graybeal & Baby (2019) conducted uniaxial tensile test on prismatic specimens of 50.8 mm x 50.8 mm cross-section (2-inch x 2-inch) and two different lengths (17 inch and 12 inch). Aluminum grip plates were bonded to the specimen using high-strength structural epoxy. A parallel ring extensometer equipped with 4 LVDTs was used at a gauge length of 101.6 mm (4-inch) and 76.2 mm (3-inch) for long and short specimens, respectively, as depicted in Figure 2- 5. Loading rate of 0.00254 mm/sec was used. An elaborate review including details on material, geometry and grip configuration corresponding to various direct tensile test setups for FRC materials can be found in Wille et al. (2014).

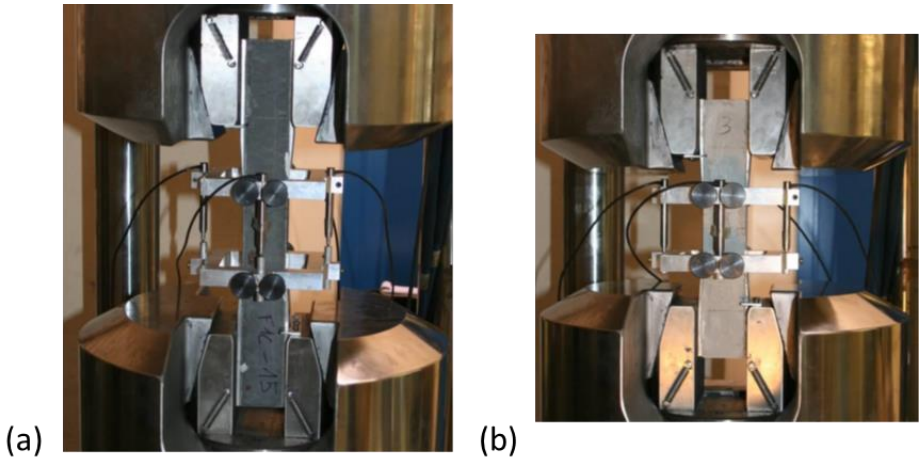

Figure 2- 5: Direct tensile test setup (a) Long specimen (b) Short specimen (Graybeal & Baby, 2019)

2.2.4 Flexure

Flexural testing of UHPFRC has been used as an alternative to the direct tension test due to ease of specimen preparation and test execution. However, experimental results obtained by bending

tests need to be complimented with an inverse analysis procedure for appropriate interpretation of the direct tensile behavior of UHPFRC. Three-point bending on notched specimen and four-point bending on un-notched specimen are the most common type of bending tests performed to obtain tensile characteristics of fiber reinforced concrete (Chanvillard, 2000). Notched three-point bending tests enable the measurement of the contribution of fiber as reinforcement of a cracked section and post-peak cracking response of UHPFRC by measuring load vs crack mouth opening response. On the other hand, four-point bending tests on un-notched specimen are used to derive elastic properties and the strain-hardening response of UHPFRC by measuring the load vs midspan deflection response (SIA 2052, 2016). The most common type of four-point bending test recommended by many standards (NF P18-470, 2016; ASTM C1609/C1609M-19, 2019; CSA A23.1:19, 2019; SIA 2052, 2016) for tension hardening UHPFRC material is the one with third-point loading, where both the distance between loading rollers and the shear span are equal to one third of the prism span as shown in Figure 2- 6.

Annex-D of SIA 2052 (2016) also provides an iterative inverse analysis procedure for determining the tensile stress-crack opening behavior of notched prisms. In the case of four-point bending test, the distance between the loading rollers offer a constant moment region, however, a disruption in the stress field is created close to the loading points whose effect is reduced with increasing slenderness ratio (L/h) of the specimen (López, 2017). Moreover, prismatic flexural specimens with square cross-section and shear span to depth ratio (aspect ratio) equal to 1 has stronger shear component than the specimens with depth equal to half of shear span (i.e., aspect ratio=2) (Ralli et al., 2021). Thus, the specimen recommended by AFNOR standard (NF EN 13670, 2013) that has a shallow cross-section and provides a shear span aspect ratio of 2, has been used effectively by French researchers who promoted the use of step-by-step inverse analysis method for UHPFRC (Rigaud et al., 2012; NF P18-470, 2016; SIA 2052, 2016; etc.). Similarly, Pantazopoulou et al. (2019) recommended the use of longer prisms with shear span to depth ratio of 2 rather than 1; owing to the moment-shear interaction that gives non-conservative results in case of specimens with aspect ratio equal to 1.

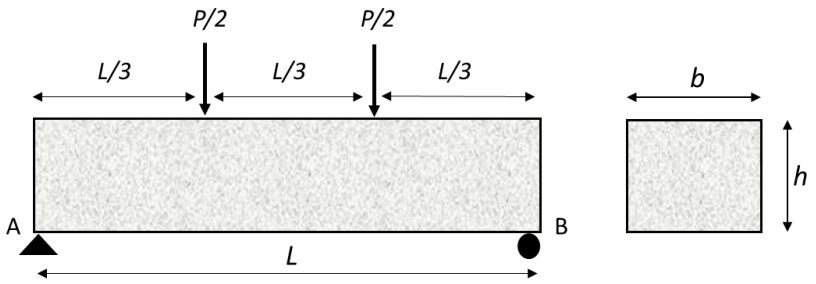

Figure 2- 6: Typical four-point bending test specimen with middle-third loading

2.3 Factors Influencing UHPFRC Behavior

The study carried out in this project consists of commonly used brass-coated straight steel fibers only. Fibers being an important constituent of the UHPFRC mix have a significant influence on the mechanical behavior of the test specimens and the structural members. Fibers' material type, dimensions, geometry, aspect ratio, orientation, and percentage volume in the mix are the factors that could influence strength and deformability of UHPFRC. Fibers enhances the ductility and energy absorption capacity of UHPFRC members which otherwise would be relatively brittle in nature (Yang, 2019). Steel and polyvinyl alcohol (PVA) fibers are generally used in UHPFRC. Steel fibers are commercially available in different shapes (straight, hooked, twisted) and sizes (e.g., 13 mm and 20 mm long with a diameter of 0.2 mm). Mixing of fibers with different properties would lead to a hybrid form of UHPFRC and could also lead to enhancement of strain-hardening behavior (Prisco et al., 2009; Sohail et al., 2018). Fibers can be considered as smeared reinforcement and they limit crack widths besides providing favorable crack distribution. It can also be used as a partial substitute to conventional reinforcement in redundant structural members (Prisco et al., 2009). Chan & Li (1997) found improved adhesion between fiber and matrix with use of brass-coated steel fibers compared to regular steel fibers.

Huang et al. (2021) investigated the effect of fiber alignment and volumetric ratios on the flexural behavior of UHPFRC. Flow induced casting that provides better alignment of fibers resulted in 30%-60% increase in flexural strength of the prismatic specimens. Moreover, increase in the length of fibers from 6 mm to 20 mm improved the flexural strength by 40% to 80% and the increase was about 60% due to an increase in fiber volume from 1% to 3%. Flexural strength and toughness of UHPC beams were substantially improved with the increase in fiber length as found by Yoo et al. (2016). Moreover, use of longer fiber promoted higher number of micro-cracks and average lower

average crack spacing. Length of fibers did not have significant influence on pre-cracking response of the specimen (Yoo & Yoon, 2015).

In another study by Wille et al. (2011), it was found that a mere a volume fraction of 1% straight steel fibers was enough to trigger multiple cracking and strain-hardening behavior in tensile testing. Wille tried to increase the ductility of UHPFRC by keeping the fibers volume within 2.5%. Ductility and ultimate tensile strength of the specimens were improved by using deformed or twisted fibers, whereas the workability was reduced. Wille et al. (2011) reported that the ultimate tensile strength of UHPFRC specimens with twisted steel fibers was 60% higher than that containing smooth fibers, and similarly the tensile strain at peak stress increased by about 3 times. Maca et al. (2012) recommended that a fiber volume of 2% to 3% is optimal for desirable mechanical behavior of UHPFRC.

Aspect ratio (ratio of length to diameter) of the fibers have also been reported to have influence on characteristics of UHPFRC. Sohail et al. (2018) reviewed that the dimensions of steel fibers used in UHPFRC varies from 6 mm to 60 mm in length and 0.15 mm to 0.75 mm in diameter. However, the most commonly used steel fibers are 13 mm long with a diameter of 0.2 mm (Schmidt et al., 2003). Ye et al. (2012) reported that higher aspect ratio of fibers provided an increase in flexural capacity as UHPC mix containing fibers of small diameter (higher aspect ratio) would have more fibers per unit area and hence bridged the cracks more effectively when compared to specimens with fibers of lower aspect ratio. Yoo et al. (2016) also reported improved flexural strength and higher ductility in flexural specimens due to better alignment and higher fiber percentage per unit area achieved by placing the mix at one end and allowing it to fill the mold by flowing till the other end. Yang et al. (2010) found that prismatic specimens cast at the mid span exhibited 16% lower strength when compared to specimens cast from one end of the mold.

Previous studies have shown that the increase in the fiber volume of UHPFRC mix did not have considerable influence on the compressive strength results (Hassan et al., 2012) and specimens with higher volume fraction of fibers are prone to fiber clotting which causes adverse effects on the compressive strength (Schmidt et al., 2003). The addition of fibers to a mix would not only increase the compressive strength but also the ductility and impacts the failure mode, compared to the mix with no fibers. Fibers enable the specimens to hold integrity upon attainment of peak

strength in compression and foster a ductile mode of failure (El Helou, 2016; Graybeal, 2006; Wu et al., 2016).

2.4 Tension Stiffening Effect of UHPFRC

Tension stiffening is an important characteristic of this material essential for developing robust analytical models required for wide implementation of UHPFRC/UHPC across various structural members. Owing to its higher tensile strength and bond strength, UHPC offers a significant tension stiffening effect in reinforced-UHPC (R-UHPC) members (Jungwirth & Muttoni, 2004). Hence, understanding the interaction and compatibility between tension hardening UHPC and steel reinforcement is critical. Tensile loading capacity R-UHPC members consists of the contributions of UHPC and steel responses in tension. Tension stiffening effect of UHPC can be obtained by deducting the response of bare steel rebar from the overall tensile response of the R-UHPC member (Kang et al., 2017; Moreno et al., 2014). Moreover, Makita & Brühwiler (2014) have also reported that tensile behavior of R-UHPC follows the linear superposition of the tensile responses of steel rebar and UHPC.

Bian & Wang (2019) studied the behavior of R-UHPC dogbone specimens in direct tension loading for tension-hardening and tension-softening UHPC mixes with two different reinforcement ratios. In case of tension-hardening material, the elastic tensile strength of UHPC in reinforced specimens was found to be lower than that of unreinforced specimens to about 69% and 60%, while the ultimate tensile strength was reduced to about 68% and 43% for 2.3% and 4.6% reinforcement ratios, respectively. This was attributed to the interaction of UHPC and steel rebar that led to the localized stress concentration in UHPC matrix around the rebar ribs. Moreover, the response of R-UHPC was divided into three segments as shown in Figure 2- 7. Stage I corresponds to the elastic behavior of both rebar and UHPC, followed by elastic-plastic stage (II) where the UHPC experiences hardening, and the rebar is still in elastic stage. Stage III marks the start of the plastic response where both UHPC and rebar display the plastic behavior.

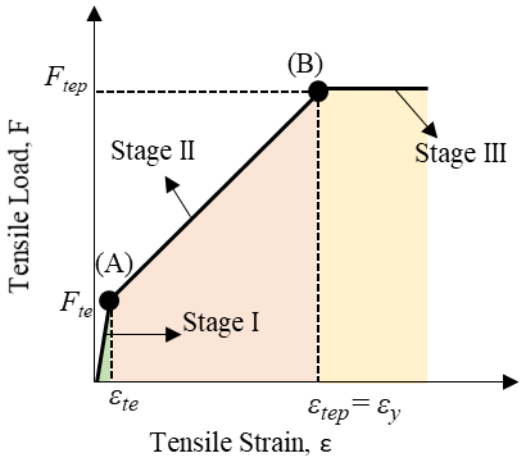

Figure 2- 7: Schematic representation for tensile response of strain-hardening R-UHPC (Bian & Wang, 2019)

Jungwirth & Muttoni (2004) conducted tests on tension stiffening and bond stress of rebars embedded in UHPC mix. The average bond strength of UHPC was reported to be about 10 times higher than that of conventional concrete leading to a shorter development length. Tensile tests of R-UHPC members were carried out on prismatic specimens with different reinforcement ratios varying from 1% to 4.8%. The specimens exhibited multi cracking due to fiber reinforcement. The tensile stiffening effect of UHPC on rebar was found to be significantly higher than that of ordinary concrete.

Several other studies have reported the tension stiffening behavior of various types of high-performance fiber reinforced cementitious composites (HPFRCC) such as hybrid fiber-reinforced concrete (HyFRC), self-consolidating fiber-reinforced concrete (SCFRC) and engineered cementitious composite (ECC) reinforced with steel bar (Jansson et al., 2012; Kang et al., 2017; Lárusson et al., 2012; Moreno et al., 2012, 2014). Moreno et al. (2012) conducted large scale tension stiffening tests on reinforced dogbone specimens with ECC and HyFRC. It was hypothesized that the rebar exhibited distributed yielding and strain-hardening on account of multiple cracking which was evident in all specimens. Early fracture of the reinforcement was not observed.

Moreno et al. (2014) further investigated tension stiffening response up to the fracture of reinforcement in HPFRCC using three different materials (ECC, HyFRC and SC-HyFRC) and also compared results with those of normal concrete (NC). Prismatic test specimens comprised a 16mm

diameter rod connected to 25 mm diameter grip rods with a high strength steel welded coupler. Few specimens were also tested with uniformly located strain gauges on the rebar. ECC specimen demonstrated the most extensive multi-cracking behavior followed by HyFRC, SC-HyFRC and NC. NC exhibited early longitudinal splitting cracks and did not carry tensile load after cracking whereas the subsequent response was similar to that of the bare rebar. In HPFRCCs, the transverse cracks were bridged by the fibers which prevented the sudden load transfer from the matrix to the reinforcing bar. This resulted in less or no slippage, and no splitting cracks, at least in the early stages. HPFRCCs demonstrated to carry loads beyond the yielding of rebar as opposed to NC. Post multi-cracking stage, HPFRCCs failed by developing a dominant localized crack. ECC specimens experienced reinforcement fracture at lower strains compared to HyFRC specimens. Moreover, early strain-hardening and rebar fracture was observed in all HPFRCC specimens compared to NC specimens which was also confirmed through the measurements from strain gauges. Early strain hardening of the reinforcement was noted to have provided the strengthening mechanism in HPFRCC specimens at the expense of overall deformation capacity (ductility). Similar observations on reduced deformation capacity of reinforced ECC members were reported by Kang et al. (2017). Moreover, they also reported that ECC suppressed the longitudinal splitting cracks and sustained tensile stresses beyond the yielding of reinforcement.

Makita & Brühwiler (2014) determined the fatigue behavior of R-UHPC in tension. It was found that fatigue capacity of both UHPC and steel rebar was enhanced by the stress distribution and transfer between both materials depending on the maximum force fatigue level.

2.5 Corrosion Mechanism in Reinforcing Steel

Corrosion of steel rebar in concrete is an electrochemical process similar to a galvanic cell that requires a cathode and an anode. For corrosion to take place, a metallic conductor (reinforcing bar) is necessary to connect the anode and the cathode that facilitate the movement of electrons. The presence of electrolyte conductor (concrete pore solution) is also necessary to facilitate the ions movement as depicted in Figure 2- 8 (Martín-Pérez, 1999). In the reinforced concrete, steel reinforcement itself acts as the cathode and anode at different locations leading to corrosion of the bar due to difference in potential. The difference in potential is caused by any non-uniformity within the corroding system, significant variations along rebar surface, or due to difference in concentration of ions present in the pore solution.

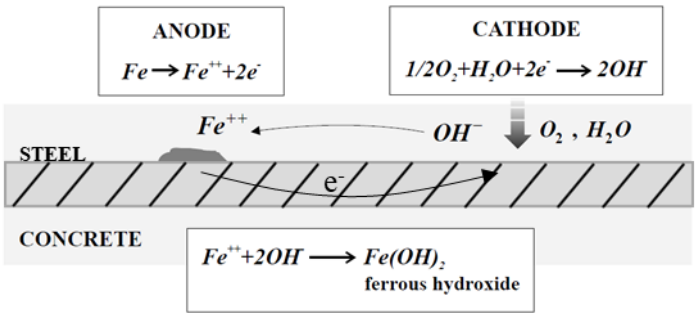

Figure 2- 8: Corrosion cell in reinforced concrete (adapted from Pérez, 1999)

Due to the potential difference along rebar, iron is oxidized at the anode as per Equation 2-1. The electrons released at the anode travel towards the cathode while Fe^{2+} ions are dissolved in the pore solution. Reduction of dissolved oxygen is the main cathodic reaction (Pérez, 1999) given by Equation 2-2. Under the influence of an electric field, the hydroxide ions from the cathode migrate towards the anode to combine with dissolved Fe^{2+} to form ferrous hydroxide [$Fe(OH)_2$] as shown in Equation 2-3. The reduction reaction at cathode depends on the presence of sufficient moisture and oxygen. Other probable anodic reactions are shown in Equation 2-4 and Equation 2-5 (ACI 222R-19, 2019).

$$Fe \rightarrow Fe^{2+} + 2e^- \quad (2\text{-}1)$$

$$2H_2O + O_2 + 4e^- \rightarrow 4OH^- \quad (2\text{-}2)$$

$$2Fe^{2+} + 4OH^- \rightarrow 2Fe(OH)_2 \quad (2\text{-}3)$$

$$2Fe(OH)_2 + 0.5O_2 \rightarrow 2FeOOH + H_2O \quad (2\text{-}4)$$

$$Fe + OH^- + H_2O \rightarrow HFeO_2^- + H_2 \quad (2\text{-}5)$$

Given enough oxygen at the anodic sites, iron hydroxide can further oxidize to other corrosion products. The conversion of Fe^{2+} ions into higher oxidation states is accompanied by an increase in volume. Depending on the degree of oxidation, iron can expand up to six times its original volume. Figure 2- 9 shows the proportion volume increase for different oxides of iron compared to the parent steel volume. This increase in volume exerts radial pressure on the surrounding concrete which upon exceedance of its tensile strength of concrete will cause cracking and cover spalling in concrete. Corrosion by-products could also cause the degradation of reinforcement

bond as the ribs on reinforcement are smoothened leading to reduction of friction between bar and the concrete. Moreover, reinforcing steel is also susceptible to lose its stable lattice structure causing brittleness in its response to deformation (Pantazopoulou et al., 2019).

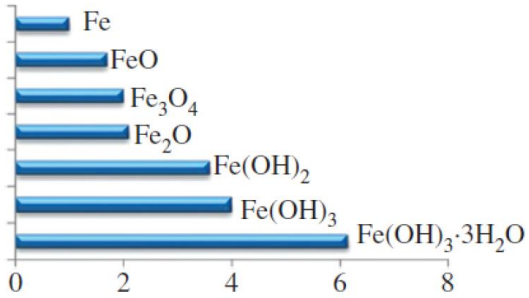

Figure 2- 9: Relative volume ratio of iron oxides compared with parent metal (Pantazopoulou et al., 2019)

2.5.1 Pitting and Uniform Corrosion

When the half-cell reactions are separated by small distances along the reinforcement, they are called microcells and cause uniform corrosion. This occurs with a uniform de-passivation of the protective film surrounding the rebar, which is the case with carbonation of the concrete cover. However, uniform corrosion can also be caused due to high concentration of chlorides along the rebar eventually causing a large number of closely spaced pits to coalesce. The reinforcement suffers small reduction in the cross-sectional area along the length of the bar leading to loss in bond strength, which in some cases can change the failure mode from bending to anchorage failure.

On the other hand, if the half-cell reactions are established further apart, they are called macrocell and are known to cause pitting corrosion. This phenomenon occurs when a potential difference is established between a large cathodic area and a relatively small anodic site in the presence of a high concentration of chloride ions (El-Joukhadar, 2022). Pitting or local corrosion causes an extreme local reduction in the bar's cross-sectional area leading to significantly reduced tensile or flexural capacity of the corroded member and could cause a brittle reinforcement failure.

2.5.2 Effects of Corrosion on Reinforcement Steel

Corrosion is reported to be accelerated after cracking of the concrete cover, because of the faster and deeper ingress of reactive corrosive agents such as chloride ions, carbonation, oxygen or moisture. Once the cover is fully cracked, the bond between concrete and reinforcement begins to

be depleted and it deteriorates completely upon cover delamination (Pantazopoulou & Papoulia, 2001). The effect of corrosion on mechanical properties of reinforcement was assessed by many researchers. Almusallam (2001) performed corrosion on rebars using the impressed current technique with a current density of 200 μA/cm2 and 5% NaCl solution. Corroded bars were subjected to tensile testing after cleaning with Clarke's solution. Increase in true tensile strength was found to be negligible (using minimum area of bar), whereas the nominal tensile strength (using nominal area of bar) was dramatically reduced to 16% of the original strength at 80% corrosion. In a separate study by Palsson & Mirza (2002), mechanical behavior of corroded rebars collected from an abandoned bridge in Montreal, Canada was studied. They found a substantial reduction in structural toughness due to the intense pitting corrosion. Reduced fracture energy and lower tensile strength was observed. The strain at failure was also found to be reduced by 50% due to a relative difference in area between the largest and smallest sections of 20%.

Du et al. (2005) studied the effect of corrosion on bare and embedded bars in concrete having plain and ribbed surface types. Nominal yield strength and ultimate strength were found to be significantly reduced and the strength reduction was faster in pitting corrosion than in uniform corrosion. For the same corrosion level, the effect of plain or ribbed surface on the response studied was negligible. Moreover, in another investigation by Apostolopoulos, (2007) the mechanical properties of S500 were subjected to direct tension and low cycle fatigue tests. Specimens were corroded by salt spraying for various periods ranging from 10 to 90 days. With increasing corrosion, results showed a significant drop in tensile strength and ductility of the rebar. Service life of RC structures in seismic regions is highly affected by corrosion and the degradation in material behavior is to be accounted in seismic evaluation guidelines. Normally, the effect of corrosion was found to be much higher on ductility than the strength of corroded rebar.

2.6 UHPFRC as a Retrofit Material

Since its advent in the 19th century, the use of reinforced concrete as a construction material quickly spread throughout the world. Ever since it has become the most commonly used construction material which found its application in almost every infrastructure project. Although RC structures are durable and are generally built for a defined service life, regular maintenance and repairs are required to be carried out even during its designed life to keep these structures serviceable. RC structures are damaged when exposed to extreme environment conditions or in the event of natural

disasters such as earthquakes. One of the common and crucial modes of deterioration is the corrosion of reinforcement. Hence, the deficient infrastructure of present-day requires extensive repairs costing huge sums of money to restore their safe use. It is estimated that 50,000 bridges are structurally deficient in the United States with an estimated repair cost of $150 Billion (El-Joukhadar & Pantazopoulou, 2021). Extensive research has been conducted in order to develop retrofitting methodologies that can recover structural integrity of RC structures, such as partial or major repair through jacketing with reinforced concrete, TRMs, steel shells, FRP jacketing etc.

A good retrofit technique not only restores the structural performance but also mitigates the deterioration mechanism that caused the need of repair in first place. On account of properties like superior mechanical strength, high density, low permeability, and high durability, UHPFRC is a promising material not only for new construction but also for repair and rehabilitation of deficient structures (El-Joukhadar & Pantazopoulou, 2021). It is one of the most recent repair materials to be introduced in the construction and retrofitting industry. Currently, extensive research is conducted in order to determine its reliability and performance aspects for a wide range of retrofitting solutions. In Switzerland, the application of UHPFRC to improve structural performance of existing RC structures was first performed in 2004, and more than 50 structures have been strengthened using UHPFRC (Brühwiler, 2020). Brühwiler classified the configuration of structural elements combining RC and UHPFRC material into three types based on the objective of intervention, as shown in Figure 2- 10. Figure 2- 10a shows a UHPFRC layer applied for protection of underlying RC against ingress of aggressive agents. Figure 2- 10b shows R-UHPFRC layer added on existing RC to enhance the structural resistance which serves a protection function as well. In case of corroded reinforcement or contamination due to high chloride concentration, R-UHPFRC is applied by removing the existing RC to the required depth as depicted in Figure 2-10c. Furthermore, Brühwiler (2020) presented the conceptual design details for strengthening intervention of two large highway viaducts and a road bridge.

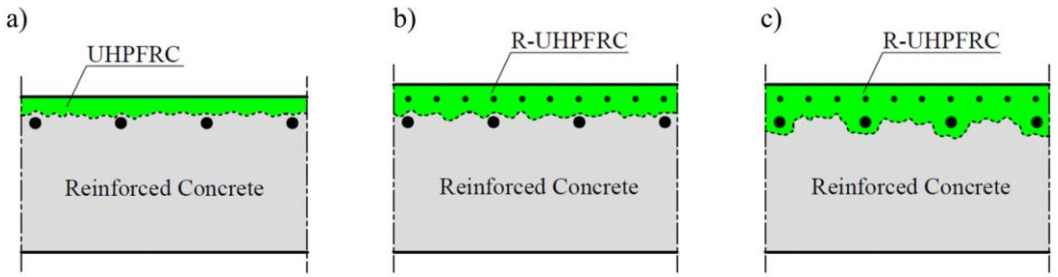

Figure 2- 10: Classification of UHPFRC interventions on existing Reinforced Concrete (adapted from Brühwiler, 2019)

Corvez & Masson (2013) explored the potential use of UHPFRC in the containment walls of nuclear reactors. Experimental investigation was conducted to study the mechanical behavior, shrinkage, permeability properties and "under pressure" strength tests were performed on UHPFRC. It was concluded that UHPFRC can be a promising solution for retrofit of nuclear reactor containment walls mainly due to the attributes like resistance to air permeability and superior bonding properties. In another study by Xu et al. (2021), the feasibility and effectiveness of UHPFRC as connection element for precast columns and footings in bridges was examined on a large-scale specimen. The failure response of this new type of connection was similar to that of a reference cast-in-place (CIP) pier specimen and it was found to eliminate local premature failures in the connection region which indicated sufficient structural robustness. This new UHPFRC connection was proposed to be suitable for accelerated bridge construction (ABC) techniques even in regions of high seismicity.

Murthy et al. (2018) examined the fatigue behavior of damaged RC beams retrofitted with 10 mm precast UHPFRC strip on the tension face of the beam bonded using a commercial epoxy. RC beams were pre-loaded to three levels of damage before retrofitting with UHPFRC and performing fatigue tests. The maximum number of cycles to failure was significantly higher in case of UHPFRC retrofitted flexural members when compared to that of control beams. It was concluded that UHPFRC is a much better alternative for repair of RC flexural elements as it overcomes many drawbacks corresponding to other retrofitting techniques such as steel plates and FRP laminates. A similar study by Huang et al. (2022) compared the response of RC beams retrofitted with UHPFRC and CFRP. The yield strength and ultimate strength capacity of the RC beam was increased by about 52% and 35%, respectively, with 3 cm thick UHPFRC as compared to 28% and 34%, respectively, with 1 layer of U-shaped CFRP on the tension face of the beam. The failure

mode of the RC beams retrofitted with UHPFRC was flexural as opposed to shear failure found in case of CFRP retrofit. Moreover, it was found that the cost of two layers of CFRP retrofit was four times higher than that of UHPFRC retrofit.

Doiron, (2016) reported recent case studies of four repair and rehabilitation projects commissioned by Lafarge North America Inc. by using Ductal® UHPFRC across North America. The projects include CN Rail in Montreal, QC, where an existing railway bridge pier was repaired through UHPFRC jacketing to protect against chloride ingress and freeze/thaw. The repair cover was required to be as thin as possible to allow for the necessary clearance for road traffic which was only possible with UHPFRC. A V-shaped concrete pier of the Mission Bridge across the Fraser River in British Columbia was retrofitted with UHPFRC to improve seismic deformation capacity of the columns and also saved $1.5 million (CAD) compared to other traditional methods. The superstructure replacement project of 3-span bridge in Hooper Road, New York was performed in 2014 where the contractor used UHPFRC for the connections of precast pier caps to existing columns. The original specification was to use UHPFRC only in closure pours and link slabs, but the contractor leveraged the properties of UHPFRC which provided huge time savings. The fourth project was the encasement of steel bent legs of the Hagwilget suspension bridge in New Hazelton, BC which experienced local corrosion at their base. Design of the retrofit demanded high-strength and flowable concrete with no shrinkage, no permeability and good tensile capacity. Hence, UHPFRC was the best fit option and a total of 32 bent leg bases were rehabilitated.

El-Joukhadar & Pantazopoulou (2021) studied the effectiveness of UHFRC (steel fibers) and ECC (PVA fibers) in mitigating corrosion of reinforcement by using cover thickness and pre-existing crack widths as parameters of the study. Accelerated corrosion was carried out by using fixed potential, and alternate wet and dry cycles were implemented to allow complete oxidization of corrosion by-products. The authors found that UHPFRC specimens showed higher mitigation capability than ECC, especially in the presence of cracks for specimens with $1D_b$ cover (D_b is the diameter of embedded rebar). A cover thickness equal to $2D_b$ was recommended to mitigate corrosion and thereby prolong the service life of structural components.

2.6.1 Performance of UHPFRC in Pier Jacketing

UHPFRC may also be used for retrofitting of structures damaged in an earthquake activity. It can be a game-changer in seismic retrofitting of old construction because they are compatible with

conventional concrete, durable, able to mitigate the occurrence of wide localized cracks, and are resilient to tensile deformation. Retrofitting of bridge piers with tension-hardening materials has been explored in numerous experimental studies already since 2010 (Dagenais et al., 2018; Deng et al., 2018; Farzad et al., 2019; Reggia et al., 2020; Tong et al., 2019; Yuan et al., 2022). The strain ductility imparted by the dense network of fibers presents an opportunity in seismic design and retrofit, whereas the significant durability enabled by the low porosity of the cementitious matrix makes this class of materials ideal for bridge retrofits since they can mitigate many of the limitations of the existing approaches.

One mechanism by which UHPFRC strengthens a reinforced concrete cross-section is through confinement, which is affected by the sustained tensile strength of the material when functioning as a jacket, thereby restraining the lateral dilation of the encased core. The confining function of UHPFRC jackets is passive, i.e., it arises in response to the expansive tendency of the encased core, as has been demonstrated by a number of tests conducted on cylindrical and rectangular concrete cores, which showed significant strain capacity enhancement, but low or moderate increase in compressive resistance of the core concrete (Rabehi et al., 2014; Tsiotsias & Pantazopoulou, 2022). Some studies have compared the performance of encased concrete to CFRP and UHPFRC jackets (Zoppo et al., 2018; Rabehi et al., 2014): Note that owing to the elastic response of the former, the passive confining pressure is continuously increasing with axial strain till either rupture or debonding; but lateral strength and energy dissipation of the UHPFRC jacketed concrete seems to be improved over that of FRP jacketed concrete (fib Bulletin 40, 2007; S. J. Pantazopoulou et al., 2016). Although both approaches were successful in eliminating failure modes associated with brittle details in older columns, such as bar buckling and shear interaction in the plastic hinge region, the UHPFRC approach has the advantage that it also contributes to the fire resilience and better durability of the encased core. When combined further with textile reinforcement, shear failure phenomena in the plastic hinge region of retrofitted specimens were eliminated (Hong et al., 2021) although in the presence of adequate deformation capacity of the jacket material shear failure appears to be mitigated even without additional reinforcement. A field application to a highway bridge for seismic strengthening of inadequately detailed piers has already been tested (Habel et al., 2017) in order to enhance the energy dissipation capacity and ductility of the piers as compared to an earlier application with FRP jacketing.

Jacket thickness has been studied as a retrofit parameter in several studies (Li et al., 2017; Yuan et al., 2022; El-Joukhadar, 2022; Tsiotsias, 2023) for circular piers and columns with rectangular cross-section: within the realm of what is considered *thin jackets*, the effectiveness of UHPC jackets thicker than 2 inch (50 mm) have been moderated by relocation of the plastic hinge zone outside the jacket region, either above the end of the jacketed length, or by increased bond demand in the footing if the later had not been also retrofitted; in fact, development of extensive damage in the footing (e.g., along the primary reinforcement anchorages) beyond a certain level of drift eliminates any benefit from the jacket (FRP or UHPFRC). Another mechanism by which jackets contribute is by means of developing normal stresses in the cross section of the structural member and therefore enhance the flexural and the shear strength of the component. Although the thickness is small, the total active area of UHPFRC in the tension and compression zones of the member produce significant stress resultants, thereby contributing to the sectional equilibrium. Thus, even such small jacket thicknesses cause a notable increase in column flexural strength and stiffness rendering this type of retrofit somewhere between what would be classified as either a global intervention (affecting the structural period) or a local intervention (not affecting stiffness at all (Thermou & Elnashai, 2006)). It was also found that the presence of axial load improved the jacket effectiveness because it affected favorably the tension reinforcement in columns, reducing the tendency for strain localization and rupture in the critical region.

2.7 Inverse Analysis for Tensile Behavior of UHPFRC

Inverse analysis is an indirect approach used to obtain the tensile characteristic properties of the fiber reinforced cementitious composites like UHPFRC by using the results obtained from a well-established flexural test, such as the four-point bending test (FPBT). This indirect approach is opted for due to well-known difficulties that occur while performing the direct tensile test. Inverse analysis methods may be broadly classified into two categories: (a) Simplified methods based on key points taken from the flexural resistance curve; (b) Methods based on complete experimental law ((López, 2017)). Simplified methods use the selected points from the bending test to predict the critical points corresponding to the tensile behavior of UHPFRC. However, methods based on the experimental law can predict the comprehensive stress-strain law in tension. These methods could be further classified into an iterative method and a point-by-point approach. The iterative approach uses the assumed constitutive stress-strain laws in compression and tension to match the

analytical and experimental response through iterations whereas the point-by-point approach uses stepwise loading to develop the constitutive law progressively (López, 2017). The latter is cumbersome and complex to implement due to instability in convergence that may arise from ups and downs recorded in the experimental curve. Figure 2- 11 shows the classification of inverse analysis methodologies by López (2017).

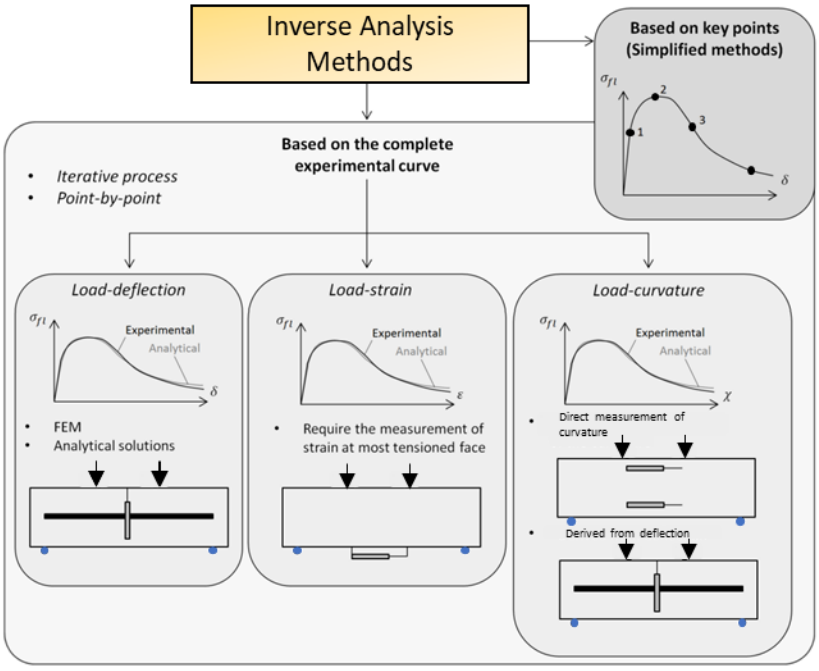

Figure 2- 11: Classification of Inverse Analysis methods (adapted from López, 2017)

Several researchers (Baby et al., 2013; López et al., 2016; Mobasher et al., 2014; Ostergaard et al., 2005; Rigaud et al., 2012; Soranakom & Mobasher, 2007, 2008; Tailhan et al., 2004; Georgiou & Pantazopoulou, 2016) have proposed inverse analysis methods that can be classified based on Figure 2- 11.

2.7.1 Inverse Analysis Method by the Canadian Standard

López et al. (2016) proposed a five-point inverse analysis method based on five critical points selected from the load-deflection curve and linked those with the tensile stress-strain behavior (see Figure 2- 12). This method derives the stress-strain behavior in tension up to the maximum tensile strength followed by stress-crack opening relationship. It utilizes a non-linear hinge model which varies based on the slenderness ratio of the specimen. Empirical relations were developed based on statistical analysis for two different sizes of FPBT specimen whose span length was equal to 3

and 4.5 times the depth of the specimen (i.e., $L=3h$ and $L= 4.5h$). The inverse analysis method for UHPFRC material recommended by Annex 8.1 of CSA S6:19 (2019) adapted the formulations developed by López et. al (2016) for an L=3h standard specimen. Moreover, Table U.2 of Annex U, CSA A23.1:19 (2019) recommends the standard prism size based on the fiber length (L_f) used in the UHPFRC mix (Figure 2- 13). The standard procedure for the inverse analysis method recommended by the Annex 8.1 is described below.

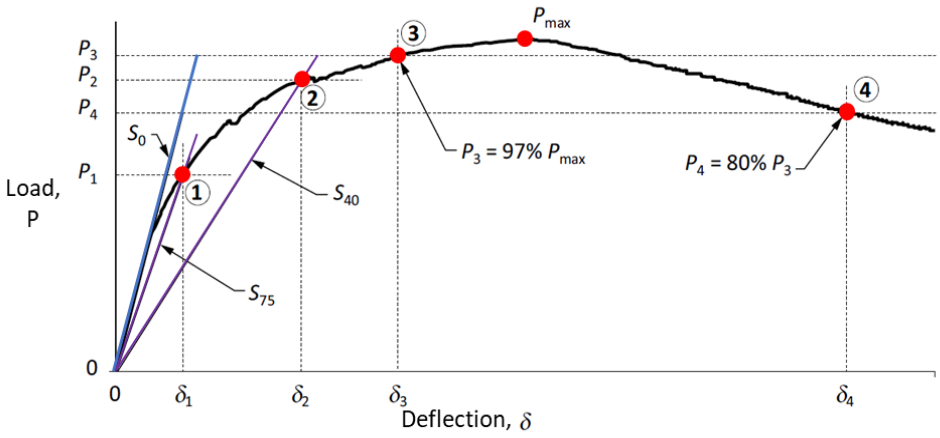

Figure 2- 12: Typical load-deflection curve from FPBT and critical points (adapted from López et al, 2016)

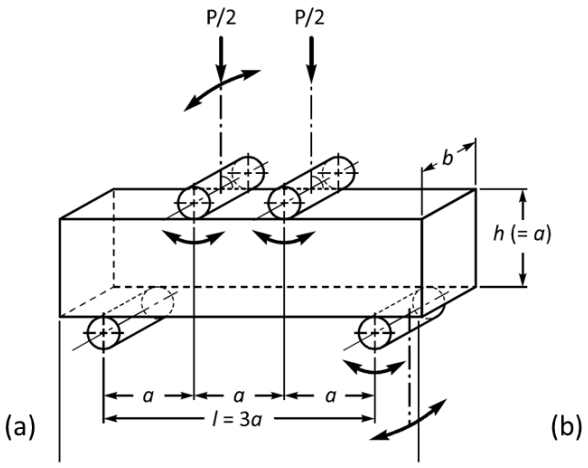

(b)

L_f	Nominal prism size
≤ 15 mm	75x75x280 mm
>15 mm to 20mm	100x100x370 mm
>20 mm to 25 mm	150x150x550 mm
>25 mm to 60 mm	200x200x720 mm

Figure 2- 13: (a) Standard four-point bending test; (b) Prism size vs Fiber length (Annex U of CSA A23.1, 2019)

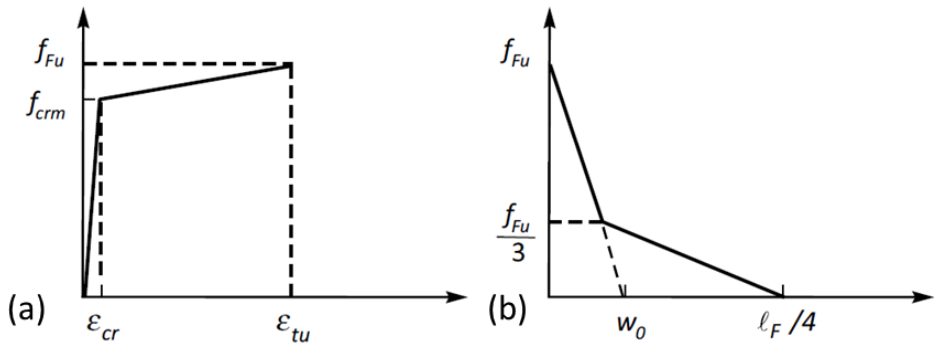

Figure 2- 14: Simplified tensile behavior extracted from the five-point inverse analysis (a) Stress-strain relation (b) Stress-crack width relation

The initial linear-elastic slope (S_o) of the load-deflection curve is determined first, followed by the estimation of lines with slopes equal to 75% (S_{75}) and 40% (S_{40}) of initial slope. Point 1 (P_1, δ_1) and point 2 (P_2, δ_2) illustrated in Figure 2- 12 are obtained by the intersection of secant stiffness lines S_{75} and S_{40} with the load-deflection curve, respectively. Point 3 (P_3, δ_3) is taken as 97% of the peak load (P_{max}) before the peak and the point 4 (P_4, δ_4) corresponds to the 80% of P_3 in the post-peak branch of the resistance curve. The fifth point P5 corresponds to 30% of P_3 in the post-peak region which is not included in the Annex 8.1. Once the characteristic points with load-deflection coordinates are obtained, the equations described in Table 2- 2 are used to obtain the tensile behavior of UHPFRC. It is important to measure the average distance of the crack tip (d_o) from the midspan of the specimen which is used in estimating the crack width (w_o). The corresponding equations of this inverse analysis for a specimen with a total length of L=4.5h can be found in López et. al (2016). The typical stress-strain and stress-crack width response corresponding to the tensile behavior of UHPFRC predicted by this method is represented in Figure 2- 14.

Table 2- 2: Inverse Analysis properties and their expressions for L=3h specimen (Annex 8.1, CSA S6:19)

Property	**L=3h**	**Normalized parameters**
E_{co}	$\frac{7.2}{b}S_o$	-
f_{crm}	$K_1\frac{P_1 L}{bh^2}$	$K_1 = \frac{(P_1/P_2)^{0.19}}{1.63}$
ε_{cr}	$\frac{f_{crm}}{E_{co}}$	-
ε_{tu}	$K_2\varepsilon_{cr}$	$K_2 = \left(7.65\frac{\delta_3}{\delta_1} - 10.53\right)$
f_{Fu}	$K_3 f_{crm}$	$K_3 = {K_2}^{-0.18}\left(2.46\frac{P_3}{P_1} - 1.76\right)$
ε_{to}	$K_4\varepsilon_{cr}$	$K_4 = {K_3}^{-0.37}{K_2}^{0.88}\left(3.0\frac{{\delta_4}^*}{\delta_3} - 1.80\right)$
w_o	$\left(\varepsilon_{to} - \varepsilon_{tu} + \frac{10 f_{Fu}}{3E_{co}}\right)\frac{3h}{2}$	-
${\delta_4}^* = K_5\delta_4$; where $K_5 = 1 + \frac{0.6}{L}d_o$		

2.7.2 Inverse Analysis Approach by the Swiss Standard

Annex E of the Swiss standard SIA 2052 (2016) also recommends the use of four-point bending test to determine the tensile behavior of UHPFRC. But here the tensile bending test is performed on a plate specimen with nominal dimensions of 100 mm x 30 mm x 500 mm (b x h x L) as per the loading configuration depicted in Figure 2- 15. The specimens are tested until the residual load is equal to 20% of the maximum load or a deflection at midspan equal to 25 mm is reached. The inverse analysis method described in SIA 2052, (2016) is classified as a simplified method as it uses a behavior model corresponding to different stages of the flexural test. The load-deflection curve obtained from FPBT is divided into two segments as shown in Figure 2- 16a. The first segment in the resistance curve characterizes the linear behavior of the material which terminates

at the yield load (Point A) where the linearity diminishes. The second segment is from the Point A to the Point B, where Point B represents the maximum load in the resistance curve.

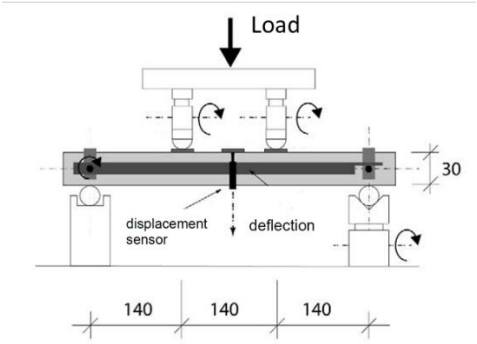

Figure 2- 15: Schematic of flexural plate specimen as per the Swiss standard (adapted from SIA 2052, 2016)

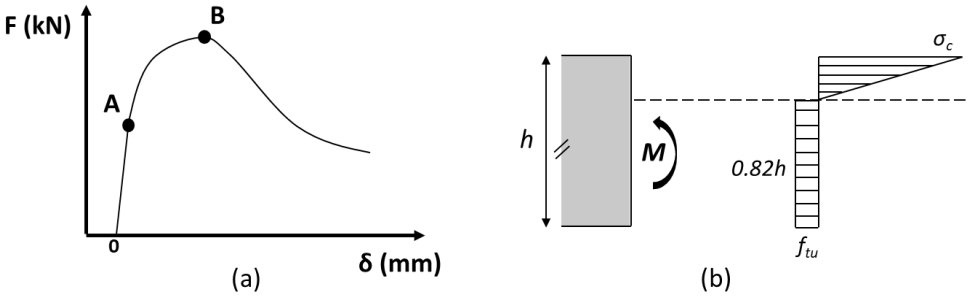

Figure 2- 16: (a) Typical response from FPBT and characteristic points (b) Assumed stress block corresponding to the maximum load (SIA 2052, 2016)

The modulus of elasticity is determined using Equation 2-6, The end of the linear elastic range is marked by the point where there is a reduction by more than 1% in the value of secant modulus.

$$E_i = (0.212) \cdot \frac{F_i}{\delta_i} \cdot \frac{L^3}{bh^3} \tag{2-6}$$

The elastic tensile strength $f_{t,cr}$ is determined based on a linear elastic model. In the linear elastic model, the neutral axis is assumed to be at the midheight of the cross-section. The load at Point A is used to obtain the elastic tensile strength as per Equation 2-7.

$$f_{t,cr} = \frac{M_A}{Z} = F_A \cdot \frac{L}{bh^2} \tag{2-7}$$

At the maximum load (point B), the cross-section is assumed to have the stress distribution shown in Figure 2- 16b. The corresponding ultimate tensile strength ($f_{t,u}$) is calculated as per Equation 2-8. The standard specifies that, if the calculated $f_{t,u}$ is lesser than $f_{t,cr}$, then the material response is not strain-hardening.

$$f_{t,u} = (0.383) \cdot F_B \cdot \frac{L}{bh^2} \tag{2-8}$$

For $f_{t,u} > f_{t,cr}$, the tensile stress and corresponding strains in the strain-hardening region can be calculated using the Equation 2-9 and Equation 2-10 by selecting 10 discrete points (F_i and δ_i) in this segment of the resistance curve. φ_i represents the curvature corresponding to the load-deflection pair considered and is obtained as per Equation 2-11. Among these points selected, the first point shall be chosen such that the corresponding value for α_i is greater than 0.5 (implying that 50% of the cross-section is already under plastic deformation). The remaining 9 points should be selected such that they are distributed uniformly between the first point and the Point B along the deflection axis.

$$\sigma_{t,i} = 0.5 \cdot (1 - \alpha_i)^2 \cdot h\varphi_i E \tag{2-9}$$

$$\varepsilon_{t,i} = \frac{\sigma_{t,i}}{E} + \alpha_i \varphi_i h \tag{2-10}$$

$$\varphi_i = \frac{216}{23} \cdot \frac{\delta_i}{L^2} \tag{2-11}$$

The term α_i may be obtained by using Table 8 of Annex E of SIA 2052 (2016) based on the value of λ_i which are calculated as per Equation 2-12 (refer to Table B-1).

$$\lambda_i = \frac{46}{216} \cdot \frac{F_i}{\delta_i E} \cdot \frac{L^3}{bh^3} \tag{2-12}$$

It is noteworthy that the expression used for estimating curvature from the experimental deflection values is based on the structural elastic mechanics' method and was found to be reasonably good by other researchers as well (Qian & Li, 2007; Rigaud et al., 2012). However, the non-linearity of the material in the strain-hardening phase is not considered which would underestimate the actual

strain experienced by the specimen and overestimates the post-cracking ultimate tensile strength of the UHPFRC (Zhu et al., 2021).

2.7.3 Stepwise Iterative Inverse Analysis Approach by the French Standard

As mentioned earlier, the French standard NF P18-470 (2016) classified the UHPFRC material into three classes (T1, T2 and T3) based on the hardening ratio ($f_{t,u}/f_{t,cr}$) obtained from characteristic and average tensile curves. Annex D of this standard recommends the inverse analysis of Class T1 and T2 material based on two types of tests: three-point bending test performed on notched prism and four-point bending test on un-notched prisms on square prisms with L=3h. However, for the Class T3 UHPFRC material that exhibits significant strain-hardening behavior, the inverse analysis described in Annex E of the standard is recommended. According to Annex E, thin plate specimens are tested in four-point bending, which enables the evaluation of the tensile behavior through the inverse analysis described below. The dimensions of the specimen should satisfy the following: thickness (h) should be not more than $3L_f$; width (b) is equal to $8L_f$; total span (L_p) should be lesser value of 20h and 60 cm; and the span between supports (L) is equal to L_p-2a, where a is the greater value of h/2 and 3 cm. L_f is the length of longest fiber used in the mix. Figure 2- 17 shows the schematic of the test setup and the relevant details pertaining to the geometry of FPBT specimen. Shear span is denoted as L_s which is equal to L/3.

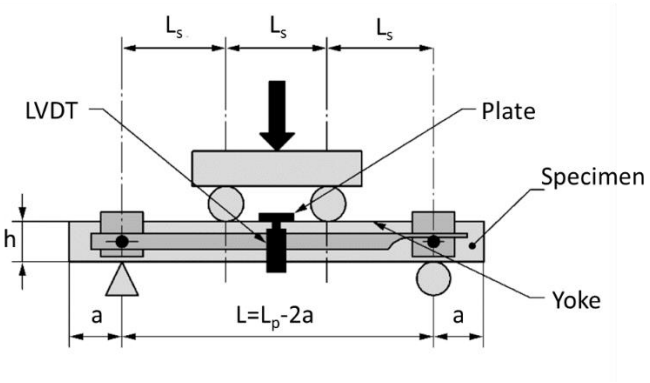

Figure 2- 17: Schematic test setup of FPBT plate specimen (adapted from NF P18-470, 2016)

The inverse analysis method prescribed by the French standard may be divided into two parts; first obtaining the moment-curvature relationship from the experimental moment-deflection response of FPBT, followed by estimating the corresponding stress-strain relation in tension. The elastic modulus (*E*) is determined by using the slope of central-third portion of the linear elastic response.

The slope of the curve obtained in this region (see Figure 2- 18) is multiplied by $(23L^2)/(216bh^3/12)$ to obtain the elastic modulus (E). The moment value corresponding to the apparent limit of elasticity ΔM is used to obtain tensile limit of elasticity $(f_{t,cr})$. ΔM shall be multiplied by $6/bh^2$ to obtain $f_{t,cr}$. Owing to the non-linear moment-curvature relationship observed after elasticity limit, the standard recommends evaluating the post-cracking tensile stress-strain properties through a stepwise inverse analysis procedure.

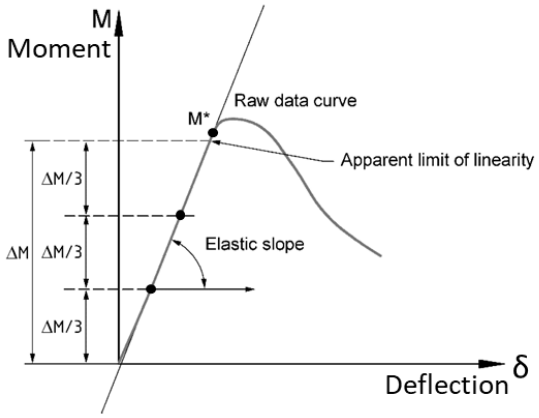

Figure 2- 18:Elastic behavior determination (adapted from NF P18-470, 2016)

For linear analysis up to the proportionality limit, Equation 2-13 can be used to obtain the curvature values from deflection readings measured during the test. The neutral axis may be assumed to be at the mid height of the cross-section up to the limit of the proportionality range. Tensile strains at the tension-most fiber of the cross-section may be calculated from Z_t (half of depth) multiplied by the curvature at each stage. Corresponding stress values may be obtained using strains, where it may be assumed that the stress equals to strain multiplied by the modulus of elasticity (E).

$$\delta_y = \frac{23L^2}{216}\varphi_y \tag{2-13}$$

Once the apparent limit of linearity is reached in the moment-deflection curve, the response in the Moment-Curvature curve will not be linear anymore. Curvature increases more for even a small increase in the applied moment due to the inelastic behavior of the material as depicted in Figure 2- 19. Hence, the relations used in the linear elastic region are not applicable beyond the yield moment. The French standard prescribes the use of an iterative procedure to determine the moment-curvature curve from the moment-deflection envelope. Curvature shall be taken as zero

at the zero moment. For a given M_n-δ_n couple, the curvatures ϕ_i associated with M_i are known for *i* =1 to n-1, then the curvature ϕ_n is determined to obtain the deflection δ_n. The curvature values ϕ_i for *i* equal to 1 to n are integrated twice to obtain the deflection δ_n. It is to be noted that the curvature is assumed to be constant in the constant moment region (middle third span).

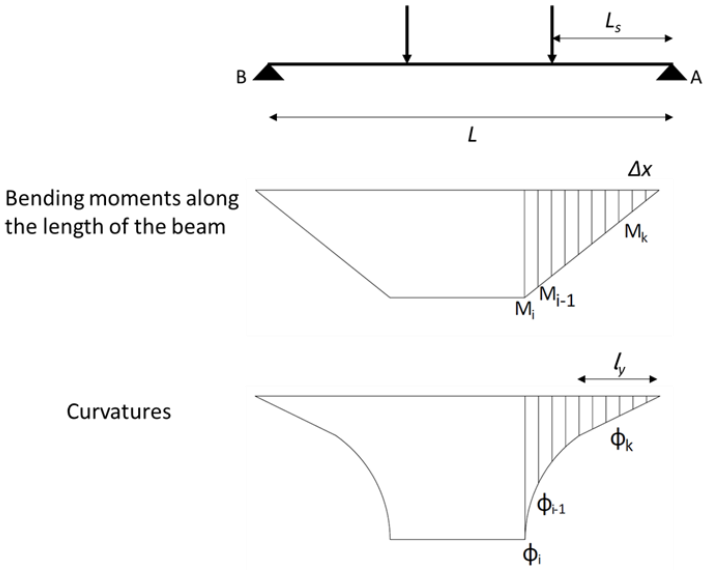

Figure 2- 19: Moment and curvature relation after yielding

A practical approach for the estimation of curvature values (ϕ_i) is described below. From Figure 2- 19, the shear span of the beam is discretized into *'n'* parts for *i=1 to n* with a value of $\Delta x_i = {L_s}/{n}$ *(small step size)*. With the known values of Moment-Curvature (M, φ) pairs up to the step *n-1*, the value of curvature (φ_i) for the *i=n* can be calculated using the measured deflection value (δ_n). Using the concepts of the 'Moment-Area method' and the 'Trapezoidal rule', and with reference to Figure 2- 19, the following expressions are derived:

$$\theta_{A,n} = \sum_{i=1}^{n} \varphi_i \cdot \Delta x_n = \sum_{i=1}^{n} \varphi_i \cdot \Delta x_n + \varphi_n \left(\frac{L_s}{2}\right) \tag{2-14}$$

$$\delta_n = \theta_{A,n} \cdot (1.5 \cdot L_s) - \left\{\sum_{i=1}^{n} \varphi_i \cdot \Delta x_n \cdot \left(1.5 \cdot L_s - \left(i - 1 + \frac{1}{2}\right) \cdot \Delta x_n\right) + \varphi_n \left(\frac{L_s}{2}\right) \cdot \left(\frac{L_s}{4}\right)\right\} \tag{2-15}$$

Substitution of Equation 2-14 into Equation 2-15 gives Equation 2-16 below, that may be used for back calculating the curvatures from the values of known deflections using an iterative approach, such as goal seek/solver in a spreadsheet.

$$\delta_n = \sum_{i=1}^{n} \varphi_i \cdot \left(i - \frac{1}{2}\right) \cdot {\Delta x_n}^2 + \frac{5}{8} \cdot \varphi_n \cdot {L_s}^2 \qquad (2\text{-}16)$$

Once the moment-curvature couples (M_i, ϕ_i) have been obtained, a second inverse analysis is performed to infer the tensile stress-strain law. The input data at each step *i* is a moment-curvature pair (M_i, ϕ_i). Objective is to estimate the values of tensile strain ($\varepsilon_{t,i}$) at the bottom-most fiber of the specimen and their corresponding stresses ($f_{t,i}$). At step i= 0, $\varepsilon_{t,0}$=0 and $f_{t,0}$= 0. Moreover, at step i=n, it is assumed that the values of $\varepsilon_{t,i}$ and $f_{t,i}$ are known for i=1 to n-1. Parameter β_i is defined as a factor for relative depth of the neutral axis, measured from the bottom fiber of the cross-section, under a given moment M_i. Equation 2-17 is determined based on the assumption of plane sections remaining plane which implies linear variation of strain distribution across the cross-section depth.

$$\varepsilon_{t,n} = -\varphi_n . \beta_n . h \qquad (2\text{-}17)$$

$$N_n = N_{c,n} + N_{t,n} = \frac{\varphi_n \cdot (1-\beta_n)^2 \cdot h^2 \cdot b \cdot E}{2} + \frac{1}{\varphi_n} \sum_{i=1}^{n} (\varepsilon_{i-1} - \varepsilon_i) \cdot \frac{(f_{t,i} + f_{t,i-1})}{2} \cdot b = 0 \qquad (2\text{-}18)$$

At step n-1, the force in compression and tension zones of the cross-section may be written as per Equation 2-19 and Equation 2-20, respectively. Similarly, at step n, $N_{t,n}$ may be written according to Equation 2-21. Figure 2- 20 illustrates the stress-strain states of the cross-section at two consecutive steps.

$$N_{c,n-1} = \frac{1}{2}(1 - \beta_{n-1})^2 \cdot bh^2 \left(\frac{\varepsilon_{t,n-1}}{\beta_{n-1} \cdot h}\right) \cdot E \qquad (2\text{-}19)$$

$$N_{t,n-1} = \left(-\frac{\beta_{n-1} \cdot h}{\varepsilon_{t,n-1}}\right) b \cdot \int_{\varepsilon_{t,n-1}}^{0} \sigma(\varepsilon) \cdot d\varepsilon = -\frac{1}{2} \frac{(1-\beta_{n-1})^2}{\beta_{n-1}} \cdot bh \left(-\varepsilon_{t,n-1}\right) \cdot E \qquad (2\text{-}20)$$

$$N_{t,n} = \left(-\frac{\beta_n \cdot h}{\varepsilon_{t,n}}\right) b \cdot \int_{\varepsilon_{t,n}}^{0} \sigma(\varepsilon) \cdot d\varepsilon = \left(-\frac{\beta_n \cdot h}{\varepsilon_{t,n}}\right) b \cdot \left[\int_{\varepsilon_{t,n-1}}^{0} \sigma(\varepsilon) \cdot d\varepsilon + \int_{\varepsilon_{t,n}}^{\varepsilon_{t,n-1}} \sigma(\varepsilon) \cdot d\varepsilon\right] \qquad (2\text{-}21)$$

$$-\frac{1}{2}\frac{(1-\beta_n)^2}{\beta_n}\cdot bh\left(-\varepsilon_{t,n-1}\right)\cdot E=\frac{\beta_n}{2\varepsilon_{t,n}}\cdot\frac{(1-\beta_{n-1})^2\cdot(\varepsilon_{t,n-1})^2\cdot bhE}{(\beta_{n-1})^2}-\frac{\beta_n}{\varepsilon_{t,n}}\cdot\frac{(f_{t,n}+f_{t,n-1})\cdot(\varepsilon_{t,n-1}-\varepsilon_{t,n})\cdot bh}{2} \quad (2\text{-}22)$$

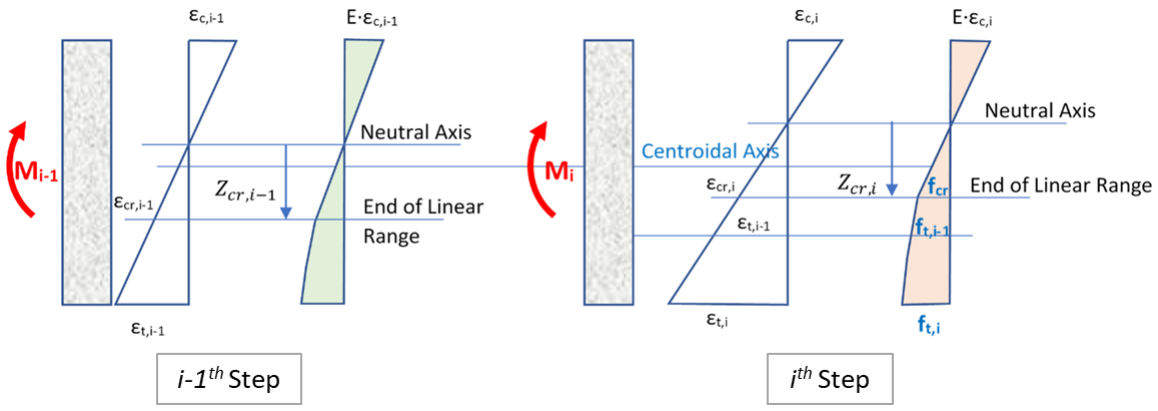

Figure 2- 20: The state of stress and strain for the cross-section at steps i-1 and i

From the Equation 2-22, a direct relationship between $f_{t,n}$ and β_n can be inferred based on the fact that $\varepsilon_{t,n}$ is obtained as a function of φ_n and β_n. Moment at step n, M_n can be determined from Equation 2-23. M_n is a function of $f_{t,n}$, $\varepsilon_{t,n}$ and β_n, whereas $f_{t,n}$ and $\varepsilon_{t,n}$ are functions of β_n. Hence, M_n is in turn a function of β_n only. Hence, it is now a problem with one equation and one unknown.

$$M_n=M_{c,n}+M_{t,n}=\frac{\varphi_n\cdot(1-\beta_n)^3\cdot h^3\cdot b\cdot E}{3}+\left(\frac{1}{\varphi_n}\right)^2\cdot\sum_{i=1}^{n}\left(\varepsilon_{t,i-1}-\varepsilon_{t,i}\right)\frac{\left[(2\varepsilon_{t,i}+\varepsilon_{t,i-1})\cdot f_{t,i}+(2\varepsilon_{t,i-1}+\varepsilon_{t,i})\cdot f_{t,i-1}\right]\cdot b}{6} \quad (2\text{-}23)$$

Hence, using the stepwise method and regression, the above procedure is followed to develop tensile stress-strain law of UHPFRC. It is to be noted that this method is very complex to implement and may involve certain instability due to convergence issues noticed during its implementation, particularly following the onset and penetration of cracking. Similar limitations of this approach were also reported by López (2017).

2.7.4 Simplified Inverse Analysis Method by the French Standard

AFNOR NF P18-470 (2016) also provides a simplified method for inverse analysis. The stress-strain distribution assumed under the maximum moment obtained from the resistance curve is

shown in Figure 2- 21. The modulus of elasticity (*E*) is determined as per the approach discussed in the preceding section (refer to Figure 2- 18). Once again, an elastic relationship is assumed between deflection and curvature as per Equation 2-24 same as in the case of other methods discussed in the preceding. However, the simplified method applies Equation 2-24 for curvature beyond yielding and up to maximum moment.

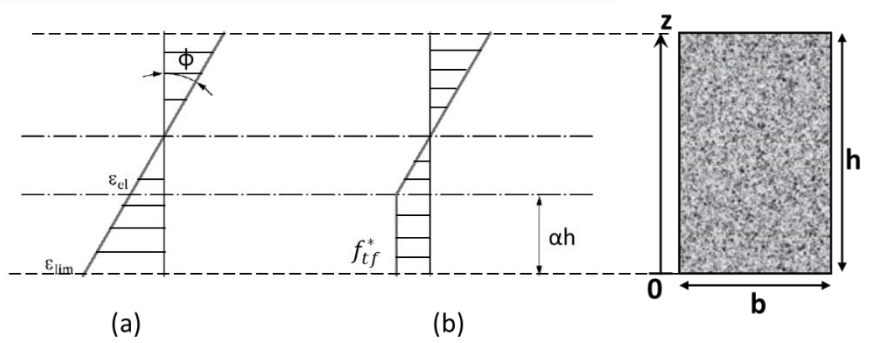

Figure 2- 21: Constitutive behavior assumed under maximum moment state with Simplified method (a) Strain distribution (b) Stress distribution. (NF P18-470, 2016)

$$\delta_i = \frac{23L^2}{216}\varphi_i \tag{2-24}$$

With reference to Figure 2- 21, the depth of cracked region is defined as αh, the elastic tensile strain is represented by ε_{el}, and ε_{lim} represents the limiting tensile strain corresponding to the strain of the bottom-most fiber at peak flexural moment. The cracked region experiences a constant tensile stress of f_{tf}^*. Based on the equilibrium of forces, the moment corresponding to the maximum load from the resistance curve is derived as per Equation 2-25.

$$M = (2\alpha^3 - 3\alpha^2 + 1) \cdot \frac{bh^3}{12} \cdot \varphi E \tag{2-25}$$

Knowing the value of maximum moment (M) and curvature (φ), α can be estimated from Equation 2-25. Subsequently, f_{tf}^* and ε_{lim} can be estimated from Equations 2-26 and 2-27, respectively. Figure 2- 22 depicts the simplified stress-strain law in tension recommended by the AFNOR standard.

$$f_{tf}^* = -\frac{1}{2}(1-\alpha)^2 \cdot h \cdot \varphi \cdot E \tag{2-26}$$

$$\varepsilon_{lim} = -\varphi \cdot \alpha \cdot h + \frac{f_{tf}^*}{E} \quad (2\text{-}27)$$

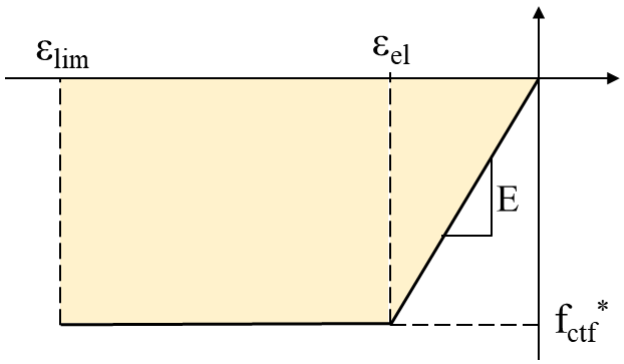

Figure 2- 22: Tensile stress-strain simplified law (adapted from NF P18-470, 2016)

2.7.5 Spreadsheet-based Inverse Analysis Approach by Mobasher et al. (2014)

The inverse analysis approach proposed by Mobasher et al. (2014, 2015) back-calculates the tensile characteristic properties of strain-hardening or strain softening FRC material with the use of spreadsheet analysis. Mobasher's work was based on the closed-form expressions developed by his peer researchers (Soranakom et al., 2007; 2008). The load-deflection response of the FRC material simulated by the inverse analysis is fitted against the experimental curve of a three-point or four-point bending test by varying parameters of the material model in tension or compression. A special report published by the American Concrete Institute ACI 544.8R-16 (2016) focuses on the indirect method to obtain stress-strain response of FRC. Appendix A of this report has proposed the inverse analysis procedure adapted from Mobasher et al. (2014, 2015).

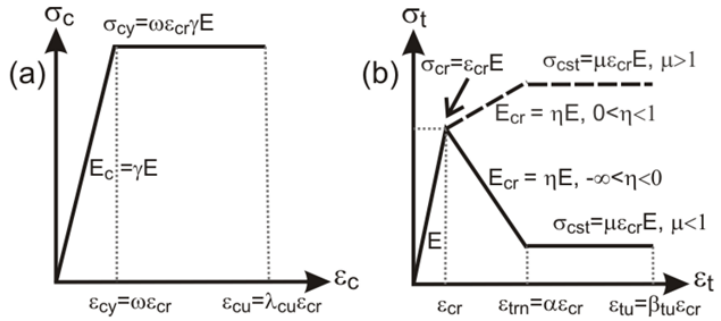

Figure 2- 23: Generalized models for strain-hardening/softening material (a) Compression (b) Tension (Mobasher et al. 2015)

Figure 2- 23 depicts the generalized material constitutive law in compression and tension along with the normalized parameters used. The compression model assumed is linear elastic perfectly plastic with the linear branch reaching a compressive strain of ε_{cy} followed by the constant stress branch that terminates at ε_{cu}. The tension model used is tri-linear, where the first region is linear elastic up to the strain ε_{cr}, followed by the branch representing the strain softening ($\eta<0$) or strain hardening ($0<\eta<1$) behavior of the material. Finally, the model consists of a constant stress branch which terminates at ε_{tu}. All the parameters used are normalized with respect to the two intrinsic parameters of first cracking in tension, which are cracking strain (ε_{cr}) and modulus of elasticity (E). The normalized parameters used in this method are shown in Equation 2-28.

$$\omega = \frac{\varepsilon_{cy}}{\varepsilon_{cr}};\ \alpha = \frac{\varepsilon_{trn}}{\varepsilon_{cr}};\ \beta_{tu} = \frac{\varepsilon_{tu}}{\varepsilon_{cr}};\ \lambda_{cu} = \frac{\varepsilon_{cu}}{\varepsilon_{cr}};\ \gamma = \frac{E_c}{E};\ \eta = \frac{E_{cr}}{E};\ \mu = \frac{\sigma_{cst}}{E\varepsilon_{cr}} \tag{2-28}$$

Usual assumptions such as plane sections remain plane and linear strain distribution across the cross-section were made to generate closed-form equations. *k* is the parameter for depth of neutral axis from topmost compression fiber. The parameter β and λ represents the ratio of maximum tensile and compressive strain of the cross-section normalized with the cracking strain. These two parameters are further related to each other based on the value of *k* as per Equation 2-29, where d is the depth of the section.

$$\beta = \frac{\varepsilon_{tbot}}{\varepsilon_{cr}};\ \lambda = \frac{\varepsilon_{ctop}}{\varepsilon_{cr}};\ \frac{\lambda\varepsilon_{cr}}{kd} = \frac{\beta\varepsilon_{cr}}{d-kd} \rightarrow \lambda = \frac{k}{1-k}\cdot\beta \tag{2-29}$$

Moment and curvature (M_i and ϕ_i) are normalized with respect to M_{cr} and φ_{cr} respectively, as per Equation 2-30 and Equation 2-31, respectively. The imposed parameter for analysis is the tensile strain factor (β) on the bottommost fiber of the cross section. There are 5 possible (behavioral) stages that a cross section can exhibit during its loading in flexure. Stage 1 corresponds to the region where both tensile and compressive zones perform linearly elastic with the neutral axis located at the mid height of the cross-section. At the end of Stage 1, Stage 2.1 corresponds to the condition where the tension zone is experiencing strain beyond the value of ε_{cr}, while the compression is still in the linear elastic range. If both the tension and compression zones are in the plastic stage, then this is represented by Stage 2.2. Similarly, when the tension zone is in the last branch of the tensile model, there are two possibilities: Stage 3.1 when compression strain ε_c is lesser than ε_{cy} and Stage 3.2 when $\varepsilon_c > \varepsilon_{cy}$. It is important to note that depending on

material parameters, any of the four stages could potentially occur after the Stage 1. However, the flexural behavior of UHPFRC is controlled by the tension, since compressive stress is generally low and within the elastic range. Moreover, the modulus in compression and tension is assumed to be nearly the same ($\gamma \approx 1$).

At any given stage (β_i), the parameters *k*, M_i' and ϕ_i' are obtained from the governing equations of that respective stage summarized in Table 2- 3. μ_{cr} is a critical parameter that defines if the deflections calculated belong to strain hardening or softening. If $\mu_u < \mu_{crit}$, then it is strain softening, and $\mu_u > \mu_{crit}$ corresponds to the strain-hardening behavior. μ_{crit} is the critical normalized post-crack tensile strength defined in Equation 2-32.

$$M_i = M_i' \cdot M_{cr} \; ; \qquad M_{cr} = \frac{bd^2}{6} \cdot E\varepsilon_{cr} \tag{2-30}$$

$$\phi_i = \phi_i' \cdot \phi_{cr} \; ; \qquad \phi_{cr} = \frac{2\varepsilon_{cr}}{d} \tag{2-31}$$

$$\mu_{crit} = \frac{\omega}{3\omega - 1} \tag{2-32}$$

For a given stage, the corresponding compressive and tensile stresses can be calculated from the expressions below:

$$\frac{\sigma_c}{E\varepsilon_{cr}} = \begin{cases} \gamma\lambda & 0 \le \lambda \le \omega \\ \gamma\omega & \omega < \lambda \le \lambda_{cu} \\ 0 & \lambda_{cu} \le \lambda \end{cases} \tag{2-33}$$

$$\frac{\sigma_t}{E\varepsilon_{cr}} = \begin{cases} \beta & 0 \le \beta \le 1 \\ 1 + \eta(\beta - 1) & 1 < \beta \le \alpha \\ \mu & \alpha < \beta \le \beta_{tu} \\ 0 & \beta_{tu} \le \beta \end{cases} \tag{2-34}$$

Moment-curvature distribution is assumed to be bilinear after the cracking stage (see Figure 2-24). Equation 2-35 is valid up to the cracking stage, whereas Equation 2-36 may be used for estimating deflection in the post-cracking stage for strain-hardening response ($\mu_u > \mu_{crit}$).

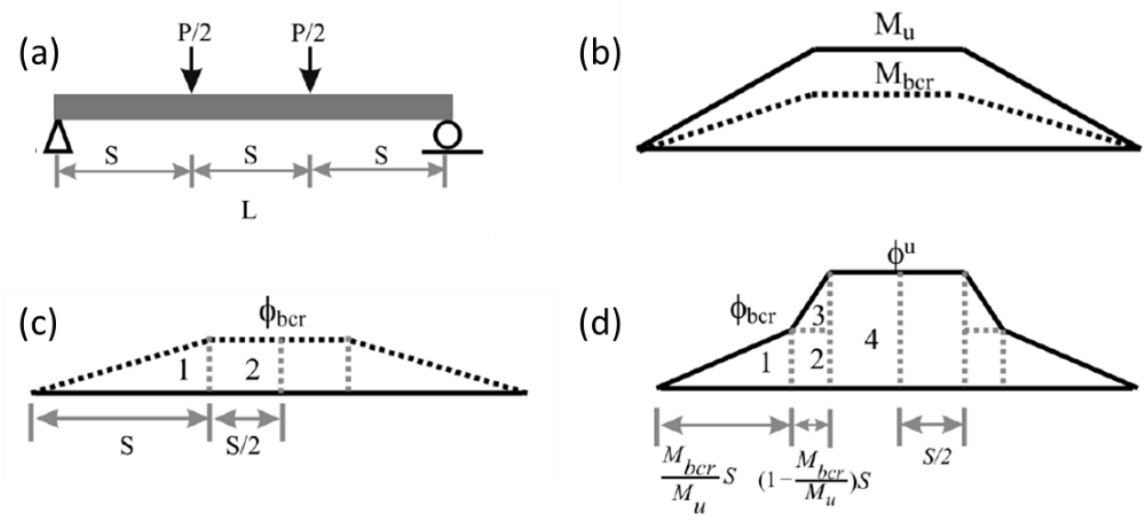

Figure 2- 24:(a) Schematic of four-point bending test (b) Moment distribution (c) Curvature distribution at first bilinear cracking (d) Curvature distribution at ultimate moment for strain-hardening (Mobasher et al. 2015)

$$\delta_{cr} = \frac{23L^2}{216}\phi_{cr} \tag{2-35}$$

$$\delta_u = \frac{L^2}{216M_u^2}[(4M_u^2 + 4M_u.M_{cr}).\phi_{cr} + (23M_u^2 - 4M_u.M_{cr} - 4M_{cr}^2).\phi_u] \tag{2-36}$$

Hence, the load-deflection response is simulated using the input of the tensile and compression models. Parameters E and ε_{cr} may be adjusted to fit the linear part of the load-deflection response and parameters $\alpha, \mu \; and \; \eta$ may be adjusted to better match the simulated response with the experimental one.

Table 2- 3: Governing equations for calculation of parameter k, M' and φ' for each stage of normalized tensile strain (β) (Mobasher et al. 2014, 2015)

Stage	Parameters	k	M', ϕ'
1	$0 \le \beta \le 1$	$k_1 = \begin{cases} \frac{1}{2}\ for\ \gamma = 1 \\ \frac{-1+\sqrt{\gamma}}{-1+\gamma}\ for\ \gamma \neq 1 \end{cases}$	$M_1' = \frac{2\beta[(\gamma-1)k_1^3+3k_1^2-3k_1+1]}{1-k_1}$ $\phi_1' = \frac{\beta}{2(1-k_1)}$
2.1	$1 < \beta \le \alpha$ $0 \le \lambda \le \omega$	$k_{21} = \frac{D_{21}-\sqrt{D_{21}\gamma\beta^2}}{D_{21}-\gamma\beta^2}$ $D_{21} = \eta(\beta^2-2\beta+1)+2\beta-1$	$M_{21}' = \frac{(2\gamma\beta-C_{21})K_{21}^3+3C_{21}K_{21}^2-3C_{21}K_{21}+C_{21}}{1-k_{21}}$ $C_{21} = \frac{(2\beta^3-3\beta^2+1)\eta+3\beta^2-1}{\beta^2}$ $\phi_{21}' = \frac{\beta}{2(1-k_{21})}$
2.2	$1 < \beta \le \alpha$ $\omega < \lambda \le \lambda_{cu}$	$k_{22} = \frac{D_{22}}{D_{22}+2\omega\gamma\beta}$ $D_{22} = D_{21}+\gamma\omega^2$	$M_{22}' = (3\gamma\omega+C_{22})K_{22}^2-2C_{22}K_{22}+C_{22}$ $C_{22} = C_{21}-\frac{\gamma\omega^3}{\beta^2}$ $\phi_{22}' = \frac{\beta}{2(1-k_{22})}$
3.1	$\alpha < \beta \le \beta_{tu}$ $0 \le \lambda \le \omega$	$k_{31} = \frac{D_{31}-\sqrt{D_{31}\gamma\beta^2}}{D_{31}-\gamma\beta^2}$ $D_{31} = \eta(\alpha^2-2\alpha+1)+2\mu(\beta-\alpha)+2\alpha-1$	$M_{31}' = \frac{(2\gamma\beta-C_{31})K_{31}^3+3C_{31}K_{31}^2-3C_{31}K_{31}+C_{31}}{1-k_{31}}$ $C_{31} = \frac{(2\alpha^3-3\alpha^2+1)\eta-3\mu(\alpha^2-\beta^2)+3\alpha^2-1}{\beta^2}$ $\phi_{31}' = \frac{\beta}{2(1-k_{31})}$
3.2	$\alpha < \beta \le \beta_{tu}$ $\omega < \lambda \le \lambda_{cu}$	$k_{32} = \frac{D_{32}}{D_{32}+2\omega\gamma\beta}$ $D_{32} = D_{31}+\gamma\omega^2$	$M_{32}' = (3\gamma\omega+C_{32})K_{32}^2-2C_{32}K_{32}+C_{32}$ $C_{32} = C_{31}-\frac{\gamma\omega^3}{\beta^2}$; $\phi_{32}' = \frac{\beta}{2(1-k_{32})}$

2.8 Analytical Stress-Strain Model for Uniaxial Compression of UHPFRC

2.8.1 Model Recommended by the French Standard

The French Standard, AFNOR NF P18-710 (2016), recommended the analytical stress-strain model for UHPFRC in uniaxial compression that could be used for the non-linear structural analysis. Relationships of the model are defined by Equations 2-37 to 2-43, where f_c' is the compressive strength, f_{tu} is the ultimate tensile strength, and E_c is the modulus of elasticity (all in MPa units).

$$\sigma = f_c' . \frac{\eta \cdot \frac{\varepsilon}{\varepsilon_{co}}}{\eta - 1 + \left(\frac{\varepsilon}{\varepsilon_{co}}\right)^{\varphi \cdot \eta}} \tag{2-37}$$

$$\varepsilon_{co} = \left[1 + 4\left(\frac{\sigma_{lat}}{f_c'}\right)\right]\left[1 + 0.16\frac{k_0}{\left(f_c'^{\,2} + 800\right)}\right]\left(\frac{f_c'^{\,2/3}}{k_0}\right) \tag{2-38}$$

$$\sigma_{lat} = \frac{f_{tu}}{K_{global}} \tag{2-39}$$

Equation 2-39 takes into account the confinement effect due to the fibers through post-cracking strength. K_{global} is the global fiber orientation factor recommended as 1.25 as per the Annex-T of NF P18-710:2016.

$$k_0 = \frac{E_c}{f_c'^{1/3}} \tag{2-40}$$

$$\eta = \frac{k}{k-1};\ k = E_c \frac{\varepsilon_{co}}{f_c'} \tag{2-41}$$

$$\varphi = \begin{cases} 1 & for\ \varepsilon < \varepsilon_{co} \\ \dfrac{\ln\left(1 - \eta + \frac{\eta \cdot \varepsilon_{cu}}{0.7 \cdot \varepsilon_{co}}\right)}{\eta \cdot \ln\left(\frac{\varepsilon_{cu}}{\varepsilon_{co}}\right)} & for\ \varepsilon > \varepsilon_{co} \end{cases} \tag{2-42}$$

$$\varepsilon_{cu} = \left[1 + 15\frac{\sigma_{lat}}{f_c'}\right]\left[1 + \frac{20}{f_c'}\right]\left[1 + 0.16\frac{k_0}{\left(f_c'^2 + 800\right)}\right]\left(\frac{f_c'^{2/3}}{k_0}\right) \quad (2\text{-}43)$$

It is noted that this model is compatible in form for the stress-strain curve with that proposed by Popovics (1973) for concrete in general. However, the important attribute here is the explicit consideration of the internal confinement in the strain capacity of the material in compression. Moreover, in very thin sections, the lateral confinement effect (σ_{lat}) is to be taken as 0 in the above expressions. This is due to the preferred orientation of fibers parallel to the walls of the mold which do not allow for confinement effect to be effective. The ultimate strain (ε_{cu}) corresponds to 70% residual stress in the post-peak region. A representative curve of the stress-strain relationships proposed by this model is shown in Figure 2- 25.

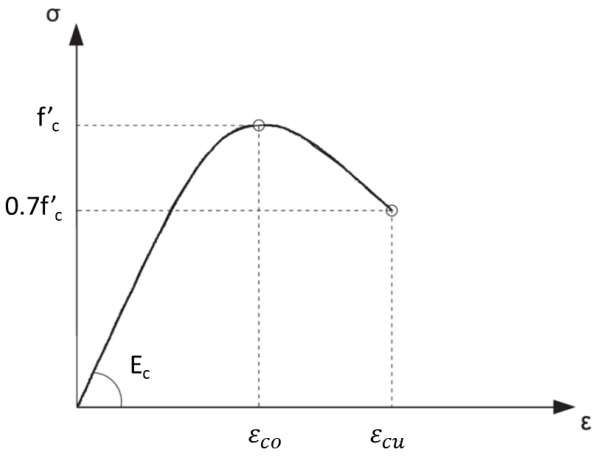

Figure 2- 25: Stress-strain relation of UHPFRC in compression as per AFNOR NF P18-710 (2016)

2.8.2 Model Proposed by Naeimi & Moustafa (2021)

Naeimi & Moustafa (2021) proposed an analytical model for the compressive behavior of steel spiral confined UHPFRC that could also be extended to unconfined UHPFRC. The model comprised of three regions of which the first two regions uses the expression proposed by Popovics (1973) but with modified parameters. The third region was expressed through an exponential relationship that maintains a residual stress owing to the confinement from steel fibers or transverse reinforcement. Material parameters associated with the stress-strain relationships were defined by the parameters $\beta_1, \beta_2, \beta_3, k_1$ and k_2 which were calibrated through extensive testing of confined and unconfined UHPFRC cylinder specimens tested by the investigator (Naeimi, 2020;

Naeimi & Moustafa, 2019, 2021). Expressions proposed by the researchers are summarized in Table 2- 4 along with their respective parameters.

Table 2- 4: Compression stress-strain relationships for UHPFRC proposed by Naeimi & Moustafa (2021)

Expression (in MPa)	Calibrated Parameter
$E_c = 3400\sqrt{f'_{c,v_f=0}} + 1310v_f$	
$f'_{cc} = f'_{c,v_f=0} + 6.26v_f + 6.57\rho_s$	
$\varepsilon'_{cc} = \varepsilon'_{c,v_f=0} + 7.82 \cdot 10^{-5} \cdot v_f + 3.49 \cdot 10^{-4} \cdot \rho_s$	
$\varepsilon'_{c,v_f=0} = 2.54 \cdot 10^{-5} \cdot f'_{c,v_f=0}$	
$f_c = f'_{cc}\left[\frac{\beta_1 \cdot \frac{\varepsilon_c}{\varepsilon'_{cc}}}{\beta_1 - 1 + \left(\frac{\varepsilon_c}{\varepsilon'_{cc}}\right)^{\beta_1}}\right] \; for\; \varepsilon_c \le \varepsilon'_{cc}$	$\beta_1 = \frac{1}{1 - \frac{f'_{cc}}{\varepsilon'_{cc}E_c}}$
$f_c = f'_{cc}\left[\frac{\beta_2 \cdot \frac{\varepsilon_c}{\varepsilon'_{cc}}}{\beta_2 - 1 + \left(\frac{\varepsilon_c}{\varepsilon'_{cc}}\right)^{\beta_3}}\right] \; for\; \varepsilon'_{cc} \le \varepsilon_c \le \varepsilon_{cc,d}$	$\beta_2 = 3.096 - 0.0941v_f - 0.2073\rho_s$ $\beta_3 = 3.793 - 0.2314v_f - 0.0100\rho_s$
$f_c = \eta_d f'_{cc}\left[e^{-k_1\left(\frac{\varepsilon_c - \varepsilon_{cd}}{\varepsilon'_{cc}}\right)^{k_2}}\right] \; for\; \varepsilon_c \ge \varepsilon_{cc,d}$	$\eta_d = 0.289 + 0.004v_f + 0.052\rho_s$ $k_1 = 0.2392 + 0.0112v_f - 0.0207\rho_s$ $k_2 = 0.8975 - 0.0613v_f - 0.0129\rho_s$

The strain value ($\varepsilon_{cc,d}$) corresponding to the end of second region may be estimated from the equation corresponding to the second region by using $f_c = \eta_d f'_{cc}$. Moreover, Naeimi & Moustafa (2021) proposed calibrated empirical expressions for estimating the modulus of elasticity, confined stress and strain of UHPC as a function of volume fraction of fibers (v_f) and transverse reinforcement ratio of steel spirals (ρ_s) as shown in Table 2-4. It is to be noted that, the parameters used in the stress-strain relationships proposed by Naeimi & Moustafa (2021) were calibrated based on specimens obtained from Ductal© mix only and did not consider any other proprietary or non-proprietary mixes. Furthermore, cylindrical specimen sizes such as 75 mm x 150 mm and 50

mm x 100 mm were considered throughout their experimental program, and the adverse effects of transverse reinforcement on fiber distribution was reported in some cases due to the small size of the specimens used.

Chapter 3: Determination of Tensile Behavior of UHPFRC

3.1 Introduction

This chapter presents the results of a characterization study conducted for developing the material identity of the UHPFRC mix used in this research. Various mechanical tests were performed including the Compression tests to evaluate peak strength and stress-strain response, Modulus of Elasticity and Poison's Ratio tests, Flexural response under four-point bending, Direct Tension and Splitting Tensile tests. Effects of casting methodology and prism size were studied in case of flexural tests besides testing two geometrically different specimens in direct tension. An inverse analysis methodology is proposed based on the layer-based sectional analysis of a prism tested under four-point bending to predict the tensile behavior of UHPFRC. Tensile properties estimated using the proposed inverse analysis method are validated with the experimental results of direct tension tests and compared with other methods from the literature. Digital image correlation (DIC) used to measure tensile stress-strain response for the direct tension test specimens is also presented.

3.2 Materials and Casting

Ultra-high-performance fiber-reinforced concrete used in this research was produced from the prepackaged dry cementitious mix powder 'Inducast TT-5' provided by the manufacturer Densit®. Hereinafter this UHPFRC premix material is simply called *Densit* and the mix produced for characterization study is referred to as *DE2,* where the integer 2 represents the volume fraction of fibers in the mix. Densit premix is a cement-based powder which contains Portland cement, ultra-fine silica fume particles, calcined bauxite sand (0-1mm) and a concrete superplasticizer. No other external superplasticizer was used. 2% by volume of straight steel fibers (from Bekaert Dramix®), 0.2 mm in diameter and 13mm in length were used as fiber reinforcement in the mix DE2 which was cast on May 25th, 2021. Nominal aspect ratio of steel fibers used was equal to 65. Fibers used were brass coated, High Carbon Steel (HCS) with a reported tensile strength of about 2,750 MPa. Mix proportions are provided in Table 3- 1.

A large pan type drum mixer with a nominal capacity of 400-litre was used to produce the UHPFRC mix. Densit dry mix powder was poured into the drum and mixed for about 2 minutes followed by addition of half the water required and mixed for 5 minutes. The remaining half of the water was then added and mixed for another 5 minutes. Lastly, steel fibers were gradually added

and mixed until they were evenly distributed (2 to 3 minutes). Figure 3- 1 illustrates the mixing procedure followed.

Table 3- 1: Mix design proportions of the UHPFRC Mix DE2

Mix DE2	Densit® dry mix	Water	Fibers
Proportions by weight	1	0.13	0.066

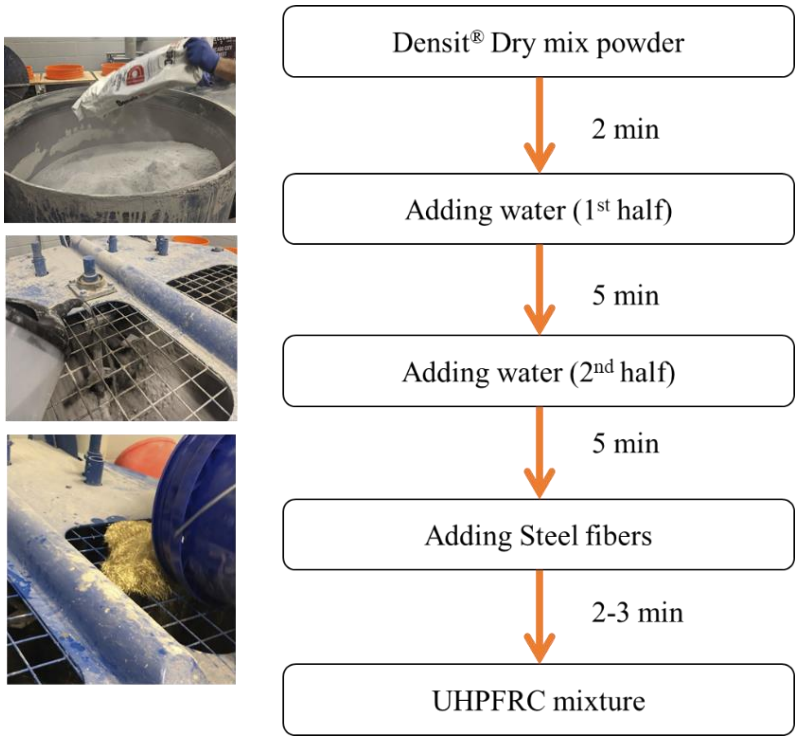

Figure 3- 1: An illustrative flowchart of UHPFRC mixing process

The UHPFRC produced was flowable and self-consolidating. Immediately after the mixing process, flowability of each mix was determined using a flow table test as per ASTM C1856 (2017). The conical mold of the flow table test was filled with fresh UHPFRC in a single pour up to the brim before being lifted over to allow the concrete to spread. Flow value was determined using the average diameter of the UHPFRC flow which was measured after about 2 minutes of lifting the mold (Figure 3- 2). The average flow value for the mix DE2 was found to be about 240 mm which indicated sufficient flowability of the UHPFRC produced.

Figure 3- 2: UHPFRC Flow test

Acrylic and wooden molds were used for casting flexural and direct tension test specimens, whereas standard plastic molds were used for casting cylindrical specimens. All the molds were lightly coated with oil prior to the casting to act as a releasing agent. Specimens were covered after casting and allowed to harden in the ambient environment before demolding. Demolding was performed after about 48 hours from casting. Thereafter all the specimens were cured in a water tank for around 28 days. Figure 3- 3 depicts the state of various specimens immediately after casting was completed.

Figure 3- 3: Specimens immediately after casting

For flexural tests, two different sizes of prism specimens along with two different casting methodologies were cast. Specimens are divided into two categories- Random (R) and One-way (OW), based on the casting methodology. One-way specimens were cast by pouring fresh UHPFRC from one end and the mold was allowed to be filled based on the self-flowing capability of the material. Random specimens were casted by pouring the mix at different locations along the

span of a specimen. In other words, no distinct pattern was followed for casting random (R) specimens. Direct tension tests included three different types of specimens based on specimen geometry and casting methodology. Cylindrical specimens of 75 mm x 150 mm were prepared for compression, modulus of elasticity and Poisson's ratio tests. Lastly, for splitting tensile test cylinder specimens of 100 mm x 200 mm were cast which were cut into two halves before testing. More details about different specimens and the tests are discussed in the forthcoming sections.

3.3 Mechanical Tests

3.3.1 Compression Test

Cylindrical specimens having nominal dimensions of 75 mm x 150 mm (diameter x height) were tested in uniaxial compression. Cylinders were cast in a plastic mold with inner surfaces oiled prior to casting. Consolidation techniques such as vibration table or a tamping rod were not utilized since the UHPFRC used is self-consolidating and flowable. Gentle tapping was done on the exterior of the molds to release any entrapped air bubbles. The top surface of the filled mold was levelled with a trowel. Molds were closed using lids on the top after casting. After allowing to harden for about 48 hours, cylinders were demolded using the air pressure applied from the bottom of the mold. Specimens were cured in a water tank maintained at room temperature for 28 days to allow for complete curing. After the curing period, cylinders were ground on both top and bottom surfaces, as depicted in Figure 3- 4, to achieve smooth and flat surface before they were tested. The flatness of the cylinder surface was ensured using a bubble level. If needed, cylinders were further ground until they would attain the desired flat surfaces. Dimensions of the cylinders were measured using a digital vernier caliper. The diameter used to calculate the cross-sectional area was obtained by averaging the diameters measured at right angles at top and bottom of the cylinder. Average height obtained from four readings taken at orthogonal locations were used in calculations.

Figure 3- 4: Cylinder grinding

Figure 3- 5: Compressive strength test setup

To obtain the compressive strength, cylinders were tested using *Controls Pilot* machine which is a load-controlled compression machine. All cylinders were tested at a mature age (just after 28 days). A loading rate of 1 MPa/s based on recommendations by Annex U of CSA A23.1 (2019) was utilized to obtain the peak load sustained by the specimen. Figure 3- 5 depicts the compression test setup. Equation 3-1 was used to calculate the compressive strength (f_c') of a specimen using the peak load (P) and the average diameter (D). The average compressive strength for Mix DE2 was estimated to be 177 MPa with the standard deviation equal to 2.26 MPa. Peak load and compressive strength estimated for each cylinder are summarized in Table 3- 2. Since it was a load-controlled test, the attainment of failure accompanied with an exploding sound marked the end of test. Cylinders generally held their integrity despite sudden failure and large crack formation upon attainment of the peak load. This is attributed to the confinement provided by the fibers and bridging action of fibers across the cracks formed. Developed cracks were diagonal and longitudinal to the direction of loading as shown in Figure 3- 6.

$$f_c' = \frac{4P}{\pi D^2} \tag{3-1}$$

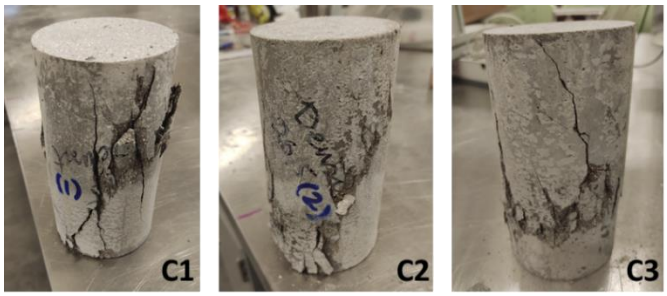

Figure 3- 6: Failure mode in Compressive Strength tests (Mix DE2)

Table 3- 2: Compressive Strength Results (Mix DE2)

Cylinder	Peak Load	Compressive Strength	Average Strength
	(kN)	(MPa)	(MPa)
C1	820	179	**177**
C2	833	178	
C3	803	174	

3.3.2 Modulus of Elasticity and Poisson's Ratio

The Modulus of Elasticity (E) and Poisson's ratio (ν) were determined as per the guidelines of ASTM C469 (2014) standard. Three cylinders (C4, C5 and C7) from the mix DE2 were tested using a servo-controlled closed loop universal testing machine (UTM by MTS). Specimens were prepared with installation of strain gauges on the lateral surface of the cylinders to obtain the strain readings in longitudinal and transverse directions. Four foil strain gauges of 10 mm gauge length were placed diametrically opposite at the mid height of the cylinder. Out of these four strain gauges, two were placed in the longitudinal direction (parallel to loading) to record longitudinal strain values and the other two were placed in the transverse direction (horizontally) to record transverse strain values. Before placing the strain gauges on to the cylinder, the surface of the cylinder was thoroughly cleaned of any dust with a sandpaper and a brush. Super glue adhesive was applied at the location where strain gauge was to be placed and a non-stick foil was used to place the strain gauge firmly before allowing it to dry. It is to be noted that the terminal surface of

the strain gauge should be facing outside on the cylinder and its electrical terminals were soldered to the electrical wires using a lead wire. The strain gauges were covered using a protective rubber tape to avoid damage due to specimen handling around the laboratory. The wires were connected to the data acquisition (DAQ) unit to record the strain data which was synchronized with the load data obtained from the compression machine. It is important to keep the two electrical terminals of a strain gauge from merging into each other during a test, which otherwise would provide erroneous measurements. Figure 3- 7 shows various stages of a cylindrical specimen as it was being prepared for Modulus of Elasticity and Poisson's ratio test.

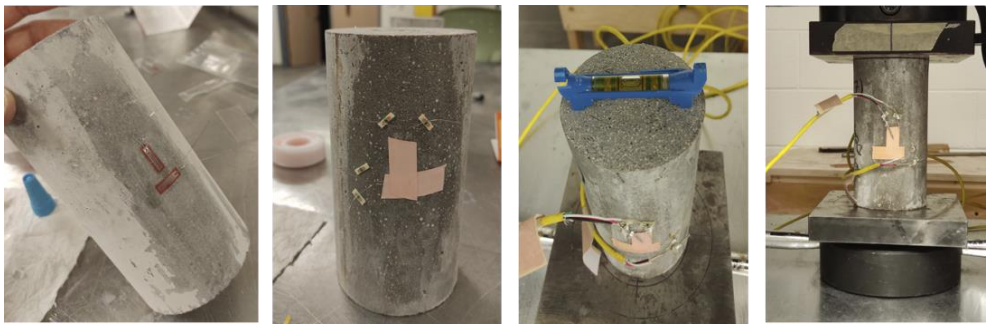

Figure 3- 7: Cylindrical specimen preparation for E & v tests

As per the standard procedure recommended by ASTM C469 (2014), the cylinder was loaded up to 40% of its maximum compressive stress alongside measuring the strain readings from the strain gauges and three such repetitions were performed for each cylinder. Result of three repetitions for each specimen and their average values are presented in Table 3- 3. Average compressive strength corresponding to the three cylinders tested for peak strength (Table 3- 2) was used to determine the 40% compressive load capacity of this particular mix.

The values of *E* and *ν* were estimated using Equation 3-2 and Equation 3-3, respectively, where σ_1 and σ_2 are the compressive stresses corresponding to a longitudinal strain of 50 μm/m and 40% of the compressive strength, respectively. Parameter ε_1 represents a longitudinal strain of 50 μm/m and ε_2 is the longitudinal strain corresponding to σ_2;also, ε_{t1} and ε_{t2} are the transverse strains corresponding to σ_1 and σ_2, respectively. Based on the results of three cylinders, the average static modulus of elasticity (E) was 49.44 GPa and the average Poisson's ratio (ν) was 0.25. Poisson's ratio estimated here was higher than most other reported values found in the literature (Graybeal, 2005; Joh et al., 2008; Simon, 2009) and further tests are recommended to arrive at a better

average. Great variability was also reported in the individual values of Poisson's ratio measured for each cylinder in a Dura mix by Husain (2021). However, the average of ten specimens was found to be relatively consistent with the expected value of about 0.2.

$$E = \frac{\sigma_2 - \sigma_1}{\varepsilon_2 - \varepsilon_1} \tag{3-2}$$

$$\nu = \frac{\varepsilon_{t2} - \varepsilon_{t1}}{\varepsilon_2 - \varepsilon_1} \tag{3-3}$$

Table 3- 3: Modulus of Elasticity and Poisson's ratio test results

Cylinder ID	ε_1 (μm/m)	ε_2 (μm/m)	ε_{t1} (μm/m)	ε_{t2} (μm/m)	σ_1 (MPa)	σ_2 (MPa)	***E*** (GPa)	***v***
C4	50	1347	14	342	2.03	70.06	52.47	0.25
	50	1351	14	343	2.03	70.20	52.39	0.25
	50	1353	13	344	1.98	70.21	52.35	0.25
	Average						**52.40**	**0.25**
C5	50	1542	10	363	1.67	69.88	45.72	0.24
	50	1529	10	361	1.75	69.93	46.12	0.24
	50	1520	10	360	1.80	69.88	46.31	0.24
	Average						**46.05**	**0.24**
C7	50	1363	13	349	2.87	67.98	49.60	0.26
	50	1354	13	349	2.79	67.99	50.03	0.26
	50	1357	12	348	2.65	67.95	49.96	0.26
	Average						**49.86**	**0.26**
	Overall Average						**49.44**	**0.25**

Several expressions have been proposed in the literature for predicting the modulus of Elasticity of UHPFRC from its average compressive strength. The expression proposed by Ma et al. (2004) suits best with the results obtained here, shown as per Equation 3-4. This expression was proposed for UHPFRC without coarse aggregates having the compressive strength range between 150 MPa to 180 MPa. Using the average compressive strength presented in Table 3- 2, Equation 3-4 predicts the modulus of elasticity to be equal to 49,515 MPa with less than 1% error compared to the experimental value reported in Table 3- 3.

$$E_c = 19000 \cdot \left(f_c'/10\right)^{1/3} \quad in\ MPa \tag{3-4}$$

3.3.3 Stress-Strain Response in Uniaxial Compression

In order to measure the full stress-strain response of the material in compression, three cylindrical samples (C4, C5 and C7) from the mix DE2 were tested. These are the same specimens that were used to perform modulus of Elasticity and Poisson's ratio test discussed in the previous section. These tests were performed in a different compression testing machine (*Controls Automax*) with a load capacity of 3000 kN which was also capable of applying displacement-controlled loading (see Figure 3- 8). The rate of displacement loading used was equal to 0.10 mm/min (~0.5 MPa/s). Strain gauges earlier installed on the cylinders were used to measure the strain readings. As described earlier in Section 3.3.2, each specimen is equipped with four strain gauges- two in each horizontal and vertical directions placed at mid height of the cylinder. Average of readings from the two vertical strain gauges were used to obtain stress-strain response in uniaxial compression as shown in Figure 3- 9. It is to be noted that the age of cylindrical specimens on the day of stress-strain tests was about 365 days. Hence, an increase in average compressive strength of about 8% was observed on account of further hydration caused due to aging of specimens. These cylinders were stored at room temperature but not in refrigerators to avoid any possible damage to the installed strain gauges. Excess cylinders that were cast during this mix had been kept inside a refrigerator to inhibit strength increase beyond 28 days and may be used for future work.

Figure 3- 8: Displacement-controlled compression testing machine

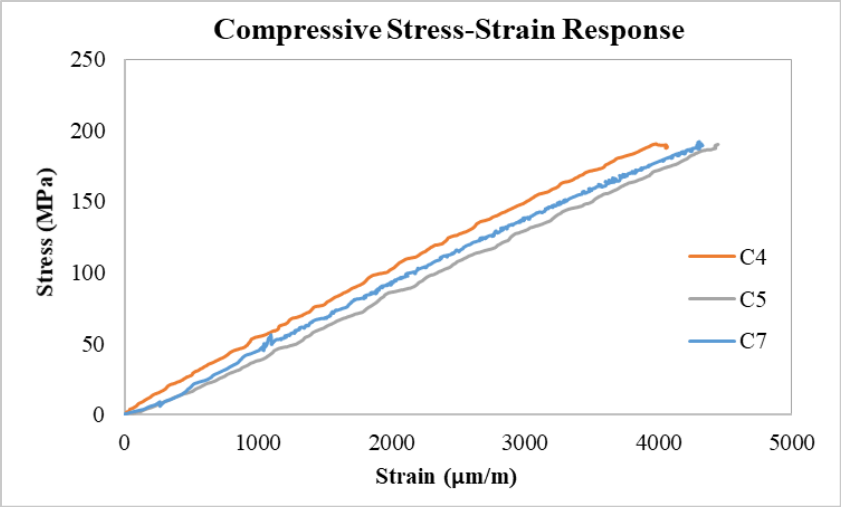

Figure 3- 9: Stress-Strain response of cylinders in uniaxial compression (Mix DE2)

Table 3- 4: Compressive strength vs strain results (Mix DE2)

Specimen ID	Peak Load	Compressive Strength	Strain at Peak Stress
	(kN)	(MPa)	(mm/mm)
C4	876	190	0.00398
C5	877	190	0.00445
C7	910	192	0.00431
Average		**191**	**0.00425**

Based on compressive stress-strain results summarized in Table 3- 4, the average compressive stress corresponding to the peak load is 191 MPa and the corresponding average strain is 4.25 mm/m. Mode of failure and crack pattern observed in compressive stress-strain tests are shown in Figure 3- 10. Upon attainment of peak load, it was observed that the cylinder specimen produces an explosive sound due to the release of very high strain energy accumulated in the process of loading, but the cylinder still held its integrity and did not burst apart completely and continued to sustain load in the post-peak region. Same behaviour was observed despite the use of a much slower loading rate of about 0.05 mm/min on other dummy specimens tested. Hence, it is hypothesized that a much more stiff system is required to capture the post-peak response of UHPFRC in compression. Moreover, rupture of strain gauges was observed due to crack formation which occurred at the attainment of peak stress. Thus, strain gauges did not provide measurements

corresponding to the post-peak branch. Effective and reliable estimation of the post-peak branch of UHPFRC material in compression is possible in future studies. Hassan et al. (2012) suggested the use of LVDT to measure the movement of machine's crosshead, to obtain vertical deformation in post-peak region of the compression response, and a chain gauge to measure the lateral expansion.

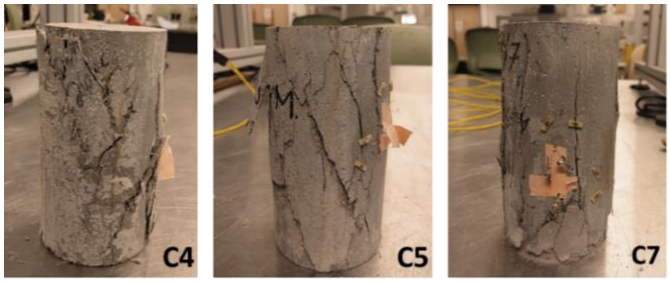

Figure 3- 10: Mode of failure in compressive stress-strain tests (Mix DE2)

3.3.4 Direct Tension Test

A servo-controlled, closed loop universal testing machine MTS was used to conduct direct tension tests to obtain the tensile characteristics of the UHPFRC material studied. Tensile test was conducted using a constant displacement loading rate of 0.00254 mm/s (0.15 mm/min) as recommended by Graybeal & Baby, (2013). For mix DE2, two types of tensile specimens, named as *Type P* (prismatic specimen) and *Type I* (*I* shaped specimen), were tested. These specimens differed with each other in terms of their geometry and loading action. Type P is a prismatic specimen proposed by Graybeal & Baby, (2013), whereas Type I is an I shaped, thicker specimen proposed by Georgiou & Pantazopoulou, (2016). Nominal dimensions and geometry of the specimens are shown in Figure 3- 11. The thickness of the Type P specimen was restricted to 30 mm including the FRP, as the available MTS machine could not grip specimens more than 30mm thick. Hence, Type P specimen had a nominal cross-sectional dimensions of 30 mm x 50 mm. Type I specimen had a nominal cross-sectional size of 50 mmx 40 mm in the central gauged region. Random and One-way poured specimens are designated with 'R' and 'OW', respectively. For example, P-R1 means that it is the first Random poured sample of Type P.

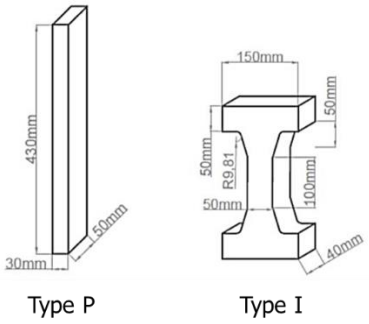

Figure 3- 11: Geometry and nominal dimensions of Type P and Type I direct tension specimens

In all cases, carbon FRP was glued longitudinally at the top and bottom ends of the specimens (Figure 3- 12) using a commercial thixotropic epoxy adhesive. This was done to avoid the formation of localized cracks outside the central gauged region. Moreover, the front face of all the specimens was painted with white acrylic paint followed by creating a black speckle pattern to facilitate the digital image correlation (DIC). The experimental test set ups for Type P and Type I specimens are shown in Figure 3-13. In Type P specimens, the flat hydraulic grips from the MTS machine directly clamp the specimen, whereas in the Type I specimens, a customized test frame was used to apply loading through the bearing action. Lateral movement of the grips had to be arrested using the brackets shown in Figure 3-13b to avoid any adverse actions. A high-resolution digital camera was setup facing the specimen front to automatically capture images at a constant interval of 10 seconds during a test. The images captured were used for performing DIC as discussed later in this chapter.

Figure 3- 12: Direct tension specimens after CFRP application (Mix DE2)

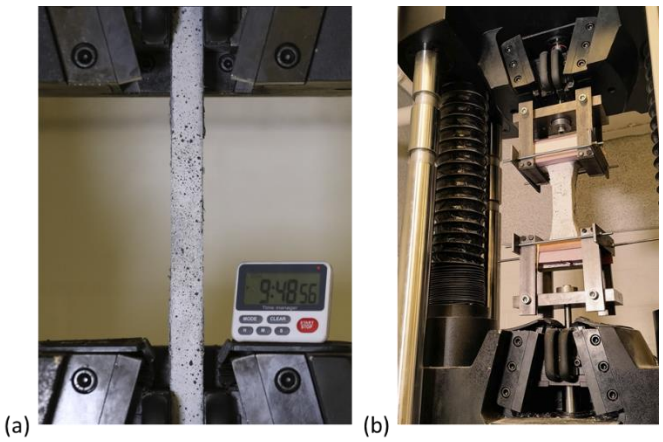

Figure 3-13: Direct tension test setup (a) Type P (b) Type I

For Type I specimens, the alignment in the direction of tension was ensured by using foam spacers and wood shims to avoid the out of plane movement during the test as shown in Figure 3-13b. The result of the specimen I-OW1 was discarded as it failed at the flange grip possibly due to improper gripping or stress concentration (see Figure 3-14b). Results of the direct tensile strength are summarized in Table 3- 5. Random specimens of Type P showed an average tensile strength of 11.16 MPa, whereas the corresponding one-way specimens were found to have a slightly higher average tensile strength of 11.93 MPa. However, average tensile strength found from Type I one-way specimens was 8.72 MPa. Tensile strength values reported in Table 3- 5 are calculated from the Equation 3-5, where F is the peak force and A is the average cross-sectional area measured within the gauge length. Figure 3-14 shows the desirable and undesirable failure pattern for direct tensile test specimens. Desirable mode of failure is achieved when the localized crack occurs within the gauge length of the specimen and if out of plane bending is not observed. Undesirable modes of failure occur when out of plane bending is caused due to- eccentricities produced at the crack initiation stage, or by the specimen setup or by irregularities in specimen geometry. Crack localization outside the gauge length or within the CFRP confined region is considered undesirable. With regard to Type I specimens, the specimen could fail on the flange grips due to stress concentration caused by the change in geometry. Such failure occurred in case of the specimen I-OW1 whose result was discarded.

$$\sigma_t = \frac{F}{A} \tag{3-5}$$

Table 3- 5: Results of direct tension tests (Mix DE2)

Specimen ID	Peak Load	Tensile Strength	Average Tensile Strength
	(kN)	(MPa)	(MPa)
P-R1	13.2	10.27	**11.16**
P-R2	14.1	10.99	
P-R3	15.8	12.08	
P-R4	15.0	11.30	
P-OW1	13.8	11.41	**11.93**
P-OW2	16.2	12.50	
P-OW3	14.8	11.88	
I-OW1	13.5	6.78	-
I-OW2	17.4	8.97	**8.72**
I-OW3	18.4	8.48	

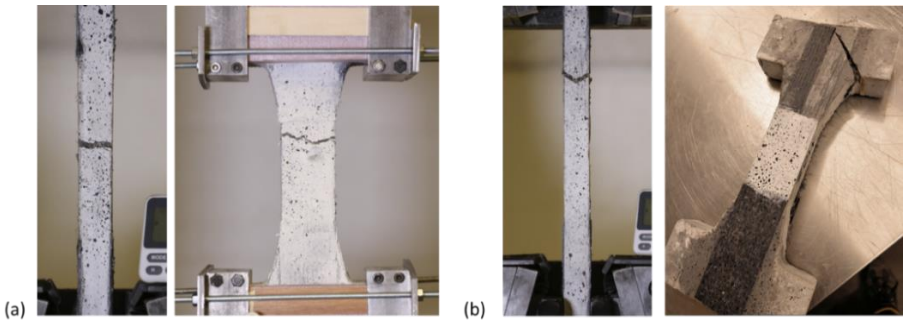

Figure 3-14: Modes of failure for direct tension tests (a) Desirable (b) Undesirable

3.3.5 Splitting Tensile Test

The splitting tensile test was conducted on 100 mm x 100 mm cylindrical specimens. These specimens were obtained by cutting a larger cylinder of size 100 mm x 200 mm into two halves using a concrete cutting saw (see Figure 3- 15). Cylinders were ground on the top and bottom surfaces before cutting them into two halves. Grinding of the ends was performed to obtain a smooth surface useful for deformation measurement. A Linear Variable Differential Transformer (LVDT) was placed horizontally at the back of the specimen to measure the transverse deformation as shown in Figure 3- 16b. Transverse tensile deformation occurred due to indirect tensile action

which caused the formation of a failure plane along the vertical diameter of the specimen. A digital camera was used to record the deformations on the front face of the specimen. The stainless-steel jig shown in Figure 3- 16a was used under the MTS universal testing machine. It is a two-column steel frame with a self-centering specimen holder and a flat steel top suspended with springs that allow for easy adjustment of the frame. This steel frame was placed on a self-levelling spherical support with a flat top surface. However, before the start of each test the bottom plate was levelled using a bubble level. A displacement-controlled loading was applied at a constant rate of 0.6 mm/min. The splitting tensile strength was estimated using Equation 3-6, where *P* represents the maximum load, *L* is length of the cylinder and *D* is the diameter of the cylinder. The average splitting tensile strength corresponding to peak load (σ_s) was found to be 23.8 MPa.

$$\sigma_s = \frac{2P}{\pi DL} \tag{3-6}$$

With regard to the mechanism of splitting tensile test, UHPFRC being a strain-resilient material behaves differently when compared to conventional concrete under splitting. Due to the presence of fiber reinforcement, the specimen did not split into two halves upon formation of failure plane. Subsequently, the fiber bridging mechanism observed in UHPFRC caused change in the mode of load transfer. Therefore, further load applied was no longer representative of tension, but rather it represented a compressive behavior in the direction of loading. Hence, interpreting the results of splitting tensile strength is not accurate for UHPFRC specimens. Figure 3- 17 depicts the mode of failure in splitting test. It was clearly evident that the cylinder specimen deformed significantly in the vertical direction indicating the compressive action which flattened the loading surfaces. Splitting tensile test results including cracking and peak strength are presented in Table 3- 6. Figure 3- 18 shows the responses of load vs horizontal expansion measured during the splitting test where the red triangular marks correspond to the first cracking for different specimens. The first cracking is defined as the point where the load vs transverse strain response displayed a distinct change in slope. Average cracking strength was evaluated to be 8.7 MPa which correlates well with the direct tensile behavior of UHPFRC.

Figure 3- 15: Splitting test specimen preparation by sawing

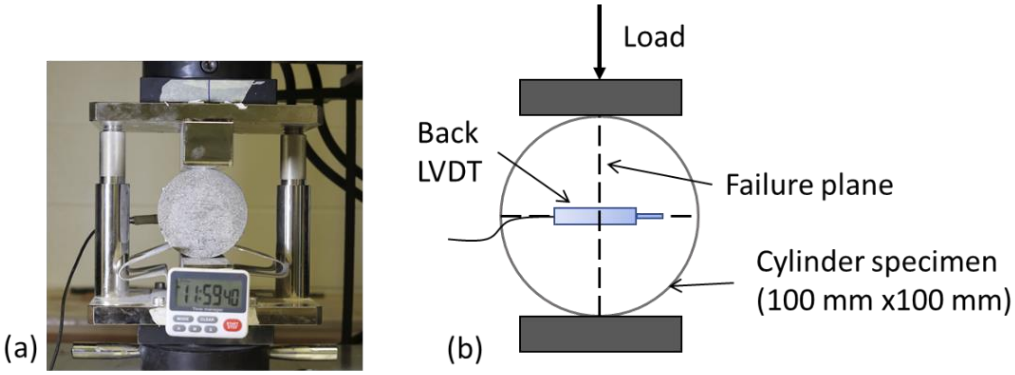

Figure 3- 16: Splitting tensile test (a) Experimental test setup (b) Schematic drawing

Table 3- 6: Splitting tensile test results (Mix DE2)

Specimen ID	Cracking Load	Cracking Strength	Avg. Cracking Strength	Peak Load	Split Tensile Strength	Avg. Split Tensile Strength
	(kN)	(MPa)	(MPa)	(kN)	(MPa)	(MPa)
S1	135	8.4	**8.7**	370.5	23.1	**23.8**
S3	116	7.5		341.3	22.1	
S4	163	10.3		413.0	26.1	

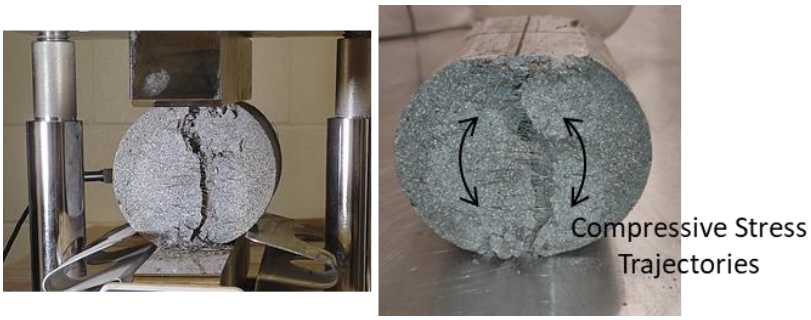

Figure 3- 17: Mode of failure in splitting tensile test

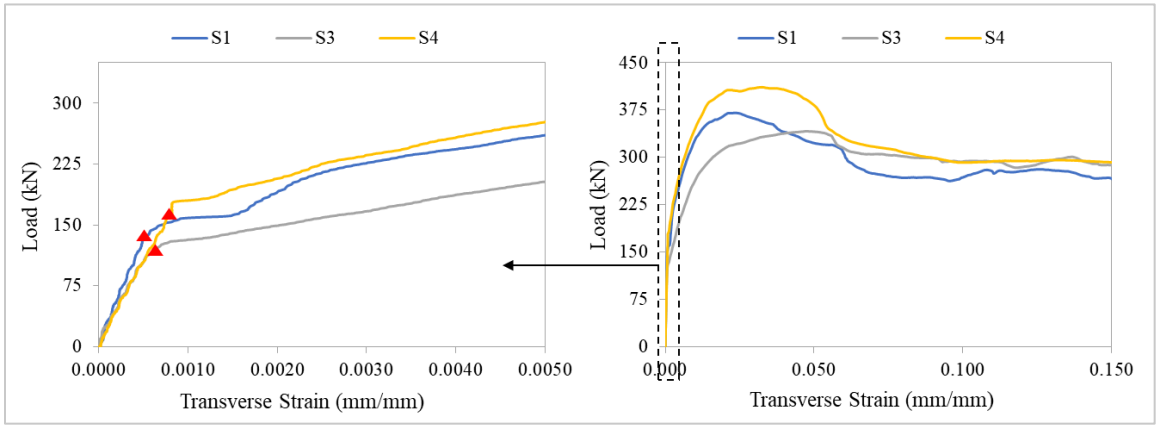

Figure 3- 18: Load vs Transverse Strain response measured in splitting tensile test

3.3.6 Flexural Test

Four-point bending test was performed on prismatic specimens of aspect ratio equal to 2. Aspect ratio of a flexural specimen is defined as the ratio of shear span to depth of the member. Mix DE2 was cast in two different specimen sizes with nominal dimensions – 100 mm x 50 mm x 400 mm (referred to as small specimens) and 150 mm x 100 mm x 700 mm (referred to as large specimens), to study the size effect on tensile response. Small prisms were designed based on the recommendations of AFNOR NF EN 13670, (2013). Besides the size difference, flexural prisms also contained Random (R) and One-way (OW) poured specimens to study the effect of casting methodology. Flexural tests were conducted in the servo-controlled, closed loop MTS machine at a displacement-controlled loading rate of 0.15 mm/min. All the prisms were tested beyond the peak load up to a residual load of about 20% of the peak. Loading rollers used can adjust themselves by free rotation about the longitudinal axis of the prism and were also capable of translation along the beam. Support rollers used were free to rotate about their own axis and placed in wide U shaped steel sections as shown in Figure 3- 19.

With regard to the small prisms, the net deflection at the midspan was measured using two LVDTs, one on either side of the prism, attached to a fabricated instrumentation jig mounted at the mid height of specimen above the support rollers (Point 1 and 2 in Figure 3- 19) and average deflection was obtained. In case of large prisms, only one LVDT was used, and other face of the prism was used to capture images for DIC. An S-shaped stiff aluminum angle was hot glued to the top of the prism at the midspan and LVDT mounted from the frame was bearing on the angle. The LVDT measures the net deflection of the top compression fiber of the specimen relative to the chord of the deflecting specimen which is defined by the midheight points above the roller supports. Schematic drawing of the test setup is depicted in Figure 3- 19, where A is the distance between the two loading rollers which is also equal to the shear span of the specimen (i.e., the distance between support and loading roller). Shear span is equal to 100 mm for small prisms and 200 mm for large prisms. D represents the depth of flexural prism which is equal to 50 mm and 100 mm for small and large prisms, respectively. Total clear span of the prism is equal to three times of distance A or six times that of depth, D. The aspect ratio (shear span to depth ratio) of both small and large AFNOR prisms was equal to 2. Figure 3- 20 shows the pictures of the test setup used for four-point bending test of small prisms. Equivalent flexural strength of the specimen was calculated using Equation 3-7, where P is the peak load obtained from the experimental response, L is the clear span of the specimen (distance between the two supports), b and h are the cross-sectional width and height, respectively. Cross-sectional dimensions (b and h) used in calculations were the average of three readings measured in the constant moment region of the prism where the failure plane was expected to occur. Cross-sectional dimensions were consistent within a tolerance of +/- 3 mm for all prisms except OW-3 large prism due to an error that occurred during casting. Therefore, the resistance curves presented in Figure 3- 21 and Figure 3- 22 compares the flexural stress vs midspan deflection response of small and large AFNOR prisms, respectively. Flexural stress is calculated as per Equation 3-7.

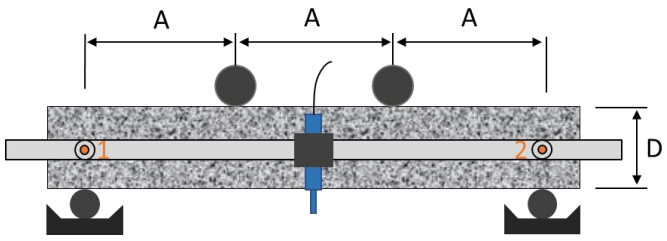

Figure 3- 19: Schematic drawing of four-point bending test

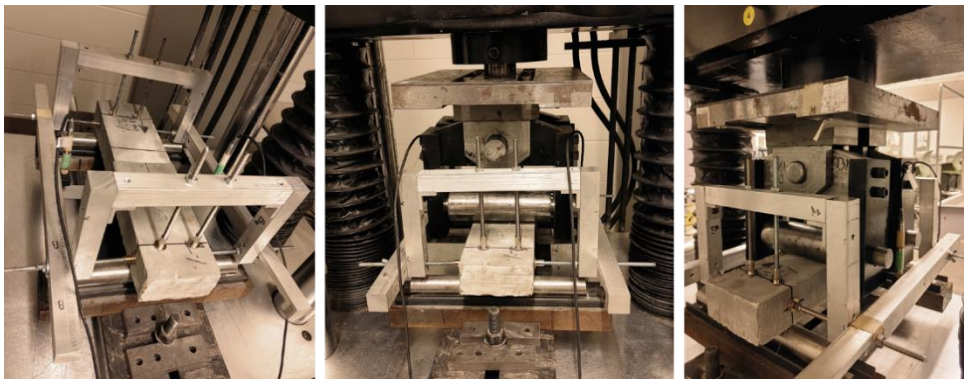

Figure 3- 20: Pictures of setup of four-point bending test

Table 3- 7: Flexural strength results (Mix DE2)

Small Prisms						
Prism ID	Peak Load	Flexural Strength	Avg. Flexural Strength	Deflection at Peak	Drift at Peak	Avg. Drift at Peak
	(kN)	(MPa)	(MPa)	(mm)	(%)	(%)
OW-1	24.38	26.33	26.24	1.38	0.92%	0.78%
OW-2	25.60	25.35		0.77	0.51%	
OW-3	23.78	27.02		1.38	0.92%	
R-1	21.26	24.15	23.99	1.84	1.23%	1.36%
R-2	24.64	28.61		1.75	1.17%	
R-3	17.55	19.22		2.52	1.68%	
Large Prisms						
Prism ID	Peak Load	Flexural Strength	Avg. Flexural Strength	Deflection at Peak	Drift at Peak	Avg. Drift at Peak
	(kN)	(MPa)	(MPa)	(mm)	(%)	(%)
OW-1	58.30	24.88	22.60	3.40	1.13%	0.96%
OW-2	51.20	21.33		2.67	0.89%	
OW-3	84.97	23.31		2.26	0.75%	
OW-4	50.20	20.88		3.19	1.06%	
R-2	38.03	14.89	13.72	1.24	0.41%	0.40%
R-3	31.51	12.55		1.14	0.38%	

$$\sigma_f = \frac{PL}{bh^2} \tag{3-7}$$

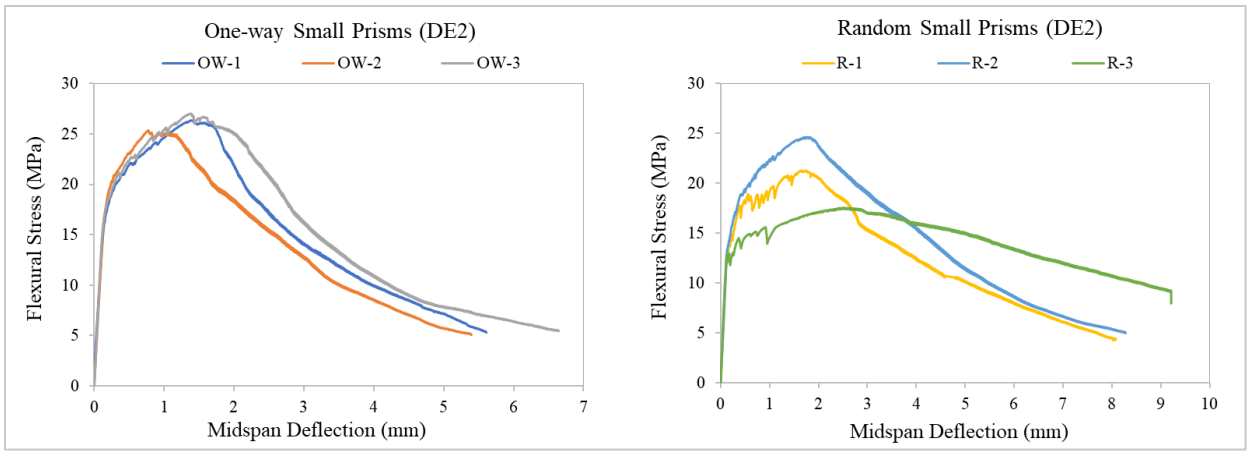

Figure 3- 21: Flexural resistance curves of small prisms (Mix DE2)

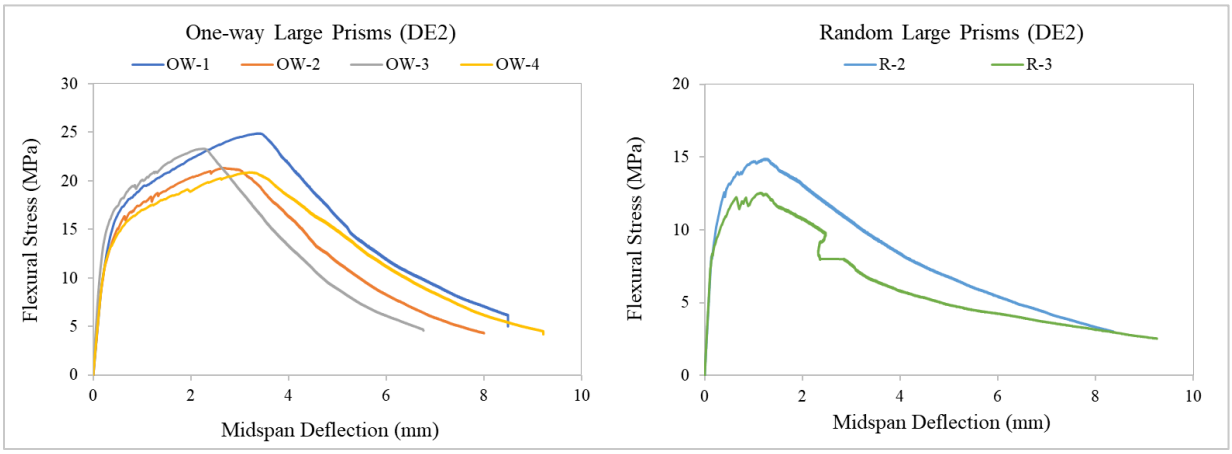

Figure 3- 22: Flexural resistance curves of large prisms (Mix DE2)

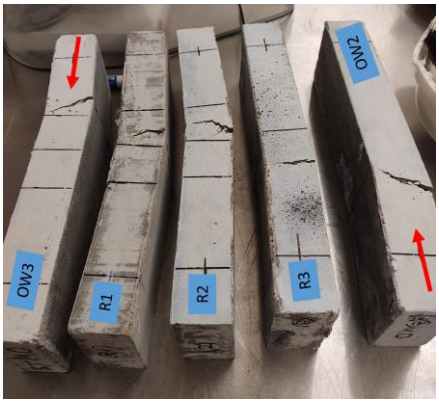

Figure 3- 23: Typical mode of failure in small flexural prisms (Mix DE2)

Figure 3- 24: Typical mode of failure in large flexural prisms (Mix DE2)

Table 3- 7 presents the results for flexural strength and drift values corresponding to the peak load. Drift values were calculated as the ratio of midspan deflection to half of the span length (L/2). In case of small prisms, the average flexural strength was 26.24 MPa and 23.99 MPa for one-way and randomly poured specimens, respectively, and the average drift at the peak load was found to be 0.78% for one-way and 1.36% for random prisms. With regard to large prisms, the average flexural strength was 22.60 MPa and 13.72 MPa for one-way and random prisms, respectively, and the average drift at peak load was found to be 0.96% for one-way and 0.40% for random prisms. The difference between flexural strength of one-way and random poured specimens was more prominent in the case of large prisms. This difference was noted to be about 65% in the case of large prisms as opposed to 9.4% in case of small prisms. This indicates the importance of fiber alignment in case of large-scale specimens and actual structural members.

Typical mode of failure and crack pattern is depicted in Figure 3- 23 and Figure 3- 24 for small prisms and large prisms, respectively, tested in four-point bending. With respect to small prisms, all random specimens failed by developing the localized crack within the constant moment region. In contrast, the one-way specimens displayed flexure-shear type of failure in which the localized crack initiated outside of the constant moment region but inclined towards the midspan. It was also noted that the crack initiation consistently occurred in the shear span where the pouring was performed for one-way small prisms. Therefore, this failure mode in one-way poured small specimens is anticipated to be caused due to a possible disturbed region formed near the location of pouring during the casting process (Ralli, 2022). However, the same behavior was not observed in the case of one-way poured large specimens where the localized crack was formed within the

constant moment region indicating that the influence of disturbed region was not significant because of the larger cross-sectional size. Drift capacity corresponding to the flexural strength was found to be lowest in case of randomly poured large prisms whose average value was only equal to 0.40%.

3.4 Proposed Inverse Analysis Method

Although several inverse analysis (IA) methods are available in the literature, it was found upon practical implementation that all methods present advantages and challenges. The current inverse analysis method proposed by Annex U of CSA A23.3 was found to be user biased, and it is ought to be replaced or amended. For this purpose, a CSA task force is established to explore a more robust and effective inverse analysis method to replace the existing one. To this end, an inverse analysis is proposed here based on the layer-by-layer sectional analysis of a four-point bending test. Results of flexural tests obtained in the previous section were used to obtain the tensile behavior of UHPFRC material and compared with the experimental results of the direct tension tests. The proposed inverse analysis is applicable to any flexural prism irrespective of cross-sectional dimensions as long as it is tested in third point bending (i.e., distance between the loading rollers is equal to the shear span) as depicted in Figure 3- 25. However, the methodology could also be applied to specimens loaded in different configuration by using suitable equations for estimating deflections. A spreadsheet was programmed to perform the analysis with a single action. Using the equilibrium of the forces acting across the midspan section, the moment-curvature resistance curve of the prism specimen was estimated followed by its conversion to the load-deflection response.

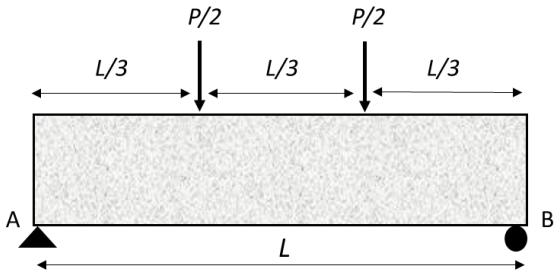

Figure 3- 25: Illustration of a typical third point bending test

3.4.1 Methodology for the Inverse Analysis

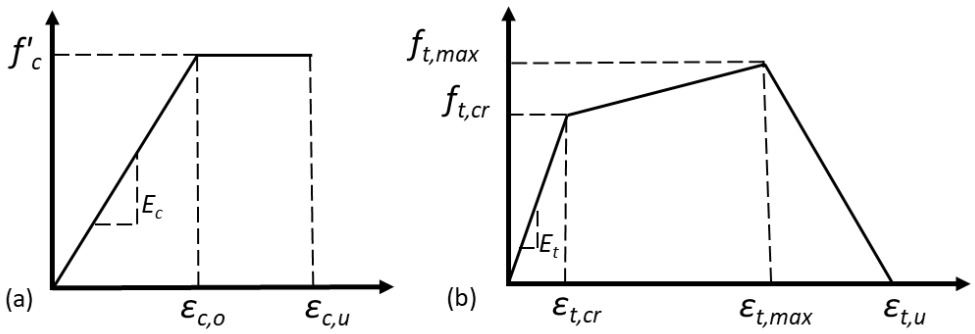

Figure 3- 26: Stress-strain laws used in the analysis (a) Compression (b) Tension

Figure 3- 26 represents the constitutive stress-strain laws in compression and tension that were used in the inverse analysis. The compressive stress-strain law of UHPFRC considered is a bilinear model, with linear elastic and perfectly plastic branches as shown in Figure 3- 26a. The linear elastic branch extends up to the peak compressive strength ($f_c^{'}$) at its corresponding strain, $\varepsilon_{c,o}$, followed by a constant stress response (plastic) up to the attainment of ultimate strain, $\varepsilon_{c,u}$. On the tension side, a tri-linear model was assumed as per Figure 3- 26b, where its linear elastic branch extends up to the cracking stress, $f_{t,cr}$, at the cracking strain limit, $\varepsilon_{t,cr}$, which is followed by a strain-hardening branch up to the attainment of maximum tensile stress, $f_{t,max}$, at its corresponding strain represented as $\varepsilon_{t,max}$. The linear descending branch of the model reaches zero tensile stress at the ultimate tensile strain ($\varepsilon_{t,u}$). Modulus of elasticity of the material was assumed to be equal in tension and compression (i.e., $E_c = E_t$).

The controlling variable of the algorithm is the assumed tensile strain (ε_t) at the bottommost fiber of the cross-section (tension fiber). Strain distribution across the depth of the section is linear based on the assumption that plane sections remain plane. Thus, at a given stage of loading, the curvature (φ) acting on the section can be calculated using the tensile strain of the bottommost fiber (ε_t), depth of the neutral axis (Z_c) and height of the cross-section (h) as per Equation 3-8.

$$\varphi_i = {}^{\varepsilon_{t,i}}/_{(Z_c - h)} \tag{3-8}$$

The cross-section at the midspan is selected and is divided into thin layers along the depth followed by calculation of strain at the midpoints of each layer based on their corresponding depth value

and the assumed curvature. Compressive strains in the layers above the neutral axis are considered as positive, whereas the tensile strains below the neutral axis are negative. Stress acting on each layer is calculated based on the above defined stress-strain constitutive laws (Figure 3- 26). Stress developed in each segment of the cross-section is converted into force components by multiplying the stress with the area of each layer and the moment due to each force component can be calculated by multiplying the force with the corresponding distance from the centroidal axis.

As there is no external axial load acting on the member, the sum of the axial forces across all the layers is supposed to be zero based on the equilibrium of forces, thus estimating a value for the depth of neutral axis. Neutral axis depth was evaluated using an iterative function in the spreadsheet such as Goal Seek or Solver. Once the neutral axis depth is determined, the moment and curvature acting on the section are automatically calculated. Moment was taken as the sum of individual moments acting upon each layer at a given equilibrium state. This procedure was repeated for a wide range of tensile strain values to obtain the full moment-curvature response.

After the moment-curvature response was obtained, the closed-form expressions as per Equations 3-9 to 3-11 were used to calculate the deflection values from curvature distribution across the span. These expressions were derived based on the principle of Virtual Work. Prior to yielding, the curvature is linearly related to the moment based on the elastic theory. In the non-linear stage after cracking, the curvature distribution is assumed to be bi-linear in the plastic zone and constant along the middle-third span of the specimen as shown in Figure 3- 27. Expressions like Equations 3-9 and 3-10 have also been used by other researchers with good agreement for estimating deflection values up to the peak load (Georgiou & Pantazopoulou 2016, Mobasher et al. 2014, López 2017).

Figure 3- 28 depicts the loading and unloading paths followed by different sections of the specimen. The idealized moment-curvature resistance diagram shows that, except for the critical section where localization occurs, the rest of the flexural prism starts to unload after reaching the peak moment and enters the post-peak region. Green arrows represent the path of loading and yellow arrows show the unloading paths. The unloading path followed by various sections across the span may vary depending on the state of local moment experienced by that section when the global moment reached maximum. For increase in the magnitude of curvature beyond the value that corresponds to the maximum moment, the section that encountered the peak moment follows the descending branch of moment-curvature curve. At the same time, any sections that were in the

strain hardening region start to unload on a path parallel to the linear elastic branch, however, leaving a residual plastic deformation when completely unloaded. Furthermore, the portion of the beam that was still within the elastic range, unloads on its original path.

It is assumed that the span between the loading points of the prism (constant-moment region) follows the same behavior (i.e., post-peak softening trend after the peak moment). Based on the above concepts and with reference to Figure 3- 29, the expression for estimating the deflection in the post-peak region was derived, as per Equation 3-11.

Midspan deflection in the linear elastic range,

$$\delta_y = \frac{23L^2}{216}\varphi_y \tag{3-9}$$

Midspan deflection for post-cracking branch and up to the ultimate (peak) load,

$$\delta_u = \frac{L^2}{216M_u^2}\left[\left(4M_u^2 + 4M_u.M_y\right).\varphi_y + \left(23M_u^2 - 4M_u.M_y - 4M_y^2\right).\varphi_u\right] \tag{3-10}$$

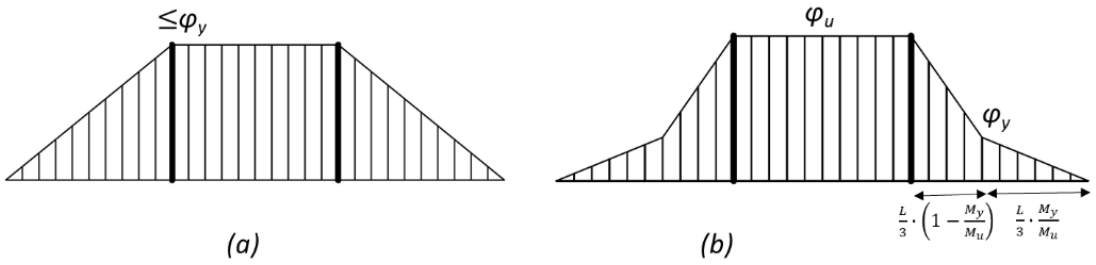

Figure 3- 27: Curvature distribution across the span (a) before cracking and (b) after cracking

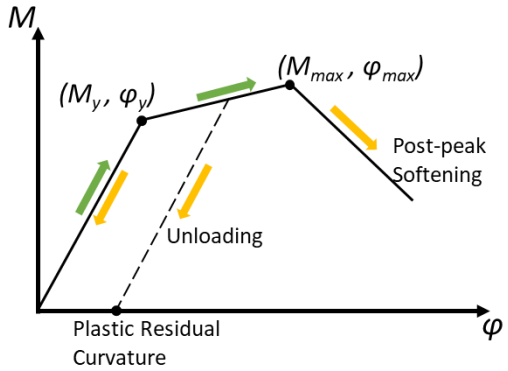

Figure 3- 28: Moment-Curvature trend followed during loading and unloading stages

Midspan deflection beyond the peak load,

$$\delta_{u2} = \varphi_1 \left\{ Z_1 \cdot \left(\frac{2l_y}{3} + L_s + \frac{5l}{3} \right) + Z_2 \cdot \left(\frac{l}{3} \right) \right\} + \varphi_{u2} \left\{ Z_1 \cdot \left(\frac{4l}{3} \right) + Z_2 \cdot \left(\frac{2l}{3} + \frac{L_s}{2} \right) - \left(\frac{L_s . l}{8} \right) \right\} \quad (3\text{-}11)$$

where; $l_y = \frac{L}{3} \cdot \frac{M_y}{M_{max}}$, $Z_1 = Z_2 \cdot \frac{l_y}{L_s}$, $Z_2 = \frac{L}{6}$

Moment at l_y, $M_1 = M_{u2} \cdot \frac{l_y}{L_s} \rightarrow \varphi_1 = \frac{M_1}{EI}$

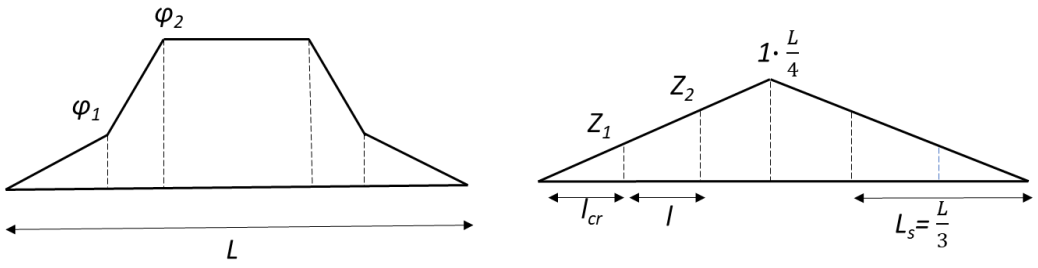

Figure 3- 29: Curvature and equivalent unit moment distribution for post-peak response

Shear deformations can also be considered and accounted for in the deflections up to the peak load using Equation 3-12, where G is the elastic shear modulus (MPa), A^* is the effective shear area (mm^2): for rectangular cross-section it is, $A^* = \frac{5}{6}(b.h)$.

$$\delta_s = \left(\frac{P.L}{6} \right) \frac{1}{G.A^*} \quad (3\text{-}12)$$

The load-deflection response estimated through this inverse analysis was plotted and compared with the respective experimental response of the four-point bending test. The analysis procedure was repeated by changing the parameter values of the tensile stress-strain model until the analytical curve fits well with the experimental one. In this regard, for each new increment the converged values obtained in previous increments are used as given, so that in each phase only one unknown is to be resolved.

3.4.2 Results from the Inverse Analysis

The above discussed inverse analysis method was performed on experimental test results of the four-point bending specimens of Mix DE2 (Section 3.3.6). The average compressive strength used

for Mix DE2 was 177 MPa. Results obtained from the inverse analysis are summarized in Table 3- 8 and the corresponding tensile behavior is plotted in Figure 3- 30. Figure 3- 31 shows the comparison between the analytical and experimental load-deflection resistance curves for OW-3 small AFNOR prism of Mix DE2.

Table 3- 8: Results obtained from the proposed inverse analysis method (Mix DE2)

Small Prisms						
Specimen ID	E	$f_{t,cr}$	$\varepsilon_{t,cr}$	$f_{t,max}$	$\varepsilon_{t,max}$	$\varepsilon_{t,u}$
	(MPa)	(MPa)	(mm/mm)	(MPa)	(mm/mm)	(mm/mm)
OW-1	57222	10.3	0.00018	12.5	0.0052	0.0140
OW-2	61000	12.2	0.00020	13.5	0.0030	0.0140
OW-3	60606	10.0	0.00017	12.2	0.0050	0.0150
Average	**59609**	**10.8**	**0.000182**	**12.7**	**0.0044**	**0.0143**
R-1	50000	9	0.00018	10.8	0.0065	0.0180
R-2	51282	10	0.00020	12.8	0.0064	0.0160
Average	**50641**	**9.5**	**0.00019**	**11.8**	**0.0065**	**0.0170**
Large Prisms						
OW-1	45000	9.0	0.00020	10.2	0.0070	0.0120
OW-2	47500	7.6	0.00016	9	0.0050	0.0120
OW-3	57143	8.0	0.00014	9.6	0.0054	0.0110
OW-4	45625	7.3	0.00016	8.8	0.0065	0.0140
Average	**48817**	**7.97**	**0.00017**	**9.4**	**0.0060**	**0.0123**
R-2	50000	5.5	0.00011	6.6	0.0010	0.0130
R-3	50000	5	0.00010	5.4	0.0010	0.0115
Average	**50000**	**5.3**	**0.00011**	**6.0**	**0.0010**	**0.0123**

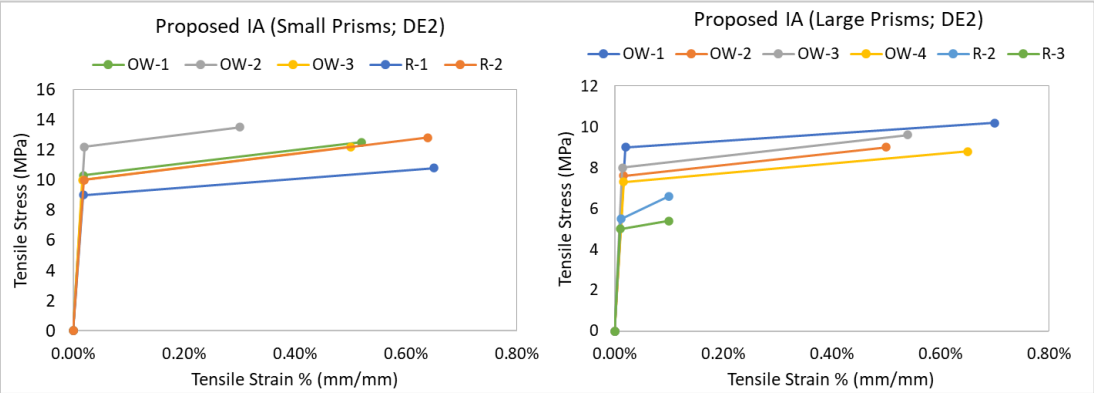

Figure 3- 30: Tensile stress-strain behavior obtained from the proposed inverse analysis (Mix DE2)

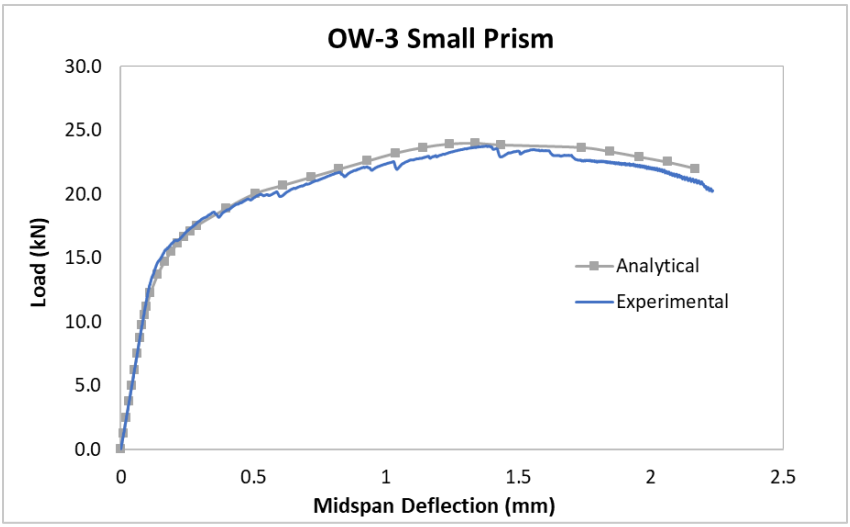

Figure 3- 31: Comparison between analytical and experimental response (Mix DE2, Small OW3)

Average tensile cracking and maximum strength obtained from small prisms were equal to: 11.0 MPa and 12.9 MPa for One-way cast specimens, and 9.5 MPa and 11.8 MPa for Randomly cast specimens. However, for large prisms, the average cracking and maximum tensile strength obtained were equal to; 8.0 MPa and 9.4 MPA for One-way cast specimens, and 5.3 MPa and 6.0 MPa for Randomly cast specimens. It is clearly evident that the tensile strength values obtained for large specimens were significantly lower than for smaller ones. Moreover, the Randomly cast large specimens were highly deficient both in tensile strength and ductility which highlights the importance of fiber orientation in actual structural members constructed with UHPFRC. Therefore,

appropriate standardization of the specimen geometry is critical when performing flexural (indirect) tests for determining the tensile behavior of UHPFRC.

The results obtained from the proposed inverse analysis of small prisms compare very well with those of direct tension tests performed on Type P specimens (Table 3- 5) as per which the maximum tensile strength obtained was 11.6 MPa and 11.93 MPa for Randomly and One-way cast specimens, respectively.

3.5 Comparison with SIA Recommended Inverse Analysis

In this section, the tensile stress-strain behavior predicted from the proposed layer-by-layer inverse analysis in the previous section is compared with the results from inverse analysis recommended by the Swiss standard (SIA 2052, 2016). SIA inverse analysis method has been discussed in detail earlier (refer to Section 2.7.2). The inverse analysis method recommended in Annex 8.1 of CSA S6 (2019) is only applicable to the specimens whose length is three times the depth of the section ($i.e., L = 3h$) but the prisms used in this study had length equal to six times the depth. Therefore, the CSA method is not compared here. Figure 3- 32 presents the tensile stress-strain behavior predicted using SIA inverse analysis method.

Figure 3- 33 illustrates the graphic comparison between tensile parameters obtained from the proposed inverse analysis and SIA inverse analysis methods with satisfactory convergence with the exception of the cracking stress which was found to be slightly higher in case of the proposed inverse analysis method.

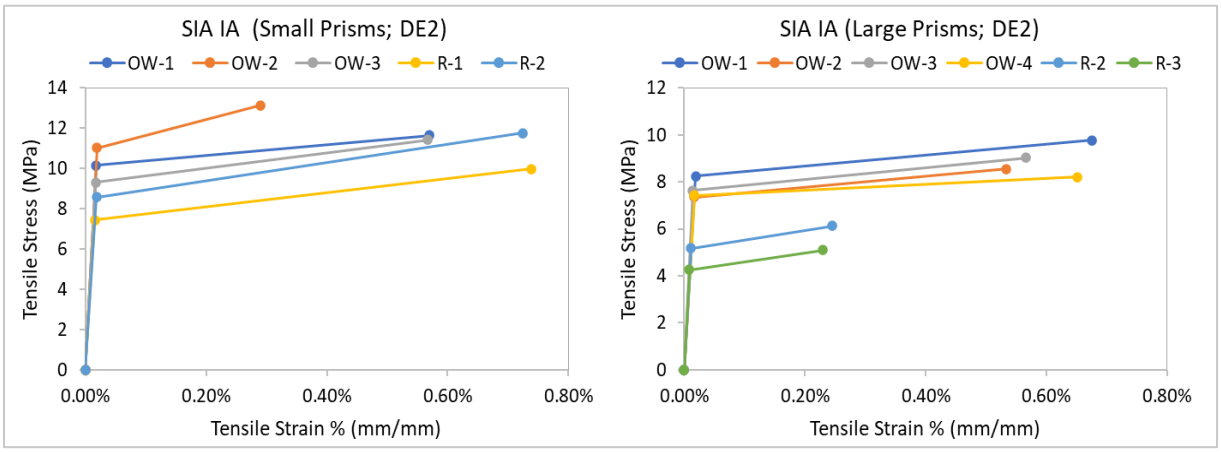

Figure 3- 32: Tensile stress-strain behavior obtained from SIA inverse analysis (Mix DE2)

Table 3- 9: Results obtained from SIA inverse analysis method (Mix DE2)

Small Prisms					
Specimen ID	E	$\varepsilon_{t,cr}$	$f_{t,cr}$	$\varepsilon_{t,max}$	$f_{t,max}$
	(MPa)	(MPa)	(mm/mm)	(MPa)	(mm/mm)
OW-1	58702	0.00017	10.2	0.00570	11.7
OW-2	58534	0.00019	11.0	0.00290	13.1
OW-3	55636	0.00017	9.3	0.00567	11.4
Average	**57624**	**0.00018**	**10.2**	**0.00476**	**12.1**
R-1	47835	0.00016	7.4	0.00738	10.0
R-2	46197	0.00019	8.6	0.00724	11.8
Average	**47016**	**0.00017**	**8.0**	**0.00731**	**10.9**
Large Prisms					
OW-1	44466	0.00019	8.2	0.00675	9.8
OW-2	45605	0.00016	7.4	0.00534	8.6
OW-3	55180	0.00014	7.6	0.00567	9.0
OW-4	45410	0.00016	7.4	0.00652	8.2
Average	**47665**	**0.00016**	**7.7**	**0.00607**	**8.9**
R-2	48058	0.00011	5.2	0.00245	6.1
R-3	51641	0.00008	4.3	0.00230	5.1
Average	**49850**	**0.00010**	**4.7**	**0.00237**	**5.6**

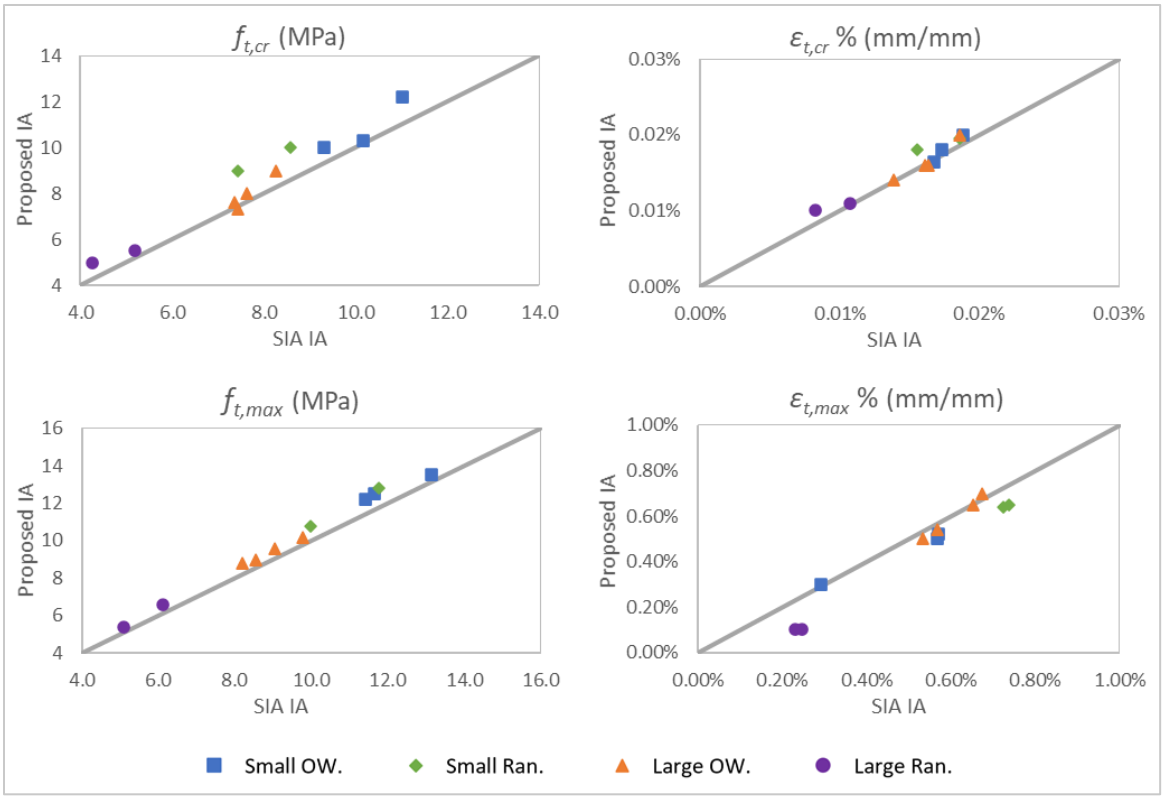

Figure 3- 33: Comparison between respective tensile parameters predicted from proposed and SIA inverse analysis methods

3.6 Digital Image Correlation

Digital Image Correlation (DIC) is a non-contact technique used for measuring deformations in the material (Blaber et al., 2015). This technique is highly valuable for the tests where local deformations and strain readings are difficult to measure during the experiment. At present, several software suites are available for image correlation; one such tool is Ncorr (http://www.ncorr.com/). This is an open-source 2D digital image correlation tool based on MATLAB code used in this research. Moreover, Ncorr-post is a post-processing tool that may be used for visualization and export of meaningful results from the DIC analysis. Detailed explanation on use of these software tools can be found in the instruction manuals provided by the developers.

As mentioned earlier, for the DIC process, the images used for analysis were captured using a high-resolution digital camera. The surface used for DIC measurements was painted with white paint followed by spraying of black color to form a distinct speckle pattern. Such a speckle pattern helps in achieving accurate results from DIC. A sequence of images (usually 10-15) corresponding

to different stages of a test and a reference image corresponding to zero strain stage was selected and imported into the program. Figure 3- 34 shows the user interface of Ncorr, where a direct tension test was analyzed, and Figure 3- 35 shows the general analysis parameters used in DIC analysis. These parameters are not standard and can vary for different specimens depending on the convergence achieved during an analysis.

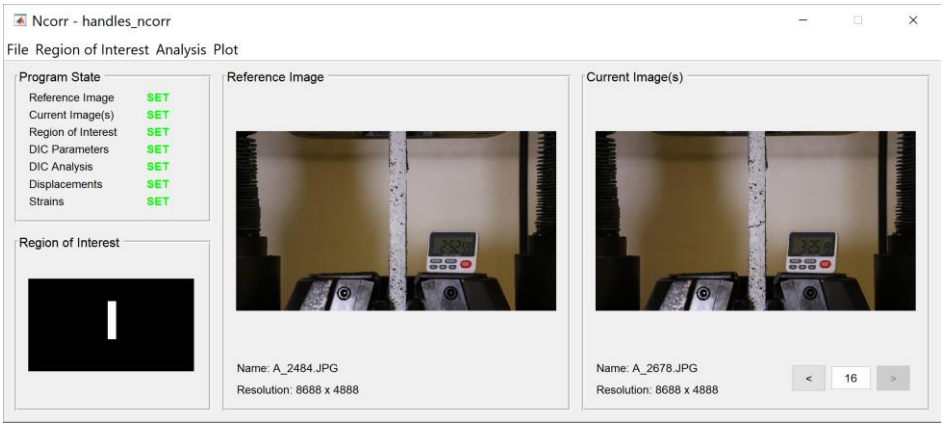

Figure 3- 34: User interface of Ncorr DIC program

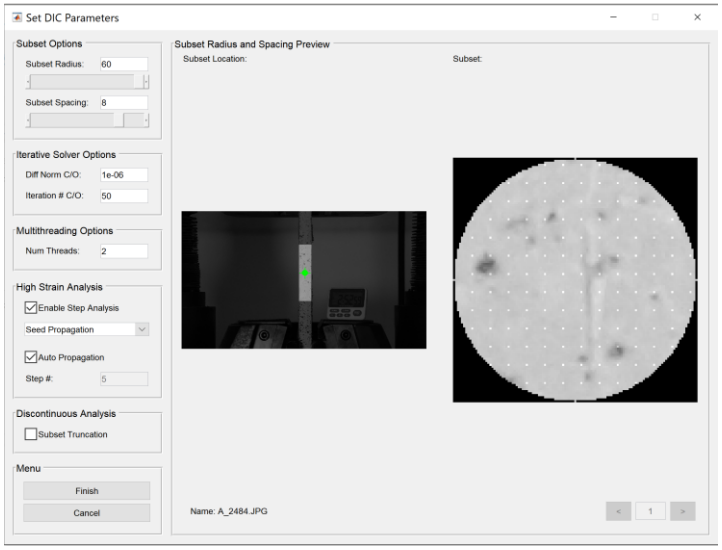

Figure 3- 35: Example parameters used in DIC analysis

After importing the images, the region of interest (ROI) was defined for the program to perform deformation calculations in a specified region. From Figure 3- 35, it can be observed that 2 seeds were used for the analysis of direct tension specimen. These seeds were selected across the crack location to achieve good convergence. It is important that a seed should not overlap with the crack

as it would result in poor convergence and the analysis may not proceed. As the specimens involved in the analysis had experienced cracking, the High Strain Analysis option in the program was enabled. Subset truncation may also be used that prevents the wrapping of subsets around the crack tip which cause distortions (Blaber & Antoniou, 2017).

After the DIC analysis of a sample, the Ncorr program allows the user to get several plots such as displacement and strain in X or Y direction. The user can hover the mouse pointer around a plot to observe the required deformations. It also provided pictures or animations of the analysis that can be exported. However, collecting deformation or strain values for the chosen points over a range of pictures (each picture corresponds to a specific load stage) could become tedious. Hence, for this purpose the Ncorr post-processor can be used after completing the DIC analysis in Ncorr. In the post-processor, a virtual extensometer may be placed with a chosen gauge length in the location of interest following which deformation and strain readings can be obtained which are easily exportable. It is important to note that, if the user intends to extract information from the post-processor, the unit conversion (i.e., pixels to mm) should be applied only in the post-processor and not in the Ncorr analysis tool. If unit conversion is performed in both places, then the units would be converted twice, and results obtained would be incorrect.

Figure 3- 36 depicts the tensile stress-strain response predicted using DIC for Random1 and One-way 1 sample of Type P direct tension specimen. Tensile stress on the vertical axis was calculated using the corresponding load divided by the area of cross-section, whereas the strain on X-axis represents the average of strain estimated using three virtual extensometers placed equidistantly across the front face of the specimen. The gauge length of these virtual extensometers was chosen to be 75 mm. Strain distribution and crack pattern obtained from DIC analysis corresponding to different stress states for specimen P-OW1 are shown in Figure 3- 37. With the increase of the applied load, it was noted that the deformations were localized into two major cracks. In the post-peak region, the localized crack that was formed first, begun to unload as the second crack prevailed. Strain values corresponding to the pre-cracking stage was found to be less consistent.

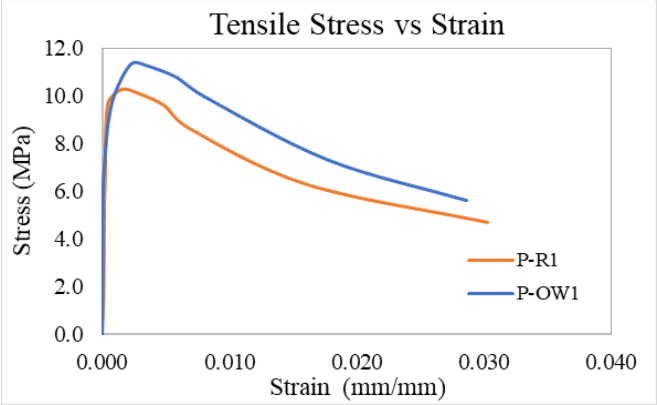

Figure 3- 36: Tensile Stress-Strain response from DIC (Mix DE2)

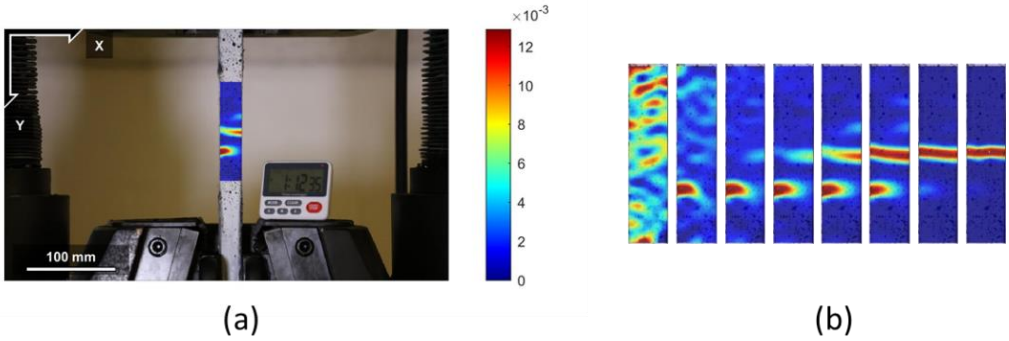

Figure 3- 37: Strain distribution in Y-direction (a) At peak load (b) Evolution of crack pattern (Sample: P-OW1)

3.7 Summary

Material characterization tests performed on Densit UHPFRC material used in this study were presented in this chapter. Several mechanical tests were conducted including compression, tension, flexure and splitting tensile tests. The major findings from the tests performed on Mix DE2 prepared using Densit premix and 2% volume fraction of fibers are listed below:

a. Average compressive strength was found to be 177 MPa.
b. Modulus of Elasticity was found to be 49.44 GPa whereas Poisson's ratio was about 0.25.
c. Stress-strain response in compression was recorded where average stress at peak was found to be 191 MPa and the corresponding strain was 0.00425 mm/mm.
d. Type P direct tension tests provided 11.16 MPa and 11.93 MPa tensile strength for random and one-way cast specimens, respectively.

e. Average cracking strength from the splitting tensile tests was found to be 8.7 MPa whereas average peak splitting tensile strength was found to be 23.8 MPa.
f. Average flexural strength of one-way and random small prisms was found to be 26.24 MPa and 23.99 MPa, respectively. A profound difference in the estimated strengths was attributed to the casting methodology observed in case of large prisms, where one-way and random cast specimens exhibited 22.6 MPa and 13.7 MPa, respectively.

In addition, an inverse analysis methodology based on layer-by-layer sectional analysis was proposed. Results obtained from the proposed inverse analysis method were compared with that of the SIA 2052 (2016) recommended method, and a comparative analysis was provided for crucial stress-strain points obtained from the above two methods. Direct tension tests were also found to be in good agreement with the inverse analysis methods. Moreover, digital image correlation (DIC) was performed using Ncorr program. The tensile stress-strain curve, strain distribution and crack pattern produced using the DIC tool was presented.

Chapter 4: Forward Analysis Method

Inverse analysis methods proposed by researchers (Rigaud et al. 2012, Mobasher et al. 2014, Lopez 2017) and Standards (CSA S6, 2019; AFNOR NF P18 470, 2016; SIA 2015, 2016) are cumbersome to perform, and need a skilled professional to derive objective and accurate results. Moreover, the inverse analysis method proposed by Annex 8.1 of CSA S6 (2019) was found to be subjective, very sensitive, and lacked robustness when applied to different prism sizes (Husain, 2021). Providing an easy and quick method for reliable estimation of the tensile characteristic properties of UHPFRC is the objective of the proposed Forward Analysis approach. Similar to inverse analysis methods, the Forward Analysis approach also requires results of the load-displacement response curve obtained from a third point bending test (see Figure 4- 1) to indirectly estimate the tensile behaviour of UHPFRC. The proposed charts are developed for some of the commonly used flexural specimens with geometry details as shown in Table 4- 1. This approach could be highly useful for quality control purpose or in the design of UHPFRC structural members.

4.1 Methodology for the Forward Analysis

Forward analysis design charts are based on the parametric study of the tensile analysis procedure described in Chapter 3. The load-deflection response in flexure was calculated from the assumed stress-strain diagrams of the UHPFRC material following the same analytical procedure described in the methodology proposed in Section 3.4. Layer-by layer sectional analysis was used to estimate the moment-curvature response and from there, the load-displacement envelope. With regard to the typical flexural prism shown in Figure 4- 1, *b* and *h* correspond to width and depth of the cross-section, respectively, and *L* represents the supported span length of the specimen. As defined earlier, the assumed tensile constitutive model shown in Figure 4- 2a is comprised of five independent parameters which include the modulus of Elasticity, (*E)*, the tensile stress at cracking, ($f_{t,cr}$), the maximum tensile stress, ($f_{t,max}$), strain corresponding to the maximum stress ($\varepsilon_{t,max}$) and the ultimate strain ($\varepsilon_{t,u}$) at zero tensile stress.

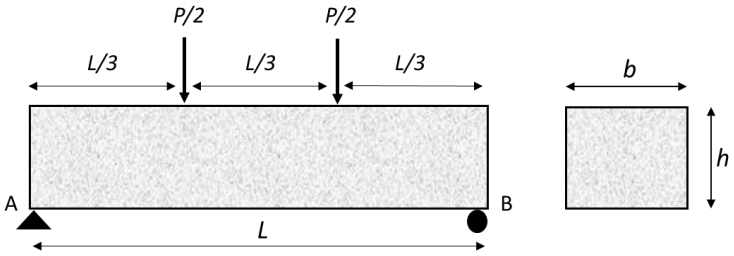

Figure 4- 1: Typical four-point bending test specimen with third point loading

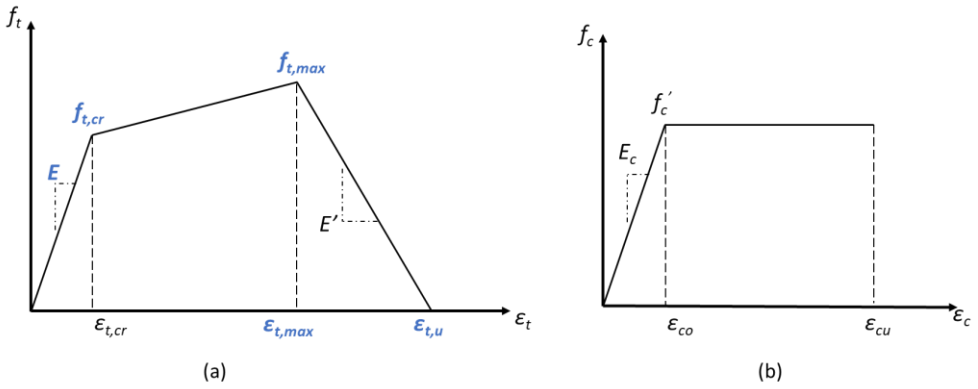

Figure 4- 2: Constitutive Stress-Strain laws used in (a) Tension (b) Compression

Table 4- 1: Flexural specimen classification based on dimensions

Type	Specimen Size (mm)			Aspect Ratio
	b	h	L	
A	100	50	300	2
B	100	100	300	1

The compressive stress-strain model is assumed to be bilinear having linear elastic and perfectly plastic branches, as shown in Figure 4- 2b. The linear elastic branch extends up to the peak compressive strength (f_c') at yield strain ($\varepsilon_{c,o}$) followed by a constant stress response (plastic) up to the attainment of ultimate strain in compression, ($\varepsilon_{c,u}$). As mentioned, the algorithm described earlier in Section 3.4 was used in calculating the flexural load-deflection response using the above defined constitutive models.

Firstly, the moment-curvature curve was obtained by using the layer-by-layer sectional analysis followed by its conversion into the load-deflection curve using the closed-form expressions

defined in Equations 3-9 to 3-11. The calculation procedure described above was performed for various values of parameters of the tensile model and for different cross-sectional sizes of the specimen to develop the design charts presented in this study.

4.2 Preliminary Analysis

Based on the analysis procedure discussed above, multiple sets of analysis were carried out as a preliminary step to observe the effect of constitutive models on the calculated load-deflection response. The two sets of preliminary analysis discussed in the following were performed on Type-A flexural specimen (100mm x 50mm x 300mm) using the compression models shown in Table 4- 2, where *C160* and *C125* represent the models with compressive strength equal to 160 MPa and 125 MPa, respectively. Values of the compression models *C160* and *C125* were chosen to represent generic UHPFRC materials based on findings from previous studies (refer to Table A-1). It is to be noted that the modulus of elasticity was assumed to be equal in tension and compression. Hence, the value of $\varepsilon_{co}$was calculated using the ratio of compressive strength to the modulus of elasticity (i.e., $\varepsilon_{co} = f_c'/E$), where modulus of Elasticity *(E)* in tension was assumed to be 46000 MPa for the preliminary analysis.

Table 4- 2: Compression models for preliminary analysis

Compression Model	f_c' (MPa)	ε_{co} (mm/mm)	ε_{cu} (mm/mm)
C160	160	0.00350	0.006
C125	125	0.00272	0.006

Parametric variations of the tensile model and their effect on the calculated load-deflection resistance curves using *C160* compression model are shown below in Figure 4- 3 to Figure 4- 6. The data table within each figure represents the tensile model corresponding to a particular curve along with the highlighted variable for which the sensitivity analysis is conducted.

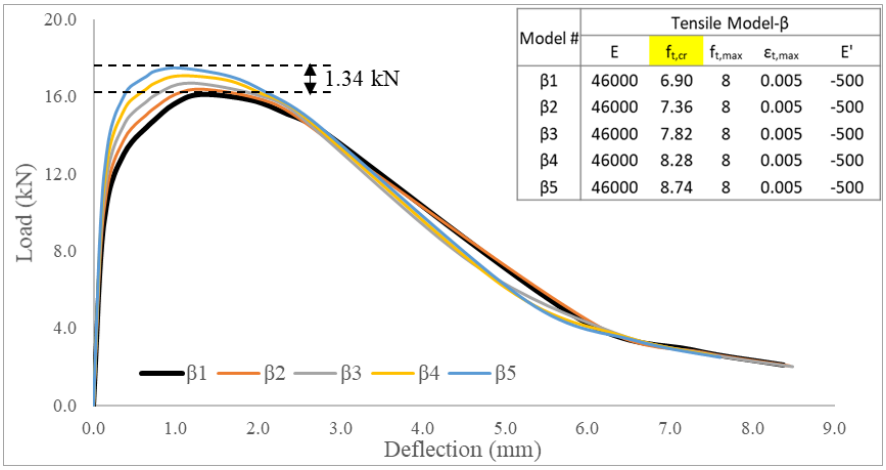

Figure 4- 3: C160 resistance curves based on variation of $f_{t,cr}$

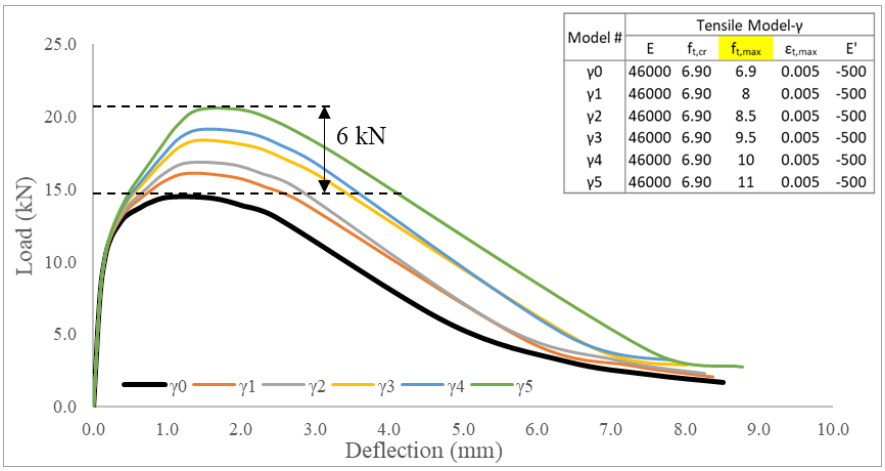

Figure 4- 4: C160 resistance curves based on variation of $f_{t,max}$

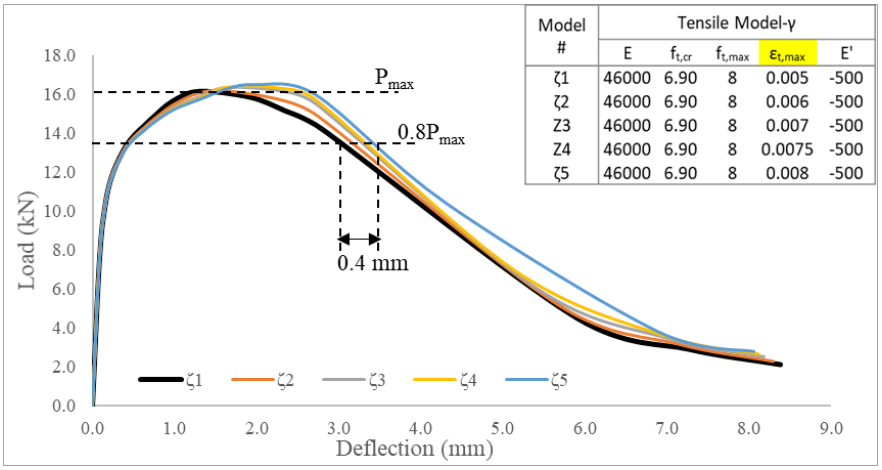

Figure 4- 5: C160 resistances curves based on variation of $\varepsilon_{t,max}$

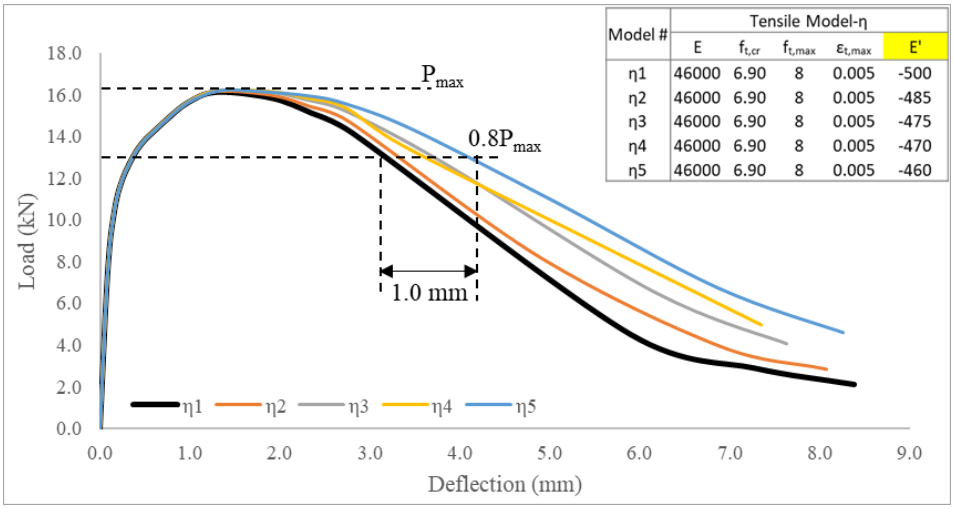

Figure 4- 6: C160 resistance curves based on variation of E'

Similarly, parametric variations of the tensile model and their effect on the load-deflection resistance curves using *C125* compression model are shown below in Figure 4- 7 to Figure 4- 10.

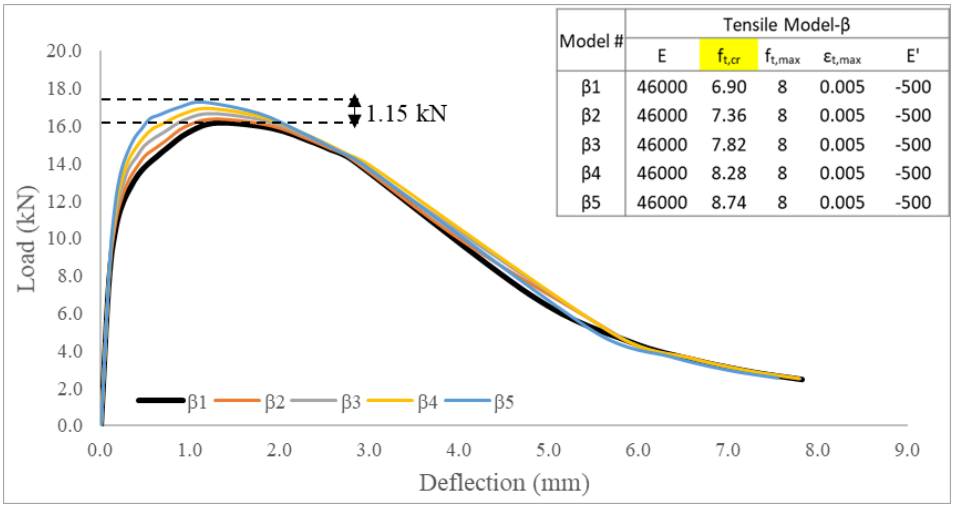

Figure 4- 7: C125 resistance curves based on variation of $f_{t,cr}$

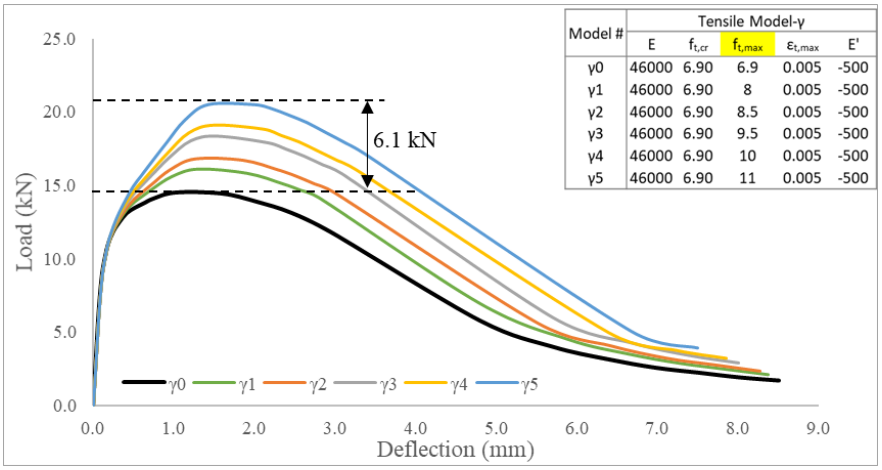

Figure 4- 8: C125 resistance curves based on variation of $f_{t,max}$

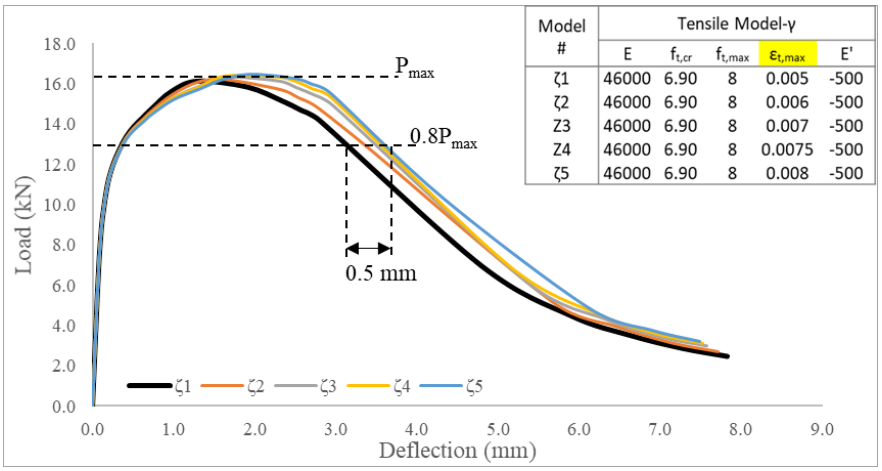

Figure 4- 9: C125 resistances curves based on variation of $\varepsilon_{t,max}$

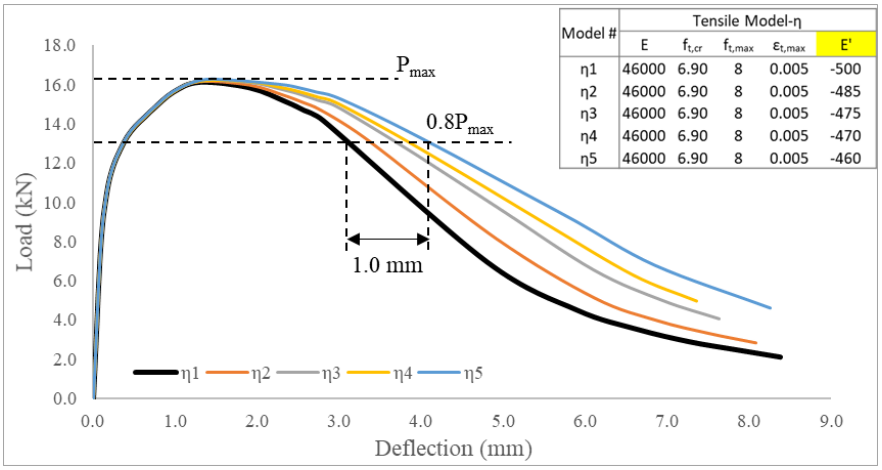

Figure 4- 10: C125 resistance curves based on variation of E'

It is noted that, for the same variables of tensile model, the resistance curves were barely affected by the compression models used (*C160* or *C125)*. A negligible difference of about 2% to 3% was observed between the load-deflection values corresponding to the critical points in flexural response. Hence, this implies that the flexural behaviour of UHPFRC is mainly governed by the tensile stress-strain law whereas the compression law of the material has insignificant influence. Fluctuation in the cracking strength had only a mild influence. The greatest influence was owing to the assumed peak tensile strength. Furthermore, it was observed during the preliminary analysis in both cases (*C160 and C125*), that the assumed strain at peak stress only affected mildly the displacement capacity in the post-peak load-deflection envelope (from 3.2 mm to 3.7 mm).

Another important finding was that the slope of the tensile post-peak softening branch, which depends on the maximum point ($\varepsilon_{t,max}$,$f_{t,max}$) and ultimate strain ($\varepsilon_{t,u}$), only affected the post-peak deformation capacity of the load-displacement diagram. The load-deflection point corresponding to the maximum tensile stress remained unaffected by $\varepsilon_{t,u}$.

4.3 Analysis Details of the Charts Proposed

After the preliminary analysis study, the final round of analyses was conducted with a selected compression model having average properties as follows. Results of the analyses performed using the properties describe hereon are presented in the design charts developed.

$$E_c = E_t; \quad f_c' = E_c \cdot \varepsilon_{co}\ ; \quad \varepsilon_{co} = 0.003; \quad \varepsilon_{cu} = 0.006$$

It is noted that the modulus of elasticity was assumed to be equal in the tension and compression branches of the stress-strain response of the material ($E_c = E_t$). Hence, the compressive strength (f_c') was calculated using the modulus of elasticity and the assumed peak compressive strain, $\varepsilon_{co} = 0.003$. The combinations of the tensile model parameters considered for further analyses are presented in Table 4- 3. Several combinations of the tensile model were developed where the stress parameters, $f_{t,cr}$ and $f_{t,max}$, ranged from 5 MPa to 8MPa, and 6 MPa to 12 MPa, respectively. Two different values were considered for cracking strain ($\varepsilon_{t,cr}$) equal to 0.0001 mm/mm and 0.0002 mm/mm. In addition, strain corresponding to the maximum stress ($\varepsilon_{t,max}$) were also considered to take on two different values, equal to 0.001 mm/mm and 0.003 mm/mm, respectively. Lastly, the ultimate tensile strain ($\varepsilon_{t,u}$) was taken as equal to 0.015 mm/mm. Tensile parametric values used in the analysis are summarized in Table 4- 3.

Table 4- 3: Tensile model parameters for main sets of analyses

$\varepsilon_{t,cr}$	$f_{t,cr}$	$f_{t,max}$	$\varepsilon_{t,max}$	$\varepsilon_{t,u}$
mm/mm	MPa	MPa	mm/mm	mm/mm
0.0001 and 0.0002	5.00	6.00	0.001 and 0.003	0.015
	6.00	6.00		
	5.00	7.00		
	6.00	7.00		
	7.00	7.00		
	5.00	8.00		
	6.00	8.00		
	7.00	8.00		
	8.00	8.00		
	5.00	9.00		
	6.00	9.00		
	7.00	9.00		
	8.00	9.00		
	5.00	10.00		
	6.00	10.00		
	7.00	10.00		
	8.00	10.00		
	5.00	11.00		
	6.00	11.00		
	7.00	11.00		

	8.00	11.00		
	5.00	12.00		
	6.00	12.00		
	7.00	12.00		
	8.00	12.00		

Based on the resistance curves obtained through analyses, normalized values of the milestone points such as cracking and peak were calculated to develop the design charts. Moments obtained from load values were normalized as per Equation 4-1 and deflections were normalized with half the beam span to provide drift ratios (%) as per Equation 4-2. Units for different parameters are as follows: Moment (M) is in N-mm; width (b), height (h), supported span (L) and measured deflection (δ) are in mm.

$$K = {M}/{(bh^2)} \tag{4-1}$$

$$D\ (\%) = \frac{\delta}{(0.5 \cdot L)} \cdot 100 \tag{4-2}$$

Cracking point is taken as the load where the flexural resistance curve starts to lose its linearity as shown in Figure 4- 11. It is important to carefully select the cracking point; a user may be susceptible to picking a wrong point depending on the range of the plot (full curve vs partial curve). Hence, it is advised to zoom in on the elastic portion of the resistance curve so that the cracking point can be clearly distinguished. From the experiments and analysis, it was observed that the peak tensile stress in the material law occurs just before the load reaches its peak value (P_{max}) in the resistance curve. This means that the localization starts to occur just before the peak load. This was also confirmed through DIC analysis of flexural test specimens. Hence, the point corresponding to 95%-97% of the actual peak load should be used to estimate $f_{t,max}$ and $\varepsilon_{t,max}$.

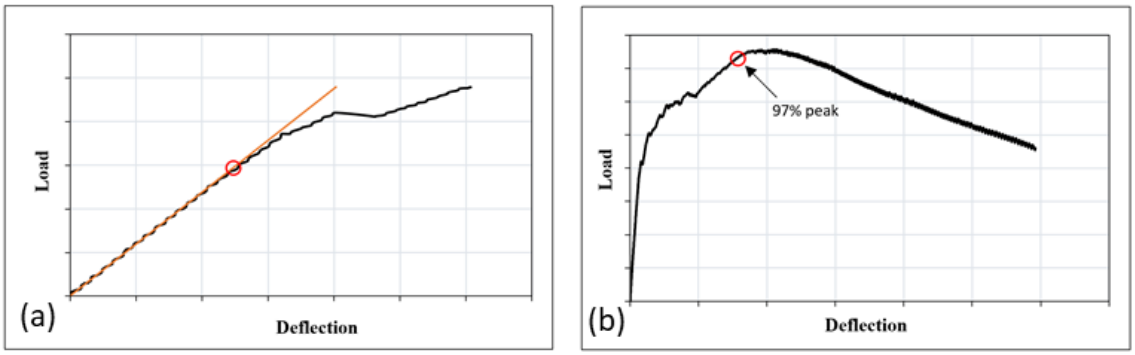

Figure 4- 11: Illustration of critical points used (a) cracking point (b) 97% of max. load (before peak)

4.3.1 Procedure to use Forward Analysis Charts

Design charts developed through the proposed Forward Analysis method and the procedure to be employed to obtain the tensile properties of UHPFRC are presented below. It is to be noted that linear interpolation must be carried out wherever required while using the charts proposed.

1. Perform a four-point bending test as per the configuration described earlier in Figure 4- 1.
2. Extract the load-deflection coordinates of the critical points (i.e., cracking and 97% peak) from the experimental response.
3. Determine the corresponding shear deformation at the critical points using Equation 3-12 and subtract it from the respective experimentally measured readings to obtain the net deflection values.
4. Estimate the normalized parameters (*K* and *D*) for the critical points as per Equation 4-1 and Equation 4-2.
5. Estimate the tensile cracking stress and strain values, $f_{t,cr}$, and $\varepsilon_{t,cr}$, from their corresponding charts by using K_{cr} and D_{cr}, respectively.
6. Determine the maximum tensile stress using the two K_{max} vs $f_{t,max}$ charts corresponding to $\varepsilon_{t,cr} = 0.0001$ and $\varepsilon_{t,cr} = 0.0002$ followed by interpolation to the actual cracking strain calculated in the previous step.
7. Using the value of $f_{t,max}$ determined in previous step, $\varepsilon_{t,max}$ is estimated from the D_{max} vs $f_{t,max}$ plot, using interpolation.

4.3.2 Forward Analysis Charts for 100 mm x 50 mm x 300 mm Prism

The design charts shown below represent normalized results obtained for a prism of 50x100x300 mm nominal dimensions (Type A, Table 4-1). Clear span and the shear span of the prism are 300 mm and 100 mm, respectively.

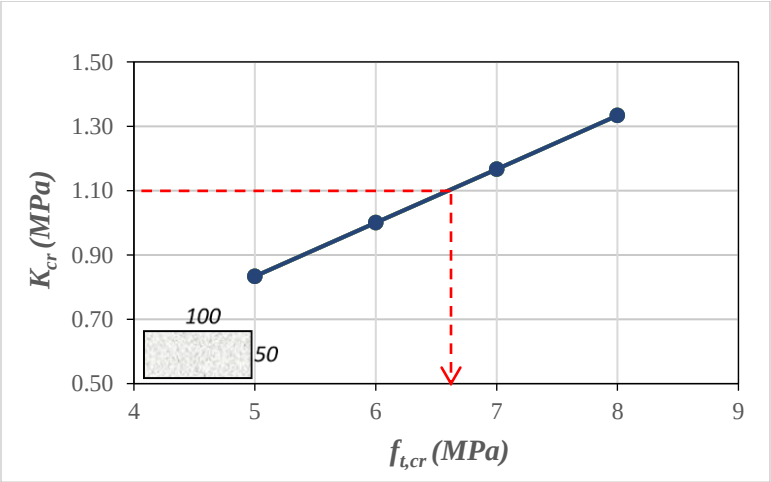

Figure 4- 12: Chart for cracking stress ($f_{t,cr}$) (100x50x300 mm specimen)

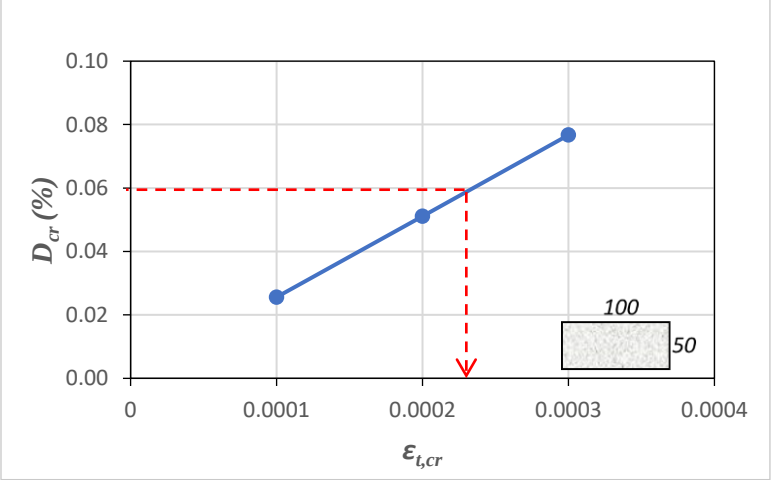

Figure 4- 13: Chart for cracking strain (ε_{tcr}) (100x50x300 mm specimen)

It is clearly evident that the cracking tensile stress and strain values ($f_{t,cr}$ and $\varepsilon_{t,cr}$) only depend on K_{cr} and D_{cr}, respectively, and remain unaffected by variations in $f_{t,max}$ or $\varepsilon_{t,max}$.

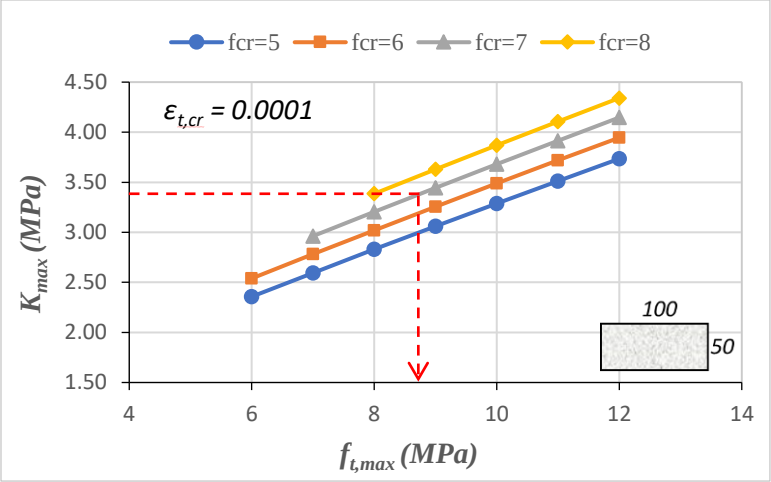

Figure 4- 14: Chart for maximum stress ($f_{t,max}$) for $\varepsilon_{t,cr}$= 0.0001 (100x50x300 mm specimen)

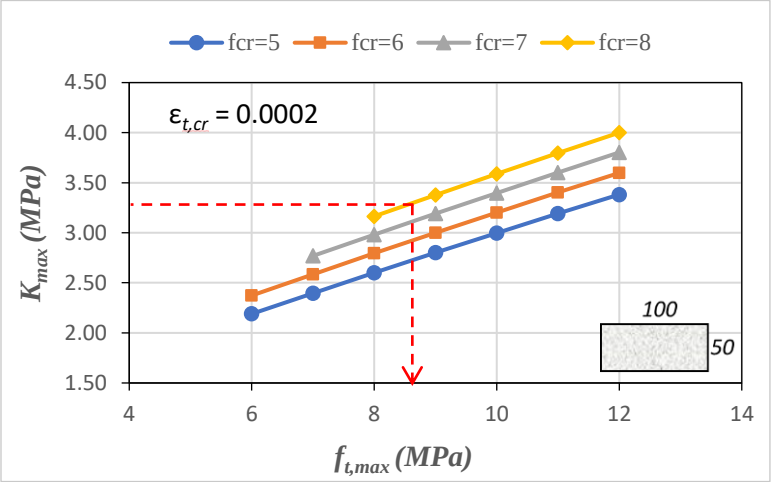

Figure 4- 15: Chart for maximum stress ($f_{t,max}$) for $\varepsilon_{t,cr}$= 0.0002 (100x50x300 mm specimen)

The two plots shown in Figure 4- 14 and Figure 4- 15 correspond to a different cracking strain limit (0.0001 vs 0.0002). It is noted that these charts are very similar to each other with small differences in the values of K_{max} owing to the change in the cracking strain value ($\varepsilon_{t,cr}$) from 0.0001 to 0.0002; however, this difference could lead to a considerable change in the final results. Hence, interpolation between two plots as per the estimated cracking strain ($\varepsilon_{t,cr}$) is recommended.

Having found the value of $f_{t,max}$, the next step is to obtain the value of $\varepsilon_{t,max}$ using D_{max}. For simplicity's sake, the average properties of cracking ($\varepsilon_{t,cr}, f_{t,cr}$) are considered here for developing the charts for $\varepsilon_{t,max}$. Based on the value of D_{max}, $\varepsilon_{t,max}$ can be estimated by interpolation as per the chart below (Figure 4- 16).

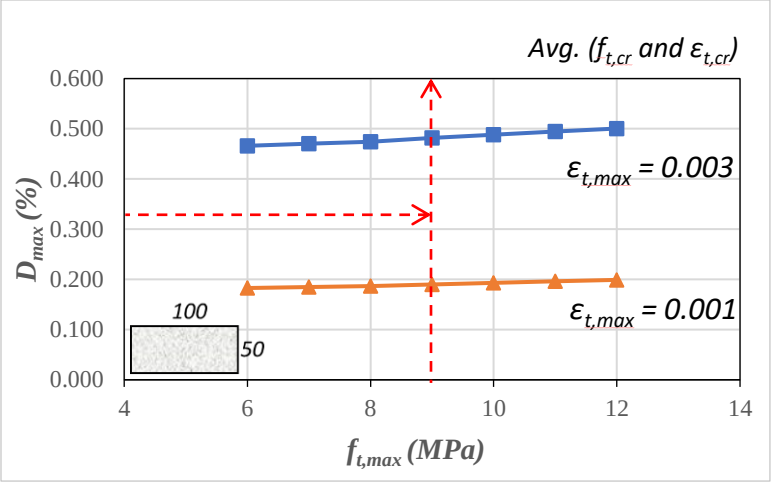

Figure 4- 16: Chart for $\varepsilon_{t,max}$ (100x50x300 mm specimen)

4.3.3 Forward Analysis Charts for 100 mm x 100 mm x 300 mm Prism

Following a similar procedure, the forward analysis charts are derived for different types of standardized dimensions, which in turn are generally defined to be 5 times or more the length of the commercially available fibers (Annex U, CSA A23.1, 2019). For 13mm long fibers, the standard dimension is 75 mm (but also the 50 mm case for depth is considered per the AFNOR recommendation); for up to 20 mm long fibers, 100 mm specimen cross-section is defined; and for the fiber lengths varying between 20 mm to 25 mm, the cross-section of 150 mm is recommended. Therefore, the design charts shown in Figure 4- 17 to Figure 4- 21 represent normalized results obtained for a prism of 100 mm x 100 m x 300 mm nominal dimensions (Type B, Table 4-1). Clear span of the prism and the shear span are 300 mm and 100 mm respectively. Similar charts developed for other standard prism cross-sectional sizes such as 75 mm x 75 mm and 150 mm x 150 mm were found to be same as those of 100 mm x 100 mm prism size as long as the aspect ratio was equal to 1.

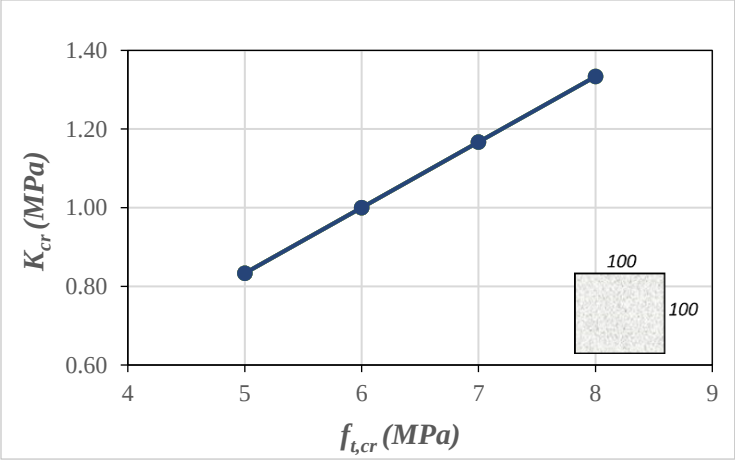

Figure 4- 17: Chart for cracking stress ($f_{t,cr}$) (100x100x300 mm specimen)

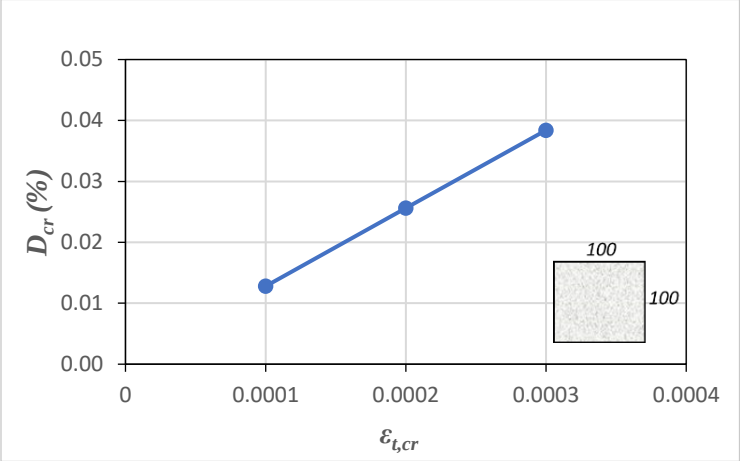

Figure 4- 18: Chart for cracking strain ($\varepsilon_{t,cr}$) (100x100x300 mm specimen)

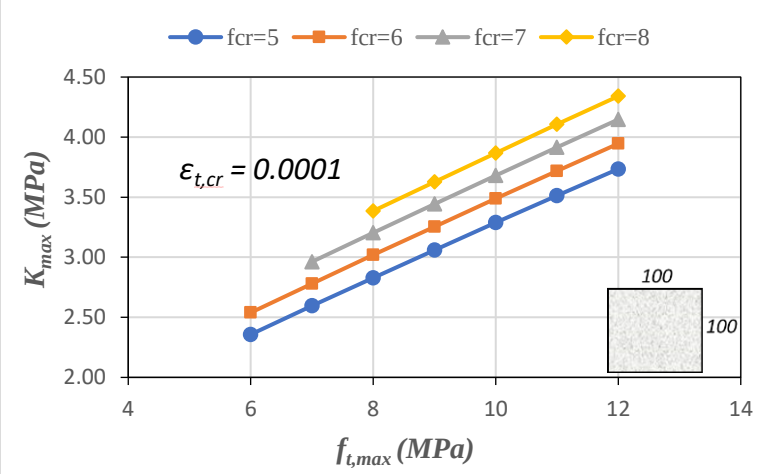

Figure 4- 19: Chart for maximum stress ($f_{t,max}$) for $\varepsilon_{t,cr}$=0.0001 (100x100x300 mm specimen)

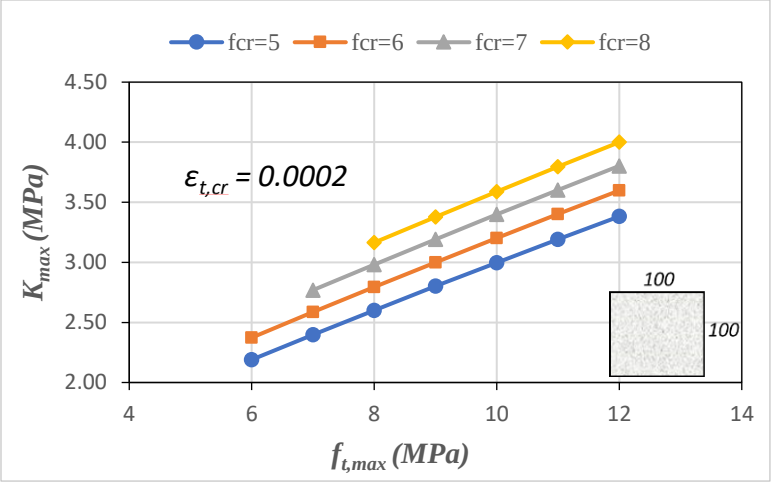

Figure 4- 20: Chart for maximum stress ($f_{t,max}$) for $\varepsilon_{t,cr}$=0.0002 (100x100x300 mm specimen)

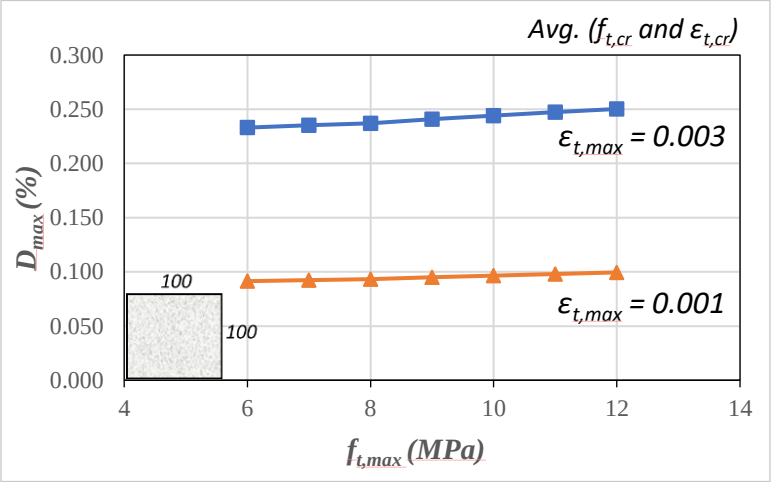

Figure 4- 21: Chart for $\varepsilon_{t,max}$ (100x100x300 mm specimen)

It is reminded that, to account for shear deformations, the deflection value obtained from Equation 3-12 needs to be subtracted from the experimentally measured deflection readings before using the above design charts. Also, it is noteworthy that the shear deformation contribution is less significant in thin prisms with aspect ratio of 2 when compared with a square prism of aspect ratio 1. An example of the Forward Analysis application and comparison with results obtained from the CSA inverse analysis is shown below for a flexural test experiment taken from Husain (2021).

4.4 Example of a 100 mm x 100 mm Flexural Specimen

Below is an example on the comparison of characteristic tensile properties obtained from the CSA inverse analysis (Annex- 8.1 of CSA S6, 2019) and the proposed forward analysis procedures. The

inverse analysis procedure recommended by the Annex 8.1 was described in detail in Section 2.7.1. Experimental data corresponding to specimen P2 of Batch-1 mix casted on Jan27th, 2020 from Husain (2021) was chosen for this example. The specimen had a square cross-section of size 100 mm, and the supported span was 300 mm conforming to Type-B specimen from Table 4- 1.

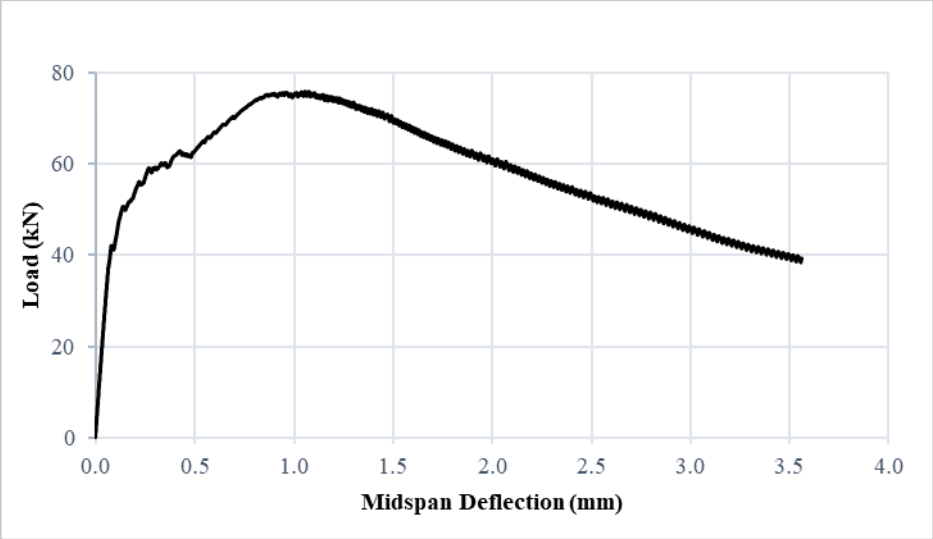

Figure 4- 22: Experimental resistance curve of a 100x100x300 mm flexural test (Husain, 2021)

a) Result obtained as per Annex 8.1, CSA S6 (2019)

Table 4- 4: Characteristic points required for CSA Inverse Analysis

Characteristic Points		
Load	Midspan Deflection	Characteristic Points
P (kN)	*δ (mm)*	*(P, δ)*
0.098	0.0000	Initial Slope, S_o
20.037	0.03418	
41.26	0.0952100	(P_1, δ_1)
55.69	0.2410900	(P_2, δ_2)
73.53	0.7963053	(P_3, δ_3)
75.80	1.0563660	(P_{max}, δ_{max})
58.82	2.0855501	(P_4, δ_4)

Characteristic points required for the inverse analysis were chosen from the flexural load-deflection curve (Figure 4- 22) and are summarized in Table 4- 4. Using the expressions described in Table 2-2, stress-strain and stress-crack width relationship for tensile behaviour of UHPFRC were calculated as depicted in Figure 4- 23.

Table 4- 5: Tensile behaviour properties obtained from CSA Inverse Analysis

Stress	**Strain**	**Crack Width**
f_t (MPa)	ε_t (mm/mm × 10^{-3})	w (mm)
0.00	0.000	-
7.17	0.171	-
9.20	9.128	-
2.53	-	3.07
0	-	5.0

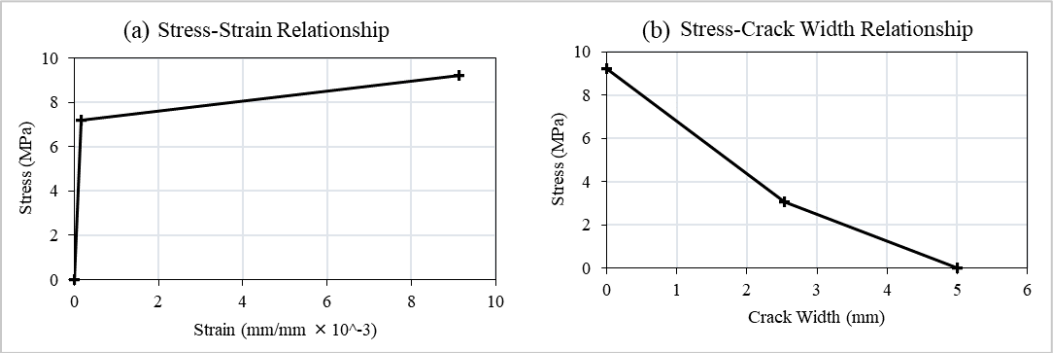

Figure 4- 23: Tensile behaviour of the sample specimen as per CSA inverse analysis procedure

b) Result obtained using the Forward Analysis design charts

Table 4- 6 summarizes the characteristic points selected from flexural resistance curve and their normalized values calculated for performing the Forward Analysis. Net deflection was estimated by subtracting the shear deformation calculated from Equation 3-12. Cracking point was carefully identified as shown in Figure 4- 11. Several interpolations were carried out before arriving at the results shown in Table 4- 7. Figure 4- 24 depicts the comparison between the estimated tensile behaviour obtained from the two methods mentioned above.

Table 4- 6: Characteristic points for Forward Analysis

	Load	Deflection	Net Deflection	Moment	K	D
	(N)	(mm)	(mm)	(N-mm)	(MPa)	(%)
Cracking Point	26870	0.04763	0.0381	1343500	1.34	0.025%
Peak Point (97% peak)	73525	0.79584	0.7698	3676274	3.68	0.513%

Table 4- 7: Tensile properties obtained from Forward Analysis

Tensile Property	Shear not considered	Shear considered
E (MPa)	32528	40645
$f_{t,cr}$ (MPa)	8.1	8.1
$\varepsilon_{t,cr}$ (mm/mm)	0.00025	0.00020
$f_{t,max}$ (MPa)	11.02	10.40
$\varepsilon_{t,max}$ (mm/mm)	0.00681	0.00662

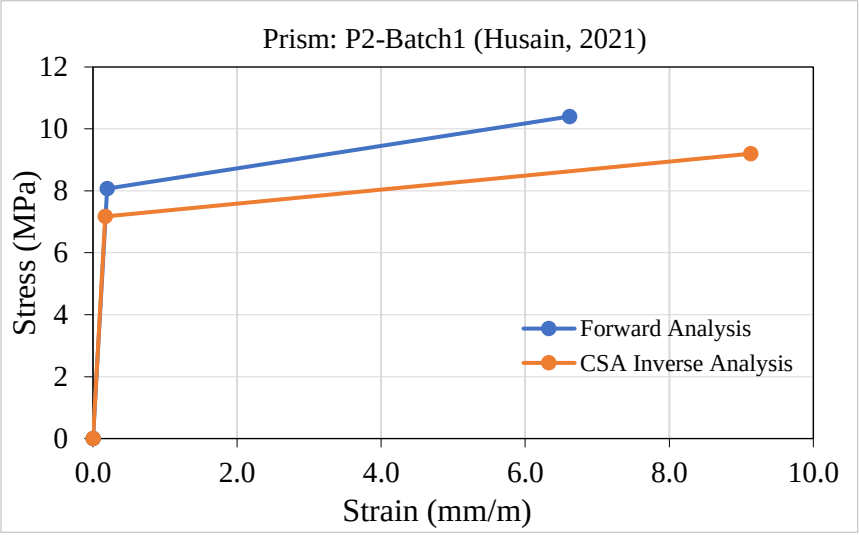

Figure 4- 24: Comparison between CSA inverse analysis and Forward Analysis

4.5 Forward Analysis Results

Table 4- 8 summarizes the tensile results obtained from Forward Analysis carried out for the thin flexural prisms (100 mm x 50 mm x 300 mm) corresponding to three different mixes used in this study. Flexural tests corresponding to Mix DE2 were discussed in Chapter 3, however, for Mix TSO2 and Mix TSO1 they will be presented in the next chapter. Figure 4- 25 and Figure 4- 26 depicts the direct tensile behaviour determined using Forward Analysis for different mixes. In addition, a comparison between respective tensile properties predicted using the proposed inverse analysis method (refer to Chapter 3) and the Forward Analysis method is shown in Figure 4- 27 which shows satisfactory convergence between the two methods.

Table 4- 8: Results from Forward Analysis corresponding to different castings

Mix	Specimen ID	E	$f_{t,cr}$	$\varepsilon_{t,cr}$	$f_{t,max}$	$\varepsilon_{t,max}$
		(MPa)	(MPa)	(mm/mm)	(MPa)	(mm/mm)
DE2	R1	51140	7.4	0.00015	12.1	0.00622
	R2	49283	8.6	0.00018	14.6	0.00569
	OW1	61764	10.2	0.00017	12.8	0.00473
	OW2	62563	11.1	0.00018	13.4	0.00259
	OW3	59454	9.4	0.00016	12.9	0.00492
TSO2	A1	45865	8.0	0.00017	11.6	0.00432
	A2	46788	9.2	0.00020	13.1	0.00342
	A3	46732	8.9	0.00019	11.0	0.00394
TSO1	A1	50292	4.6	0.00009	7.0	0.00523
	A2	58541	6.6	0.00011	8.5	0.00717
	A3	59688	6.4	0.00011	8.9	0.00627

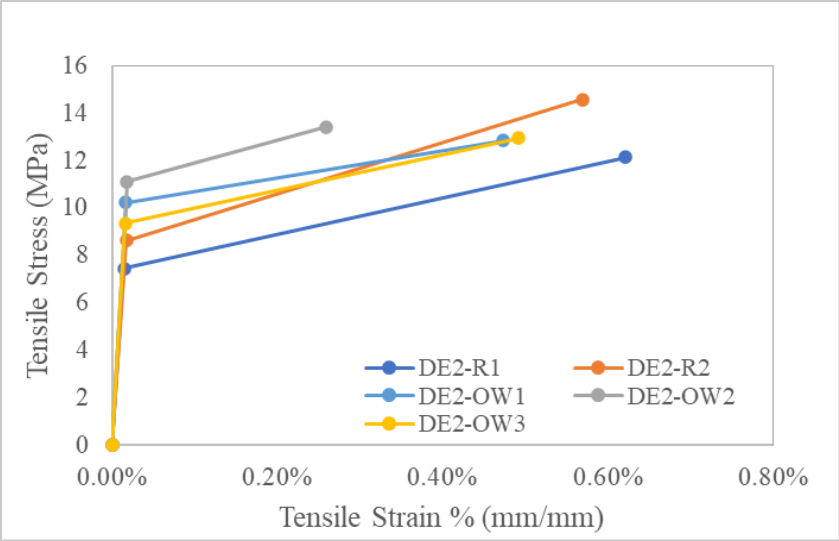

Figure 4- 25: Forward Analysis results for mix DE2 flexural prisms

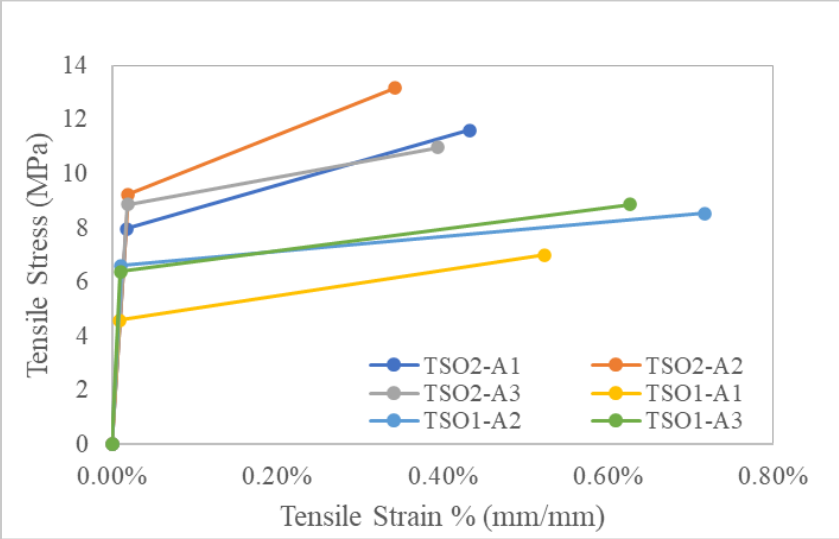

Figure 4- 26: Forward Analysis results for mix TSO2 and TSO1 flexural prisms

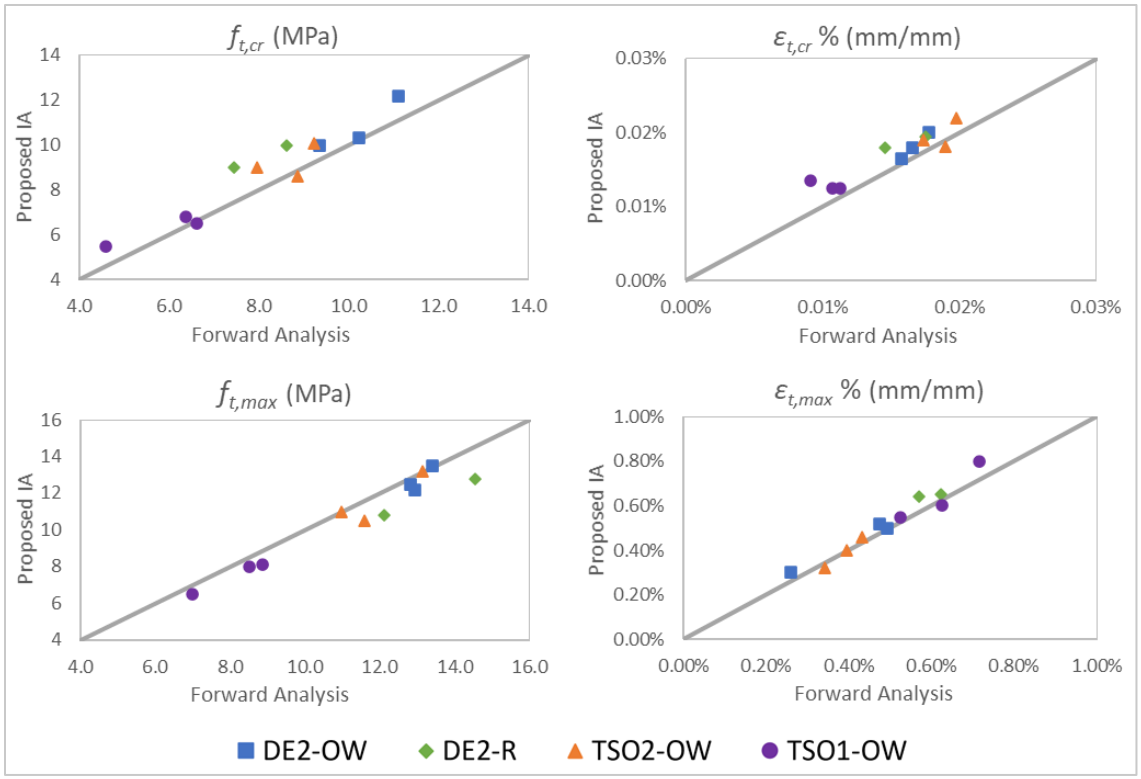

Figure 4- 27: Comparison between tensile properties predicted from Proposed IA and Forward Analysis methods

4.6 Summary

In this chapter, a direct and simple Forward Analysis method was presented to predict the tensile stress-strain properties corresponding to cracking and maximum stress points of UHPFRC by using flexural response curves. Effects of different tensile properties on the flexural behaviour was found through the preliminary analysis. The constitutive model in compression was found to have negligible influence, implying that the tensile stress-strain law governs the flexural behaviour of UHPFRC material characterization beams. Critical points from the flexural response curve were correlated with the cracking and maximum stress points in direct tension. Cracking stress point was associated with the loss of linearity in flexural load-deflection curve whereas the maximum stress point was associated with 97% peak moment in the pre-peak region. Subsequently, the Forward Analysis design charts were developed for commonly recommended prism sizes that can be used to predict the required tensile properties of UHPFRC. An example square prism of 100 mm x 100 mm cross-section was analyzed to derive direct tensile properties using the proposed Forward Analysis charts and with the existing inverse analysis method in Annex 8.1 (CSA S6,

2019). Moreover, the results of tensile properties estimated from the Forward Analysis for various UHPFRC mixes used in this thesis were compared with that of the proposed inverse analysis method. This direct and effective method to estimate the critical tensile properties of UHPFRC was aimed to serve the purpose of material producers and design engineers alike.

Chapter 5: Tension Stiffening of UHPFRC

Superior mechanical and durability characteristics of UHPFRC make it a highly suitable material for retrofit and rehabilitation of damaged structures. As discussed earlier, UHPFRC can be a suitable material for strengthening, repair and rehabilitation of damaged and corrosion deteriorated reinforced concrete structural members. Tension stiffening is an important property to be considered in the design and analysis of reinforced-UHPFRC members on account of the high bond strength, tensile strength and strain capacity offered by UHPFRC which is usually ignored in conventional concrete. In this chapter, an experimental program carried out to study the tension stiffening behavior of UHPFRC based on several parameters is presented. Parameters studied include percentage of steel fibers in the mix, casting methodology and the loading protocol. Moreover, the effect of corrosion on tension stiffening of UHPFRC was explored by testing specimens with pre-corroded reinforcement bars obtained using accelerated corrosion technique.

5.1 Specimen Preparation

15M Canadian standard reinforcement steel bars were cut to a straight length of 400 mm approximately, and 24 such specimens were obtained. Twelve of these specimens were used for carrying out accelerated corrosion on the bars while the remaining 12 were stored aside in a dry place to be used as control specimens. Additionally, 3 more rebar specimens from the same lot were cut to test the behavior of bare rebar in tension. Average properties of the 15M reinforcement bar were found to be E_s = 202 GPa, f_y= 420 MPa, f_u= 600 MPa, ε_{sh} = 0.0133 and ε_u= 0.06. Coupon tests performed on the reinforcement are discussed later.

Accelerated corrosion technique was used to corrode the rebar specimens in a controlled manner. A total of 12 rebars were subjected to corrosion. Figure 5- 1 shows the schematic diagram of the corrosion test setup and Figure 5- 2 shows the actual experimental set up. A ± 20 Volts DC voltage source was used as a power source to apply a constant voltage of 6 V. Rebars were connected to the power source via solderless breadboard through jumper wires. In this setup, the rebar specimen acted as the anode and an external 25M rebar piece, placed inside the corrosion bath with salt solution, acted as the cathode of the circuit. 3% NaCl solution was used in the corrosion bath that acted as the electrolyte medium and completed the electrical circuit. Rebars were wrapped on the

middle 200 mm length using a burlap with an extended portion dipped into the NaCl solution (see Figure 5- 1).

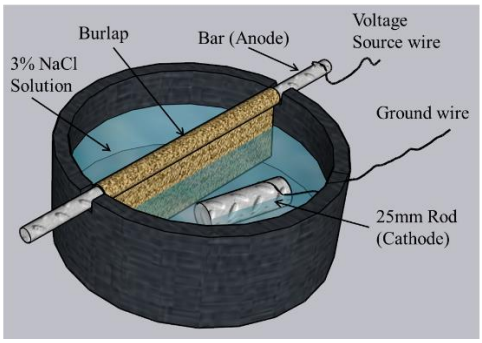

Figure 5- 1: Sketch of the accelerated corrosion setup

Initially, the specimens were subjected to alternate wet and dry cycles to allow for complete oxidation of the corrosion products. Later, it was noted that as the reinforcement bars were not inside concrete yet, the oxidation still occurred if they were corroded in wet cycle continuously for a longer period (3-4 days). A True RMS multimeter was used to measure the electrical current passing through each rebar at the start and end of a wet cycle and the average current was used to estimate the mass loss due to corrosion. The amount of current passing through a rebar was controlled to not exceed a current density of 200 μA/cm^2, which is the upper threshold of current density for a corroding bar found in nature (El-Joukhadar & Pantazopoulou, 2021).

Figure 5- 2: Setup for accelerated corrosion process of rebars

$$\Delta m\ (grams) = \frac{t \cdot i \cdot M}{Z \cdot F} \tag{5-1}$$

$$Mass\ loss\ (\%) = \frac{\Delta m}{m_o} \cdot 100 \qquad (5\text{-}2)$$

Mass loss was estimated based on two ways. Firstly, through Faraday's law as per Equation 5-1 and 5-2, where t is the time of exposure to current (s); i is the current (Amperes); M is the atomic weight of iron (M=55.847 g/mol); Z is the ion charge (2 mol of electrons); F is Faraday's Constant representing the amount of electrical charge in 1 mol of electron (F = 96,487 C/mol). Δm and m_o are the mass loss (in grams) and the original mass, respectively. The second method to calculate mass loss (%) was performed using the physical weights of the rebar specimens before and after the corrosion phase. Bars were corroded over a period of four months till they accumulated a mass loss in the range of 12-13%, approximately. Summary of the corrosion data and the mass loss calculations are shown in Table 5- 1. Mass loss values estimated from both methods demonstrated good agreement with each other.

Table 5- 1: Summary of estimated mass loss due to accelerated corrosion process

	A: From Faraday's law			**B: From measured mass**				Comparison (A-B)
Bar #	Initial Mass	ΣCurrent	**Mass Loss**	M_o (middle 200mm)	M_c (middle 200 mm)	Mass Loss	**Mass Loss**	
	gm	mA	%	gm	gm	gm	%	%
1	602	1200	**13.29%**	299	262	37	**12.31%**	0.98%
2	598	1088	**12.13%**	299	260	40	**13.25%**	-1.12%
3	592	1228	**13.83%**	299	263	36	**12.17%**	1.66%
4	598	1175	**13.10%**	299	264	35	**11.78%**	1.32%
5	600	1026	**11.40%**	299	261	38	**12.83%**	-1.42%
6	604	1157	**12.77%**	299	262	37	**12.34%**	0.43%
7	608	959	**10.52%**	299	260	40	**13.21%**	-2.70%
8	602	1010	**11.19%**	299	261	38	**12.66%**	-1.46%
9	580	1161	**13.34%**	299	262	37	**12.46%**	0.88%
10	602	1220	**13.51%**	299	263	37	**12.25%**	1.26%
11	598	1252	**13.97%**	299	262	37	**12.34%**	1.62%
12	602	1089	**12.06%**	299	260	39	**13.07%**	-1.01%

Upon completion of the corrosion process, two steel rods of 25mm diameter and ~150 mm length were welded, one on each end, to the rebar specimen before being cast into UHPFRC. This was done to allow the failure of the specimen to occur within the concrete region. A similar weld joint was also found in tension stiffening experiments performed by Moreno et al. (2014) with HPFRCC materials. If a single rebar was used throughout, the bar would yield and fracture outside of the UHPFRC specimen due to the significant tensile strength contributed by UHPFRC. This was also confirmed from the results of preliminary Finite Element analysis performed before finalizing the design of the specimen.

Rust accumulated on the surface of the corroded rebars was cleaned using a wire brush grinder before casting. This was done to remove the loose rust remains from the rebar and improve its bond with the surrounding UHPFRC matrix. Figure 5- 3 shows the corroded rebars before and after rust removal. The cleaned specimen was then placed inside the formwork before pouring UHPFRC. Typical geometry details of the tension stiffening specimen are shown in Figure 5- 4.

Figure 5- 3: Specimen before and after rust cleaning

The tension stiffening specimen with a cross-section of 75mm x 50mm and a length of 430 mm was used. The formwork shown in Figure 5- 5 was prepared to place the rebar along the centroidal line of the cross-section using firm foam pieces on both ends. Foam pieces had a 25 mm diameter hole in the center to ensure proper alignment of the bar inside the concrete specimen. Moreover, dowel bars of approximately 100mm length were tied near the welded joint to strengthen the connection zone. This arrangement provided a clear length of 160 mm to 180 mm in the middle of the specimen for measuring strain deformations during the experiments.

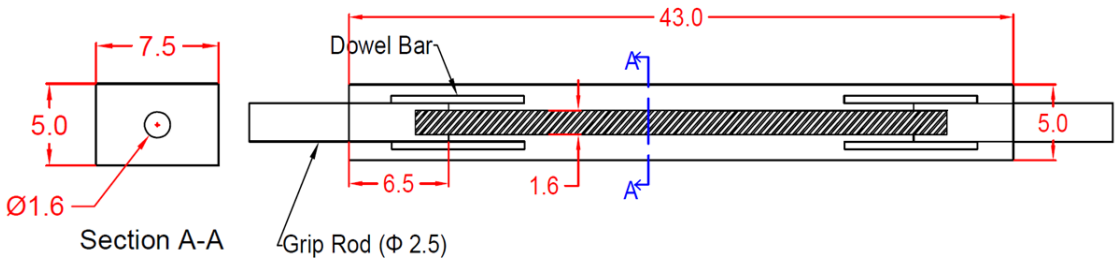

Figure 5- 4: Tension Stiffening Specimen drawing (in cm)

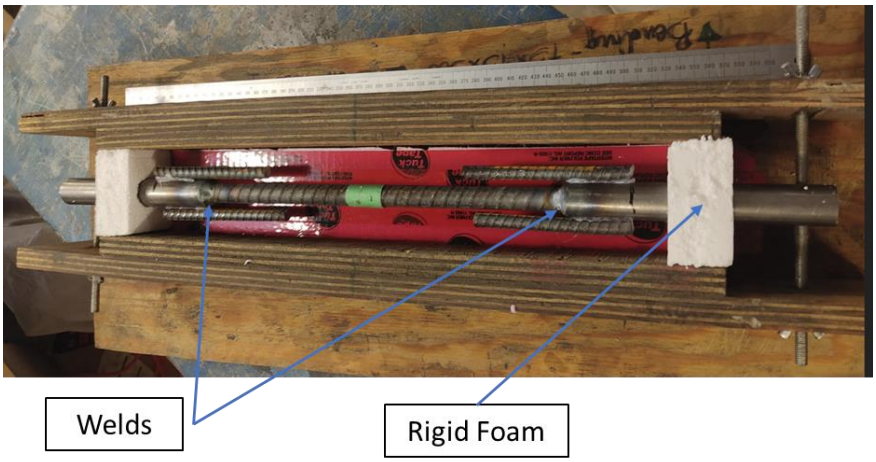

Figure 5- 5: Formwork for Tension Stiffening specimen

5.2 Preliminary Finite Element Analysis

Finite Element Modeling was performed using GID-ATENA 3D software suite to study the feasibility of the designed tension stiffening specimen. Primary objective of the preliminary analysis was to understand the general tension stiffening response provided by different specimen designs and their failure patterns. Detailed non-linear finite element analysis performed after conducting the experiments is presented in Chapter 6.

For this preliminary analysis, nominal properties of the UHPFRC material corresponding to Mix DE2 (described in Section 3.3) were used as they represent a similar material to what is used in this particular study. In case of reinforcement pull-out models, an external steel block with undeformable solid volume has to be modelled in order to apply the controlled displacement loading to the specimen. UHPFRC was modeled as a solid volume with hexahedral elements whereas the rebar was modeled as a 1D reinforcement element as depicted in Figure 5- 6. Owing

to the high bond strength of UHPFRC, the reinforcement was assumed to have perfect bond condition with UHPFRC for the analysis purpose.

Two kinds of models were prepared, one where a single reinforcement bar (15M) was used throughout the specimen and another where the 15M rebar was connected with the 25M rebar. Figure 5- 6 shows the finite element response corresponding to the above two models at their failure stage, in terms of stress distribution in reinforcement and UHPFRC. It is noted that the specimen with a single 15M rebar throughout (Figure 5- 6a) develops yielding and fracture in the rebar outside of UHPFRC unlike the other specimen where 15M rebar was joined with 25M rebar to act as a gripping rod, Figure 5- 6b. The latter being the targeted objective of the experiment, the final specimen chosen for tests had a 15M rebar in the middle of UHPFRC prism, connected by two steel rod pieces of 25 mm diameter towards each end. The embedded length of 25 mm grip rods was equal to about 65 mm from the formed ends of the specimen.

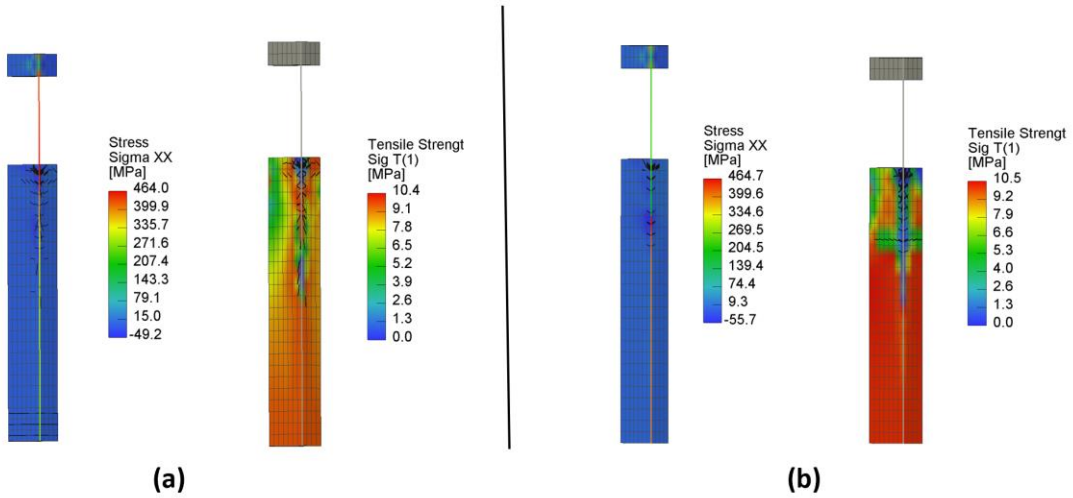

Figure 5- 6: Steel and concrete stresses at failure in TS Specimen with: (a) single 15M rebar (b) 15M rebar joint with 25M

5.3 Material Design

This experimental program comprised three different UHPFRC mixes which were produced using the same prepackaged dry cementitious mix (Densit® Inducast TT-5). Inducast TT-5 is a cement-based composite product that contains Portland cement, ultra-fine silica fume particles, calcined bauxite sand (0-1mm) and a concrete superplasticizer. No other external superplasticizer was used.

Bekaert Dramix® straight steel fibers of 0.2 mm in diameter and 13 mm long were used in all the three mixes. A sample of steel fibers used is shown in Figure 5- 7. The fibers were brass coated with a reported tensile strength of 2,750 MPa. The mix proportions are provided in Table 5- 2. Three mixes were prepared which are named as TSO2, TSO1 and TSR2. In the mix titles, TS represents Tension Stiffening, O and R correspond to *One-way* and *Random* casting, respectively, and the succeeding integer represents the volume percentage of fibers in a given mix.

The first mix, TSO2, contained 2% fibers by volume and all the specimens cast from this mix were cast from one end. Tension stiffening, flexure, compression, and direct tension specimens were prepared from TSO2 mix. TSO1 contained 1% fibers by volume and specimens cast from this mix were also poured from one end. Specimens from TSO1 mix included tension stiffening, flexure, compression, and direct tension. Lastly, TSR2 mix containing 2% steel fibers was used to pour specimens in a random way to study the effect of casting methodology compared with TSO2 mix specimens. Different mixes and their corresponding specimens are summarized in Table 5- 3.

Figure 5- 7: Sample of Steel Fibers and Densit® dry mix bag

Table 5- 2: Mix proportions by weight

	Proportions by weight	
	TSO2 & TSR2 (2% fibers)	TSO1 (1% fibers)
Densit® dry mix	1	1
Water	0.117	0.117
Fibers	0.066	0.033

5.4 Casting and Curing of Specimens

All three mixes were produced by following an identical mixing procedure to eliminate any undesirable variability between them. A large pan type mixer of 400-litre capacity was used. In the start of the batching, the mix had to be totally dry. Densit dry mix powder was mixed for about 2 minutes followed by addition of half the water required and mixed for 5 minutes. The remaining half of the water was then added and mixed for another 5 minutes. Lastly, steel fibers were gradually added, and mixing was continued until the fibers were evenly distributed (2 to 3 minutes).

Table 5- 3: Details of UHPFRC mixes and specimens

Mix	Cast Date	Fibers % (by vol.)	Flow (mm)	Casting methodology	Specimen types
TSO2	3/25/2022	2%	235	One-way	Tension stiffening (6 regular and 6 corroded), compression, AFNOR-flexure and direct tension
TSO1	3/31/2022	1%	230	One-way	Tension stiffening (3 regular and 3 corroded), compression, AFNOR-flexure and direct tension
TSR2	3/31/2022	2%	240	Random	Tension stiffening (3 regular and 3 corroded), compression and direct tension

The UHPFRC produced was flowable and self-consolidating. Immediately after the mixing process, the flowability of each mix was determined by performing a flow table test as per ASTM C1856 (*ASTM 2017*). The conical mold of the flow table was filled with fresh UHPFRC in a single layer up to the brim before being lifted over to allow the concrete to spread (Figure 5- 8). Average diameter of the flow was measured after 2 mins of lifting the mold. Flowability results are summarized in Table 5- 3. After pouring the concrete, molds were fully covered by plastic sheets to avoid moisture loss and shrinkage cracking. All specimens were demolded after 48 hours from casting. Tension stiffening specimens were wrapped with a wet burlap and then cured in small tubs, to avoid corrosion of the steel grips that were outside of the specimen, for 28 days as shown

in Figure 5- 9. All other specimens were completely immersed in a curing water tank that was maintained at room temperature for at least 28 days.

Figure 5- 8: Flowability test of fresh UHPFRC from different mixes

Figure 5- 9: Curing of companion test specimens and tension stiffening specimens

5.5 Instrumentation

A servo-controlled, closed loop universal testing machine (MTS) was used to conduct tension stiffening, direct tension and flexural tests associated with this study. A parallel ring extensometer was designed using an aluminum frame to hold LVDTs on all four sides of the tension stiffening specimen. However, two LVDTs were used on either side and a differential transducer (DT) was used on the back side of the tension stiffening specimen as shown in Figure 5- 10. The gauge length of the extensometer used was 105 mm. The extensometer rings were equipped with four calibration plates that were designed to maintain a fixed gauge length for all the specimens tested.

Once the extensometer was placed onto the specimen gripped in the MTS machine, the calibration plates were removed before starting the test. The data measured during the test was recorded at frequency of 10 Hz using a DAQ unit synched with the load cell of MTS machine. The front face of the tension stiffening specimen was prepared to have a speckle pattern for performing DIC. A high-resolution digital camera was setup to automatically capture images at a constant interval of 10 seconds during a test. The ends of the UHPFRC specimen were strengthened with CFRP in the longitudinal direction on all four sides along with a CFRP jacket wrapped transversely around the specimen ends as shown in Figure 5- 10. For monotonic testing, a constant displacement loading rate equal to 0.75 mm/min was used. With regard to the cyclic testing, a displacement rate equal to 0.75 mm/min was used for loading and 1.25 mm/min was used for unloading. Three cycles were performed at load values equal to 35 kN, 70 kN and 90 kN which were unloaded till 20 kN.

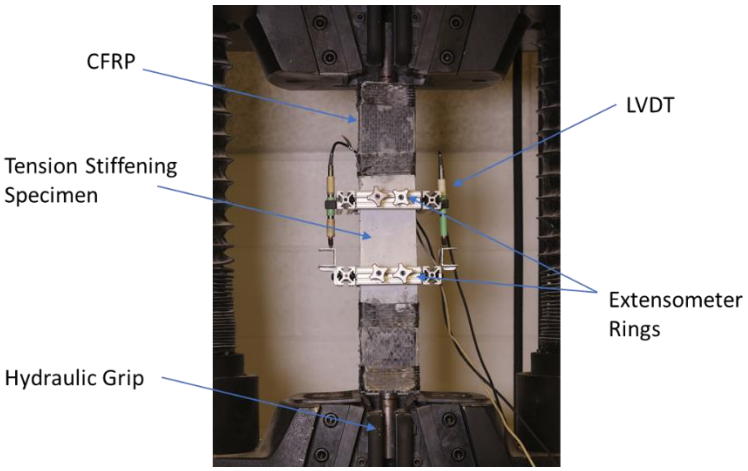

Figure 5- 10: Experimental test setup of Tension Stiffening test

Table 5- 4: Nomenclature for Tension Stiffening Specimens

Mix	Loading Protocol	Specimen ID (R = Regular; C = Corroded)
TSO2	Monotonic	2R, 3R, 7R, 1C, 3C, 4C
	Cyclic	8R, 9R, 10R, 2C, 5C, 6C
TSO1	Monotonic	11R, 12R, 7C, 8C
	Cyclic	13R, 9C
TSR2	Monotonic	14R, 15R, 10C, 11C
	Cyclic	16R, 12C

5.6 Experimental Results

5.6.1 Reinforcement Bar Coupon Tests

To obtain the material properties of the 15M reinforcement bar used in this study, direct tension tests were performed on bare rebar samples. Three rebar coupons of identical length (~400 mm length) were obtained from the same reinforcement material used for the tension stiffening specimens. Two samples were tested under monotonic loading whereas the third one was tested under a cyclic loading protocol, as defined earlier in Section 5.5. Figure 5- 11 and Figure 5- 12 show the monotonic and cyclic stress-strain response of bare rebars, respectively. The extensometer used to measure the strain in the rebar was detached during the hardening region as a precautionary measure to avoid any damage, but the loading was continued up to the attainment of fracture. Hence, the dashed lines drawn represent the extrapolated response up to fracture of the rebar. Average reinforcement properties obtained from these coupon tests are as follows: f_y = 420 MPa; ε_y= 0.00208 mm/mm; E = 202 GPa; ε_{sh} = 0.0133 mm/mm; f_u = 600 MPa and ε_u = 0.06 mm/mm.

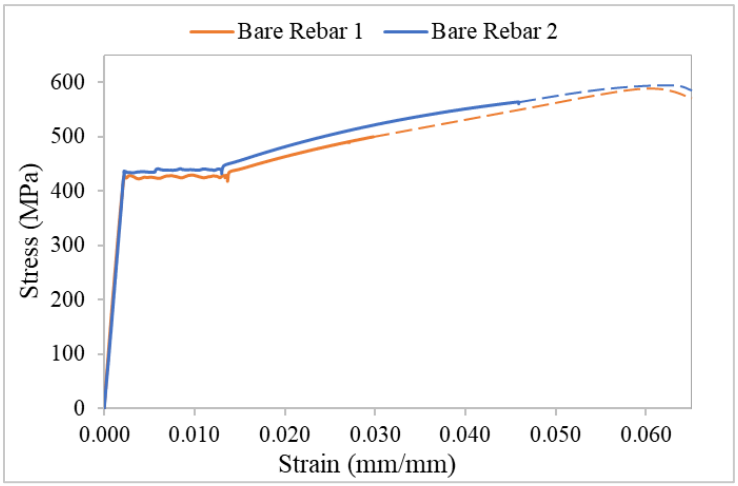

Figure 5- 11: Monotonic stress-strain response of rebar in tension

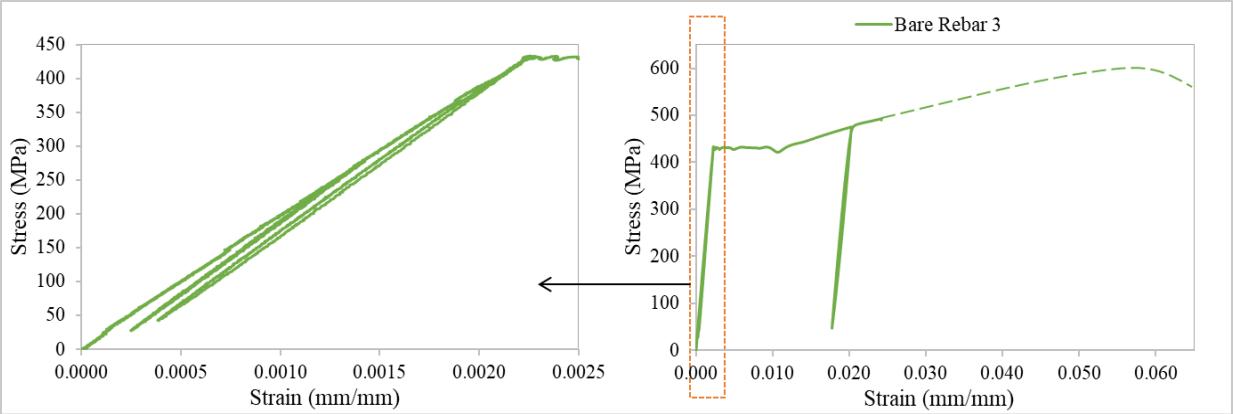

Figure 5- 12: Cyclic stress-strain response of rebar in tension

5.6.2 Tension Stiffening – Mix TSO2

Nominal dimensions of the cross-section at the mid height for Mix TSO2 specimens were equal to 50 mm x 75 mm. A total of 12 specimens were tested out of which 6 specimens contained pre-corroded (C) rebars and 6 contained regular (R) rebars. Out of these two sets with 6 specimens each, three were tested under monotonic loading and the remaining 3 were tested under a cyclic loading protocol. All specimens in this mix were one-way cast in the longitudinal direction with 2% steel fibers by volume. Experimental load-strain curves corresponding to Mix TSO2 specimens are shown in Figure 5- 13 to Figure 5- 16.

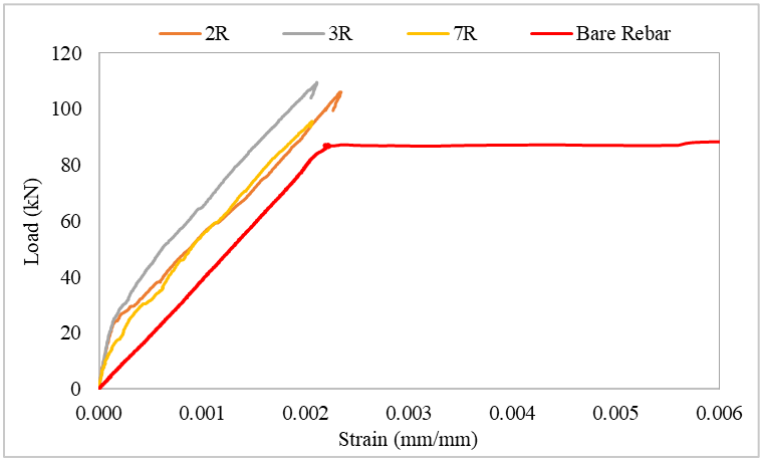

Figure 5- 13: Monotonic Load-Strain response of Regular specimens (Mix TSO2)

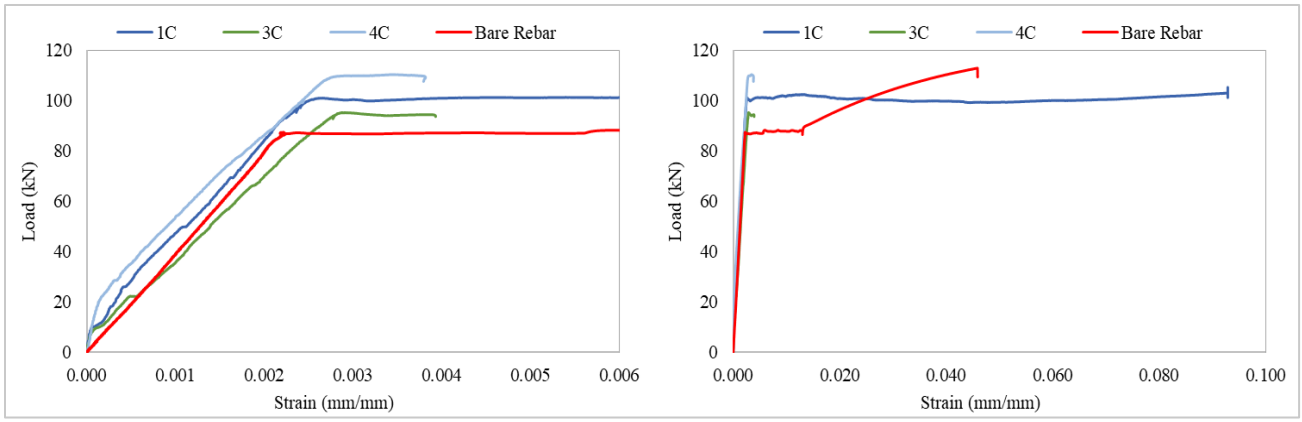

Figure 5- 14: Monotonic Load-Strain response of Corroded specimens (Mix TSO2)

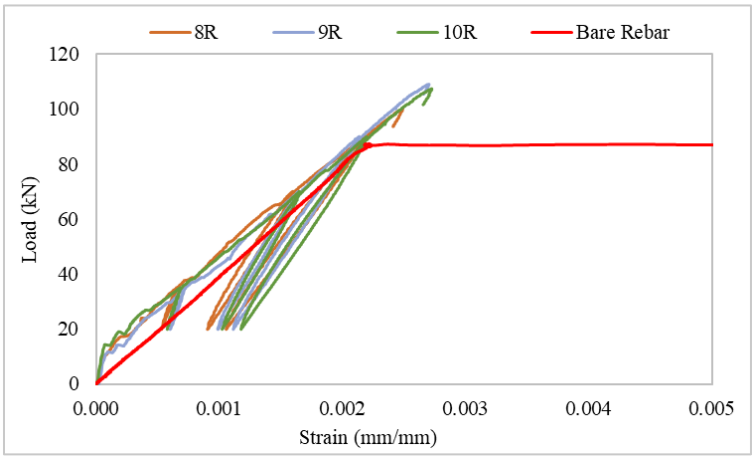

Figure 5- 15: Cyclic Load-Strain response of Regular specimens (Mix TSO2)

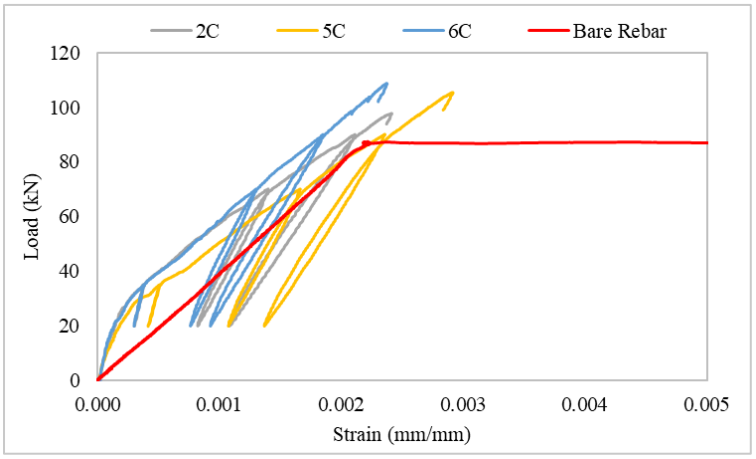

Figure 5- 16: Cyclic Load-Strain response of Corroded specimens (Mix TSO2)

Figure 5-17a represents the progressive cracking for the specimen TSO2-1C whereas Figure 5-17b shows the state of the specimen after failure. Multiple transverse cracks due to tension were developed at first, followed by a longitudinal crack that may have been induced by radial pressure from ribs of the rebar onto the surrounding UHPFRC matrix. Similar crack pattern was observed in other specimens that reached failure stage.

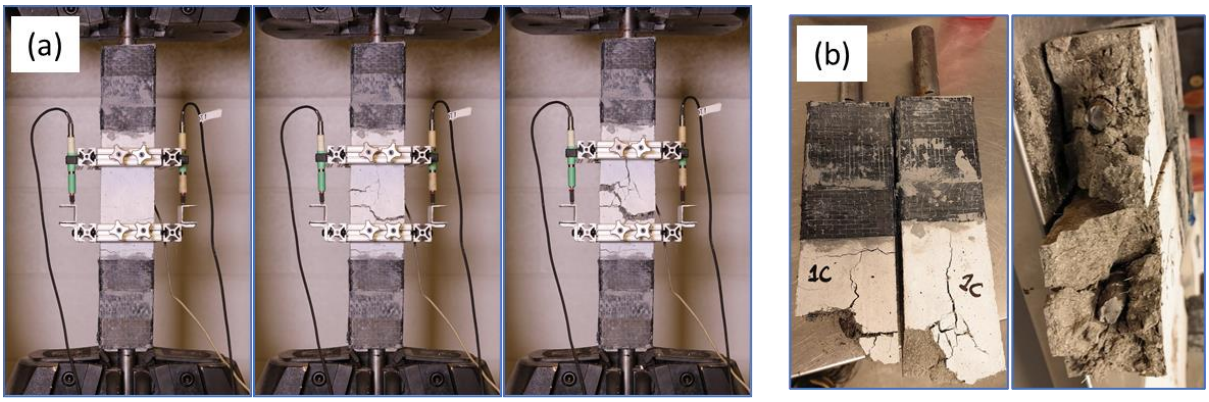

Figure 5- 17: (a) Crack development through various load stages (b) Specimen after failure (TSO2-1C)

5.6.3 Tension Stiffening – Mix TSO1

In an effort to obtain the complete resistance curve beyond the yielding of reinforcement, the specimens from Mix TSO1 and Mix TSR2 were notched at mid height of the specimen so as to encourage failure occurrence in the central region. Nominal dimensions of the notched cross-section were equal to 50 mm x 50 mm as shown in Figure 5- 18. A total of 6 specimens were tested out of which 3 specimens comprised pre-corroded (C) rebars and 3 contained regular (R) rebars. Out of these two sets with 3 specimens each, two were tested under monotonic loading and the remaining one was tested under cyclic loading protocol. Similar to specimens from Mix TSO2, all specimens in this mix were one-way cast in the longitudinal direction but with 1% steel fibers by volume. Load-strain experimental curves corresponding to Mix TSO1 specimens are shown in Figure 5- 19 to Figure 5- 21.

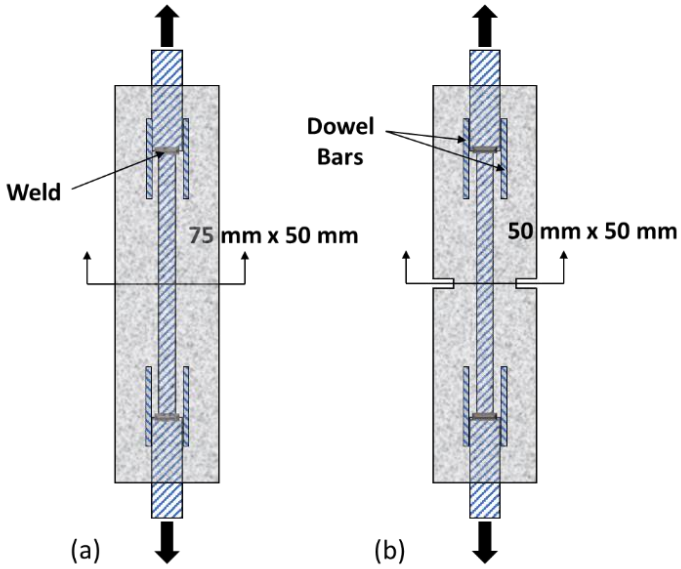

Figure 5- 18: Schematic of test specimen (a) Un-notched (Mix TSO2), (b) Notched (Mix TSO1 and TSR2)

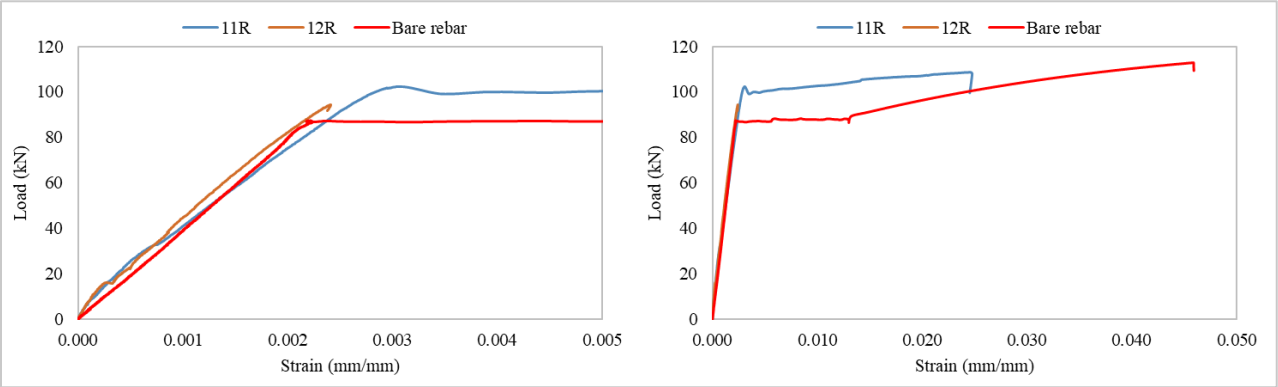

Figure 5- 19: Monotonic Load-Strain response of Regular specimens (Mix TSO1)

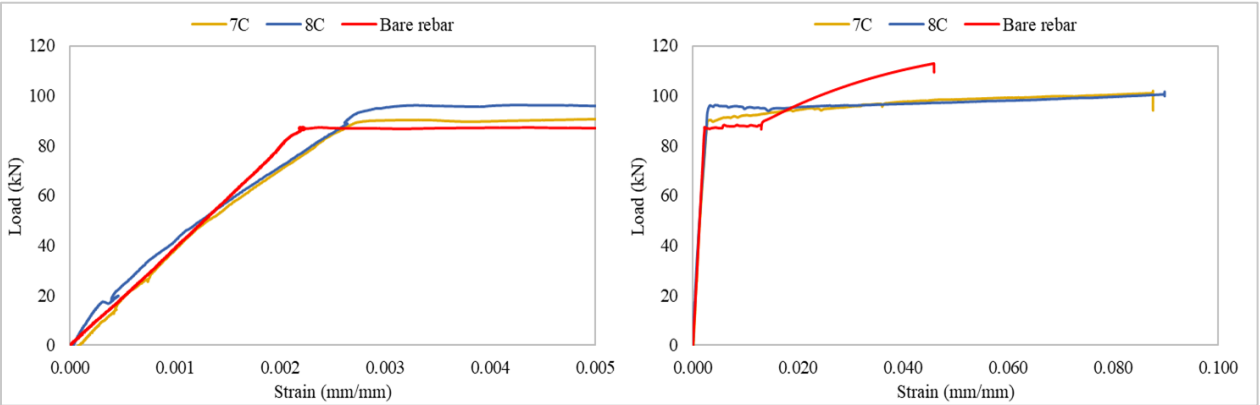

Figure 5- 20: Monotonic Load-Strain response of Corroded specimens (Mix TSO1)

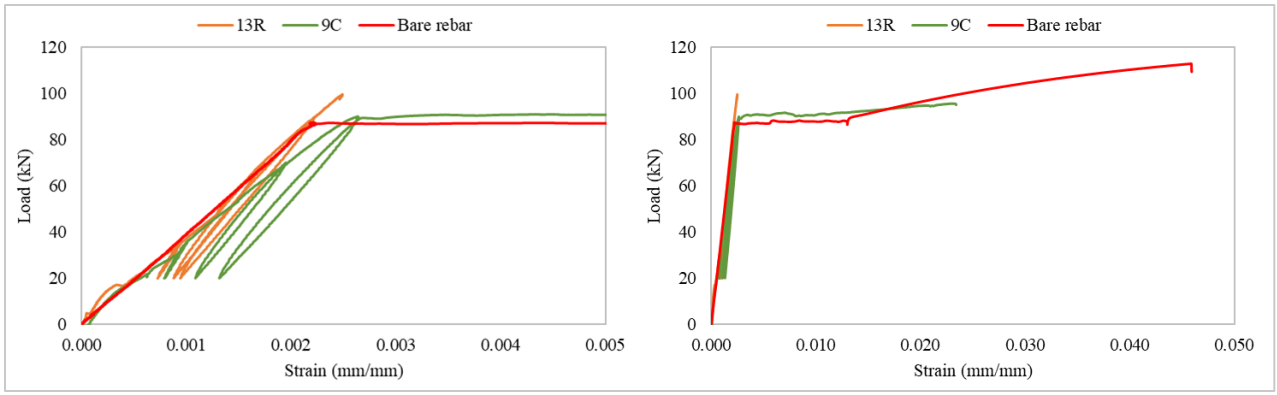

Figure 5- 21: Cyclic Load-Strain response of Regular and Corroded specimen(Mix TSO1)

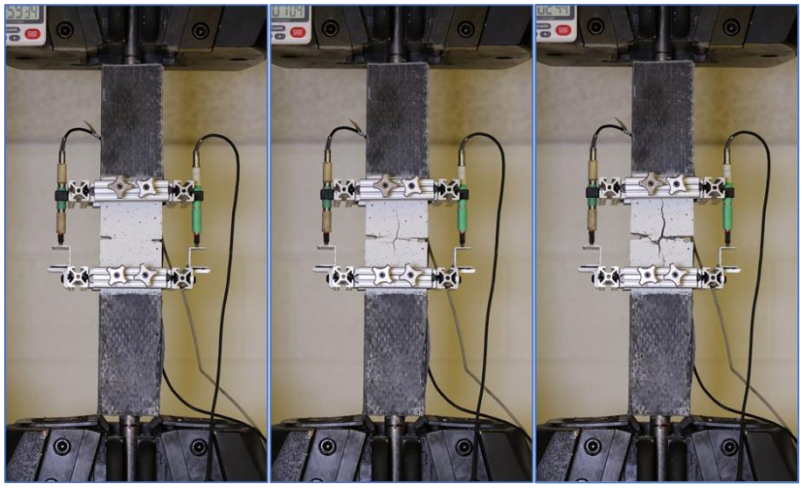

Figure 5- 22: Typical crack pattern in a notched tension stiffening specimen

5.6.4 Tension Stiffening – Mix TSR2

Similar to the previous mix, specimens from Mix TSR2 were also notched at mid-height. Nominal dimensions of the notched cross-section were equal to 50 mm x 50 mm. A total of 6 specimens were tested out of which 3 specimens comprised pre-corroded (C) rebars and 3 contained regular (R) rebars. Out of these two sets with 3 specimens each, two were tested under monotonic loading and the remaining one was tested under cyclic loading protocol. All specimens in this mix were cast randomly with 2% steel fibers by volume. Load-Strain experimental curves corresponding to Mix TSR2 specimens are shown in Figure 5- 23 to Figure 5- 25 at two different strain levels to represent the response before and after yielding.

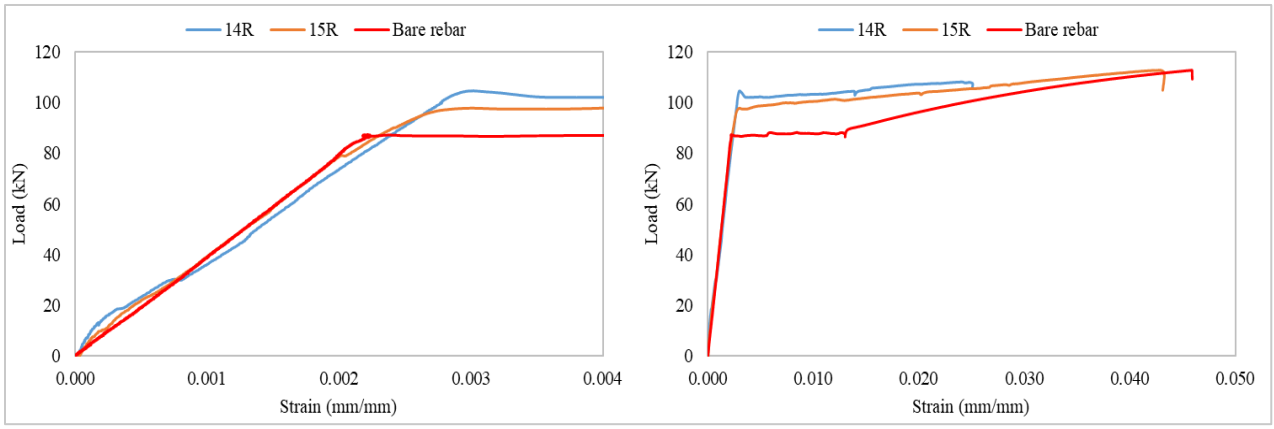

Figure 5- 23: Monotonic Load-Strain response of Regular specimens (Mix TSR2)

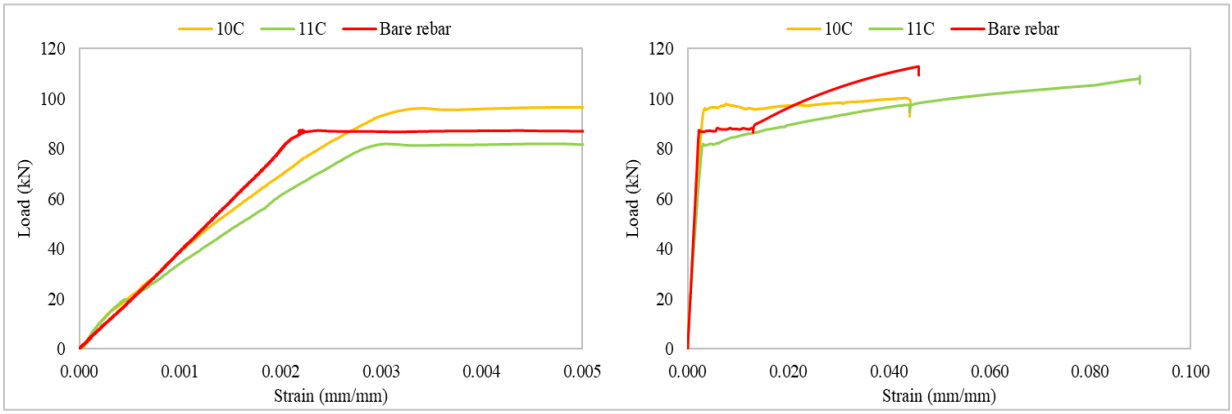

Figure 5- 24: Monotonic Load-Strain response of Corroded specimens (Mix TSR2)

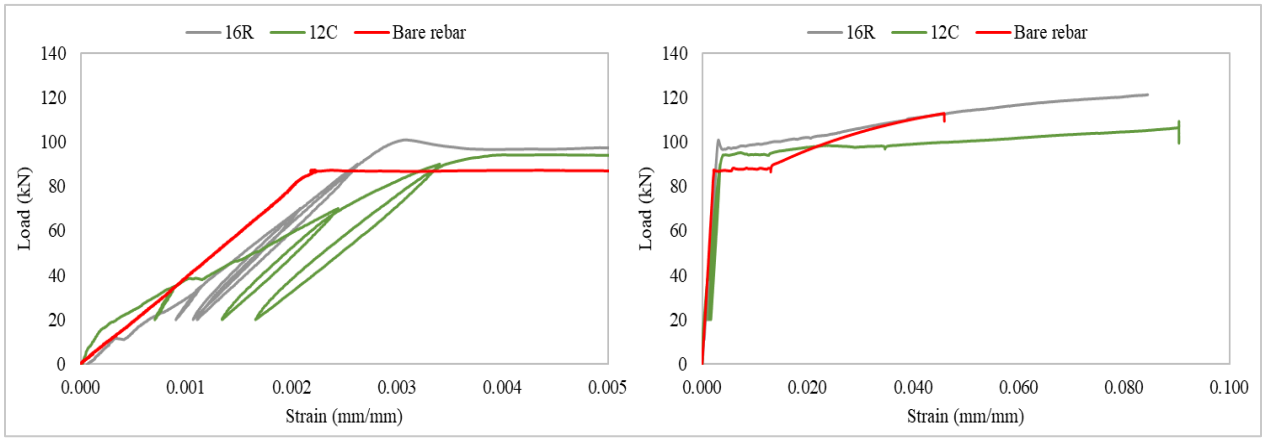

Figure 5- 25: Cyclic Load-Strain response of Regular and Corroded specimen(Mix TSR2)

5.7 Tension Stiffening Contribution

Scatter plots shown in Figure 5- 27 to Figure 5- 29 represent the tension stiffening contribution of UHPFRC to the un-corroded and corroded rebar specimens in each of the three mixes. Load differential was calculated as the difference between the load resisted by the tension stiffening member (that include the reinforcing bar and UHPFRC) and by the rebar alone at specific strain levels; thus, the differential represents the tensile force carried by UHPFRC concrete cover. For the un-corroded specimens, load carried by the bare bar was determined from tensile tests of rebar as presented in Section 5.6.1, whereas for the corroded specimens, reduced yield strength of the bar was estimated based on the experimental evidence provided by El-Joukhadar et al. (2023) using the percentage mass loss. With reference to Figure 5- 26, the reduced yield strength of the corroded bar corresponding to an average mass loss of 12.5% was estimated to be $0.85f_y$, which was also consistent with the value estimated as per Equation 5-3 proposed by El-Joukhadar et al. (2023). Variable *x* in Equation 5-3 denotes the percentage mass loss, and f_y and $f_{y,res}$ represents the yield strength of un-corroded and corroded bars, respectively.

$$f_{y,res} = f_y \cdot e^{-0.013x} \tag{5-3}$$

For each mix, the tension stiffening specimens were divided into four groups named- TS#RMo, TS#RCy, TS#CMo, and TS#CCy, where TS# represents the mix identity as described earlier, the following letter, R or C, represent Regular or Corroded rebar, respectively, Mo and Cy represent Monotonic and Cyclic loading, respectively. Average test data corresponding to each category was considered to develop the scatter plots shown below.

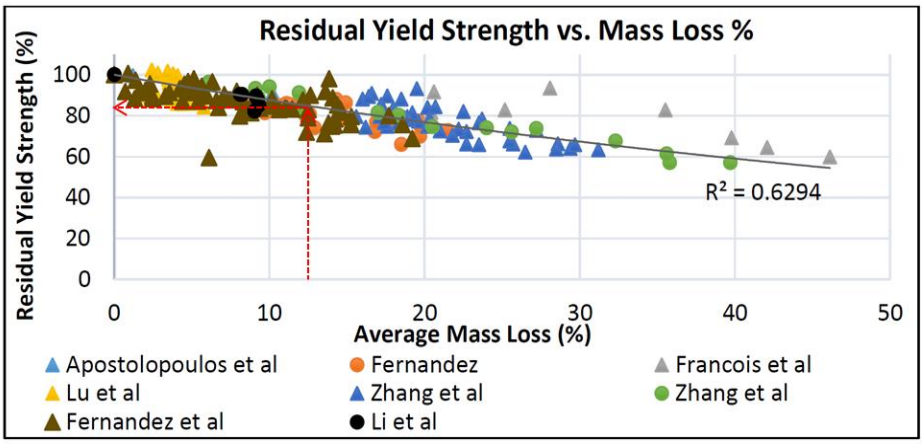

Figure 5- 26: Reduction in yield strength with increasing mass loss for corroded reinforcement (adapted from El-Joukhadar et al., 2023)

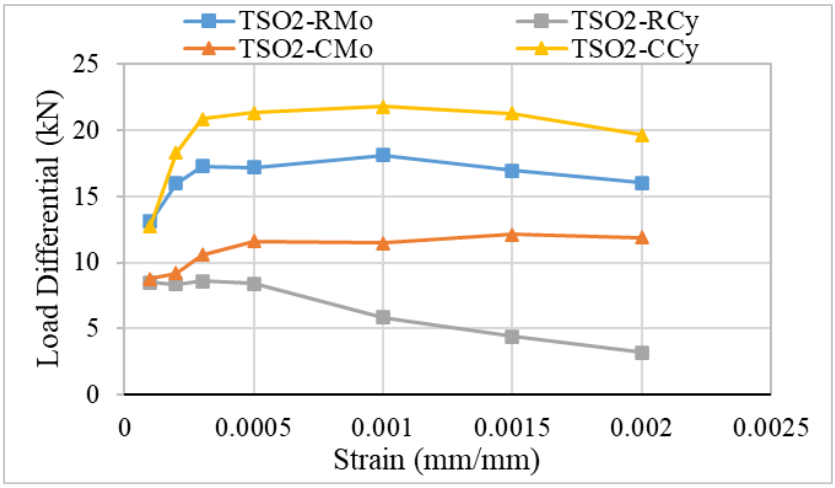

Figure 5- 27: Average Tension Stiffening Contribution (Mix TSO2)

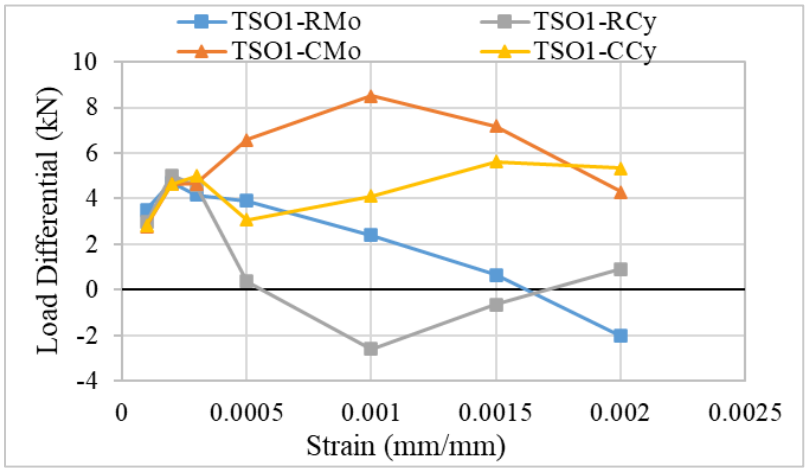

Figure 5- 28: Average Tension Stiffening Contribution (Mix TSO1)

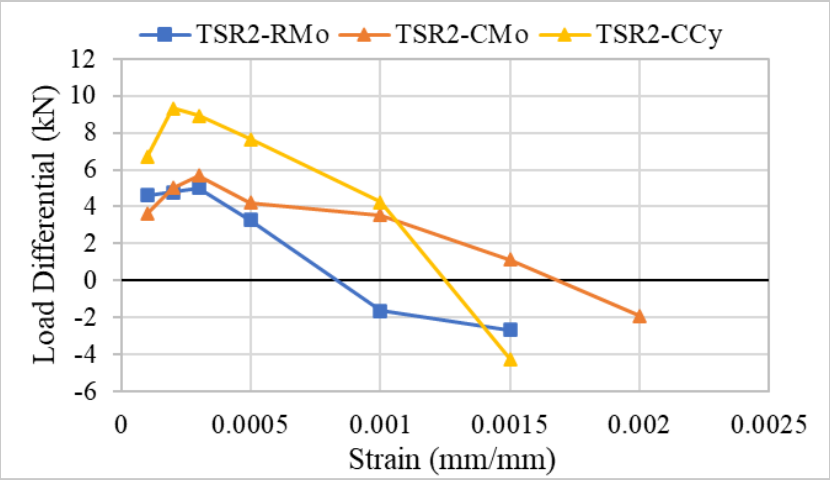

Figure 5- 29: Average Tension Stiffening Contribution (Mix TSR2)

It can be noted from the above plots that the tension stiffening contribution was more pronounced in case of Mix TSO2 for two reasons; one that it contains 2% steel fibers with fiber orientation parallel to the tensile loading direction, and also due to the fact that these specimens were not notched (meaning they had 75 mm x 50 mm section) at the mid height as shown in Figure 5- 18. In the pre-cracking stage of UHPFRC (i.e., strain <0.0003 mm/mm), the tension stiffening contribution was found to be lowest in case of specimens corresponding to Mix TSO1 with 1% steel fibers. Furthermore, the tension stiffening contribution in a few cases was found to be depleting with increasing strain levels. This could be attributed to any local deformations that may have occurred at the weld joint or the slip between rebar and concrete.

5.8 Results of Companion Tests

Besides the tension stiffening test specimens, each mix included specimens for obtaining material properties in tension and compression, which are referred to as companion tests. As summarized in Table 5- 3, for the mixes TSO2 and TSO1, specimens were prepared for compression, direct tension and bending tests, whereas for Mix TSR2, compression and direct tension test specimens were prepared. With regard to direct tension tests, prismatic specimens having a cross-section of 50 mm by 50 mm were prepared to be tested as per the recommendations of AASHTO Standard (AASHTO T 397, 2022). However, the direct tension tests were not completed due to practical issues associated with the new grips prepared for the test frame. Therefore, results corresponding to the uniaxial compression tests and four-point bending tests are presented here. Compression and bending experiments were performed following the same procedure and test setup detailed in

material characterization study in Chapter 3 of the thesis. Nominal dimensions corresponding to different tests are summarized in Table 5- 5.

Table 5- 5: Nominal dimensions of companion test specimens

Specimen	Nominal Size
Compression	Diameter= 75 mm; Height= 150 mm
Direct Tension	Width= 50 mm; Depth= 50 mm; Length= 430 mm
Four-point Bending	Width= 100 mm; Depth= 50 mm; Length= 400 mm; Clear span= 300 mm

5.8.1 Compression Tests

Results of compression tests carried out to determine the maximum compressive strength capacity are summarized in Table 5- 6, which were tested at an approximate age of 40 days after casting. Average compressive strength for the mixes TSO2, TSO1 and TSR2 was equal to 172MPa, 165 MPa and 178 MPa, respectively. It is evident that the compressive strength of Mix TSO1 was lower than TSO2 and TSR2 by about 4.3% and 7.8%, respectively, owing to the percentage of fiber used in the respective mixes. Subsequently, compressive stress-strain response presented in Figure 5- 30 was obtained for a few cylinder specimens and results are summarized in Table 5- 7. It is to be noted that the compressive stress-strain tests were performed around 70 days after casting and hence increased strength values were observed compared to results shown in Table 5- 6. Modulus of Elasticity presented in Table 5- 7 was calculated as per ASTM C469/C469M (2010) but with only a single load cycle which continued monotonically up to the failure, as the primary objective here was to obtain stress-strain behavior in uniaxial compression. It is noted that the strain corresponding to the peak compressive stress was found to be lower in case of Mix TSO1 specimens. Hence, Mix TSO1 with 1% fibers was found to have slightly lower strength and ductility in compression when compared to Mixes TSO2 and TSR2 with 2% fibers. Figure 5- 31 shows the typical failure pattern observed in compression tests that showed inclined shear cracks and vertical splitting cracks at failure of cylinder specimens.

Table 5- 6: Compressive strength test results

Mix	Cylinder ID	Peak Load	Compressive Strength	Average Strength
		kN	MPa	MPa
TSO2	TSO2-C1	869	186	172
	TSO2-C3	779	168	
	TSO2-C4	717	156	
	TSO2-C5	814	177	
TSO1	TSO1-C1	688	148	165
	TSO1-C2	766	165	
	TSO1-C3	863	181	
TSR2	TSR2-C1	932	198	178
	TSR2-C2	772	164	
	TSR2-C3	794	171	

Table 5- 7: Compressive stress-strain results summary

Mix	Specimen ID	Peak Load	Compressive Strength	Strain at Peak	Elasticity Modulus
		kN	MPa	mm/mm	GPa
TSO2	TSO2-C2	1006	212	0.00502	50.9
TSO1	TSO1-C4	918	199	0.00474	50.6
TSO1	TSO1-C5	835	180	0.00413	52.9
TSR2	TSR2-C4	977	211	0.00513	51.6

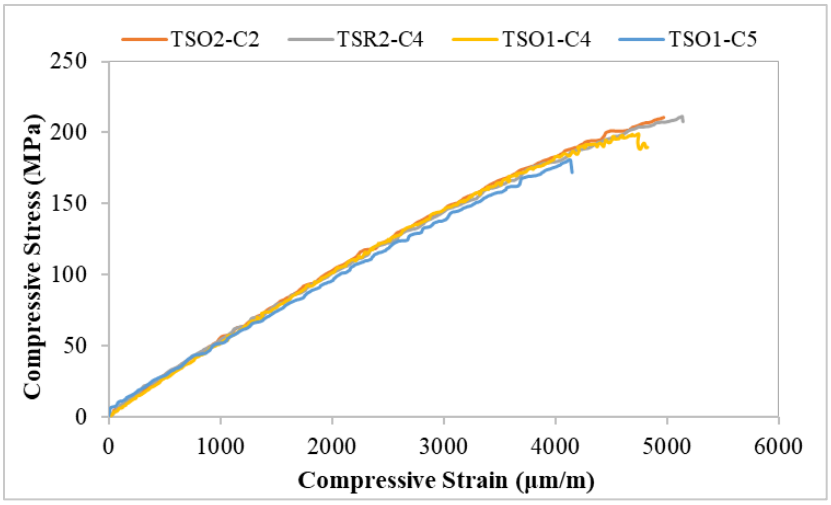

Figure 5- 30: Compressive stress-strain response

Figure 5- 31: Typical failure pattern observed in compression test cylinders

5.8.2 Bending Tests

As indicated in Table 5- 5, the prisms tested in four-point bending was 100 mm x 50 mm x 300 mm (width x depth x clear span) as per AFNOR recommended specimen size (NF EN 13670, 2013). The prismatic specimens were prepared for Mixes TSO2 and TSO1 only. Both the mixes contained flexural specimens cast from one end to represent the casting methodology used in their respective tension stiffening batches. Test procedure and setup used for flexural tests was same as described in Section 3.3.6. Figure 5- 33 and Figure 5- 34 shows the resistance curves obtained from four-point bending tests for mixes TSO2 and TSO1, respectively. Table 5- 8 presents the results for flexural strength and drift values corresponding to the peak load obtained for each specimen.

Average flexural strength was estimated to be 25.5 MPa for Mix TSO2 and 18.4 for Mix TSO1, indicating an increase of 38.5% due to increase of fibers from 1% to 2%. However, the average

drift was found to be 0.78% and 1.28% for specimens of Mixes TSO2 and TSO1, respectively. It is understood that the deflection capacity of UHPFRC in flexure may not be accurately represented by the AFNOR recommended thin prisms. Furthermore, specimens were cut near the localized crack in the constant moment region to estimate the average number of fibers per unit area of the cross-section. Images of the sawed cross-section were exported in AutoCAD and the fibers were counted manually, as depicted in Figure 5- 32. Average fiber count estimated for flexural specimens from Mix TSO2 (2% fibers) was equal to 0.371 fibers/mm^2 whereas Mix TSO1 (1% fibers) was estimated to have 0.177 fibers/mm^2 which indicated a ratio of 2:1, approximately. This correlation was expected based on the respective fiber contents of the mixes. Theoretical value of number of fibers per unit area (n_f) was estimated to be 0.637 fibers/mm^2 and 0.318 fibers/mm^2 for mixes TSO2 and TSO1, respectively, as per Equation 5-4. Hence, the fiber orientation factor for these mixes was estimated to be equal to 0.58 and 0.56, respectively. Figure 5- 35 shows the typical failure pattern of the prisms tested. Barring specimen TSO2-A2 that displayed flexural-shear failure mode, all other specimens experienced flexural failure with localized crack formation within the constant moment region.

$$n_f = {4V_f}\Big/{\pi d_f^2} \tag{5-4}$$

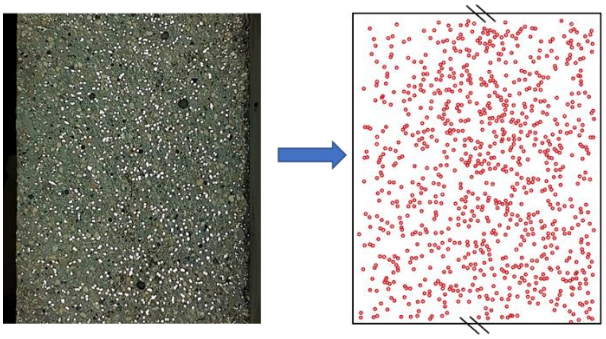

Figure 5- 32: Illustration of fiber count for a sawn section of UHPFRC

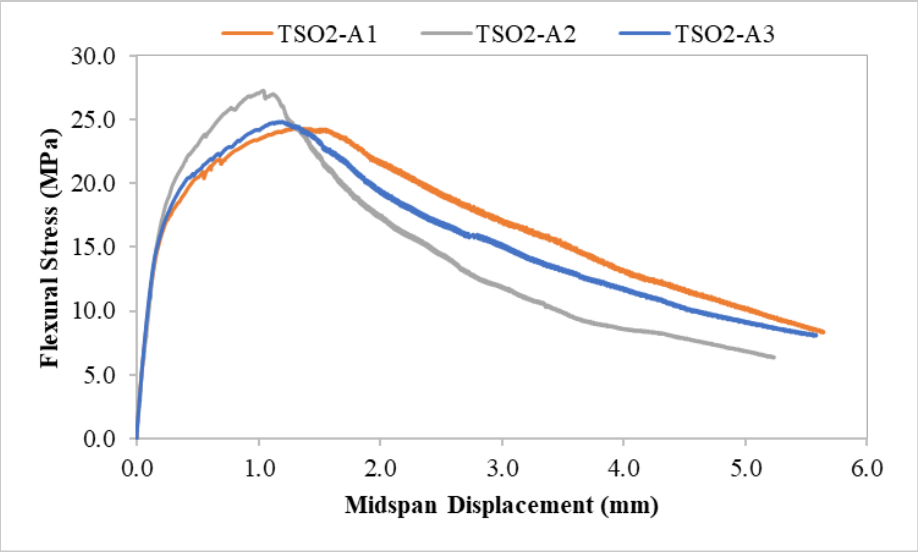

Figure 5- 33: Flexural resistance curves (Mix TSO2)

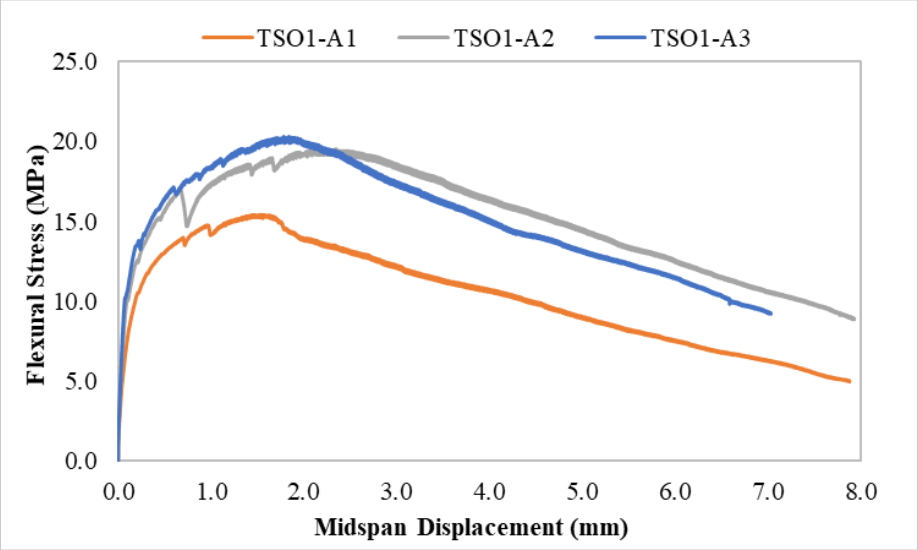

Figure 5- 34: Flexural resistance curves (Mix TSO1)

Table 5- 8: Results from four-point bending tests

Mix	Prism ID	Peak Load	Flexural Strength	Avg. Flexural Strength	Deflection at Peak	Drift at Peak	Avg. Drift at Peak
		kN	MPa	MPa	mm	%	%
TSO2	TSO2-A1	20.7	24.35	25.47	1.296	0.86%	0.78%
	TSO2-A2	23.6	27.22		1.039	0.69%	
	TSO2-A3	20.7	24.84		1.190	0.79%	
TSO1	TSO1-A1	13.1	15.41	18.38	1.553	1.04%	1.28%
	TSO1-A2	16.6	19.46		2.348	1.57%	
	TSO1-A3	16.9	20.28		1.839	1.23%	

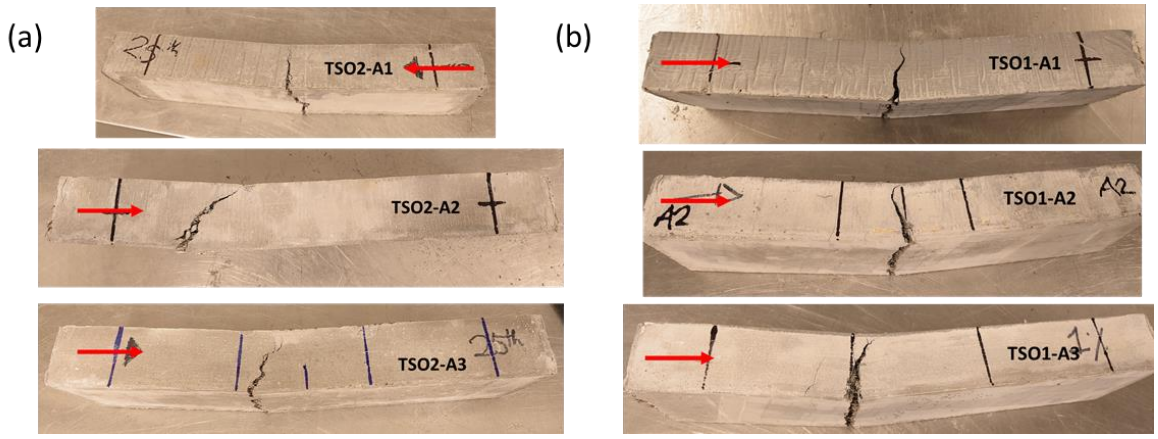

Figure 5- 35: Failure mode of flexural specimens (a) Mix TSO2 (b) Mix TSO1

Table 5- 9 summarizes the direct tensile properties obtained using the proposed inverse analysis (refer to Section 3.4 for details) for the mixes TSO2 and TSO1 flexural prisms. In addition, the derived tensile stress-strain behavior is depicted in Figure 5- 36.

Table 5- 9: Tensile stress-strain properties obtained from the proposed inverse analysis method

Mix	Specimen ID	E	$f_{t,cr}$	$\varepsilon_{t,cr}$	$f_{t,max}$	$\varepsilon_{t,max}$	$\varepsilon_{t,u}$
		(MPa)	(MPa)	(mm/mm)	(MPa)	(mm/mm)	(mm/mm)
TSO2	TSO2-A1	47368	9.0	0.000190	10.5	0.0046	0.0170
	TSO2-A2	45909	10.1	0.000220	13.2	0.0032	0.0100
	TSO2-A3	47514	8.6	0.000181	11.0	0.0040	0.0130
Average		**46930**	**9.2**	**0.000197**	**11.6**	**0.0039**	**0.0133**
TSO1	TSO1-A1	40741	5.5	0.000135	6.5	0.0055	0.0250
	TSO1-A2	52000	6.5	0.000125	8.0	0.0080	0.0300
	TSO1-A3	54400	6.8	0.000125	8.1	0.0060	0.0300
Average		**49047**	**6.3**	**0.000128**	**7.5**	**0.0065**	**0.0283**

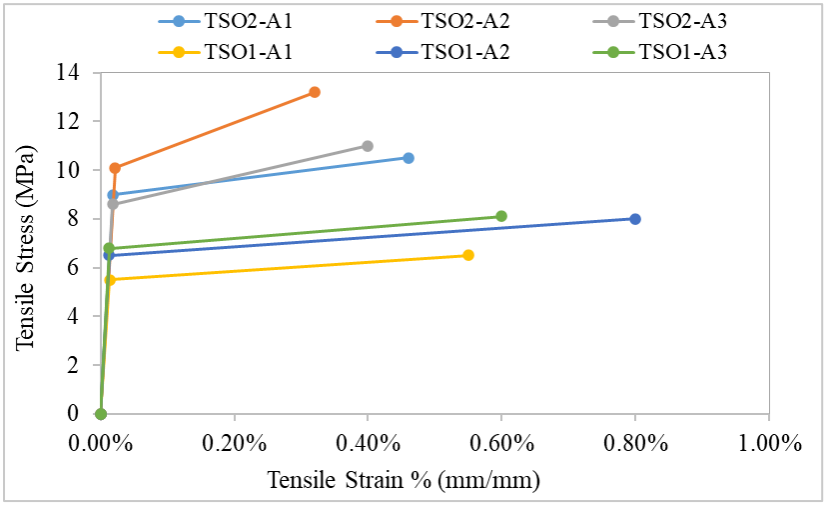

Figure 5- 36: Tensile behavior obtained from the proposed inverse analysis (Mix TSO2 & TSO1)

5.9 Summary

The tension stiffening property of UHPFRC with two different fiber contents was explored using un-corroded and corroded reinforcement bars besides other parameters like casting orientation and loading protocols. Specimen design was finalized after conducting the preliminary finite element analysis on different models to study their tension stiffening behavior and failure modes. The tension stiffening effect of UHPFRC was marked by a significantly high slope in the pre-cracking

stage of the response. Beyond the cracking stage of UHPFRC cover, the slope of the resistance curve gradually reduced to match the slope of the bare rebar, but the extra strength provided by UHPFRC was sustained well beyond the yielding of reinforcement in most cases. Evidently, the tensile strength contribution from UHPFRC mix with 2% fibers was approximately 2 times that of 1% fibers mix. Randomly cast specimens provided less strength contribution than their counterpart one-way cast specimens. Corrosion of reinforcement to a mass loss of 12.5% affected the tension stiffening behaviour of UHPFRC significantly. Fracture failure of the embedded rebar was achieved by using the notched tension stiffening specimens that had a reduced UHPFRC cover (50 mm x 50 mm) at the mid height. Reinforcement in some of the specimens ruptured at a total elongation that exceeded what corresponded to the ultimate strain of the bare rebar. However, this point cannot be generalized yet. A significantly broader experimental campaign would be needed that can effectively capture tension stiffening response beyond the yielding of reinforcement.

Companion tests such as compressive strength, compression stress-strain and four-point bending tests were performed for each UHPFRC mix. With increase in the fiber content of UHPFRC from 1% to 2%, the compressive strength was found to be increased by 6% from 165 MPa to 175 MPa, respectively. Compressive strain at the peak stress was also found to be slightly lower in case of Mix TSO1 that comprised 1% fibers by volume. With regard to flexural tests, UHPFRC prism specimens with 2% fibers exhibited 38% higher flexural strength than those with 1% fiber content. Similarly, the tensile strength estimated from the inverse analysis of bending test results showed an increase of about 54% from 7.5 MPa to 11.6 MPa, respectively, for the increase in fiber content.

Chapter 6: Finite Element Modeling of Tension Stiffening Behaviour

This chapter includes the discussion on three dimensional nonlinear Finite Element Model (FEM) developed and analyzed to estimate the experimental behaviour of tension stiffening tests using GiD-ATENA software suite (Červenka Consulting, 2007). Objective of the finite element study was to obtain a detailed insight regarding stress transfer between the reinforcement and UHPFRC, and correlation of the experimental results with the calculated cover tension contribution. The modeling was performed using GiD (graphical user interface program) whereas the finite element analysis and post-processing were performed using ATENA studio program. Relevant information on the software used may be found in ATENA program documentation (Part 1, Part 3-1, Part 8 and Part 12). Two alternative modeling approaches were used to model the interaction between the reinforcement bar and UHPFRC, named as 1-D and 3-D rebar model. 1-D rebar model idealizes the reinforcement as a series of one-dimensional elements connected to the solid elements that model concrete using calibrated bond links (local springs); the 3-D rebar model uses a three-dimensional reinforcement solid object with ribs explicitly modeled to simulate the actual interaction between the embedded rebar and the surrounding concrete. However, the latter method is rather complicated and not feasible to implement in case of large structural members. Establishing a relationship between the 1-D rebar model with calibrated bond-slip law, with the results of the detailed 3-D representation is useful, as the former can be used for modeling of large-scale members. Lastly, the finite element analysis responses obtained through above methods were compared with the experimental behaviour so as to validate the experimental observations with satisfactory correspondence.

6.1 3-D Rebar Model

As mentioned above, the 3-D model is constructed using three-dimensional solid elements only. Modeling of rebar with 3-D elements including ribs on the bar requires advanced computational capacity and is not easy to implement in case of full-scale engineering problems. In this model, both the UHPFRC prism and the reinforcing bar are modeled using tetrahedral solid elements. The objective here was to assess the actual behaviour of the specimen through a model that accounts for the effects of rib interlocking as a mechanism of force transfer and to study the lateral pressure fields that are induced from the reinforcement bar geometry onto the surrounding concrete.

6.1.1 Model Geometry and Boundary Conditions

Leveraging the advantage of symmetry, $1/8^{th}$ of the actual tension stiffening specimen was modeled to save computational time. Geometry details corresponding to the 15M rebar used in experiments were measured using a digital caliper. The inner diameter of the rebar was about 15 mm, the thickness of the rib tapered from 3 mm to 1.5 mm outwards, the center to center spacing of ribs was 10 mm and the rib height was approximately equal to 1 mm. Figure 6- 1a shows the geometry details of the modeled rebar element. Dimensions of the three macro-elements modeled are shown in Table 6-1. To avoid further complexity, the inclination of ribs relative to the longitudinal axis of the rebar was not considered in the model.

Table 6- 1: Model geometry details for 3-D rebar model

Element	Dimensions
Tension Stiffening Specimen ($1/8^{th}$)	L = 215 mm, b = 37.5 mm, t = 25 mm
Main rebar (15M)	R = 7.5 mm (excl. rib), L = 150 mm
Grip rod	R = 12.5 mm, L = 65 mm

Using the GiD program, the 15M rebar geometry was drawn followed by that of the gripping rod of 25 mm diameter. The two steel elements were connected using the fixed contact surface 'Master-Slave' condition. Master-slave boundary condition is used to fix two elements such that there is no relative movement between the connected elements hence eliminating the instability of the model (ATENA documentation, Part 8, 2021). The surrounding UHPFRC matrix was drawn excluding the area occupied by the steel bars. Once the line diagram was completed, corresponding surfaces and volumes were generated using the contour option for the macro-elements involved. The volume of concrete was restricted to the surface of the embedded steel bars so that volume of steel and concrete do not overlap. Boundary conditions were applied on the surfaces that intersect with the symmetry planes such that those surfaces were restrained from movement in the direction normal to their plane (e.g., XY symmetrical surface was restrained in Z direction).

6.1.2 Materials, Loading and Mesh

A predefined solid steel material prototype named 'CC3DBilinearSteelVonMises' was used to model the main rebar and the 25 mm gripping rod. The hardening behaviour of the rebar could not

be modeled due to material model limitation for 3-D steel elements in the program. Hence, the steel rebar was modeled to display linear elastic-perfectly plastic behaviour with the average properties: E_s= 202 GPa, f_y= 420 MPa, that were determined experimentally using 3-15M rebar specimens (refer to Section 5.6.1).

The UHPFRC matrix was modeled using the predefined solid concrete material prototype named 'CC3DNonLinCementitious2SHCC' whose properties were modified to represent different UHPFRC material mixes used in this study. Average material properties of UHPFRC corresponding to Mix TSO2 determined from experiments described in Section 5.8 were utilized for the initial analysis. A surface displacement loading was applied on the top surface of the grip rod in the tensile longitudinal direction of the specimen. The effective deformation loading used was equal to 0.025 mm/step. The displacement monitor point used to record the deformation in the concrete was placed at about 53 mm from the bottom of the modeled specimen. This was chosen to represent a total gauge length of 106 mm which was almost equal to the gauge length of the parallel ring extensometer (105 mm) used in the experiments. A reaction monitor was also placed on the top surface of the grip rod where the displacement is being applied in order to record the load acting on the model.

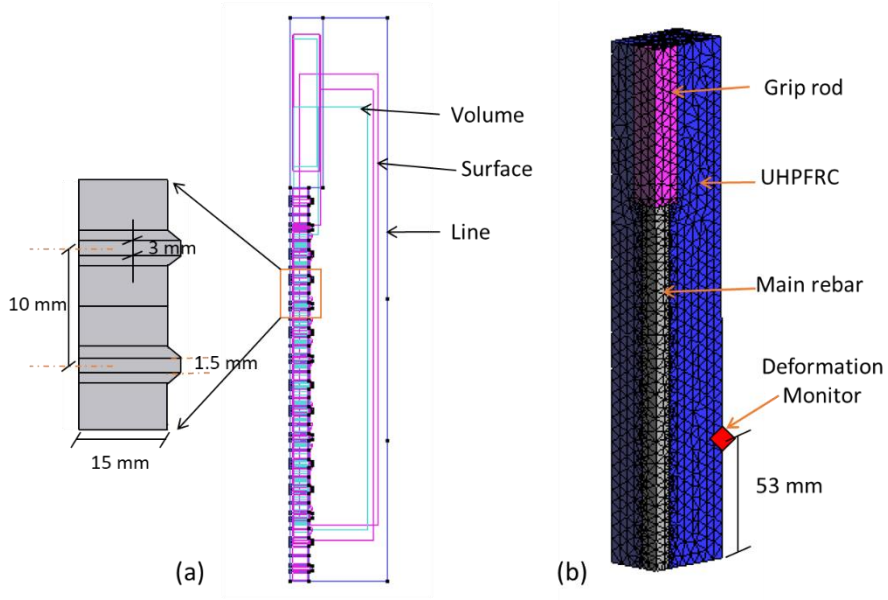

Figure 6- 1: (a) Outline of 3-D rebar model and rib geometry details (b) 3-D model with tetrahedral mesh

The finite element mesh was generated using the automatic meshing option of GiD. After performing a mesh sensitivity analysis, tetrahedral elements of nominal size equal to 7 mm were used for all the three elements. The dimension of the tetrahedral mesh was automatically refined around the ribs of the 15M rebar to a size as low as 1.25 to 1.50 mm. The three-dimensional view of the model with the tetrahedral mesh generated is shown in Figure 6- 1b. The standard Newton-Raphson solution method was used for the non-linear analysis with a limit of 30 iterations per step increment and the Parallel Direct Sparse Solver (PARDISO) was utilized for all the analysis presented in this study (Figure 6- 2). More details about the solver and non-linear solution method can be found in the ATENA documentation (Part 1, 2019). The visual representation of convergence criteria used by ATENA Studio is shown in Figure 6- 2, as per which the four criteria for solution errors checked by the program are displacement increment, normalized residual force, absolute residual force and energy dissipation, respectively (see lower right insert in Figure 6- 2).

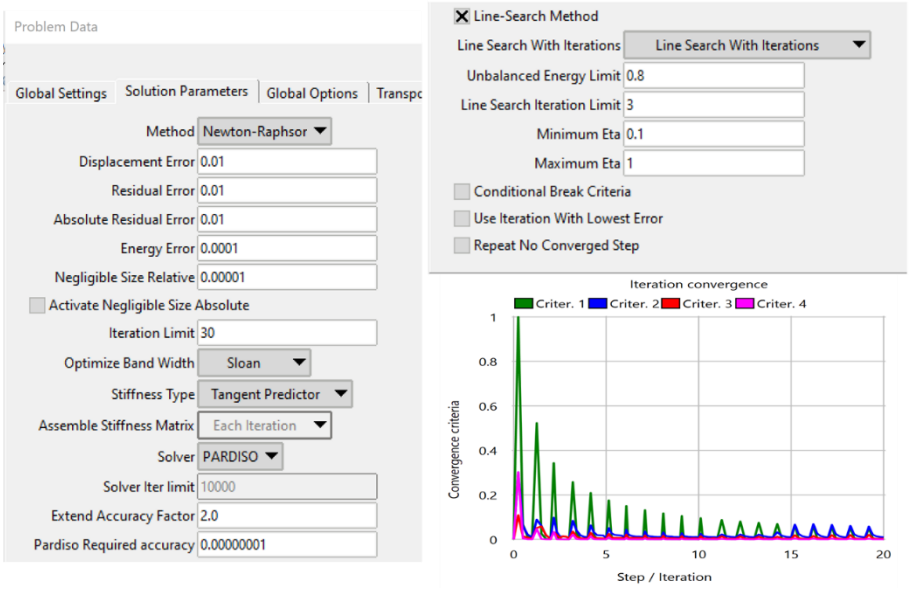

Figure 6- 2: Solution parameters used and iteration convergence in ATENA

6.1.3 Results from 3-D Rebar Model

After the mesh generation, the model was analyzed using static analysis in ATENA Studio. Results from the analysis corresponding to the load and deflection monitors were extracted to be plotted in a spreadsheet. ATENA Studio was also used as a post-processor to analyze the distribution plots corresponding to stress, strain, deformation, crack pattern etc. It was noted that the analytical response depends mainly on the tensile behaviour of the material. Figure 6- 4 represents the

comparison between experimental and analytical response for specimen 3R pertaining to the mix TSO2. Figure 6- 3 shows the compression and the tension model inputs used to calibrate the FEM analytical response for specimen TSO2-3R. The analytical response was calibrated by varying the tensile behavioral model of the material whereas the compression stress-strain model used was consistent with the average experimental stress-strain values obtained for the mix TSO2. Other relevant parameters used in this model are listed in Table 6- 2. Stress and strain distribution in UHPFRC and the 3-D rebar elements are shown in Figure 6- 5 at the onset of crack localization. In addition, the crack development and crack widths at various loading stages are depicted in Figure 6- 6. From the stress-strain distribution depicted in Figure 6- 5, slight stress concentrations were noted in UHPFRC matrix around the ribs of the rebar.

Table 6- 2: Relevant material parameters used for 3-D rebar model

Parameter	Value	Units
'CC3DNonLinCementitious2SHCC'		
Youngs Modulus	48000	MPa
Poisson's Ratio	0.2	
Tensile Cracking Strength	7	MPa
Compression Strength	-180	MPa
Tension/Compression Characteristic Size	10	mm
Fiber Volume Fraction	0.02	
Fiber Modulus	200	GPa
Fiber Diameter	0.0002	m
Fiber Shear Modulus	75	GPa
Material Density (default)	2300	kg/m^3
Mesh Size	7	mm
'CCDBiLinearSteelVonMises'		
Youngs Modulus	202	GPa
Poisson's Ratio	0.3	
Yield Strength	420	MPa
Hardening Modulus	0	MPa

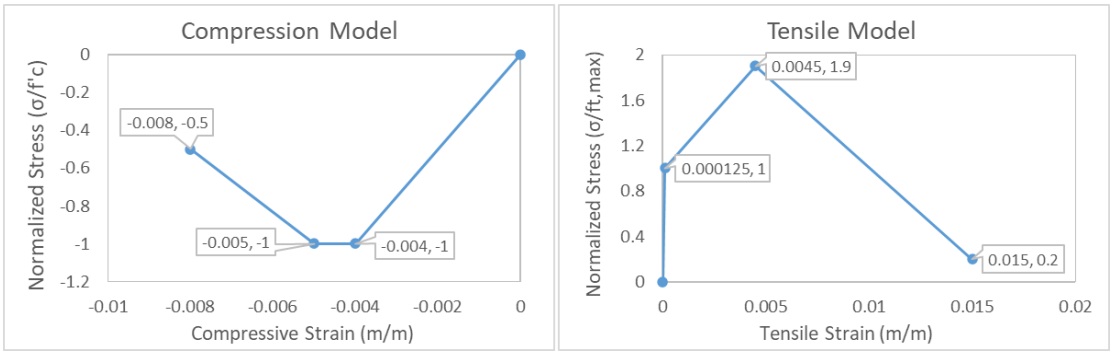

Figure 6- 3: Tensile and Compression stress-strain inputs for 3-D rebar model

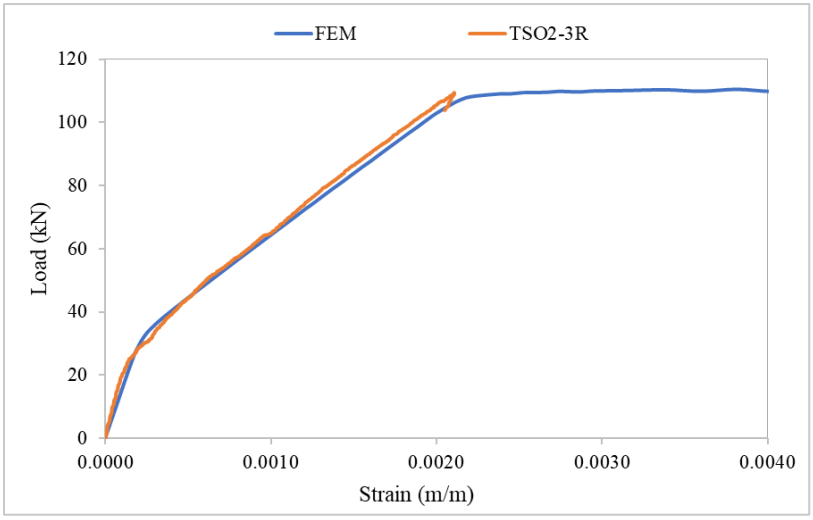

Figure 6- 4: Comparison between experimental and analytical response of the specimen TSO2-3R using 3-D Rebar Model

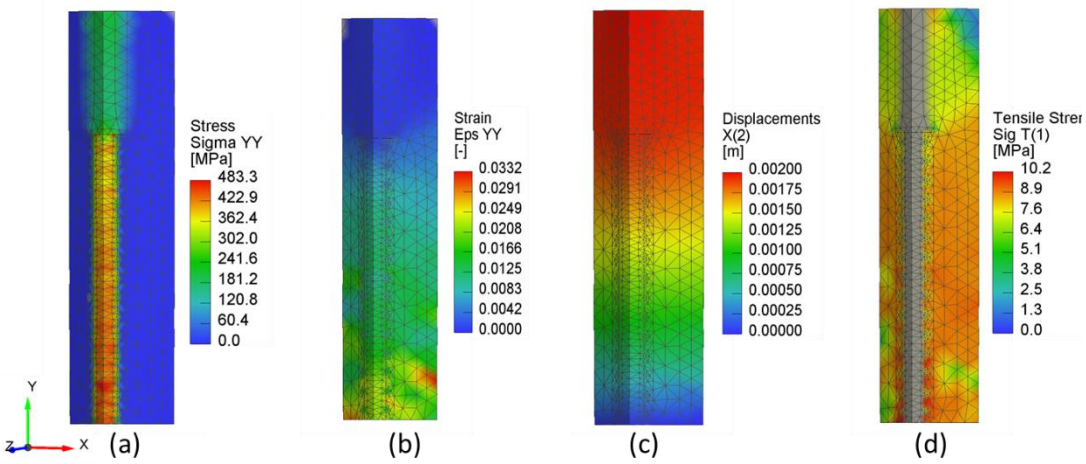

Figure 6- 5: Distribution plots: (a) Stress (b) Strain (c) Displacement; (d) Stresses in UHPFRC

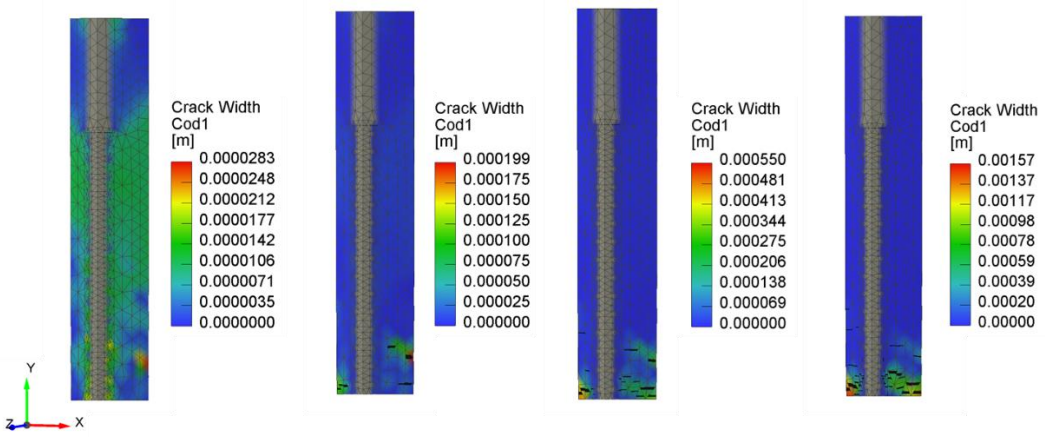

Figure 6- 6: Crack development through various stages

Figure 6- 7 depicts the analytical tension stiffening response obtained through this model using the average tensile properties for the mix TSO2 that were obtained through the proposed inverse analysis method (refer to Section 3.4). Experimental curves 2R, 3R and 7R shown in Figure 6- 7 correspond to the tension stiffening responses of regular rebar specimens from Mix TSO2.

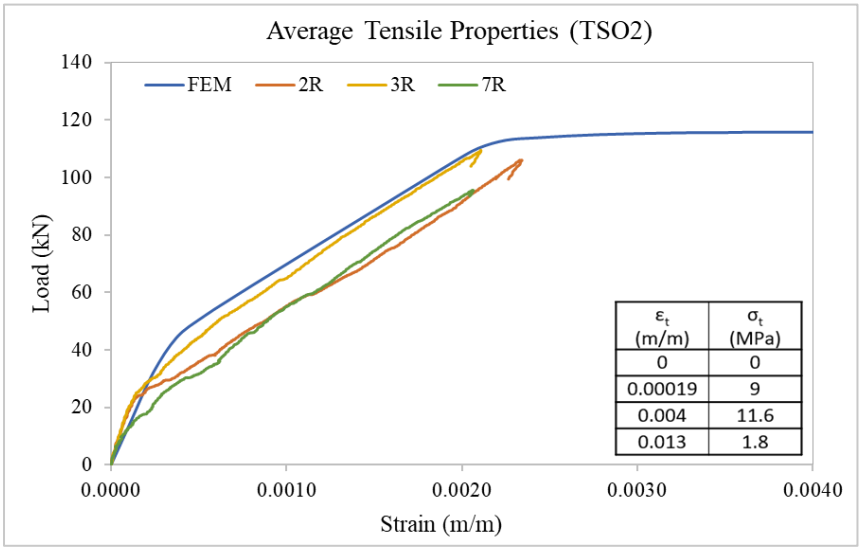

Figure 6- 7: Finite Element response obtained using average tensile properties (Mix TSO2)

The analytical result obtained from the 3-D rebar finite element model presented here compared well with the experimental response. The analytical response needs to be calibrated for a particular specimen to best match its experimental behaviour, as there was reasonable variability between the experimental responses of similar tension stiffening specimens owing to the complexity associated with the testing. However, it may not be implied that the average tension stress-strain

properties of the material shown in Figure 6- 7 were not estimated correctly through the flexural tests and inverse analysis performed.

6.2 1-D Rebar Model

As the name suggests, the reinforcement here was modeled as a simple one-dimensional (1-D) truss element. Once again, only 1/8th of the full specimen was modeled due to the symmetry of the specimen. This model comprised of 4 macro elements; a three-dimensional solid prism representing UHPFRC volume, 1-D truss elements corresponding to 15M and 25M reinforcement bars placed along the edge of the modeled concrete, and a solid steel metal block used for the load application. As suggested in the documentation of ATENA program (Part 11, 2020), an undeformable external solid macro-element block has to be used for the purpose of load application on a 1-D reinforcement element (e.g., pullout test, tension stiffening test). Appropriate boundary conditions were applied to all symmetrical surfaces pertaining to the concrete and solid block volumes, and the reinforcement truss elements. The two reinforcement elements were connected with each other by using the 'Master-Slave' condition in the GiD program. Dimensions of the respective elements are summarized in Table 6- 3. Outline and mesh geometry of the 1-D rebar finite element model are shown in Figure 6- 8.

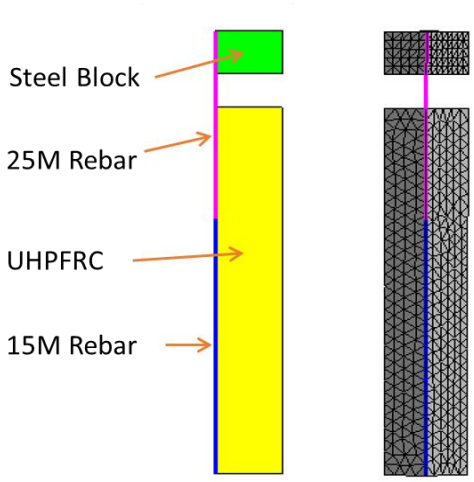

Figure 6- 8: Illustration of 1-D rebar finite element model

Table 6- 3: Geometry details for 1-D rebar model

Element	Dimensions
Tension Stiffening specimen ($1/8^{th}$)	L = 215 mm, b = 37.5 mm, t = 25 mm
Main rebar (15M)	L = 150 mm; Area = 50 mm^2 ($1/4^{th}$)
Grip rod (25M)	L = 110 mm; Area = 125 mm^2 ($1/4^{th}$)
Steel block	L = 25 mm, b = 37.5 mm, t = 25 mm

The 1-D reinforcement material named 'CCReinforcementEC2' was assigned to 15M and 25M bar elements. This material model allows input of a multilinear constitutive stress-strain law for the reinforcement with up to 7 branches. The average material properties of 15M rebar were experimentally determined as mentioned earlier and the same values were assumed for 25M rebar (grip rod), shown in Table 6- 4. The area assigned to the rebar elements was equal to one-fourth of their respective total cross-sectional area. With regard to UHPFRC, the material properties were the same as defined in Table 6- 2 but with the exception of tensile cracking strength. Tension properties used for this model are presented later.

Once again, tetrahedral mesh geometry was used for the UHPFRC volume and linear truss elements were used for the 1-D reinforcement bars. Automatic mesh option of the GiD program was utilized to generate the required mesh with a nominal size of 7 mm for the solid rectangular volume. Controlled displacement was applied at the top corner of the steel block which was connected to the extended 25M rebar. Deformation loading rate used is similar to that of 3-D rebar model as per which 0.025 mm per step is used.

Table 6- 4: Reinforcement properties for 15M rebar

Parameter	Value	Units
'CCReinforcementEC2'		
Youngs Modulus	202	GPa
Yield Strength	420	MPa
Ultimate Strength	600	MPa
Hardening Strain	0.0133	m/m
Ultimate Strain	0.06	m/m
Cross-sectional Area (Quarter)	50	mm^2

6.2.1 Results from 1-D Rebar Bond Model

As per the default conditions of the GiD-ATENA program (ATENA Program Documentation Part-8, 2021), the reinforcement element ('CCreinforcementEC2') is assumed to be perfectly bonded with the surrounding concrete unless it is modeled with a pre-defined bond-slip law. The effect of bond-slip relationship on the analytical tension stiffening response was investigated with the finite element model having a single rebar (15M) throughout the specimen, as it was the only viable option for this particular case. To assign bond-slip relationship to the rebar element, the bond stress-slip law was enabled with the sub-element named 'CCBarWithBond' and the 'fixed ends' condition was utilized. This was done to keep the 15M rebar fixed at the start (bottom) owing to the symmetry of the model (ATENA Program Documentation Part-1, 2021), and at the end (top) to avoid any slip inside the undeformable loading block.

Two different bond stress-slip models, Model-A and Model-B were considered for the UHPFRC as depicted in Figure 6- 9. Ultimate bond strength (f_{bu}) was assumed to be approximately equal to square root of the compressive strength ($f_{bu} = \sqrt{f_c'} \rightarrow 13\ MPa$). Slip values for Model-A were considered according to the bond tests performed by Tsiotsias (2019) whereas Model-B considered significantly lesser slip value required to develop the bond strength. The tension stiffening response obtained using the above two models is shown in Figure 6- 10 along with the perfect bond condition. With regard to Model-A and Model-B, the latter provided tension stiffening response that was closer to the experimental behaviour of TSO2-3R specimen. Furthermore, it can be noted that, the analytical responses obtained by using Model-B and perfect bond condition are almost the same indicating that the reinforcement can be modeled by assuming a perfect bond condition.

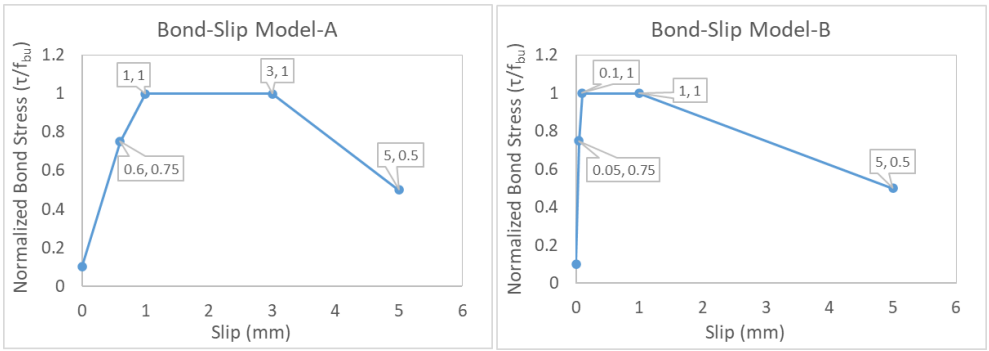

Figure 6- 9: Bond stress vs slip models

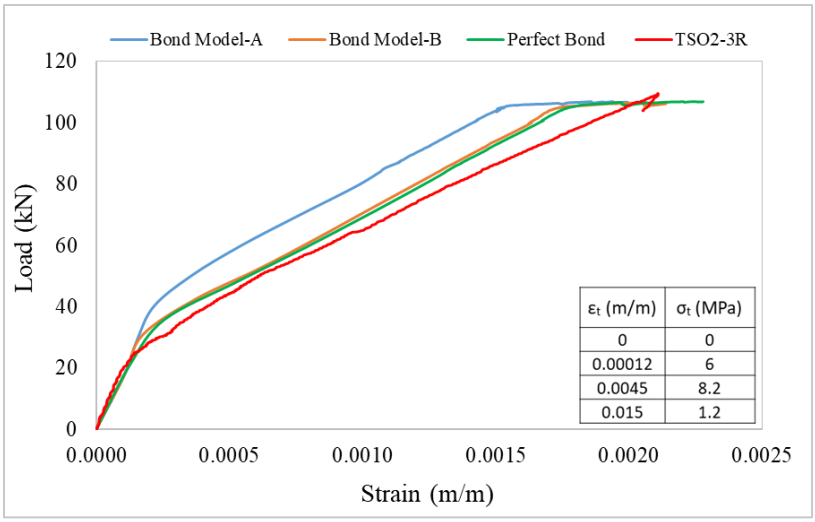

Figure 6- 10: Analytical response obtained using 1-D rebar model with bond-slip law

Figure 6- 11 depicts the bond stress and slip distribution developed in the bar corresponding to Model-B. The limitation of this model was that the reinforcement fractures outside the specimen, and the stress distribution in UHPFRC as shown in Figure 6- 11 was not representative of the actual experimental behaviour as the stress was found to be concentrated at the top of the specimen and no stresses developed towards the center. Hence, the model presented in Figure 6- 8 was considered for further analysis along with the perfect bond condition.

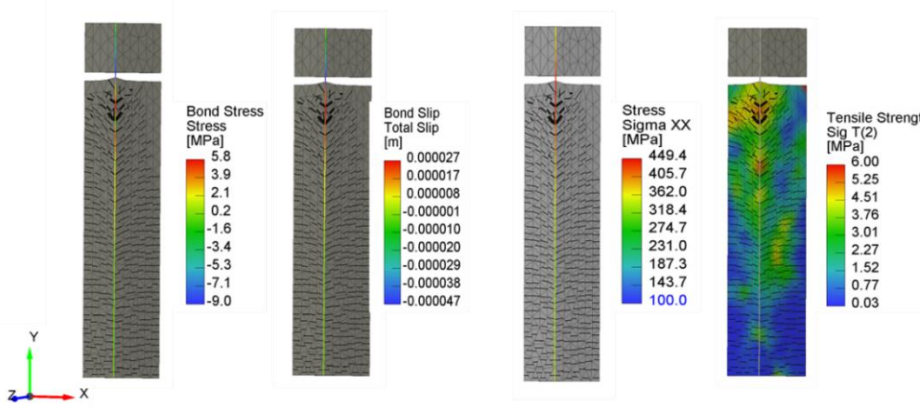

Figure 6- 11: Bond properties and tensile stress distribution observed from Model-B analysis

6.2.2 Results from 1-D Rebar Model Using the Perfect Bond Condition

As mentioned earlier, 1-D reinforcement material model in ATENA allows the input of complete stress-strain behaviour corresponding to the rebar used, shown in Figure 6- 12, unlike the 3-D steel material model. This enabled the model to analyze the tension stiffening response well beyond the

yielding of reinforcement. Based on the discussion in previous section, the 1-D rebar model could be further simplified by using perfect bond condition for the reinforcement. Figure 6- 13 depicts the initial and complete tension stiffening response (load vs strain) obtained from the analysis of 1-D rebar model with perfect bond condition. In addition, a default tension stiffening factor (equal to 0.4) for the material model was utilized that would keep the tensile stresses in UHPFRC from dropping below 40% in the post-peak region of its constitutive behaviour. Figure 6- 14 depicts the stress-strain and displacement distribution whereas Figure 6- 15 shows the development of cracking through various stages obtained using the 1-D rebar perfect bond model.

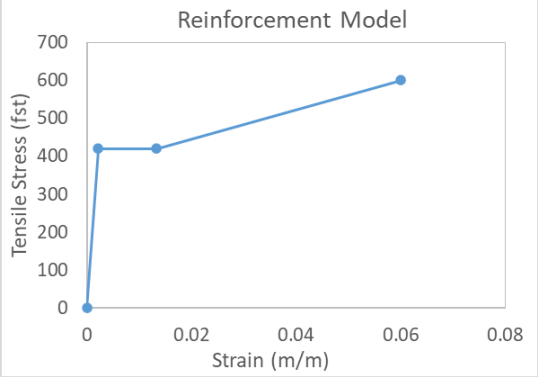

Figure 6- 12: Idealized stress-strain model used for reinforcing steel

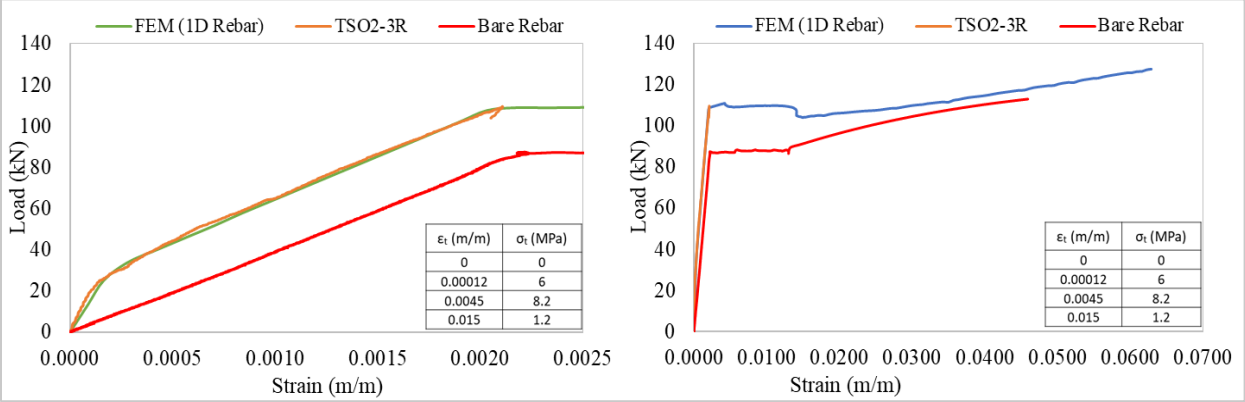

Figure 6- 13: Analytical response obtained using 1-D Rebar Model with perfect bond

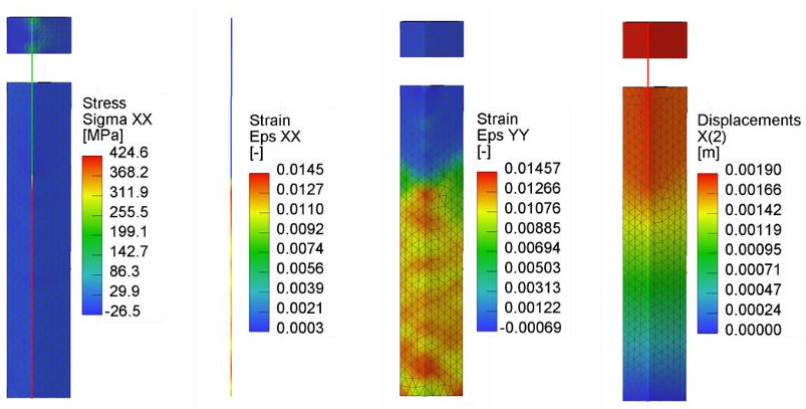

Figure 6- 14: Stress-Strain and displacement distribution post yielding of 15M rebar obtained using the perfect bond model

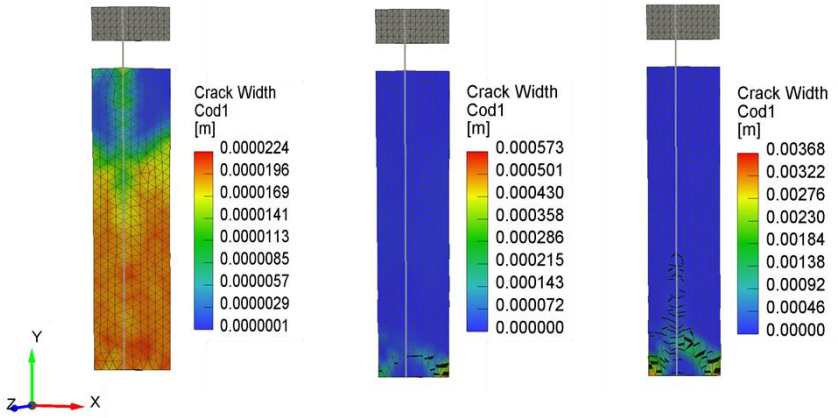

Figure 6- 15: Crack development through various stages (1-D Rebar Perfect Bond Model)

6.3 Summary of Analysis

Non-linear finite element models were developed using GiD-ATENA software to analyze the tension stiffening response of UHPFRC. Predefined concrete material model of the program for SHCC/HPFRC material was used for the solid volume of UHPFRC with user-defined constitutive stress-strain laws in compression and tension. The reinforcing bar was modeled in two different ways to have either one-dimensional or three-dimensional geometry, referred as 1-D rebar and 3-D rebar models, respectively. With regard to 3-D rebar model, the reinforcement behaviour inside of UHPFRC was simulated with the arrangement of physical ribs on the surface of solid rebar volume. This model was developed in order to provide the best possible representation of actual experiment set up and the response obtained was calibrated using the tensile constitutive stress-strain law. Moreover, the tension stiffening response obtained by the 3-D rebar model by using the

average tensile constitutive law, obtained using flexural tests and subsequent inverse analysis, was found to be slightly overestimated. This could be attributed to the interaction of UHPFRC and steel rebar that led to the minor localized stress concentrations in the concrete matrix around the ribs of rebar. Similar behaviour was reported by Bian & Wang (2019) in case of tension hardening UHPFRC material.

With regard to the 1-D rebar model, the reinforcement was modeled using 1-D truss elements. The effect of two different bond-slip laws on the analyzed response was evaluated besides studying the perfect bond condition. One-directional orientation of the fibers may have caused significant bond stiffness longitudinally and reduced the slip capacity on account of the absence of transverse fibers. This led to better approximation of the perfect bond assumption as compared to bond-slip laws obtained from different directions of casting. From the various 1-D models analyzed, it was found that the perfect bond condition for the reinforcement was able to generate the tension stiffening response closest to the experimental behaviour at least up to the onset of strain-hardening in rebar. This is attributed to the high characteristic bond strength of UHPFRC that can be developed at relatively much lower slip values. However, the influence of bond-slip law beyond yielding and strain-hardening region of the reinforcement is to be explored in future studies.

Chapter 7: Design of Bridge Pier Seismic Retrofit using UHPFRC

Retrofit applications of UHPFRC are currently being extensively researched. Several possible retrofit implementations have been discussed earlier in Section 2.6. Research conducted in the past decade illustrated that jacketing of reinforced concrete (RC) components with UHPFRC is a viable and attractive alternative to other methods of seismic retrofitting – such as other forms of jacketing (FRP, RC, steel) (refer to Section 2.6.1). It also provides for various other retrofitting alternatives such as replacement of core concrete in plastic hinge regions and damaged cover in the presence of reinforcement corrosion. On account of its increased density and durability, UHPC has been shown to also protect reinforcement against ingress of corrosive agents slowing down significantly the progress of corrosion and is therefore a particularly attractive solution for seismic retrofitting of corrosion damaged piers (El-Joukhadar & Pantazopoulou, 2021). Mitigating the susceptibility to hidden corrosion of embedded reinforcement in FRP jacketed piers has been an issue of concern in recent years and has been the reason why the combined properties of ductility and durability of tension hardening UHPC materials have resonated with the needs for novel retrofit opportunities for bridge piers Pantazopoulou et al. (2017).

However, no design provisions exist regarding the application of UHPFRC in seismic design and retrofit, particularly in seismic jacketing of piers where they appear most effective in cost and performance. In this chapter, a summary of a pertinent framework of seismic design guidelines is presented, which are needed for determination of both seismic demands and criteria for performance-based design of UHPFRC based retrofits. To this end, stress-strain relationships are formulated considering the confinement effect imparted by the fiber reinforcement. Strain limits in compression are established by reference to test data from various studies of UHPFRC.

7.1 Confinement Effect of UHPFRC

In order to quantify the mechanistic implications of UHPFRC jackets in encasing a column through jacketing, material stress-strain laws are required to carry out sectional and member analysis. In this context, the favorable contribution of the hardening characteristics of the material is traced to two different types of confining action that occurs in the jacket: These are,

(a) The *internal confinement* which is owing to the action of fibers. The action of this source of confinement is depicted in Figure 7- 1a which shows an elementary volume of material crossed by

a crack: fibers intercepted by the crack develop tensile stresses, f_f, and these are equilibrated in the matrix by an internal confining pressure $q_{f,lat}$ (Manita & Pantazopoulou, 2002). This internal pressure effectively delays the process of lateral expansion when the material is tested under compression (where, based on classical theory, cracks would tend to develop parallel to the axis of compression). In developing a practical stress-strain model for UHPFRC in compression, the restraint to dilation through internal confinement need be accounted for through two different aspects: By allowing for a prolonged range of linear elastic response on account of the enhanced damage control that is imparted by the internal confinement (therefore, a stress-strain model based on Hognestad's parabola such as what is used in conventional concrete, is no longer applicable for UHPC and HPFRC); and by considering the increased deformation capacity of the UHPFRC material in compression.

(b) The *external confinement* that the UHPFRC jacket applies on the encased conventional core which, together with the action of stirrups, causes a passive internal confining pressure $\sigma_{j,lat}$ that effectively enhances the deformation capacity and even mildly may affect the encased concrete strength (Figure 7- 1b). Based on the previous experimental evidence, conventional confinement models still apply, after some minor modifications so as to account for the effectiveness and the magnitude of $\sigma_{j,lat}$ (Tsiotsias & Pantazopoulou, 2022; Manita & Pantazopoulou, 2002; Richart et al., 1928; Mander et al., 1988).

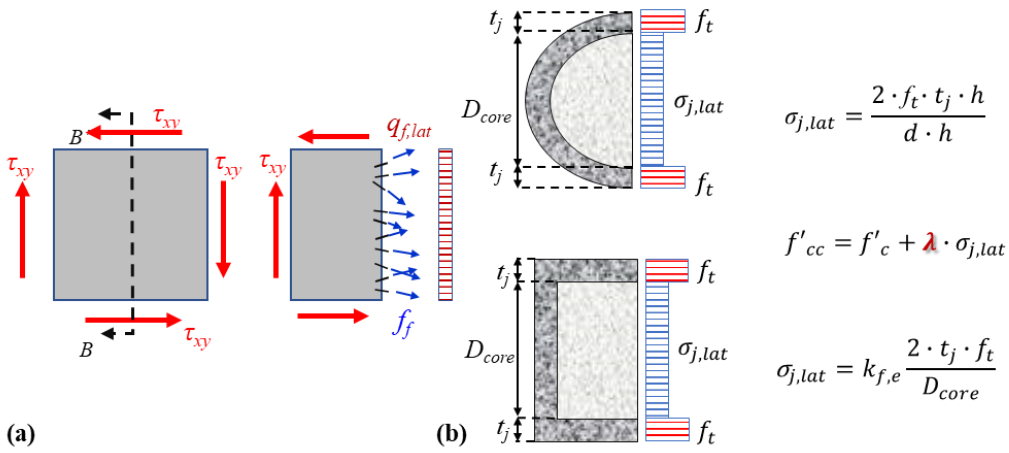

Figure 7- 1: (a) Internal confinement pressure, $q_{f,lat}$, imparted by the fibers; (b) Illustration of the effective confining pressure, $\sigma_{j,lat}$

7.2 Stress-Strain Model for UHPFRC in Tension and Compression

Most of the published experimental research has focused in characterizing the stress-strain response of the UHPFRC material in tension, either through inverse analysis of flexural prism tests or through direct tension tests (Annex 8.1 CSA S6, 2019; FHWA, 2013; SIA 2052, 2016; AFNOR NF P18 470, 2016). Generally, the accepted response is as depicted in Figure 7- 2a, whereas for design purposes the hardening part is neglected, and the plot shown in Figure 7- 2b is assumed (Annex 8.1 CSA S6, 2019). Coefficient γ_f is a fiber orientation factor, intended to account for the randomness in the fiber distribution for large depth castings in concrete components. Thus, in the remainder, the design value of the tensile strength of the material, f_{td}, is used instead of the value obtained from characterization tests, in consideration of the attenuating influence of the fiber orientation factor:

$$f_{td} = \gamma_f \cdot f_t \tag{7-1}$$

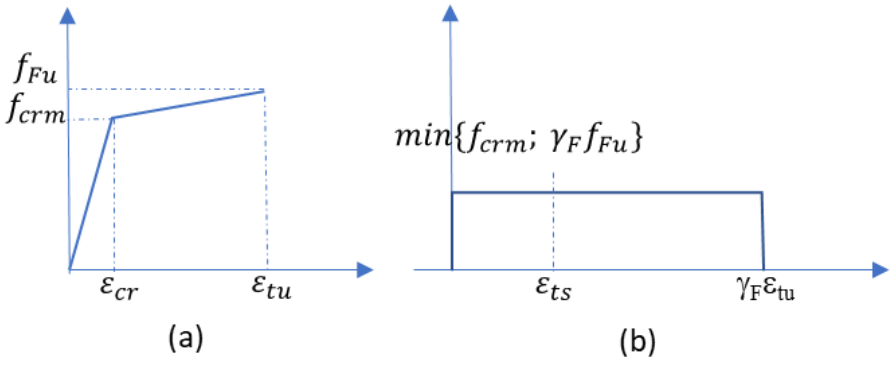

Figure 7- 2: (a) Actual tensile behavior of UHPFRC (b) Design Stress-Strain Model for UHPFRC in Tension (Annex 8.1 CSA S6, 2019)

Detailed data on the complete stress-strain response under compression are surprisingly scarcer than for tension, particularly for cases where f_c'>150 MPa. Although tests are recommended to be conducted on unconfined cylinders 75 mm in diameter by 150 mm in height (an aspect ratio of 2 (Annex U CSA A23.1, 2019; AFNOR NF P18 710, 2016)), the crushing load is still very high, building significant strain energy in the testing frame, so that unless a very stiff frame is available, it is not easy to capture a post-peak envelope. Note that only few studies reported the post-peak stress-strain response, although UHPC cylinders generally maintain their integrity in the post-peak range after failure. Surface strain gauges used for recording strain may either rupture or become

detached after attaining the peak strength (Hassan et al. 2012), whereas the existing test procedures in the standards (ASTM C469/C469M, 2019; BS-1881, 1983) are not suitable for recording the post-peak behavior; use of LVDTs to measure the movement of machine crosshead in the post-peak region might be the only option in many such experiments. For these reasons, data-calibrated stress-strain models for UHPC in compression - which are needed for structural analysis of UHPFRC components or retrofits, are relatively scarce.

In the present work, in order to establish the milestone strain parameters of a uniaxial compression stress-strain relationship, the available experimental evidence is assembled to form a basis for data regression. To this end, a variety of past experimental studies including tests described in Section 3.3.3 and Section 5.8.1 have been considered [refer to Table A-1], amounting to a total of 16 different collections of tests done on materials that qualify as UHPFRC or HPFRC that practically have strengths of at least 100 MPa. Relevant details such as cylinder specimen dimensions, fiber type, length and diameter of fibers, and volumetric ratio of fibers are also provided. Reported values include the compressive strain corresponding to peak stress, and the post-peak strain at a residual stress equal to 50% of the peak value where such are available. Only test results from unconfined cylindrical specimens are considered. Wherever possible, individual specimen stress-strain data was collected, otherwise reported average values were considered (of 3 or more identical specimens).

Figure 7- 3a plots the pairs of values of peak stress and corresponding strain, whereas Figure 7-3b shows the data for 50% residual stress vs corresponding strain. The dispersion observed in the data is owing to the variability in mix constituents, mix proportions, curing regime and age at testing among different studies listed in Table A-1.

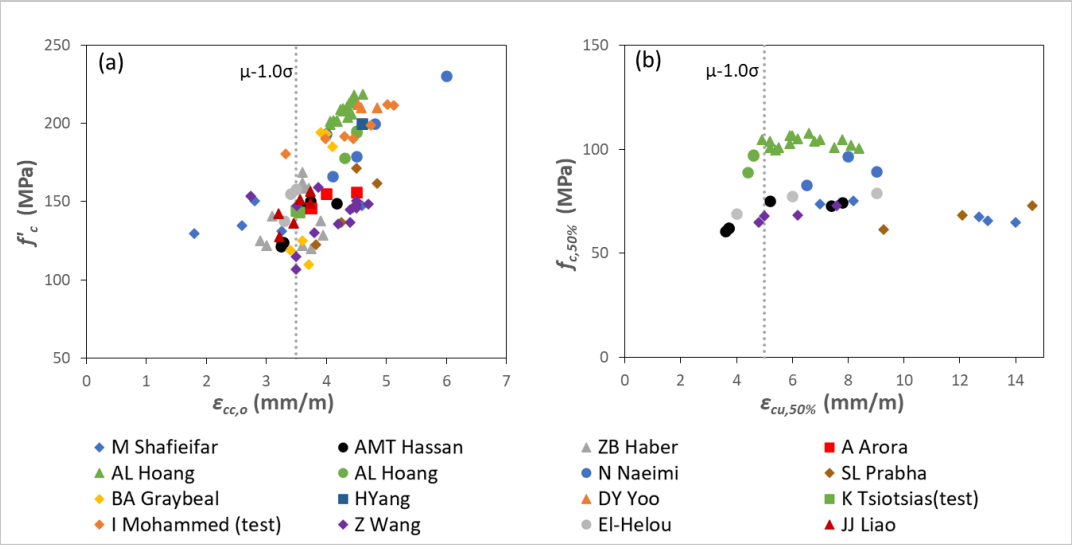

Figure 7- 3: Summary of experimentally measured values for the strain capacity of UHPFRC (a) Peak stress vs corresponding strain (b) 50% residual peak stress vs corresponding strain

7.2.1 Analytical Stress-Strain Model of UHPFRC in Compression

In the following, analytical calculations of retrofitted elements are based on the proposed model for UHPFRC in compression depicted in Figure 7- 4a. For the ascending branch of the stress-strain law in compression, the mathematical expression originally proposed by Thorenfeldt et al. (1987) for high strength concrete has been used: where the empirical coefficients have been adjusted to produce a nearly linear elastic response for a large range of the ascending branch, consistently to what is observed in HPFRC and UHPC tests in compression. This model is based on the fitted polynomial by Popovics (1973) which is the basis for other proposed models in the literature and which are summarized for comparison in the Section 7.5 (AFNOR NF P18 710, 2016; Naeimi and Moustafa, 2021).

$$\sigma_a = f'_c \cdot \left[\frac{n \cdot (\varepsilon_a/\varepsilon_{co})}{n - 1 + (\varepsilon_a/\varepsilon_{co})^{nk}}\right] \tag{7-2}$$

where, n is adjusted so that the slope of the ascending branch matches the Initial Tangent Modulus of Elasticity; here, n = 15. Also, k = 1 for axial compressive strains $\varepsilon_a < \varepsilon_{co}$. This may be further simplified by the linearized ascending branch shown by the black dashed line in Figure 7- 4a. In this case, the strain at peak stress is obtained from,

$$\varepsilon_{co} = f'_c / E_c \quad (7\text{-}3a)$$

Values for E_c are obtained from pre-qualification tests conducted for UHPFRC material characterization; a conservative estimate for E_c of UHPFRC is (Graybeal, 2012),

$$E_c = 4070\sqrt{f_c'} \quad \text{(MPa)} \quad (7\text{-}3b)$$

The characteristic strain points in the stress-strain model plotted in Figure 7- 4a, were estimated with reference to the experimental response values plotted in Figure 7- 3, after consideration of the internal confinement effect that the fibers provide thereby securing the strain ductility of the material both in tension and in compression (Manita & Pantazopoulou, 2002). Note that the internal confining pressure imparted by the fibers has been estimated to be equal in magnitude to the tensile strength of the material (Georgiou & Pantazopoulou, 2016). For stress and strain calculations to be used in design, the internal confining stress, $q_{f,lat}$, is estimated from:

$$q_{f,lat} = \varphi_c \cdot f_{td} \quad (7\text{-}4)$$

The material resistance factor, φ_c used for high performance concrete in bridge design is 0.75 (CSA S6, 2019). For theoretical calculations, considering the uncertainty regarding the true fiber orientation in a field cast, the nominal tensile strength may be taken equal to the lowest acceptable limit for UHPC, i.e., $f_t = 0.6\sqrt{f_c'}$ and $q_{f,lat} = 0.75 f_t$. The strain at peak stress of confined concrete is estimated with reference to the magnitude of confining stress from the following:

$$\varepsilon_{cc,o} = \varepsilon_{co}\left(1 + 6\left(\frac{q_{f,lat}}{f'_c}\right)\right) \quad (7\text{-}5)$$

Parameter ε_{co} is the uniaxial strain at attainment of peak stress in the absence of confinement: attainment of that strain magnitude (see Equation 7-3a), defines the beginning of a plateau of constant stress at peak for UHPC; the end of the plateau is determined by strain magnitude $\varepsilon_{cc,o}$, which is obtained from Equation 7-5 (Richart et al., 1928; Mander et al., 1988) upon substitution of Equation 7-4. Similarly, considering the confined strength and strain enhancement of concrete, a strain capacity (ε_{cu}) corresponding to 75% of peak stress in the post-peak envelope is estimated as per Equation 7-6 (Imran & Pantazopoulou, 1996; Richart et al., 1928):

$$\varepsilon_{cu,75\%} = \varepsilon_{co}\left(1 + 20\left(\frac{q_{f,lat}}{f'_c}\right)\right) \leq 0.0045 \qquad (7\text{-}6)$$

The upper limit of 0.0045 was determined as a lower bound value obtained from the available data at 75% of peak strength in the descending envelope (Figure 7- 5b): mean value minus one standard deviation, corresponding to a probability of 85%. The linear descending branch extends from the end of the plateau at peak (point with coordinates (f_c', $\varepsilon_{cc,o}$)) down to the point with stress equal to $0.75f_c'$ and strain of $\varepsilon_{cu,75\%}$. Beyond that point, the post-peak envelope extends down to $0.5f_c'$ and strain of $\varepsilon_{cu,50\%}$ - the latter is determined as a lower bound value of *0.005* based on Figure 7- 3b; a residual stress equal to $0.2f_c'$ which is sustained to large strains is assumed as a conservative lower limit based on the experimental evidence.

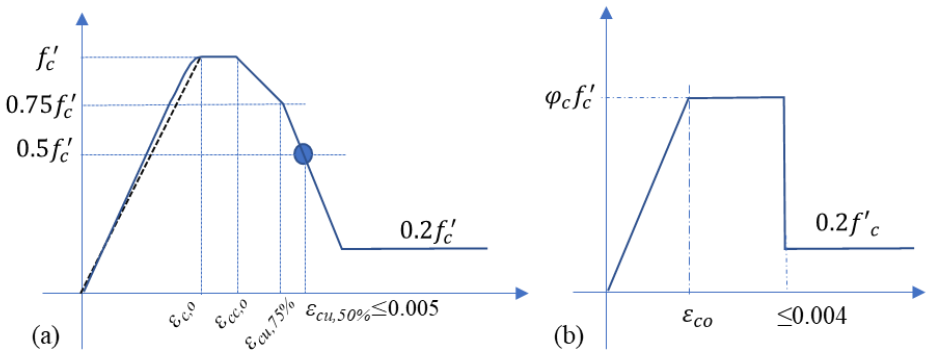

Figure 7- 4: (a) Proposed Analytical Stress-Strain Model for UHPFRC in Compression (b) Proposed design compression model

Figure 7- 5a and Figure 7- 5b illustrate the comparison between experimental and analytical strain values for $\boldsymbol{\varepsilon_{cc,o}}$ and $\boldsymbol{\varepsilon_{cu,75\%}}$, obtained from Equations 7-5 and 7-6, respectively; the 45° diagonal represents ideal correlation between the analytical estimates and the experimental values. The analytical values are obtained from Equations 7-5 and 7-6 for $\varepsilon_{cc,o}$ and $\varepsilon_{cu,75\%}$, respectively. The parallel yellow lines in Figure 7- 5a and 7-5b represent the limits corresponding to the mean (μ) experimental value ± *x* times standard deviation (σ), where *x*=1.7 for $\varepsilon_{cc,o}$ and *x*=1.3 for $\varepsilon_{cu,75\%}$ (for given size of the sample these bounds correspond to about 90% and 80% confidence interval, respectively, based on t-distribution).

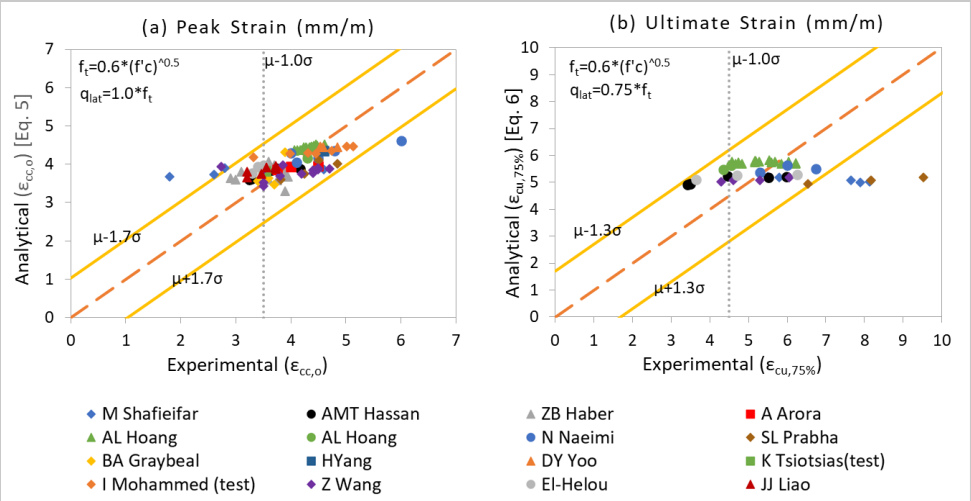

Figure 7- 5: Comparison of experimental and analytical values for (a) $\varepsilon_{cc,o}$ (b) $\varepsilon_{cu,75\%}$

7.2.2 Design Stress-Strain Model for UHPFRC in Compression

For design calculations of UHPFRC in compression, the model specified by Equations 7-7 to 7-9 are recommended to be used. Design calculations should be conducted using the model depicted in Figure 7- 4b, whereas the model of Figure 7- 4a is intended for seismic assessment of available resistances. Thus, a linear relationship between stress and strain in compression is assumed up to a compressive strain not exceeding 0.003, whereas the maximum usable strain at the extreme concrete compression fiber cannot exceed 0.004 unless it can be shown from material characterization tests that a higher value of strain can be justified. A residual strength equal to *0.2f_c'* is assumed beyond this strain limit. Thus,

$$\varepsilon_{co} = f'_c/E_c < 0.003 \tag{7-7}$$

$$f_{cd} = \alpha_1 \cdot \varphi_c \cdot f'_c,\ \varphi_c = 0.75; and\ \varepsilon_{co,d} = f_{cd}/E_c < 0.00225 \tag{7-8}$$

$$\varepsilon_{cu,d} \leq 0.004 \tag{7-9}$$

7.3 Application of UHPFRC in Seismic Design and Retrofit

Seismic actions for design or retrofit using UHPFRC materials may be defined as per any bridge design code that is compatible with Performance-Based Design Principles. In the present discussion, reference is made to Chapter 4 of the Canadian Highway Bridge Design Code (CSA S6, 2019). For bridges in Seismic Performance Category 1, or where force-based design (FBD) is

required as per Table 7- 1 adapted from Table 4.11 of the Code (CSA S6, 2019) (i.e., in regions of moderate seismicity, for regular major route bridges and for other bridges of lesser importance), elastic analysis (with R=1) is conducted. When tension hardening materials are used, gross (uncracked) Moment of Inertia properties for the part of the member's cross-section that consists of UHPFRC and a reference value of $E=50\ GPa$ in calculating the seismic demands (through the fundamental period of the bridge structure, T). For bridges requiring performance-based design (PBD), (which is the case of Lifeline bridges in regions of moderate seismicity or higher, and in Major bridges in regions of high seismicity), the displacement demand is determined from spectral acceleration $S_a(T)$ using basic principles (e.g., for the equivalent single degree of freedom system representing the pier-deck system, spectral displacement S_d, may be obtained from: $S_d(T) = S_a(T)\cdot T^2/4\pi^2$). The fundamental structural period, T, is obtained from detailed analysis of the structural system, where the effective flexural stiffness EI_{eff}, of the individual member need be defined from Moment-Curvature analysis of their critical section as depicted in Figure 7- 6. Where sectional analysis is necessary, it should be conducted considering the detailed Stress-Strain Material Laws defined in the preceding sections; in cases of new design, the material resistance factor, φ_c, is taken = 0.75.

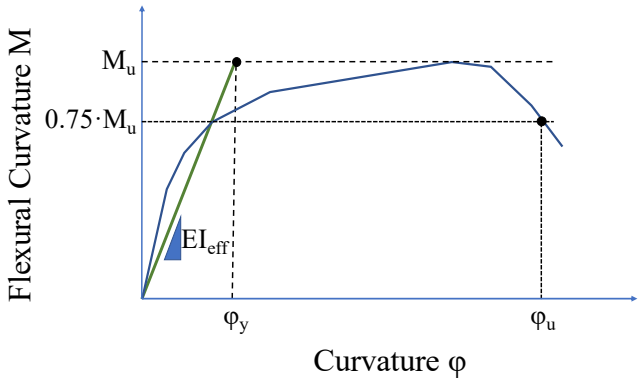

Figure 7- 6: Definition of Elastic Stiffness of Structural Members in PBD

With reference to the minimum performance levels outlined in Table 7- 2 (adapted from Table 4.15 of CSA S6 (2019)), and the performance criteria elaborated in Table 4.16 of CSA S6 (2019), it is recommended that UHPFRC components and component retrofits should meet the following criteria:

- to ensure *minimal damage* the concrete compressive strains should not exceed 0.004, and likewise the reinforcing steel strains should not exceed 0.008.
- For *repairable damage*, steel tensile strains should not exceed 0.015.
- Lastly, for the *life safety limit*, damage incurred to the member should not cause crushing of the encased concrete core of the jacketed component and reinforcing steel tensile strains should not exceed 0.06.

These values are based on systematic review of the available experimental evidence on UHPFRC material characterization tests summarized in Figure 7- 3, Figure 7- 4, Figure 7- 5, and the lab tests summarized in the Section 2.6.1 on *Performance of UHPFRC in Pier Jacketing*. For structures that have been designed to remain elastic, the displacement demands need to be re-assessed after calculating the extent of tension cracking according to the stress level attained in design. Where PBD is conducted, seismic resistances should be quantified using the respective models of design codes (e.g., CSA S6, 2019) for the various actions, considering the fiber contribution in the stress-strain response of the material in both tension, compression, and shear (i.e., Flexural, Shear, Punching, Torsional, Lap-Splice Strengths, e.g., CSA S6, 2019; ACI 239, 2018). In fact, in terms of the strength enhancement, the contribution of the tension stress resultant developed in the extreme tension range of the cross-section (for flexure) and in the web of the cross-section (for shear) can be significant: for example, the shear strength increase is estimated from the product, $2t_j \cdot f_{td} \cdot (h-t_j) \cdot \tan\theta$, where θ is the angle of diagonal cracks with respect to the longitudinal axis (for $\theta=45^o$ (CSA S6, 2019), the above reduces to the total area of the jacket in the web multiplied by the design value of the tensile strength of the jacket material).

Members that are part of the lateral resisting system of the structure must be shown to possess the required displacement ductility, μ_Δ. This is taken equal to the Response Modification Factor, *R*, in FBD, or equal to the ratio of the estimated global displacement demand at the Performance Point, divided by the system's displacement at yielding in PBD ($=S_{d,u}/S_{d,y}$). Minimum reinforcing requirements ought to be observed in designing structures with UHPFRC for earthquake resistance.

Table 7- 1: Requirements for Performance-based design (PBD) and Force-based design (FBD) (Ch. 4, CSA S6, 2019)

Seismic Performance Category	Lifeline bridges		Major-route bridges		Other bridges	
	Irregular	Regular	Irregular	Regular	Irregular	Regular
1	No seismic analysis required					
2	PBD	PBD	PBD	FBD	FBD	FBD
3	PBD	PBD	PBD	PBD	PBD	FBD

Table 7- 2: Minimum performance levels (Ch. 4, CSA S6, 2019)

Seismic ground motion probability of exceedance in 50 years (return period)	Lifeline bridges		Major-route bridges		Other bridges	
	Service	Damage	Service	Damage	Service	Damage
10% (475 years)	-	-	Immediate	Minimal	Service limited	Repairable
5% (975 years)	Immediate	Minimal	-	-	-	-
2% (2475 years)	Service limited	Repairable	Service disruption	Extensive	Life safety	Probable replacement

7.4 Retrofitting with UHPFRC Jacketing

For cases where the UHPFRC material is used as jacketing around conventional concrete (for retrofitting) the effective confining pressure of the encased concrete will be calculated from,

$$\sigma_{j,lat} = 2k_{e,f}\varphi_c f_t\left({}^{t}/_{h}\right) \tag{7-10}$$

where, t is the jacket thickness and h is the dimension of the encased cross-section confined by the jacket. The confinement effectiveness $k_{e,f}$ is obtained from the ratio of the sectional area effectively confined divided by the total encased area (assuming a rectangular cross-section with dimensions $b \times h$). Research on confinement effectiveness using UHPC jacketing on columns (Rabehi et al., 2014) has led to an estimate for the confinement effectiveness coefficient, $k_{e,f}$, that is practically identical to that obtained for FRP jackets (Pantazopoulou et al., 2016; *fib* Bulleting-40, 2007).

$$k_{e,f} = 1 - \frac{(b^2 + h^2)}{3 \cdot (1 - \rho_{sc})bh} \quad (7\text{-}11)$$

In the presence of confining reinforcement (hoops and stirrups), Equation 7-10 is modified to account for the contribution of stirrup confinement to the confining pressure, $\sigma_{st,lat}$. In Equation 7-12, k_{eff} is the confinement effectiveness factor, ρ_w is the volumetric ratio, and $f_{y,st}$ is the yield stress for the confining reinforcement (EN 1998-1, 2004).

$$\sigma_{st,lat} = 0.5 \cdot k_{eff} \cdot \rho_w \cdot f_{y,st} \quad (7\text{-}12)$$

Performance limit states defined in the preceding are applicable, however additional consideration need be given to the risk for buckling of compression reinforcement of the encased conventional concrete cross-section ($\varepsilon_{sc} \geq \varepsilon_{cu}=0.0035$). For this case, the limit state of *minimal damage* is associated with the earliest of: {$\varepsilon_{sc} \geq \varepsilon_{sy}=f_y/E_s$, where $E_s=200$ *GPa*, ε_{st} = 0.008, and maximum jacket compressive strain, $\varepsilon_{c,FRC} < 0.004$}. Repairable damage limit state and Life Safety are as defined previously.

A design example is provided for practical illustration of the contribution of UHPC jacket using the design procedure outlined. A bridge pier with a square cross-section as depicted in Figure 7-7a is used, with original (un-jacketed) cross-section dimensions of 1.0 m ×1.0 m and an external UHPFRC jacket of t_{jacket}=100 mm. Figure 7- 7d represents case (i) and case (ii) for the UHPC stress blocks based on the tension stress-strain law given by Figure 7- 2a and Figure 7- 2b, respectively. In the following discussion, subscript '*e'* on the various response parameters refers to the encased, conventional concrete. In this example, the jacket is applied after removal of the clear cover of the original section (c_c=40mm), leading to the final dimensions of the retrofitted pier cross-section to be equal to 1.12 m × 1.12 m. The total longitudinal and transverse reinforcement ratios were $\rho_l=2.0\%$ (32-25M – 9 per face evenly spaced) and $\rho_w=0.4\%$ (15M), perimeter stirrups placed at spacing of 200 mm as per old construction practices. Internal core concrete is of strength f_c'=35 MPa, E_c=25 GPa, ε_{co}= 0.2%. Since the encased material is conventional concrete, the material's ascending part of the uniaxial compressive stress-strain relationship is defined according to Hognestad's parabola (Hognestad, 1951), as shown in Equation 7-13 below. For the descending

branch, the modified constitutive model by (Kent & Park, 1971) is used, as shown in Equation 7-14, until the residual branch which is described in Equation 7-15.

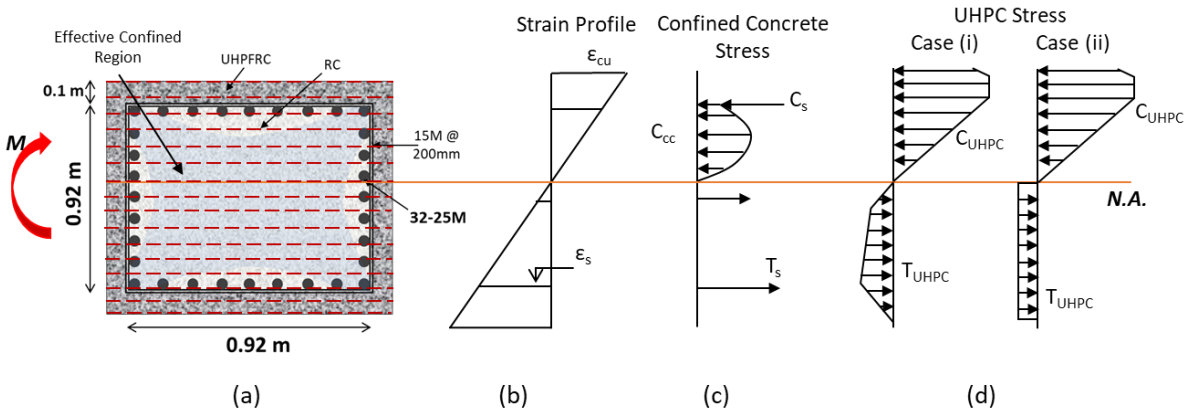

Figure 7- 7: (a) Schematic representation of section layered analysis for concrete column confined with a UHPFRC jacket (b) Strain profile across the section (c) Confined concrete stress block (d) UHPFRC stress blocks

$$f_e = f_{cc,e} \cdot \left[2 \cdot \left(\varepsilon_e/\varepsilon_{cc,e}\right) - \left(\varepsilon_e/\varepsilon_{cc,e}\right)^2\right], \qquad \varepsilon_e \le \varepsilon_{cc,e} \tag{7-13}$$

$$f_e = f_{cc,e} \cdot \left[1 - Z \cdot \left(\varepsilon_e - \varepsilon_{cc,e}\right)\right], \qquad \varepsilon_{cc,e} < \varepsilon_e \le \varepsilon_{cu,e} \tag{7-14}$$

$$f_e = 0.2 \cdot f_{cc,e}\,, \qquad \varepsilon > \varepsilon_{cc} \tag{7-15}$$

In the equations above, $f_{cc,e}$ and $\varepsilon_{cc,e}$ are the stress and strain of confined (encased) concrete as per Equations 7-16 and 7-17. Parameter Z describes the descending branch slope, which is defined in Equation 7-18 shown below.

$$f_{cc,e} = f_{c,e} \cdot K \tag{7-16}$$

$$\varepsilon_{cc,e} = \varepsilon_{co,e} \cdot K \tag{7-17}$$

$$Z = \frac{0.5}{\frac{3 + 0.29 \cdot f_{c,e}}{145 \cdot f_{c,e} - 1000} + 0.75 \cdot \rho_v \cdot \left(\frac{h}{s}\right)^{1/2} - \varepsilon_{co,e} \cdot K}, in\ MPa \tag{7-18}$$

In the equation above, K is the encased concrete's strength increase factor due to confinement, ρ_v is the volumetric ratio of transverse reinforcement, h is the width of the concrete core and s is the spacing of the stirrups. Factor K is defined as per Equation 7-19, modified from Scott et al. (1982):

$$K = 1 + \frac{\lambda \cdot \sigma_{tot,lat}}{f_{c,e}} \tag{7-19}$$

In Equation 7-19, λ is the section factor and $\sigma_{tot,lat}$ is the summation of the lateral confinement stresses of the UHPC jacket and the transverse reinforcement, as described in Equations 7-10 and 7-12, respectively. In this example, the assumption was made that $\lambda = 2$ (note that for circular cross-sections under hydrostatic pressure this factor is 4.1 (Manita & Pantazopoulou, 2002; Scott et al. 1982; Kent & Park, 1971)) due to the reduced confinement effectiveness of the jacket in the rectangular-type section.

For the reinforcing steel, an elastic-plastic strain-hardening constitutive law was used, as shown in the Equations 7-20 to 7-22 below:

$$f_s = E_s \cdot \varepsilon_s, \varepsilon_s \leq \varepsilon_y \tag{7-20}$$

$$f_s = f_y, \varepsilon_y < \varepsilon \leq \varepsilon_{sh} \tag{7-21}$$

$$f_s = f_y + E_{sh} \cdot (\varepsilon_s - \varepsilon_{sh}) \cdot \left[1 - \frac{E_{sh} \cdot (\varepsilon_s - \varepsilon_{sh})}{4 \cdot (f_{su} - f_y)}\right], \varepsilon_{sh} < \varepsilon \tag{7-22}$$

In the equations above, f_s is the steel stress, E_s is the modulus of elasticity for steel, ε_s is the steel strain, ε_y is the yielding strain, ε_{sh} is the strain at the onset of hardening, E_{sh} is the hardening modulus and f_{su} is the ultimate stress. For the following example, E_s = 200 GPa, f_y = 400MPa, ε_{sh} = 0.01, E_{sh} = 8600MPa, and f_{su} = 700MPa were used.

For the UHPFRC jacket, two types of UHPC materials with nominal properties were considered, one with f_c'=150 MPa and E_c=48 GPa, on the compression side, and f_t=11MPa, ε_{ts}=0.022% and ε_{tu}= 2.0%, on the tension side. For the second material, the values were f_c'=120 MPa, E_c=45 GPa and f_t=6 MPa, ε_{ts}=0.012%, ε_{tu}=2.0%, respectively. The material properties were selected based on expected values for UHPC materials, as denoted in (Pantazopoulou et al., 2019). The coordinates of the complete stress-strain relationship in compression were defined according to Equations 7-2 to 7-6. On the tension side, the jacket follows the stress-strain law shown in Figure 7- 2a, with the

characteristic material properties mentioned above. On the compression side, the model shown in Figure 7- 4a is used. Fiber effectiveness factor γ_F was assumed to be 0.5, for both materials, and the axial load on the section was 0.25 $f_c A_c$. The results of the analysis are shown in Figure 7- 8.

The results illustrate that the contribution of the jacket improves the flexural capacity of the normal concrete section, with the maximum moment increasing by 58% and 44%, for the UHPFRC jackets of f_t =11 MPa and f_t =6 MPa, respectively. The corresponding confinement pressure of the encased concrete is estimated from Equations 7-10 to 7-12 as, $\sigma_{tot,lat}$ =1.27 MPa and 1.0 MPa, respectively, also considering the contribution of the stirrups. It is also evident that the higher tensile capacity of the UHPFRC material prolongs the tensile response of the jacket, with the breadth of the ductile plateau being significantly enhanced in the moment-curvature diagram. Both curves of the UHPFRC-confined sections do not show significant post-peak strength reduction (i.e., less than 15%) up until significant levels of curvature ductility, and the curvature at peak moment is 90% and 105% higher than that of the unconfined section, for the cases of f_t =11 MPa and f_t =6 MPa, respectively. It is noted that for 1% tensile steel strain, none of the two UHPFRC jacket layers exceeded the value of ε_{co} of 0.003 (Equation 7-6).

The performance limit states (established earlier) are also identified in Figure 7- 8, with the green color marker denoting minimal damage, the orange denoting repairable damage, and the red for life safety. Additionally, two more milestones are identified, for the jacketed sections, where the reinforcement on the tension side reaches the strain of 0.8% (yellow) and 1.5% (purple). In the original (un-jacketed) section, the green point denotes the yielding of compression reinforcement (ε_{cy} = 0.002), at a curvature of 4.2×10^{-6} 1/mm, whereas the repairable damage at 7.1×10^{-6} 1/mm corresponding to crushing of the cover. The life safety limit state is obtained at the end of the curve, at 7.9×10^{-6} 1/mm, at which point the concrete core crushed.

In the UHPFRC-confined sections, the minimal damage point, denoted by curvature values of 6.4×10^{-6} 1/mm and 6.5×10^{-6} 1/mm for the jackets of f_t=11MPa and f_t=6 MPa, respectively, corresponds to onset of compression bar yielding. Then, reinforcement on the tension side reaches the strain of 0.008 at curvature values of 10.1×10^{-6} 1/mm and 10.2×10^{-6} 1/mm, for the jackets of f_t=11 MPa and f_t=6 MPa, respectively. The state of repairable damage (cover crushing) occurs after reduction of the flexural resistance, at curvature values of 15.5×10^{-6} 1/mm and 12.8×10^{-6} 1/mm, for each case. For the case of the jacket with f_t =11 MPa, the inner core is crushed at the curvature

of 18×10^{-6} 1/mm. For the case of the jacket with f_t =6 MPa, the inner core reaches crushing at the curvature of 14×10^{-6} 1/mm. At the inner core crushing, the reinforcement strain on the tension side is ε_{st} = 0.0152 and ε_{st} = 0.011, for each jacketed section; at this point, the encased concrete has reached the maximum compressive strain of ε_c = 0.0035. It is noted that both jacketed examples have ample residual deformation capacity beyond these conditions to support life safety. At the ends of the curves, the strain in the reinforcement on the tension side is ε_{st} = 0.022 and ε_{st} = 0.0135, for each jacketed section, respectively.

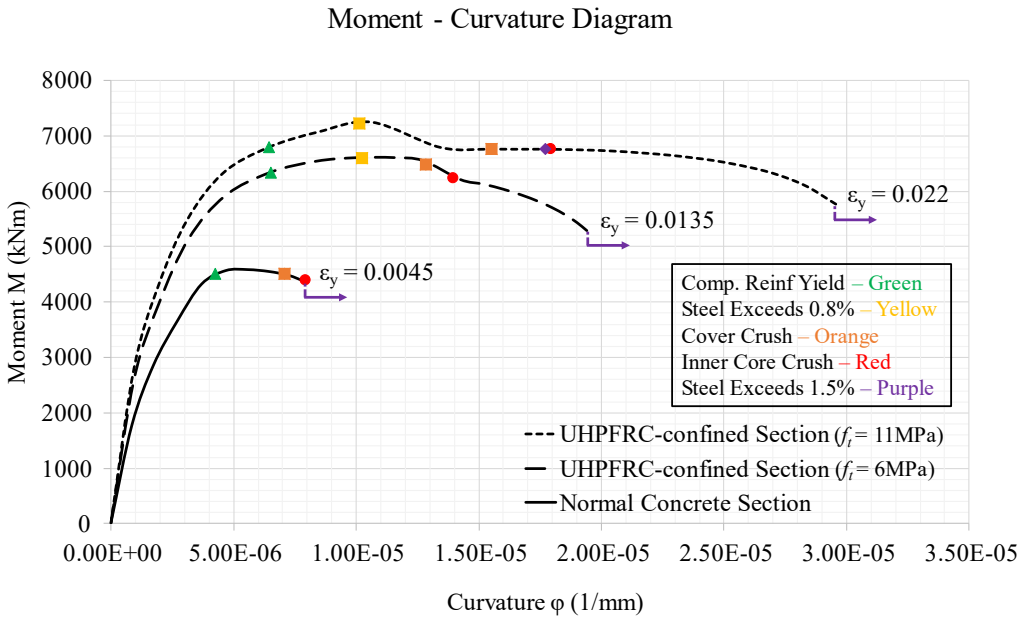

Figure 7- 8:Comparison of moment-curvature diagrams from section analysis example for normal concrete section and for section confined with UHPFRC jacket.

7.5 Comparison of Proposed Compression Model with Other Recommended Models

In this section, a comparison is drawn between the compressive stress-strain models of UHPC proposed in this study (Equations 7-2 to 7-6), and the ones proposed by NF P18-710 (2016) and Naeimi & Moustafa (2021). It is noted that all three models use as a basis the polynomial expression proposed by Popovics (1973) with minor adjustments owing to the different datasets used for calibration of the variables and the scope of the model usage. Clause 3.15 of the standard AFNOR (NF P18 710, 2016) recommends the stress-strain relation for compression behavior of UHPFRC to be used for non-linear structural analysis as shown in Figure 7- 9a. Naeimi & Mostafa

(2021) proposed an analytical model for compressive behaviour of steel spiral confined UHPC that could also be extended to unconfined UHPC. Expressions used in both the French model and Naeimi's model have been described in detail in Section 2.8 of the thesis.

Figure 7- 9b depicts the comparison between the compression models of Modified Thorenfeldt that was recommended in the present study, that of Naeimi & Moustafa (2021) and the model recommended in AFNOR (NF P18-710, 2016) fitted against an average experimental response corresponding to 'UHPFRC 28 days' curve reported in an independent study by Hassan et al. (2012). Properties of the experimental curve considered are as follows: $f_c' = 150\ MPa; E_c = 46\ GPa;\ f_t = 9\ MPa;\ v_{f,\%} = 2;\ \rho_{s,\%} = 0$. As noted in the comparison plot of Figure 7- 9b, results from various models were found to be in good agreement in the pre-peak region. However, the post-peak region predicted by the proposed model is conservative and much closer to the experimental behavior compared to the other two models.

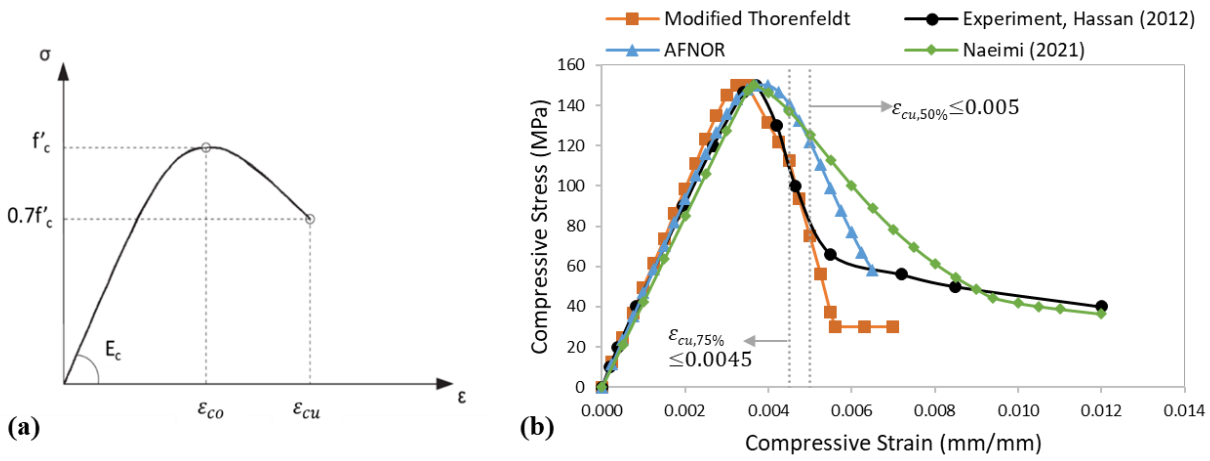

Figure 7- 9: (a) Representative curve of compressive behavior proposed for UHPC in AFNOR NF P18-710 (2016) (b) Comparison between different compression models

7. 6 Summary

In this chapter, a comprehensive proposal for seismic provisions for bridge pier retrofitting with UHPFRC materials jacketing was formulated in the context of performance-based design. Below is a summary of the list of things addressed in this chapter:

1. Relevant performance limit states are proposed consistent with the available experimental evidence, and guidelines regarding design and analysis modelling are specified with reference to the Canadian Highway Bridge Design Code framework.
2. Tension and compression stress-strain models that are required for design and analysis of structural elements jacketed with UHPFRC are presented. For tension, the models of Annex 8.1 of CSA S6 (2019) are recommended. For compression, an analysis model was formulated and compared with the French Code Provisions (NF P18 710, 2016) and with a recently published model (Naeimi & Moustafa, 2021), in both cases with satisfactory convergence. In the proposed stress-strain relationship for UHPFRC in compression, the length of the strain plateau at peak stress and the post-peak slope are related to the effective internal confining pressure imparted by the fiber content of the material.
3. A database of available tests was assembled in order to derive strain values for the milestone points of the compressive stress-strain envelope. From the analysis of the data, usable strain limits for UHPFRC in compression are determined for the characteristic points of the stress-strain envelope. Values having 85% probability of being exceeded by an arbitrary sample (based on the assembled data) were selected to define the lower bound deformation capacities at the points of reference.
4. UHPFRC jacketing as a retrofitting method for columns and piers contributes to the enhancement of both strength and deformation capacity of the component, through (a) participation of the UHPFRC layer in the development of normal compressive and tensile stresses, thereby participating in the cross-sectional equilibrium, and (b) as a mechanism of confinement through encasement of the conventional concrete cross-section. A detailed example of a bridge pier jacketed with a 50mm layer of THFRC materials (one UHPFRC and one HPFRC) is considered to illustrate the implementation of the proposed design methodology. The design or analysis of a jacketed member can be performed by using the proposed expressions related to UHPFRC confined reinforced concrete and the stress-strain models for UHPFRC.

Parts of this chapter have been utilized in a paper submission to the Special Publication of American Concrete Institute (ACI) which is currently under peer-review (January 2023).

Chapter 8: Conclusion

8.1 Summary of the Thesis

This research was focused on multiple fronts pertaining to Ultra-High Performance Fiber-Reinforced Concrete (UHPFRC) materials and their applications in design of seismic retrofits. In the recent times, UHPFRC market share and its potential use have witnessed steady growth and it is expected to grow even more if the open issues relevant to the material and structural aspects are addressed successfully through the accomplishments of advanced research studies that are currently underway in many research centers. Undoubtedly, the tensile behavior is one of the most attractive properties of this material but is equally challenging to determine. In the present work, a simple method for estimation of the tensile behavior (particularly stress-strain corresponding to cracking and ultimate points) was developed through a layer-based inverse analysis approach which was compared and validated using results from SIA (2052) inverse analysis method and direct tension tests. In addition, a different approach was developed to determine the tensile behavior using Forward Analysis design charts that were derived for this purpose in the present thesis. The thesis contains two stages of experimental work as well as extensive analytical simulations. The first stage of the experimental program included mechanical testing of compression, tension, flexural and splitting tensile specimens to establish the material identity of the proprietary UHPFRC mix used in this study. Results from this study were used to validate and compare the analytical response obtained from the proposed inverse analysis and forward analysis methods for the tensile behavior of UHPFRC. The next stage of the experimental program carried out was focused on determining the tension stiffening property of UHPFRC using un-corroded and artificially corroded reinforcement bars. Three different material castings were considered, to study different casting orientations and fiber percentage by volume in the material mix. In addition, a Finite Element Model was developed for analyzing the tension stiffening behavior of UHPFRC using two different modeling techniques. A unique 3-D rebar model explicitly included the geometry of 15M reinforcement bars along with its ribs embedded in concrete. The second modeling option considered a 1-D truss model for the bar, and bond springs over the bar length. Both the finite element models developed in this study were able to predict the experimental behavior with adequate convergence, although it was found in the course of the study that the effect of fiber orientation is not properly accounted for in the isotropic models till now for

UHPFRC. A different approach would be called for, that would allow for orthotropic tension properties in the constitutive model, where the user would be able to select the fiber effectiveness along the principal axes of the model, so as to adjust the respective hardening characteristics.

Seismic provisions for the application of UHPFRC in a bridge pier jacketing retrofit were also formulated in the context of performance-based seismic design framework of CSA S6 (2019). Design and analytical stress-strain models for UHPFRC in compression were proposed and the confinement effect imparted by the fiber reinforcement was explicitly accounted for in the improved compression strain capacity. Usable strain limits for milestone points corresponding to compression behavior were presented which were consistent with the experimental dataset from the literature. The proposed compression model was compared with other two relevant models for UHPFRC and a comparative numerical investigation of the behavior of UHPFRC jacketing in pier retrofit was performed. Based on this study, the following conclusions are drawn:

8.2 Conclusions

8.2.1 Mechanical Properties of UHPFRC

The UHPFRC mixes used in this research satisfactorily met the general requirements recommended by Annex U of CSA A23.1 (2019). Cylinder average compressive strength results for all the mixes were found to be well above 120 MPa. The least compressive strength observed was equal to 165 MPa for Mix TSO1 which comprised 1% steel fibers by volume as opposed to 2% in all other mixes. The average compressive strength for UHPFRC mixes containing 2% steel fibers was about 6% higher than that of the 1% fiber-ratio mix. Tensile strength for Mix DE2 estimated from direct tension tests was also found to be exceeding the minimum requirement laid by the Annex U. One-way cast tensile specimens possessed higher tensile strength than randomly cast ones, and prismatic tension specimens were found to be more consistent in performance than I-shaped specimens owing to the simpler gripping mechanism in the prism case. Most of the direct tension specimens were successfully tested to form a critical failure plane in the central gauge region, achieved by strengthening the end zones with the use of longitudinal layers of CFRP. Splitting tensile strength tested for Mix DE2 was found to be about 24 MPa, whereas the tensile strength from direct tension tests was in the range of 10 MPa to 12 MPa.

Flexural performance of the UHPFRC used was measured by testing thin prisms with 50 mm depth and 100 mm width as per AFNOR recommendations. Size effect was evaluated through another set of flexural specimens with 150 mm x 100 mm cross-section. Third point bending test configuration was followed throughout this thesis. One-way cast specimens were found to possess higher flexural strength than randomly cast specimens in both cases (small and large prisms). As expected, randomly cast specimens sustained lesser deformation at peak load than one-way cast specimens in the case of large prisms, but the opposite behavior was found in the case of thin prisms. Randomly cast large prisms exhibited the most inferior flexural strength (i.e., a strong size effect influence), which could be attributed to a more random fiber orientation and a smaller fiber efficiency. In fact, comparing the strength of larger vs smaller size randomly cast specimens results in a fiber efficiency factor of 1.75. The flexural performance of various mixes was consistent overall, and the specimens displayed flexural or flexural-shear type failure mode. One-way cast specimens were more prone to flexural-shear mode of failure, probably owing to their higher flexural strength, as would happen in over-reinforced beams from conventional concrete (i.e., higher shear demand as compared to the available shear resistance).

8.2.2 Tensile Behavior of UHPFRC

Tensile stress-strain behavior of UHPFRC was determined through several analytical methods by using the results of four-point bending tests. A layer-based sectional analysis method was developed that could predict the constitutive tensile behavior of UHPFRC by calculating the load-deflection response in flexure including the post-peak region using the method of virtual displacement. This method can be applied to any size of flexural prism and may also consider the shear deformations that are often neglected. Results from the proposed inverse analysis were found to be consistent with those of direct tension tests and compared well even with the results of SIA 2052 (2016) inverse analysis method. Moreover, a direct non-iterative approach named Forward Analysis was proposed for estimation of tensile stress-strain behavior corresponding to the critical points such as cracking strength and ultimate strength. Readily usable design charts were developed for various standard prism sizes. This could be a highly useful approach especially for quick quality control of UHPFRC.

Some important findings from the analysis campaign of the tensile behavior of UHPFRC include the following: 1) the ultimate tensile stress is achieved in flexural specimens before the attainment

of peak moment in the resistance curve. For most cases, this moment was found to be in the range of 95% to 97% of the maximum moment and this was also supported by evidence from DIC. 2) Although the descending slope of the tensile constitutive stress-strain behavior affects the maximum moment achieved by flexural specimens, it does not affect the moment corresponding to the ultimate tensile stress that occurs just before the peak moment.

8.2.3 Tension Stiffening

An experimental program using three different castings was carried out to determine the tensile stiffening behavior of UHPFRC which was rarely researched for this class of material. In addition, the effect of corrosion on this property was studied by using pre-corroded rebars with an average mass loss of 12.5% obtained through accelerated corrosion technique. The specimens were further reinforced with CFRP at the ends to promote the failure plan and cracking to occur in the central gauged region. Experiments indicated very high slope of load-deformation branch (stiffness) in the initial response prior to the cracking of UHPFRC matrix. Post cracking of the UHPFRC matrix, the slope of the resistance curve gradually reduced to match the slope of the bare rebar but the extra strength provided by UHPFRC was sustained well beyond yielding of reinforcement. Tension stiffening contribution of UHPFRC was more pronounced in the case of mix with 2% fibers than the mix containing 1% fibers. The post-yielding tension stiffening behavior was obtained for specimens with a notch in the central region. Corrosion of reinforcement to a mass loss of 12.5% did affect the tension stiffening behavior of UHPFRC significantly. However, in some cases, the tension stiffening contribution was found to be reducing with increasing strain values. This behavior may have been also influenced by the weld connection between the grip rod and the main rebar. Moreover, fracture failure of the embedded rebar was achieved by using notched tension stiffening specimens that were identified by reduced UHPFRC cover at the mid height.

8.2.4 Finite Element Modeling

Detailed non-linear finite element analysis was performed using the GiD-ATENA software suite. GiD has a predefined material model for high performance fiber reinforced concrete (HPFRC) material which was utilized for the solid volume of UHPFRC with user-defined constitutive stress-strain laws in compression and tension. It is noted that the model assumes isotropic properties in tension and compression and is thus suited for randomly cast specimens. Thus, it is expected to

produce inaccurate results for one-way cast specimens. However, it was used in the absence of other alternatives. Two different types of models of the complete specimens were developed which are classified based on reinforcement model geometry as a 1-D rebar model and 3-D rebar model. The latter modeled the reinforcement as 3-D solid with explicit representation of the ribs to directly simulate the reinforcement behavior embedded in UHPFRC. Tension stiffening behavior produced by both the models correlated well with the experimental results by calibrating the input of tensile stress-strain law. The effect of bond stress-slip law was also evaluated by using two different bond behaviors and the bond model with greater stiffness and reduced slip values was found to produce a better response. Furthermore, the perfect bond condition was also used for the model as it represents best the high stiffness imparted by the longitudinal casting direction used in fabricating the specimens.

8.2.5 Stress-Strain Model in Compression

Strain capacity of unconfined UHPFRC in uniaxial compression was explored with an aim to propose the critical strain limits useful for design and analysis of seismic retrofits with UHPFRC. An experimental dataset for correlation of compression stress-strain values corresponding to critical response points was assembled in the thesis, along with other relevant details. A non-linear analytical stress-strain model was proposed with modifications to an existing model from the literature capable of predicting the uniaxial compressive behavior of UHPFRC with a calibrated parameter. An analytical expression was proposed to determine the length of the strain plateau by explicitly accounting for the confinement effect imparted by the fiber content of the material. Performance design strain limits proposed for peak stress and 75% residual stress were equal to 3.5 mm/m and 4.5 mm/m, respectively, which correspond to about 85% probability of exceedance with reference to the dataset established. Furthermore, a strain limit of 5.0 mm/m was proposed for 50% residual stress in the post-peak region. The proposed model was compared with other two existing models for UHPFRC and was found to correlate with the experimental results more accurately than others, while the mathematical form of the model showed in a more transparent manner the effect of the important parameters.

8.2.6 Jacketing Retrofit of Damaged Bridge Piers

A comprehensive proposal for seismic provisions for bridge pier retrofitting by jacketing with a thin layer of UHPFRC was formulated in the context of performance-based design. Tension and

compression stress-strain models that are required for design and analysis of structural elements jacketed with UHPFRC were presented. UHPFRC jacketing as a retrofitting method for columns and piers was found to significantly enhance both strength and deformation capacity of the retrofitted member. A detailed example of a bridge pier jacketed with a 50mm thick layer of two types of UHPFRC material was considered to illustrate the implementation of the proposed methodology. Numerical analysis results demonstrated that the flexural moment capacity of the normal reinforced concrete column was improved by 58% and 44%, for UHPFRC jackets with corresponding tensile strengths of 11 MPa and 6 MPa, respectively. In addition, moment-curvature response of the jacketed columns was found to display improved ductile plateau owing to the tensile strain ductility provided by UHPFRC material, and the curvature at peak moment was 90% and 105% higher than that of the unconfined section for the above two cases, respectively. Hence, thin jackets with UHPFRC material can be effectively used as seismic retrofit solution for deficit or damaged structural members.

8.3 Challenges and Future Work

The research work presented in this thesis was involved with several challenges at both experimental and analytical levels. The most concerning issues noted during this work and recommendations for future work are listed below.

- Inverse analysis methods for UHPFRC reviewed in this work were cumbersome and difficult to implement, particularly the stepwise iterative approach proposed by the AFNOR Standard (NF P18-470, 2016). The practical issues associated with the AFNOR method was lack of convergence, mainly near and after the onset of cracking. Lack of an easily implemented inverse analysis will eventually slow down the quality control chain for this material. Despite of programing the algorithm required to solve the problem in multiple ways, the method failed to achieve convergence in post cracking response of UHPFRC. More details about this method are presented in Appendix of the thesis. An effective and practicable test method in direct tension could eliminate the need of cumbersome inverse analysis procedures and estimate tensile behavior of UHFRC in the best viable manner.
- Direct tension testing of UHPFRC is not an easy task and there is a need for provisions regarding standardized and consistent testing method to be established in the relevant

Canadian standard, Annex U of CSA A23.1 or Annex 8.1 of CSA S6. AASHTO standard on the uniaxial tensile response of UHPC (AASHTO T 397, 2022) could be referred/recommended for this purpose. This standard recommends that a direct tension test be used in material characterization. Required specimens are 50 mm x 50 mm x 430 mm prisms installed with aluminum transfer plates at the ends in special gripping devices, as shown in Figure A-5. Moreover, a parallel ring deformation measuring device (Figure A-6) equipped with four LVDTs mounted across a gauge length of 100 mm in the central region is recommended by this standard to measure stress-strain response of UHPFRC in tension.

- Implementation of Digital Image Correlation (DIC) technique for flexural specimens was hampered due to- (a) arrangement constraints within the machine that limited the possibility of having normal oriented surface for capturing accurate images, (b) interference of the rather important LVDTs that measure the midspan deflection with more precision and accuracy. Moreover, at least two high-resolution digital cameras are recommended for capturing images corresponding to opposite surfaces to achieve better results.
- Uniaxial compression test for measuring stress-strain response of UHPFRC was possible with the use of new compression machine, 'Controls Automax'. However, the post-peak response was still not captured comprehensively which is attributed to insufficient stiffness in the current test setup.
- An effective test method is yet to be developed to measure the tension stiffening response of UHPFRC beyond yielding of reinforcement and up to larger strains (near fracture) with accuracy and consistency. This could have been possible with the use of high strength steel couplers to connect two reinforcement bars of different diameter; however, this was not only cost-ineffective but also difficult to source. Specimens with variable clear cover and fiber casting orientation could be explored in future to study the influence of rebar on fiber arrangement that has a significant impact on the tensile behavior of UHPFRC, which in turn affects the tension stiffening behavior. Pertinent constitutive models that account for the orthotropy behavior of the material imparted by the one directional casting of fibers is required for successful correlation of tests where casting from one end has been used. The current isotropic models are appropriate for random casting only.

- Artificial corrosion of a reinforcement bar could take long period to achieve high amount of mass loss. This could be achieved with longer wet cycles of accelerated corrosion as long as a rebar is not already embedded in concrete.
- Although the finite element model with 3-D rebar was able to accurately predict the tension stiffening behavior, it was inhibited from predicting the complete response due to lack of full stress-strain model for 3-D reinforcement material. In case of 1-D rebar model, the effect of bond-slip law of UHPFRC on its tension stiffening behavior was difficult to tackle due to the presence of joint between the two reinforcing bars, and one-directional orientation of the fibers which caused significant bond stiffness longitudinally and reduced the slip capacity on account of the absence of transverse fibers. This led to better approximation of the perfect bond assumption as compared to bond-slip laws obtained from different directions of casting. A significantly more broad experimental campaign would be needed to explore and quantify the effect of orthotropy induced by one-directional fiber alignment.
- Experimental stress-strain dataset corresponding to UHPFRC compressive behavior may be continually updated as more test data becomes available with time. Similar databases could be established for the tensile and flexural performances of UHPFRC. Analytical tools for deriving meaningful interpretations from such databases could be explored as numerous parameters are involved in case of UHPFRC material.

References

AASHTO T 397-22 (2022). Standard Method of Test for Uniaxial Tensile Response of Ultra-High Performance Concrete. *American Association of State Highway and Transportation Officials*.

ACI 222R-19. (2019). Guide to Protection of Reinforcing Steel in Concrete Against Corrosion. *American Concrete Institute (ACI) Committee 222*, 1–65.

ACI 544.8R-16. (2016). Report on Indirect Method to Obtain Stress-Strain Response of Fiber-Reinforced Concrete (FRC). *American Concrete Institute (ACI) Committee 544*.

AFGC-SETRA. (2002). *(Association Francaise de Genie Civil-Service d'etudes Techniques des Routes et Autoroutes) Ultra-High-Performance Fibre-Reinforced Concretes, Recommendations provisoires-interim recommendations*.

AFNOR NF EN 13670/CN. (2013). *Exécution des Structures en Béton-Complément National à la Norme NF EN 1367.*

AFNOR NF P18-470. (2016). *French Standard: Concrete — Ultra-high performance fibre-reinforced concrete — Specifications, performance, production and conformity*.

AFNOR NF P18-710. (2016). *French Standard: National addition to Eurocode 2 — Design of concrete structures: specific rules for Ultra-High Performance Fibre-Reinforced Concrete (UHPFRC).*

Almusallam, A. A. (2001). Effect of degree of corrosion on the properties of reinforcing steel bars. *Construction and Building Materials*, *15*(8), 361–368. https://doi.org/10.1016/S0950-0618(01)00009-5

Alsalman, A., Dang, C. N., Prinz, G. S., & Hale, W. M. (2017). Evaluation of modulus of elasticity of ultra-high performance concrete. *Construction and Building Materials*, *153*, 918–928. https://doi.org/10.1016/j.conbuildmat.2017.07.158

Apostolopoulos, C. A. (2007). Mechanical behavior of corroded reinforcing steel bars S500s tempcore under low cycle fatigue. *Construction and Building Materials*, *21*(7), 1447–1456. https://doi.org/10.1016/j.conbuildmat.2006.07.008

ASTM C1609/C1609M-19. (2019). Standard Test Method for Flexural Performance of Fiber-Reinforced Concrete (Using Beam With Third-Point Loading). *American Society for Testing and Materials*.

ASTM C1856/C1856M-17. (2017). Fabricating and Testing Specimens of Ultra-High-Performance Concrete. *American Society for Testing and Materials*.

ASTM C469/C469M-14. (2014). Standard Test Method for Static Modulus of Elasticity and Poisson's Ratio of Concrete in Compression. *ASTM International, West Conshohocken, PA*. https://doi.org/https://doi.org/10.1520/C0469_C0469M-14

ATENA Program Documentation, (2021). Part 1: *Theory*; by Červenka, V., Jendele, L., & Červenka, J. Prague, Czech Republic, 1–360.

ATENA Program Documentation, (2010). Part 3-1: *Example Manual, ATENA Engineering*; by

Kabele, P., Červenka, V., & Červenka, J. Prague, Czech Republic, 1–90.

ATENA Program Documentation, (2021). Part 8: *User's Manual for ATENA-GiD interface; by* Červenka, V., Červenka, J., Janda, Z. & Pryl, D. Prague, Czech Republic, 1–153.

ATENA Program Documentation, (2020). Part 11: *Troubleshooting Manual*; by Pryl, D. & Červenka, J. Prague, Czech Republic, 1–69.

ATENA Program Documentation, (2021). Part 12: *User's Manual for ATENA Studio*; by Beneš, S., Mikolášková, J. & Altman, T. Prague, Czech Republic, 1–83.

Azmee, N. M., & Shafiq, N. (2018). Ultra-high performance concrete: From fundamental to applications. *Case Studies in Construction Materials*, *9*. https://doi.org/10.1016/j.cscm.2018.e00197

Baby, F., Graybeal, B., Marchand, P., & Toutlemonde, F. (2013). UHPFRC tensile behavior characterization: Inverse analysis of four-point bending test results. *Materials and Structures/Materiaux et Constructions*, *46*(8), 1337–1354. https://doi.org/10.1617/s11527-012-9977-0

Bian, C., & Wang, J. Y. (2019). Mechanical and damage mechanisms of reinforced ultra high performance concrete under tensile loading. *Construction and Building Materials*, *226*, 259–279. https://doi.org/10.1016/j.conbuildmat.2019.07.162

Blaber, J.; Antoniou, A. (2017). *Ncorr Instruction Manual*. *V1.2.2*.

Blaber, J., Adair, B., & Antoniou, A. (2015). Ncorr: Open-Source 2D Digital Image Correlation Matlab Software. *Experimental Mechanics*, *55*(6), 1105–1122. https://doi.org/10.1007/s11340-015-0009-1

Blais, P. Y., & Couture, M. (1999). Precast, prestressed pedestrian bridge - world's first Reactive Powder Concrete structure. *PCI Journal*, *44*(5), 60–71. https://doi.org/10.15554/pcij.09011999.60.71

Bonneau et al. (1996). *Reactive Poweder Concretes: From Theory to Practice*.

Brühwiler, E. (2020). UHPFRC technology to enhance the performance of existing concrete bridges. *Structure and Infrastructure Engineering*, *16*(1), 94–105. https://doi.org/10.1080/15732479.2019.1605395

Červenka Consulting. (2007). ATENA Program. *https://www.cervenka.cz/products/atena/* Prague, Czech Republic.

Chan, Y; Li, V. C. (1997). Effects of Transition Zone Densification On Fiber/Cement Paste Bond Strength Improvement. *Advanced Cement Based Materials*, *5*(1), 8–17. https://doi.org/10.1016/s1065-7355(96)00077-6

Chanvillard, G. (2000). Characterisation of fibre reinforced concrete mechanical properties: a review. *In Fifth International RILEM Symposium on Fibre-Reinforced Concrete (FRC). RILEM Publications SARL.*, 29–50.

Corvez, D., & Masson, B. (2013). Uhpfrc Solutions for the Retrofit of Nuclear Reactor Containment Walls. *RILEM-Fib-AFGC Int. Symposium on Ultra-High Performance Fibre-*

Reinforced Concrete, UHPFRC 2013, *1*, 147–156.

CSA A23.1:19, Annex U. (2019). 'Ultra-High-Performance Concrete, Annex-U'. *Canadian Standards Association*.

CSA S6:19, Annex 8.1. (2019). Standard: Canadian Highway Bridge Design Code. In *Canadian Standards Association*.

Dagenais, M.A., Massicotte, B., & Boucher-Proulx, G. (2018). Seismic Retrofitting of Rectangular Bridge Piers with Deficient Lap Splices Using Ultrahigh-Performance Fiber-Reinforced Concrete. *Journal of Bridge Engineering*, *23*(2), 1–13. https://doi.org/10.1061/(asce)be.1943-5592.0001173

de Larrard, F., & Sedran, T. (1994). Optimization of ultra-high-performance concrete by the use of a packing model. *Cement and Concrete Research*, *24*(6), 997–1009. https://doi.org/10.1016/0008-8846(94)90022-1

Del Zoppo, M., Di Ludovico, M., Balsamo, A., & Prota, A. (2018). Comparative analysis of existing RC columns jacketed with CFRP or FRCC. *Polymers*, *10*(4), 1–20. https://doi.org/10.3390/polym10040361

Deng, M., Zhang, Y., & Li, Q. (2018). Shear strengthening of RC short columns with ECC jacket: Cyclic behavior tests. *Engineering Structures*, *160* (November 2017), 535–545. https://doi.org/10.1016/j.engstruct.2018.01.061

Doiron, G. (2016). 'Pier Repair/Retrofit Using Uhpc Examples Of Completed Projects In North America' - Ductal ® , Lafarge North America Inc., Canada. *First International Interactive Symposium on UHPC*.

Du, Y. G., Clark, L. A., & Chan, A. H. C. (2005). Residual capacity of corroded reinforcing bars. *Magazine of Concrete Research*, *57*(3), 135–147. https://doi.org/10.1680/macr.2005.57.3.135

El-Joukhadar, N., Dameh, F., & Pantazopoulou, S. (2023). Seismic Modelling of Corroded Reinforced Concrete Columns. *Engineering Structures*, *275*, 115251.

El-Joukhadar, N. H. (2022). Seismic Assessment , Repair and Retrofit of Existing Corroded Structures Using UHPC Jacketing. *PhD. Dissertation* (Issue June).

El-Joukhadar, N., & Pantazopoulou, S. J. (2021). Effectiveness of UHPFRC cover in delaying bar corrosion. *Construction and Building Materials*, *269*, 121288. https://doi.org/10.1016/j.conbuildmat.2020.121288

El Helou, R. G. (2016). *Multiscale Computational Framework for Analysis and Design of Ultra-High Performance Concrete Structural Components and Systems*.

Farzad, M., Shafieifar, M., & Azizinamini, A. (2019). Retrofitting of Bridge Columns Using UHPC. *Journal of Bridge Engineering*, *24*(12), 1–13. https://doi.org/10.1061/(asce)be.1943-5592.0001497

fib Bulletin 40. (2007). *FRP reinforcement in RC structures* (Issue ISBN 978-2-88394-080-2). fib. The International Federation for Structural Concrete.

https://doi.org/10.35789/fib.BULL.0040

Georgiou, A. V., & Pantazopoulou, S. J. (2016). Effect of fiber length and surface characteristics on the mechanical properties of cementitious composites. *Construction and Building Materials*, *125*, 1216–1228. https://doi.org/10.1016/j.conbuildmat.2016.09.009

Grand View Research (GVR). (2017). *Ultra-High Performance Concrete (UHPC) Market Analysis By Product, By Application, And Segment Forecasts 2014-2025*.

Graybeal, B. A. (2005). Characterization Of The Behavior Of Ultra-High Performance Concrete. *PhD Dissertation, Univ. of Maryland, College Park*.

Graybeal, B. A. (2006). Material Property Characterization of Ultra-High Performance Concrete. *FHWA-HRT-06-103, U.S. Department of TransportationU.S. Department of Transportation*, *August*.

Graybeal, B. A., & Baby, F. (2013). Development of direct tension test method for ultra-high-performance fiber-reinforced concrete. *ACI Materials Journal*, *110*(2), 177–186. https://doi.org/10.14359/51685532

Graybeal, B. A., & Baby, F. (2019). Tension Testing of Ultra-High Performance Concrete FWHA-HRT-17-053. *FHWA, U.S. Department of Transportation United States. Federal Highway Administration. Office of Infrastructure Research and Development., (No. FHWA*-(February), 210.

Graybeal, B., & Hartmann, J. l. (2003). Strength and Durability of Ultra-High Performance Concrete Materials and Structures. *2003 Concrete Bridge Conference*, *December*, 1–20.

Habel, K., Kennedy, D., & Schaper, C. (2017). Seismic upgrading of the mission bridge. *Structural Engineering International*, *27*(1), 25–28. https://doi.org/10.2749/101686617X14676303588634

Hassan, A. M. T., Jones, S. W., & Mahmud, G. H. (2012). Experimental test methods to determine the uniaxial tensile and compressive behaviour of Ultra High Performance Fibre Reinforced Concrete(UHPFRC). *Construction and Building Materials*, *37*, 874–882. https://doi.org/10.1016/j.conbuildmat.2012.04.030

Hong, S.-G., Lee, J.-H., Choi, Y., & Gu, I.-Y. (2021). Seismic Strengthening of Concrete Columns by Ultrahigh-Performance Fiber-Reinforced Concrete Jacketing. *Journal of Structural Engineering*, *147*(10), 1–16. https://doi.org/10.1061/(asce)st.1943-541x.0003111

Huang, H., Gao, X., & Teng, L. (2021). Fiber alignment and its effect on mechanical properties of UHPC: An overview. *Construction and Building Materials*, *296*, 123741. https://doi.org/10.1016/j.conbuildmat.2021.123741

Huang, Y., Lee, M.-G., Kan, Y.-C., Wang, W.-C., Wang, Y.-C., & Pan, W.-B. (2022). Reinforced concrete beams retrofitted with UHPC or CFRP. *Case Studies in Construction Materials*, *17*(June), e01507. https://doi.org/10.1016/j.cscm.2022.e01507

Husain, S. A. B. (2021). Characterization of UHPFRC Materials for Bridge Construction: An Opportunity to Offset the Need for Prestressing in Bridge Decks. In *MS Thesis, York Univ.* (Issue December).

Jansson, A., Flansbjer, M., Löfgren, I., Lundgren, K., & Gylltoft, K. (2012). Experimental investigation of surface crack initiation, propagation and tension stiffening in self-compacting steel-fibre-reinforced concrete. *Materials and Structures/Materiaux et Constructions*, *45*(8), 1127–1143. https://doi.org/10.1617/s11527-012-9821-6

Joh, C. et al. (2008). Punching Shear Strength Estimation of UHPC Slabs. *Proceedings of the Second International Symposium on Ultra High Performance Concrete*, *Kassel*, *Ge*, 719–726.

Jungwirth, Jorg; Muttoni, A. (2004). Structural behavior of tension members in UHPC. *In International Symposium on Ultra High Performance Concrete*, 1–12.

Kanakubo, T. (2006). Tensile characteristics evaluation method for ductile fiber-reinforced cementitious composites. *Journal of Advanced Concrete Technology*, *4*(1), 3–17. https://doi.org/10.3151/jact.4.3

Kang, S. B., Tan, K. H., Zhou, X. H., & Yang, B. (2017). Influence of reinforcement ratio on tension stiffening of reinforced engineered cementitious composites. *Engineering Structures*, *141*, 251–262. https://doi.org/10.1016/j.engstruct.2017.03.029

Lárusson, L., Fischer, G., & Jönsson, J. (2012). Mechanical interaction between concrete and structural reinforcement in the tension stiffening process. *RILEM Bookseries*, *2*, 247–254. https://doi.org/10.1007/978-94-007-2436-5_30

Li, X., Wang, J., Bao, Y., & Chen, G. (2017). Cyclic behavior of damaged reinforced concrete columns repaired with high-performance fiber-reinforced cementitious composite. *Engineering Structures*, *136*, 26–35. https://doi.org/10.1016/j.engstruct.2017.01.015

López, J. Á. (2017). Characterisation of the Tensile Behaviour of Uhpfrc By Means of Four-Point Bending Tests. In *PhD. Dissertation* (Issue March). https://riunet.upv.es/handle/10251/79740

López, J. Á., Serna, P., Navarro-Gregori, J., & Coll, H. (2016). A simplified five-point inverse analysis method to determine the tensile properties of UHPFRC from unnotched four-point bending tests. *Composites Part B: Engineering*, *91*, 189–204. https://doi.org/10.1016/j.compositesb.2016.01.026

Ma, J. et al. (2004). "Comparative Investigations on Ultra-High Performance Concrete With and Without Coarse Aggregates,." *Proceedings of the International Symposium on Ultra High Performance Concrete, Ed., Schmidt, M., Fehling, E., and Geisenhanslüke, C., Kassel University Press, Kassel, Germany*, pp 205-212.

Maca, P., Zatloukal, J., & Konvalinka, P. (2012). Development of Ultra High Performance Fiber Reinforced Concrete mixture. *ISBEIA 2012 - IEEE Symposium on Business, Engineering and Industrial Applications*, 861–866. https://doi.org/10.1109/ISBEIA.2012.6423015

Makita, T., & Brühwiler, E. (2014). Tensile fatigue behaviour of Ultra-High Performance Fibre Reinforced Concrete combined with steel rebars (R-UHPFRC). *International Journal of Fatigue*, *59*, 145–152. https://doi.org/10.1016/j.ijfatigue.2013.09.004

Martín-Pérez, B. (1999). Service Life Modelling of R.C. Highway Structures Exposed to Chlorides. *PhD Dissertation*. https://medium.com/@arifwicaksanaa/pengertian-use-case-

a7e576e1b6bf

Mobasher, B; Yao, Y; Soranakom, C; Dev, V. (2015). *A Spreadsheet-Based Inverse Analysis Procedure for Flexural Specimens – Strain Softening/Hardening Behavior*.

Mobasher, B., Bakhshi, M., & Barsby, C. (2014). Backcalculation of residual tensile strength of regular and high performance fiber reinforced concrete from flexural tests. *Construction and Building Materials*, *70*, 243–253. https://doi.org/10.1016/j.conbuildmat.2014.07.037

Moreno, D. M., Trono, W., Jen, G., Ostertag, C., & Billington, S. L. (2012). Tension-stiffening in reinforced high performance fiber-reinforced cement-based composites under direct tension. *RILEM Bookseries*, *2*(June), 263–270. https://doi.org/10.1007/978-94-007-2436-5_32

Moreno, D. M., Trono, W., Jen, G., Ostertag, C., & Billington, S. L. (2014). Tension stiffening in reinforced high performance fiber reinforced cement-based composites. *Cement and Concrete Composites*, *50*, 36–46. https://doi.org/10.1016/j.cemconcomp.2014.03.004

Naaman, A. E., & Reinhardt, H. W. (2006). Proposed classification of HPFRC composites based on their tensile response. *Materials and Structures/Materiaux et Constructions*, *39*(5), 547–555. https://doi.org/10.1617/s11527-006-9103-2

NACE International. (2016). International Measures of Prevention, Application, and Economics of Corrosion Technologies Study. *IMPACT Study (Http://Impact.Nace.Org/)*, *February*, 3.

Naeimi, N. (2020a). Experimental Compressive Behavior and Numerical Modeling of Unconfined and Confined Ultra-High Performance Concrete. *University of Nevada*, *August*.

Naeimi, N. (2020b). Experimental Compressive Behavior and Numerical Modeling of Unconfined and Confined Ultra-High Performance Concrete. *PhD Dissertation, Univ. of Nevada, Reno*, *August*.

Naeimi, N., & Moustafa, M. (2019). Uniaxial Compression Behavior of Ultra- High Performance Concrete Confined by Steel Spirals. *2nd Int. Symposium on Ultra-High Performance Concrete, Albany, NY*, *1*, 1–8.

Naeimi, N., & Moustafa, M. A. (2021a). Analytical Stress – Strain model for steel spirals-confined UHPC. *Composites Part C: Open Access*, *5*(February), 100130. https://doi.org/10.1016/j.jcomc.2021.100130

Naeimi, N., & Moustafa, M. A. (2021b). Compressive behavior and stress–strain relationships of confined and unconfined UHPC. *Construction and Building Materials*, *272*, 121844. https://doi.org/10.1016/j.conbuildmat.2020.121844

Ostergaard, L., Walter, R., & Olesen, J. F. (2005). Method for determination of tensile properties of engineered cementitious composites (ECC),. *Construction Materials : Proceedings of ConMat'05 and Mindess Symposium*, *January*, 74.

Palsson, R., & Mirza, M. S. (2002). Mechanical response of corroded steel reinforcement of abandoned concrete bridge. *ACI Structural Journal*, *99*(2), 157–162. https://doi.org/10.14359/11538

Pantazopoulou, S.J.; Papoulia, K. D. (2001). Modeling Cover-Cracking due to Reinforcement

Corrosion in RC Structures. *Journal of Engineering Mechanics*, 342–351.

Pantazopoulou, S. J. et al. (2017). The performance of corroded lap splices in reinforced concrete beams. *Corrosion Reviews*, *37*(1), 31–44. https://doi.org/10.1515/corrrev-2017-0086

Pantazopoulou, S. J., Palermo, D., Yang, Y., Eshghi, N., Saikali, R., & Chasioti, S. (2019). *TechnicalReport: Development of Specifications for Determining the Tensile Behaviour of UHPFRC Materials for Structural Applications in Highway Bridges*.

Pantazopoulou, S. J., Tastani, S. P., Thermou, G. E., Triantafillou, T., Monti, G., Bournas, D., & Guadagnini, M. (2016). Background to the European seismic design provisions for retrofitting RC elements using FRP materials. *Structural Concrete*, *17*(2), 194–219. https://doi.org/10.1002/suco.201500102

Prisco, M. Di, Plizzari, G., & Vandewalle, L. (2009). Fibre reinforced concrete: New design perspectives. *Materials and Structures/Materiaux et Constructions*, *42*(9), 1261–1281. https://doi.org/10.1617/s11527-009-9529-4

Qian, S., & Li, V. C. (2007). Simplified inverse method for determining the tensile properties of strain hardening cementitious composites (SHCC). *Journal of Advanced Concrete Technology*, *6*(2), 353–363. https://doi.org/10.3151/jact.6.353

Rabehi, B., Ghernouti, Y., Li, A., & Boumchedda, K. (2014). Comparative behavior under compression of concrete columns repaired by fiber reinforced polymer (FRP) jacketing and ultra high-performance fiber reinforced concrete (UHPFRC). *Journal of Adhesion Science and Technology*, *28*, 2327–2346. https://doi.org/10.1080/01694243.2014.966885

Ralli, Z. G., (2022) Development, Material And Structural Performance Of Tension Hardening Fiber Reinforced Geopolymer Concrete (THFRGC). *Phd Dissertation, York Univ. (October 2022).*

Ralli, Z. G., Genikomsou, A. S., & Pantazopoulou, S. J. (2021). Comparative evaluation of nonlinear FEA inverse analysis of tensile properties of UHPFRC. *Fib Symposium*, *2021-June*(June), 563–573.

Ramachandra Murthy, A., Karihaloo, B. L., Vindhya Rani, P., & Shanmuga Priya, D. (2018). Fatigue behaviour of damaged RC beams strengthened with ultra high performance fibre reinforced concrete. *International Journal of Fatigue*, *116*(December 2017), 659–668. https://doi.org/https://doi.org/10.1016/j.ijfatigue.2018.06.046

Reggia, A., Morbi, A., & Plizzari, G. A. (2020). Experimental study of a reinforced concrete bridge pier strengthened with HPFRC jacketing. *Engineering Structures*, *210*(January), 110355. https://doi.org/10.1016/j.engstruct.2020.110355

Rigaud, S., Chanvillard, G., & Chen, J. (2012). Characterization of Bending and Tensile Behavior of Ultra-High Performance Concrete Containing Glass Fibers. In *RILEM Bookseries* (Vol. 2, pp. 373–380). https://doi.org/10.1007/978-94-007-2436-5_45

Russell, Henry G.; Graybeal, B. A. (2013). Ultra-High Performance Concrete: A State-Of-The-Art Report for The Bridge Community. *FHWA-HRT-13-060, U.S. Department of TransportationU.S. Department of Transportation, FHWA-HRT-1*(June).

Schmidt, M., Fehling, E., Bornemann, R., Bunje, K., & Teichmann, T. (2003). Ultra-high performance concrete: Perspective for the precast concrete industry. *Concrete Pre-Casting Plant Technology, 69(3)*, 16–29.

SIA 2052. (2016). Standard: Ultra-High Performance Fibre Reinforced Cement-based composites (UHPFRC) (English Translation). *Lausanne, MCS-EPFL, Zurich, Switzerland, April*.

Simon, A. (2009). "Les Nouvelles Recommandations AFGC sur les BFUP CHAPITRE I—Comportement et Caractéristiques Mécaniques des BFUP", (Updated AFGC Recommendations: Chapter 1 Materials). *Proceedings of the International Workshop on Ultra High Performance Fibre Reinforced Concrete—Designing and Building with UHPFRC: State of the Art Development,*.

Sohail, M. G., Wang, B., Jain, A., Kahraman, R., Ozerkan, N. G., Gencturk, B., Dawood, M., & Belarbi, A. (2018). Advancements in Concrete Mix Designs: High-Performance and Ultrahigh-Performance Concretes from 1970 to 2016. *Journal of Materials in Civil Engineering*, *30*(3). https://doi.org/10.1061/(asce)mt.1943-5533.0002144

Soranakom, Chote; Mobasher, B. (2007). Closed-Form Moment-Curvature Expressions for Homogenized Fiber- Reinforced Concrete. *ACI Materials Journal*, *10*(1), 351–359.

Soranakom, C., & Mobasher, B. (2008). Correlation of tensile and flexural responses of strain softening and strain hardening cement composites. *Cement and Concrete Composites*, *30*(6), 465–477. https://doi.org/10.1016/j.cemconcomp.2008.01.007

Tailhan, J. L., Rossi, P., & Parant, E. (2004). Inverse numerical approach to determine the uniaxial tensile behaviour of a stress hardening cement composite from its bending behaviour. *Fiber Reinforced Concretes—BEFIB 2004, Proceedings of the 6th International RILEM Symposium, M. Di Prisco, R. Felicetti, and GA Plizzari, Eds, September*, 913–922.

Thermou, G. E., & Elnashai, A. S. (2006). Seismic retrofit schemes for RC structures and local-global consequences. *Progress in Structural Engineering and Materials*, *8*(1), 1–15. https://doi.org/10.1002/pse.208

Tong, T., Yuan, S., Zhuo, W., He, Z., & Liu, Z. (2019). Seismic retrofitting of rectangular bridge piers using ultra-high performance fiber reinforced concrete jackets. *Composite Structures*, *228*(July), 111367. https://doi.org/10.1016/j.compstruct.2019.111367

Tsiotsias, K.; Pantazopoulou, S. J. (2022). Cyclic Testing of Concrete Cores Under Confinement with UHPFRC Jackets. *12th Ntnl. Conf. on Earthquake Engineering (12NCEE), Salt Lake City, Utah*.

Tsiotsias, K. (2023). Cyclic Performance of RC Columns Retrofitted with UHPFRC. *PhD Dissertation, York Univ., (Degree to Be Conferred in 2023)*.

Wang, Y. Z., Wang, Y. B., Zhao, Y. Z., Li, G. Q., Lyu, Y. F., & Li, H. (2020). Experimental study on ultra-high performance concrete under triaxial compression. *Construction and Building Materials*, *263*, 1–11. https://doi.org/10.1016/j.conbuildmat.2020.120225

Wille, K., El-Tawil, S., & Naaman, A. E. (2014). Properties of strain hardening ultra high performance fiber reinforced concrete (UHP-FRC) under direct tensile loading. *Cement and*

Concrete Composites, *48*, 53–66. https://doi.org/10.1016/j.cemconcomp.2013.12.015

Wille, K., Kim, D. J., & Naaman, A. E. (2011). Strain-hardening UHP-FRC with low fiber contents. *Materials and Structures/Materiaux et Constructions*, *44*(3), 583–598. https://doi.org/10.1617/s11527-010-9650-4

Wu, Z., Shi, C., He, W., & Wu, L. (2016). Effects of steel fiber content and shape on mechanical properties of ultra high performance concrete. *Construction and Building Materials*, *103*, 8–14. https://doi.org/10.1016/j.conbuildmat.2015.11.028

Xu, W., Ma, B., Duan, X., & Li, J. (2021). Experimental investigation of seismic behavior of UHPC connection between precast columns and footings in bridges. *Engineering Structures*, *239*(March), 112344. https://doi.org/10.1016/j.engstruct.2021.112344

Yang, I. H., Joh, C., & Kim, B. S. (2010). Structural behavior of ultra high performance concrete beams subjected to bending. *Engineering Structures*, *32*(11), 3478–3487. https://doi.org/10.1016/j.engstruct.2010.07.017

Yang, Y. (2019). Tensile behaviour of ultra-high-performance steel fiber reinforced concrete. (*MS Thesis, York Univ.)*.

Yang, Y., Ismail, M., Pantazopoulou, S. J., & Palermo, D. (2021). Tensile behaviour of ultra-high-performance steel fiber reinforced concrete. *Canadian Journal of Civil Engineering*, *48*(11), 1409–1421. https://doi.org/10.1139/cjce-2019-0592

Ye, Yinghua; Hu, Song; Daio, Bo; Yang, Songlin; Liu, Z. (2012). *Mechanical behavior of ultra-high performance concrete reinforced with hybrid different shapes of steel fiber*. 2433–2442.

Yoo, D. Y., Banthia, N., & Yoon, Y. S. (2016). Predicting the flexural behavior of ultra-high-performance fiber-reinforced concrete. *Cement and Concrete Composites*, *74*, 71–87. https://doi.org/10.1016/j.cemconcomp.2016.09.005

Yoo, D. Y., & Yoon, Y. S. (2015). Structural performance of ultra-high-performance concrete beams with different steel fibers. *Engineering Structures*, *102*, 409–423. https://doi.org/10.1016/j.engstruct.2015.08.029

Yoo, D. Y., & Yoon, Y. S. (2016). A Review on Structural Behavior, Design, and Application of Ultra-High-Performance Fiber-Reinforced Concrete. *International Journal of Concrete Structures and Materials*, *10*(2), 125–142. https://doi.org/10.1007/s40069-016-0143-x

Yuan, W., Wang, X., Guo, A., Li, C., Dong, Z., & Wu, X. (2022). Cyclic performance of RC bridge piers retrofitted with UHPC jackets: Experimental investigation. *Engineering Structures*, *259*(August 2021), 114139. https://doi.org/10.1016/j.engstruct.2022.114139

Zhou, M., Lu, W., Song, J., & Lee, G. C. (2018). Application of Ultra-High Performance Concrete in bridge engineering. *Construction and Building Materials*, *186*, 1256–1267. https://doi.org/10.1016/j.conbuildmat.2018.08.036

Zhu, Y., Zhang, Y., Hussein, H. H., & Qu, S. (2021). Existing Inverse Analysis Approaches for Tensile Stress–Strain Relationship of UHPC with Treated Steel Fibers. Journal of Materials in Civil Engineering, 33(6), 1–13. https://doi.org/10.1061/(asce)mt.1943-5533.0003731

Appendix A: Supplementary Details on Various Experiments

A.1 Database of Uniaxial Compression Stress-Strain Tests on UHPFRC

Table A- 1: Database of UHPFRC tests on compressive stress-strain at peak and 50% residual stress

Source	L_f/d_f (mm)	V_f (%)	f'_c (MPa)	ε_{co} (mm/m)	$\varepsilon_{cu,50\%}$ (mm/m)
N Naeimi (2021)	13/0.2	2.0%	230	6.00	-
			200	**4.80**	**-**
	13/0.2	0.0%	**166**	**4.10**	**6.50**
		2.0%	**179**	**4.50**	**9.00**
		4.0%	**193**	**4.00**	**8.00**
JJ Liao (2021)	13/0.2	0.0%	142	3.2	-
		1.0%	152	3.56	-
		2.0%	156	3.73	-
		0.0%	*128*	*3.21*	-
		1.0%	*136*	*3.46*	-
		2.0%	*149*	*3.73*	-
Z Wang (2020)	13/0.2	0.0%	*107*	*3.50*	-
		0.5%	*145*	*4.4*	-
		1.0%	*150*	*4.5*	-
		1.5%	*148*	*4.5*	-
		2.0%	*149*	*4.7*	-
		0.0%	*130*	*3.8*	-
		0.5%	*130*	*3.8*	*4.8*
		1.0%	*136*	*4.2*	*5*
		1.5%	*137*	*4.4*	*6.2*
		2.0%	*146*	*4.5*	*7.6*
	13/0.2	1.5%	*148*	*3.51*	-
			154	*2.74*	-
			159	*3.86*	-
A Arora (2019)	13/0.2	0.0%	146	3.75	-
		1.0%	155	4.00	-
		3.0%	156	4.50	-

AL Hoang (2019)	13/0.18	0.0%	*178*	*4.30*	*4.40*
		1.0%	*194*	*4.50*	*4.60*
		2.0%	*195*	*4.50*	*4.60*
ZB Haber (2018)	30/0.55	3.0%	**122**	**3.00**	**-**
			159	**3.60**	**-**
	20/0.3	2.0%	**122**	**3.60**	**-**
			138	**3.90**	**-**
			159	**3.70**	**-**
	13/0.3	4.5%	**162**	**3.60**	**-**
			169	**3.60**	**-**
	13/0.2	2.0%	**125**	**2.90**	**-**
			141	**3.10**	**-**
			120	**3.75**	**-**
			129	**3.95**	**-**
M Shafieifar (2017)*	12.5/0.2	2.0%	**148**	**4.60**	**7.00**
			131	**3.25**	**13.00**
			135	**2.60**	**12.70**
			130	**1.80**	**14.00**
			150	**2.80**	**8.20**
AL Hoang (2017)	-	0.0%	***217***	***4.49***	**-**
	13/0.18	1.5%	***212***	***4.40***	***6.38***
	20/0.25	1.5%	***203***	***4.17***	***5.83***
	13/0.18	3.0%	***205***	***4.25***	***6.38***
	20/0.25	3.0%	***208***	***4.32***	***7.03***
El-Helou (2016)	13/0.2	0.0%	**138**	**3.3**	**4.00**
		2.0%	**155**	**3.4**	**6.00**
		4.0%	**158**	**3.5**	**9.00**
DY Yoo (2015)	13/0.2	2.0%	*212*	*4.53*	-
	19.5/0.2	2.0%	*210*	*4.84*	-
	30/0.3	2.0%	*210*	*4.58*	-
SL Prabha (2014)	6/0.2	1.0%	*123*	*3.82*	*9.26*
		2.0%	*146*	*4.44*	*14.60*
		3.0%	*162*	*4.85*	*18.00*

	13/0.3	1.0%	*137*	*4.25*	*12.10*
		2.0%	*171*	*4.50*	*17.23*
AMT Hassan (2012)*	-	0.0%	124	3.26	3.70
			124	3.28	3.70
			121	3.24	3.60
	13/0.2	2.0%	146	3.65	7.40
			149	4.17	7.78
			151	3.73	5.20
H Yang (2010)	13/0.2	2.0%	*200*	*4.6*	-
BA Graybeal (2007)	13/0.2	2.0%	**110**	**3.70**	**-**
			119	**3.40**	**-**
			125	**3.60**	**-**
			185	**4.10**	**-**
			193	**4.00**	**-**
			200	**4.60**	**-**
			194	**3.90**	**-**
I Mohammed (test)*	13/0.2	2.0%	**190**	**3.98**	**-**
			190	**4.45**	**-**
			192	**4.31**	**-**
		2.0%	**212**	**5.02**	**-**
		1.0%	**199**	**4.74**	**-**
		1.0%	**180**	**3.32**	**-**
		2.0%	**212**	**5.13**	**-**
K Tsiotsias (test)*	13/0.2	2.0%	**143**	**3.54**	**-**
			144	**3.50**	**-**

Note: '' corresponds to the results of individual test specimens. Font code in stress-strain values represent different cylinder sizes (mm): (50x100); (**75x150**); (100x200) and (**150x300**). Suffix 'test' indicates the experiments performed in this research program and a parallel study by a peer, K. Tsiotsias.*

A.2 Compression Stress-Strain Response Including Post-Peak

Below are the complete stress-strain response curves for cylinder specimens where 'Actuator LVDT (Adjusted)' curves represent the response from machine's LVDT which is calibrated with

using the pre-peak response from strain gauges. Strain from LVDT was calculated by deformation divided by height of cylinder and a specific factor (k) equal to 2.6 & 2.0 for the specimens TSO2-C5 and DE2-C4, respectively. The need for this calibration factor indicates that the distance travelled by platens of the machine does not represent the actual deformation in the cylinder.

Strain from Actuator LVDT = $\Delta h / (H \cdot k)$

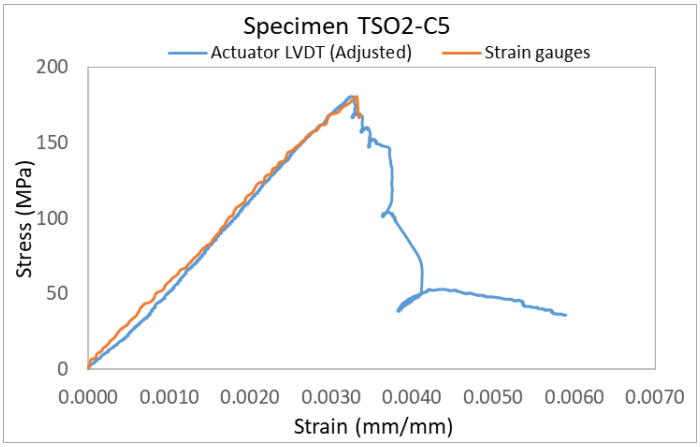

Figure A- 1: Complete compression stress-strain response for specimen TSO2-C5

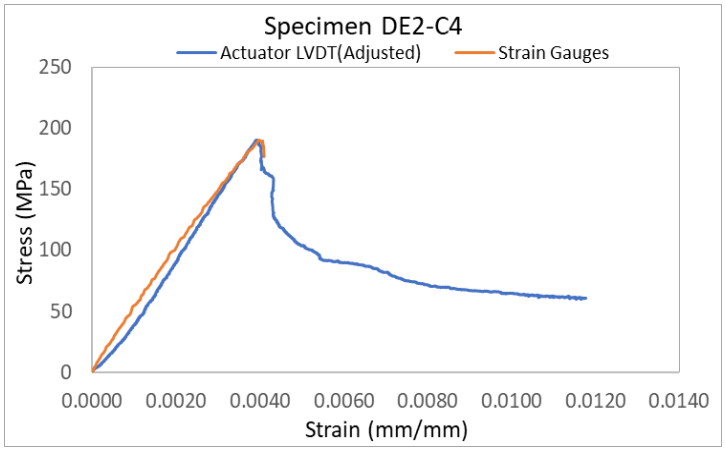

Figure A- 2: Complete compression stress-strain response for specimen DE2-C4

A.3 Direct Tension Test Resistance Curves

Below figures represent load vs actuator displacement for series of direct tension tests performed. Refer to Section 3.3.4 for experimental results estimated from direct tension tests.

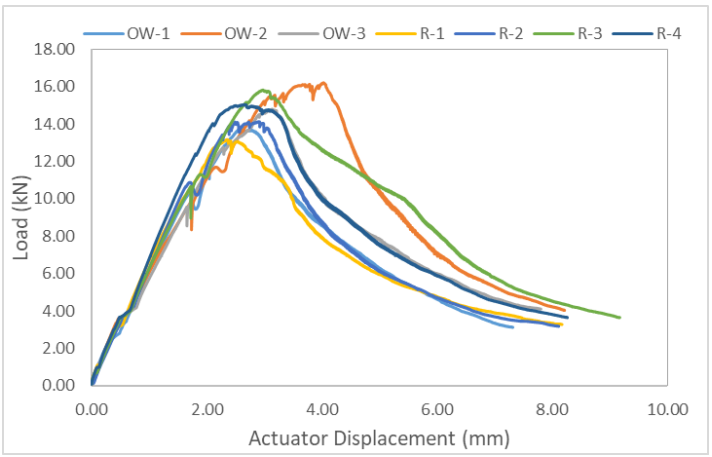

Figure A- 3: Direct tension test resistance curves-Type P specimens (Mix DE2)

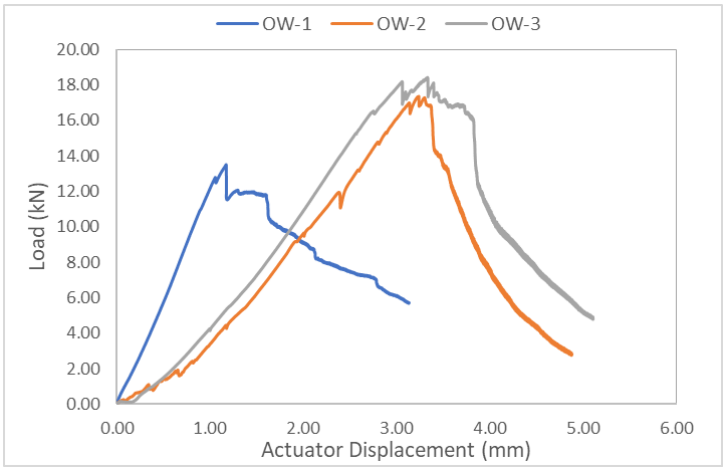

Figure A- 4: Direct tension test resistance curves-Type I specimens (Mix DE2)

It should be noted that OW-1 specimen of Type-I direct tension test demonstrated support failure, thus, its response was an outlier.

Below are the two different test setups proposed by AASHTO Standard on uniaxial tensile testing of UHPFRC (AASHTO T 397, 2022).

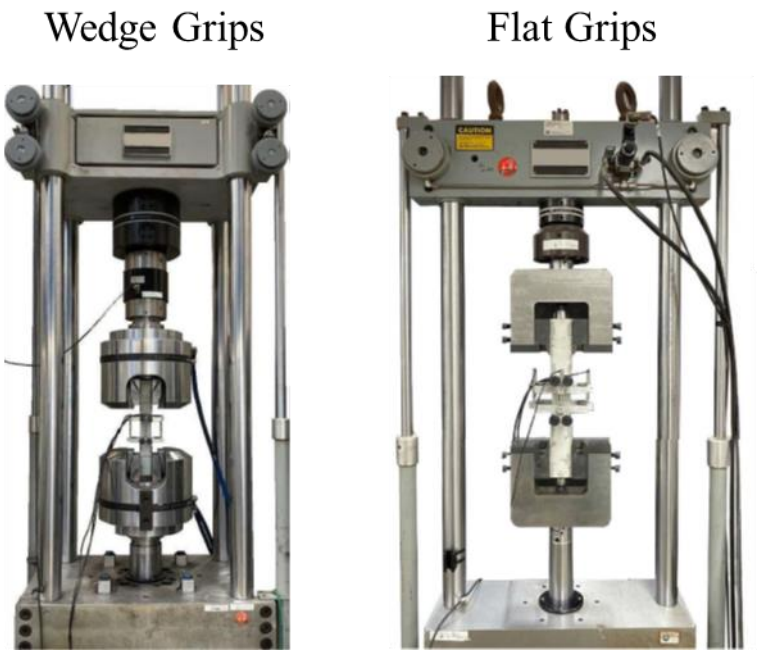

Figure A- 5: Direct tension test setups recommended by AASHTO (adapted from AASHTO T 397, 2022)

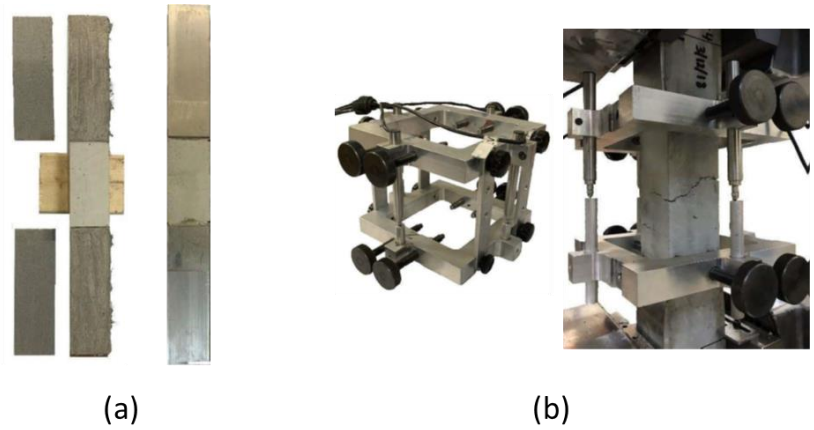

Figure A- 6: (a) Standard direct tension test specimen with aluminum plates (b) Parallel ring extensometer attachment (adapted from AASHTO T 397, 2022)

A.4 Modulus of Elasticity and Poisson's Ratio Test

Experimental curves shown below correspond to the specimens tested for Modulus of Elasticity (E) and Poisson's ratio (v). Load vs strain readings corresponding to the third loading cycle for each specimen is shown. Refer to Section 3.3.2 for calculated results.

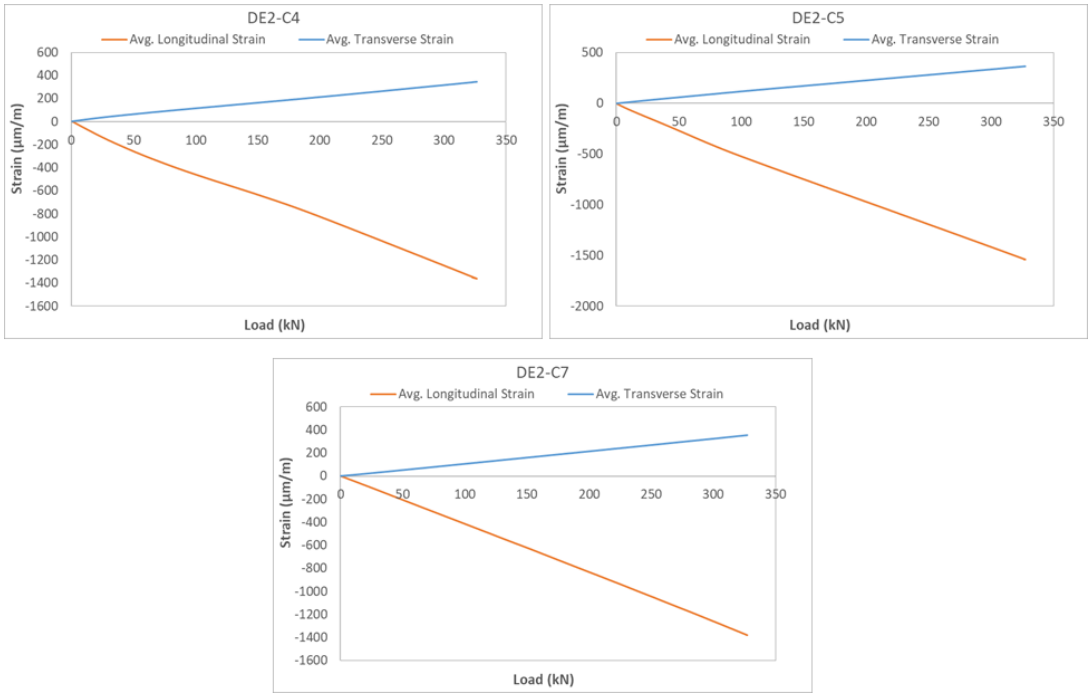

Figure A- 7: Response curves for E & v tests

Appendix B: Supplementary Data from Various Analyses

B.1 Tensile Behavior from the Swiss Recommended Inverse Analysis

Detailed tension stress-strain responses obtained using Swiss inverse analysis approach (SIA 2052, 2016) as described in Section 3.5 are shown below for UHPFRC Mix DE2 flexural prisms.

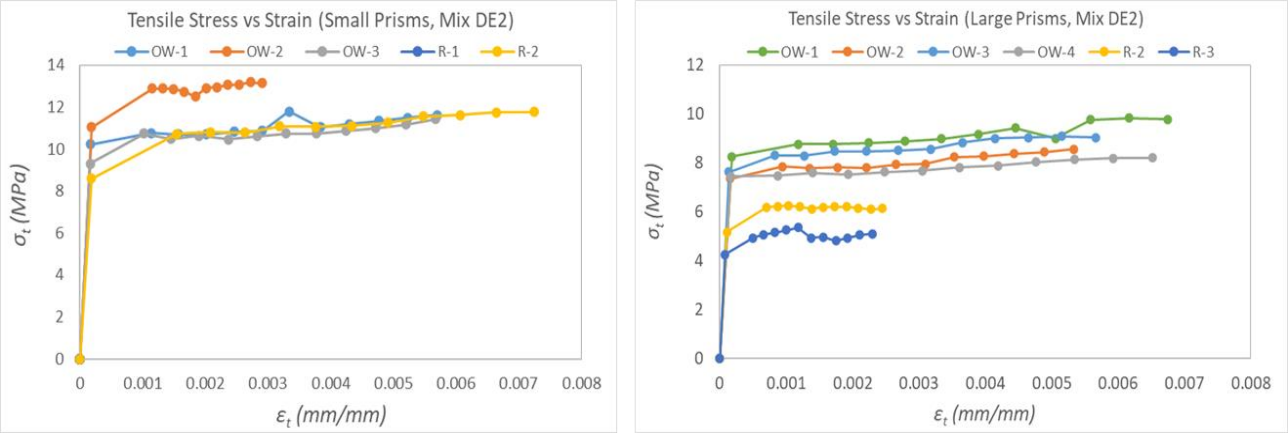

Figure B- 1: Tensile Stress-Strain response obtained using Swiss inverse analysis (Mix DE2)

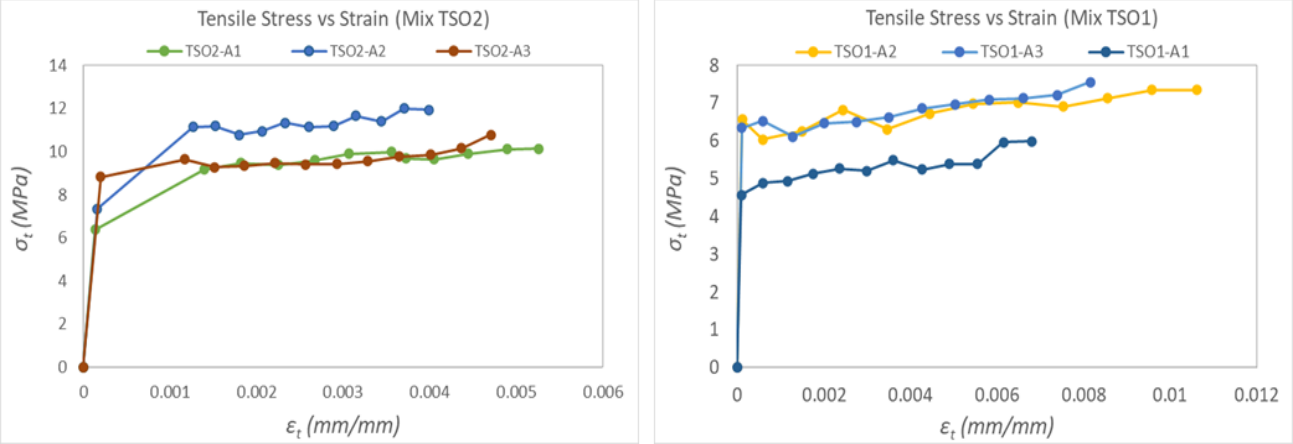

Figure B- 2: Tensile Stress-Strain response obtained using Swiss inverse analysis (Mix TSO2 & TSO1)

B.2 Coefficients Required for the Swiss Inverse Analysis Method

Table B- 1 presents the coefficients for α_i required for performing the inverse analysis calculations as recommended by SIA 2052 (2016). The detailed analysis procedure may be referred in Section 2.7.2 of the thesis.

Table B- 1: Coefficients for α_i based on a given value of λ_i (adapted from SIA 2052, 2016)

λ_i	α_i	λ_i	α_i	λ_i	α_i	λ_i	α_i
0.00	0.988	0.25	0.674	0.50	0.500	0.75	0.326
0.01	0.941	0.26	0.666	0.51	0.493	0.76	0.319
0.02	0.915	0.27	0.658	0.52	0.487	0.77	0.311
0.03	0.896	0.28	0.651	0.53	0.480	0.78	0.303
0.04	0.879	0.29	0.644	0.54	0.473	0.79	0.295
0.05	0.863	0.30	0.636	0.55	0.467	0.80	0.287
0.06	0.850	0.31	0.629	0.56	0.460	0.81	0.279
0.07	0.838	0.32	0.622	0.57	0.453	0.82	0.270
0.08	0.826	0.33	0.615	0.58	0.446	0.83	0.261
0.09	0.815	0.34	0.608	0.59	0.440	0.84	0.253
0.10	0.804	0.35	0.601	0.60	0.433	0.85	0.244
0.11	0.794	0.36	0.594	0.61	0.426	0.86	0.235
0.12	0.784	0.37	0.587	0.62	0.419	0.87	0.226
0.13	0.774	0.38	0.580	0.63	0.412	0.88	0.216
0.14	0.764	0.39	0.574	0.64	0.406	0.89	0.206
0.15	0.755	0.40	0.567	0.65	0.399	0.90	0.196
0.16	0.746	0.41	0.560	0.66	0.392	0.91	0.185
0.17	0.738	0.42	0.553	0.67	0.385	0.92	0.174
0.18	0.729	0.43	0.547	0.68	0.378	0.93	0.161
0.19	0.721	0.44	0.540	0.69	0.370	0.94	0.149
0.20	0.712	0.45	0.533	0.70	0.363	0.95	0.135
0.21	0.705	0.46	0.527	0.71	0.355	0.96	0.120
0.22	0.697	0.47	0.520	0.72	0.348	0.97	0.104
0.23	0.689	0.48	0.513	0.73	0.341	0.98	0.082
0.24	0.681	0.49	0.507	0.74	0.334	0.99	0.060
						1.00	0.000

B.3 Alternative Approach for Inverse Analysis Method by French Standard

As mentioned earlier, the stepwise iterative inverse analysis method by French Standard (AFNOR NF P18 470, 2016) is complex and often presented convergence instability in the post cracking region of the tensile response of UHPFRC. Excel spreadsheet was used to program the algorithm with expressions described in Section 2.7.3. Alternatively, all the expressions provided by the standard were rederived in order to better understand the working of this method. Unfortunately, even the rederived expressions could not provide the hard-sought results. The procedure followed to rederive the expressions is described below.

Flexural response (load vs deflection) of UHPFRC measured from a four-point bending test may be divided into two parts, namely, linear (elastic) zone and non-linear (in-elastic) zone that can be used for inverse analysis to obtain the tensile stress-strain behavior of UHPFRC. For linear analysis up to the yield point (first crack), Equation B-1 can be used to obtain the curvatures from deflection values measured during the test. Neutral axis may be assumed to be at center of the cross-section up to the limit of proportionality range. Tensile strains at the bottommost fiber of the cross-section may be calculated from T_{zu} (half of depth) multiplied by the curvature at each stage. Corresponding stress values may be obtained using strains, where it may be assumed that the stress equals to strain multiplied by the modulus of elasticity (E).

$$\delta_y = \frac{23L^2}{216}\varphi_y \tag{B-1}$$

Once the yield moment (moment where linearity terminates) is reached in the moment-deflection curve, response under the Moment-Curvature will not be linear anymore. Curvature increases more for even small increase of applied moment due to the inelastic behavior of the material. Hence, the relations used in the linear (elastic) region are not applicable beyond the yield moment. The procedure below describes the calculation of curvature values in the non-linear region.

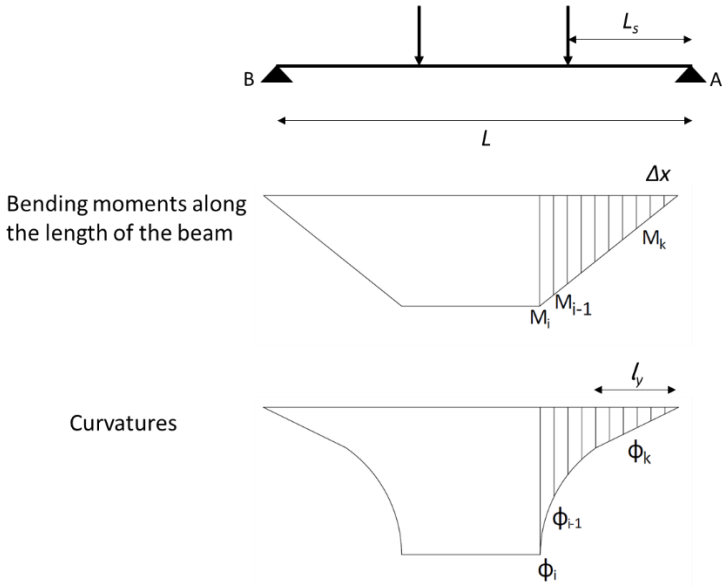

Figure B- 3: Moments and Curvatures after yielding

From Figure B- 3, the shear span of the beam is discretized into ***'i'*** parts for ***k=1 to i*** with a value of $\Delta x_i = {}^{L_s}/_{i}$ *(small step size)*. With the known values of Moment-Curvature (M, φ) pairs up to the step ***i-1,*** the value of curvature (φ_i) for the step ***i*** can be calculated using the measured deflection value (δ_i). Using the concepts of the 'Moment-Area method' and the 'Trapezoidal rule', and with reference to Figure B- 3, the expressions are derived as follows:

$$\theta_{A,i} = \sum_{k=1}^{i} \varphi_k \cdot \Delta x_i = \sum_{k=1}^{i} \varphi_k \cdot \Delta x_i + \varphi_i \left(\frac{L_s}{2}\right) \tag{B-2}$$

$$\delta_i = \theta_{A,i} \cdot (1.5 \cdot L_s) - \left\{\sum_{k=1}^{i} \varphi_k \cdot \Delta x_i \cdot \left(1.5 \cdot L_s - \left(k - 1 + \frac{1}{2}\right) \cdot \Delta x_i\right) + \varphi_i \left(\frac{L_s}{2}\right) \cdot \left(\frac{L_s}{4}\right)\right\} \tag{B-2a}$$

Substitution of Equation B-2 into Equation B-2a gives Equation B-2b below, that may be used for back-calculating the curvatures from the values of known deflections using an iterative approach;

$$\delta_i = \sum_{k=1}^{i} \varphi_k \cdot \left(k - \frac{1}{2}\right) \cdot {\Delta x_i}^2 + \frac{5}{8} \cdot \varphi_i \cdot {L_s}^2 \tag{B-2b}$$

Alternatively, Equation B-3 may be used to calculate curvature for deflections beyond yield and up to the peak moment which gives approximately same results.

$$\delta_u = \frac{L^2}{216}\left[\left(4M_u^2 + 4M_u.M_y\right).\varphi_y + \left(23M_u^2 - 4M_u.M_y - 4M_y^2\right).\varphi_u\right] \quad \text{(B-3)}$$

where, M_u is a given moment after the yield stage, M_y is the moment at the yield stage with φ_u and φ_y being the corresponding values of curvatures, respectively.

After obtaining all the moment-curvature couples that characterize the flexural member, a second inverse analysis approach is used to determine the stress-strain values for a given stage ***i***. Parameter β_i is defined as a factor for relative depth of the neutral axis, measured from the bottom fiber of the cross-section, at any given stage ***i***. The depth of compression and tension zone from the neutral axis can be written as:

$$Z_{c,i} = (1 - \beta_i).h \quad ; \quad Z_{t,i} = -\beta_i.h \quad \text{(B-4)}$$

Here it is implicitly assumed that the reference point (zero) in the system of axes is the position of the neutral axis. In the following derivation terms, sign convention is positive for compressive stresses, strains and negative for tensile stresses, strains. Assuming a linear variation of strain across the depth (plane section remaining plane), the longitudinal strain at the extreme tension fiber can be calculated using the Equation B-5.

$$\varepsilon_{t,i} = \varphi_i.Z_{t,i} \quad \text{(B-5)}$$

The end of the linear elastic range in tension is at the position where strain is equal to the cracking strain, $\varepsilon_{cr}<0$. The distance of the end of the linear range from the position of the neutral axis is,

$$\varepsilon_{cr,i} = \varepsilon_{cr} = \varphi_i.Z_{cr,i} \rightarrow Z_{cr,i} = \frac{\varepsilon_{cr}}{\varphi_i} \quad \text{(B-6)}$$

Strain at the topmost fiber of compression zone,

$$\varepsilon_{c,i} = \varphi_i.Z_{c,i} \quad \text{(B-7)}$$

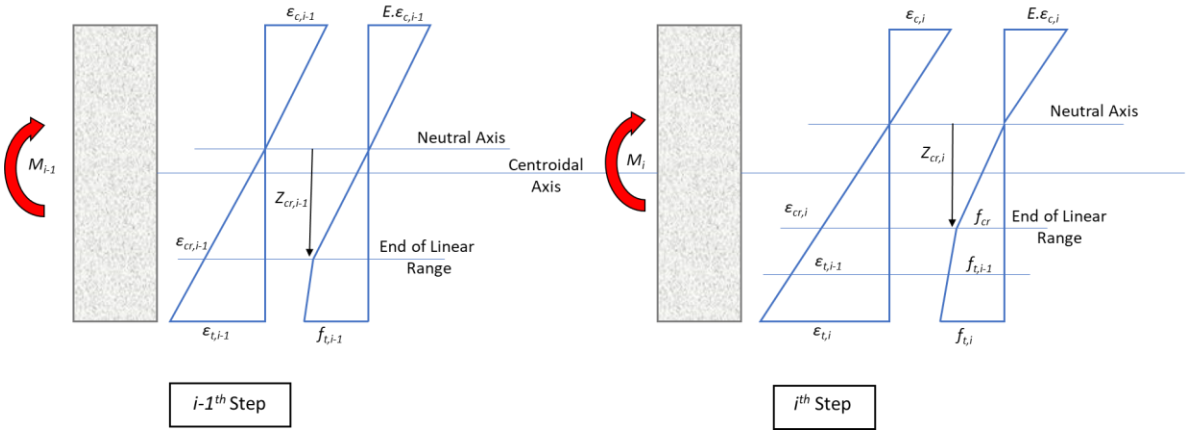

Figure B- 4: The state of stress and strain for the cross-section at step i-1 and at the next step, i

Assuming that the stress-strain response is in the strain hardening branch at step i, then with reference to Figure B- 4b, the distance from the neutral axis, $Z^i_{t,i-1}$, where the extreme strain and stress of the preceding step (i-1) now occur is calculated as follows:

$$\varepsilon_{t,i-1} = \varphi_i . Z^i_{t,i-1} \rightarrow Z^i_{t,i-1} = \frac{\varepsilon_{t,i-1}}{\varphi_i} \tag{B-8}$$

To find the resultant force in the Compression and Tension Zones at the *step i*, the following steps are considered:

$$N_i = 0 \rightarrow N^i_c + N^i_t = 0 \tag{B-9}$$

$$N^i_c = b \cdot \int_0^{Z_{c,i}} f_c(z)dz = b \cdot E \cdot \int_0^{Z_{c,i}} \epsilon_{c,i}(z)dz = b \cdot E \cdot \int_0^{Z_{c,i}} \varepsilon_{c,i} \cdot \frac{z}{Z_{c,i}} dz = \frac{\varphi_i \cdot b \cdot E \cdot (Z_{c,i})^2}{2} \tag{B-9a}$$

$$N^i_t = b \cdot \int_0^{Z_{t,i}} f_t(z)dz \; = \; b \cdot \int_0^{Z^i_{cr}} f_t(z)dz \; + b \cdot \int_{Z^i_{cr}}^{Z^i_{t,i-1}} f_t(z)dz \; + b \cdot \int_{Z^i_{t,i-1}}^{Z_{t,i}} f_t(z)dz \tag{B-9b}$$

In Equation B-9b, the sum of the first two integrals corresponds to N^{i-1}_t, occuring however over a different height of tension zone, equal to $Z^i_{t,i-1}$, whereas in the previous step it occurred over a height of tension zone equal to $Z_{t,i-1}$. To correct for this difference, the term N^{i-1}_t is multiplied by the ratio of $Z^i_{t,i-1}/Z_{t,i-1}$. Therefore, Equation B-9b is now written as:

$$N^i_t \; = \; N^{i-1}_t \cdot \frac{Z^i_{t,i-1}}{Z_{t,i-1}} + b \cdot \int_{Z^i_{t,i-1}}^{Z_{t,i}} f_t(z)dz \tag{B-9c}$$

Using Equation B-5 and Equation B-8, Equation B-9c may further be written as:

$$N_t^i < 0 \;=\; N_t^{i-1} \cdot \frac{\varphi_{i-1}}{\varphi_i} + b \cdot \int_{Z_{t,i-1}^i}^{Z_{t,i}} f_t(z)dz \underbrace{=}_{\substack{Trapezoidal \\ Rule}} N_t^{i-1} \cdot \frac{\varphi_{i-1}}{\varphi_i} + b \cdot \frac{(f_{t,i}+f_{t,i-1})}{2} \cdot \left|\Delta Z_{t,i}\right| \quad \text{(B-9d)}$$

Note that, $\left|\Delta Z_{t,i}\right| = \left|Z_{t,i} - Z_{t,i-1}^i\right|$. Using Equation B-9, Equation B-9d can be written as;

$$-N_c^i = N_t^{i-1} \cdot \frac{\varphi_{i-1}}{\varphi_i} + b \cdot \frac{(f_{t,i}+f_{t,i-1})}{2} \cdot \left|\Delta Z_{t,i}\right| \quad \text{(B-9f)}$$

$$-N_c^i - N_t^{i-1} \cdot \frac{\varphi_{i-1}}{\varphi_i} = W \;=\; 0.5b \cdot \left(f_{t,i} + f_{t,i-1}\right) \cdot \left|\Delta Z_{t,i}\right| \quad \text{(B-10)}$$

This is an equation with two unknowns, namely, $\left|\Delta Z_{t,i}\right|$ and $(f_{t,i} + f_{t,i-1})$. Similarly, for the moments the following equation is derived, with reference to the Figure B- 4; $M = M_c^i + M_t^i$. To obtain the Moment due to tensile forces in the cross-section, similar concept as per Equation B-9c is used.

$$M = M_c^i + M_t^i \quad \text{(B-11)}$$

$$M_t^i = M_t^{i-1}.\left(\frac{Z_{t,i-1}^i}{Z_{t,i-1}}\right)^2 + b \cdot \frac{(f_{t,i}+f_{t,i-1})}{2} \cdot \left|\Delta Z_{t,i}\right| \cdot \left(Z_{t,i-1}^i + 0.5 * \Delta Z_{t,i}\right) = M_t^{i-1}.\left(\frac{Z_{t,i-1}^i}{Z_{t,i-1}}\right)^2 + W \cdot \left(Z_{t,i-1}^i + 0.5 * \Delta Z_{t,i}\right) \quad \text{(B-11a)}$$

$$M_i = N_c^i \cdot \left(\frac{2}{3} \cdot Z_{c,i}\right) + M_t^{i-1}.\left(\frac{\varphi_{i-1}}{\varphi_i}\right)^2 + W \cdot \left(Z_{t,i-1}^i + \; 0.5 * \Delta Z_{t,i}\right) \quad \text{(B-11b)}$$

$$M_i \; - N_c^i \cdot \left(\frac{2}{3} \cdot Z_{c,i}\right) \; - \; M_t^{i-1}.\left(\frac{\varphi_{i-1}}{\varphi_i}\right)^2 \; = \; W \cdot \left(Z_{t,i-1}^i + \; 0.5 * \Delta Z_{t,i}\right) \; \approx W \cdot Z_{t,ave}^i, \quad where \;\; Z_{t,ave}^i = 0.5 \cdot (Z_{t,i-1}^i + Z_{t,i}) \quad \text{(B-11c)}$$

Therefore, expression for $Z_{t,ave}^i$ can also be written as shown in Equation B-12. Furthermore,

$$Z_{t,ave}^{i} = \left[M_i - N_c^i \cdot \left(\frac{2}{3} \cdot Z_{c,i}\right) - M_t^{i-1}.\left(\frac{\varphi_{i-1}}{\varphi_i}\right)^2\right] / W = 0.5 \cdot \left(Z_{t,i} + Z_{t,i-1}^{i}\right) \quad \text{(B-12)}$$

$$Z_{t,i} = Z_{c,i} - h = 2 \cdot \left[M_i - N_c^i \cdot \left(\frac{2}{3} \cdot Z_{c,i}\right) - M_t^{i-1}.\left(\frac{\varphi_{i-1}}{\varphi_i}\right)^2\right] / [-N_c^i - N_t^{i-1} \cdot \frac{\varphi_{i-1}}{\varphi_i}] - Z_{t,i-1}^{i} \quad \text{(B-13)}$$

$$Z_{c,i} = h + 2 \cdot \left[M_i - N_c^i \cdot \left(\frac{2}{3} \cdot Z_{c,i}\right) - M_t^{i-1}.\left(\frac{\varphi_{i-1}}{\varphi_i}\right)^2\right] / [-N_c^i - N_t^{i-1} \cdot \frac{\varphi_{i-1}}{\varphi_i}] - Z_{t,i-1}^{i} \quad \text{(B-14)}$$

Using the above equations, a fixed-point algorithm may be performed by using an iterative approach (i.e., by assuming a value for $Z_{c,i}$ in the right-hand side of Equation B-14, the left-hand side can be calculated which would then be used to update the initial value assumed and this process may be repeated until the desired convergence is achieved).

B.4 Observations from Digital Image Correlation (DIC)

Figure B- 5 and Figure B- 6 represent the progressive crack development in a flexural specimen tested under four-point bending and analyzed using the DIC program, Ncorr. Flexural prisms presented here were tested by Husain (2021) and had nominal dimensions of 100 mm x 100 mm x 300 mm. Crack initiation, multi-cracking, crack localization and crack opening are evident from the sequence shown. Value below each image denotes the load sustained by flexural specimen corresponding to different stages. Similar plots are presented in Figure B- 7 through Figure B- 10 for direct tension specimens tested in this study corresponding to Type P specimens with nominal dimensions 30 mm x 50 mm. Multi-cracking was also evident in most direct tension test specimens as well.

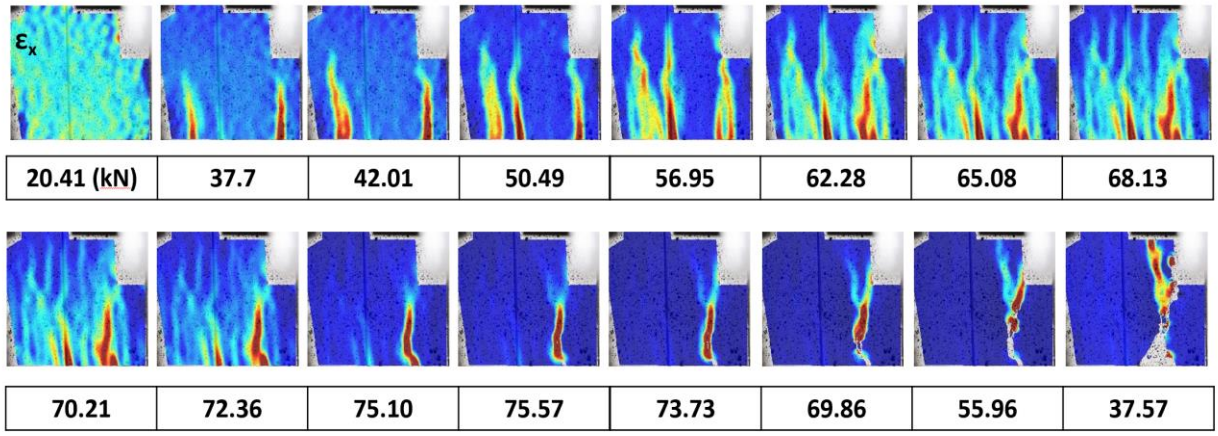

Figure B- 5: Crack development in flexural specimen (P2, Batch 1)

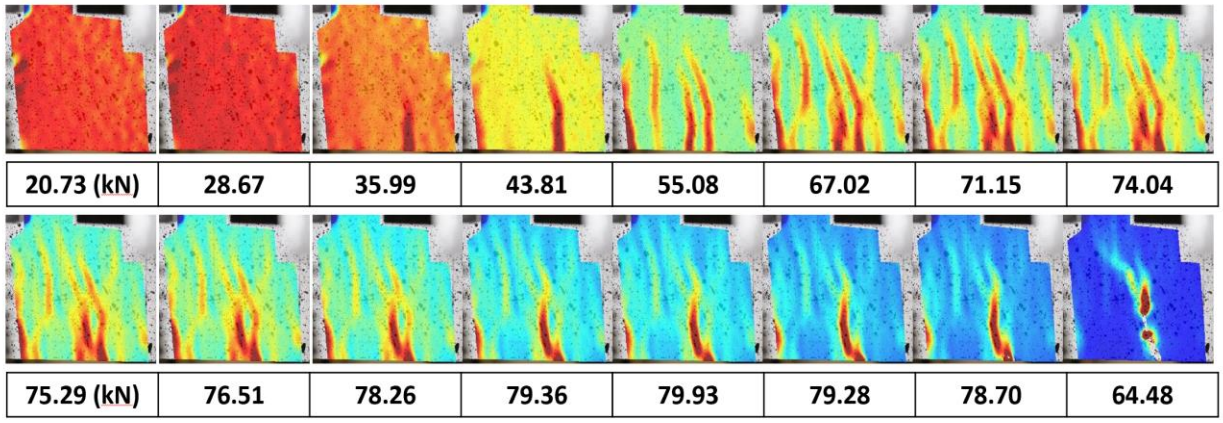

Figure B- 6: Crack development in flexural specimen (P6, Batch 1)

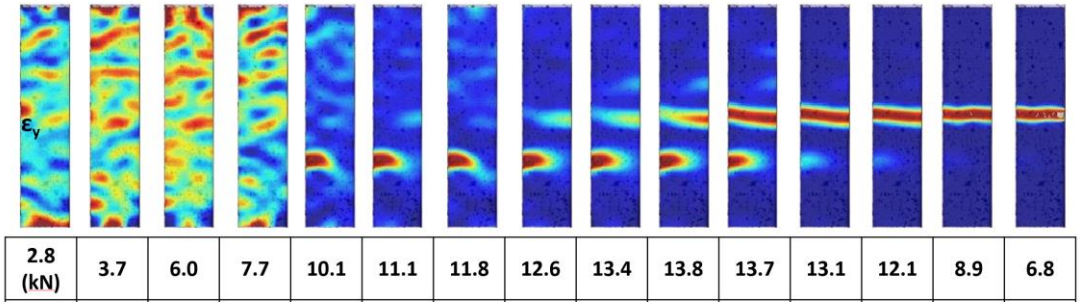

Figure B- 7: DIC analysis result for Type P direct tension specimen (OW-1, Mix DE2)

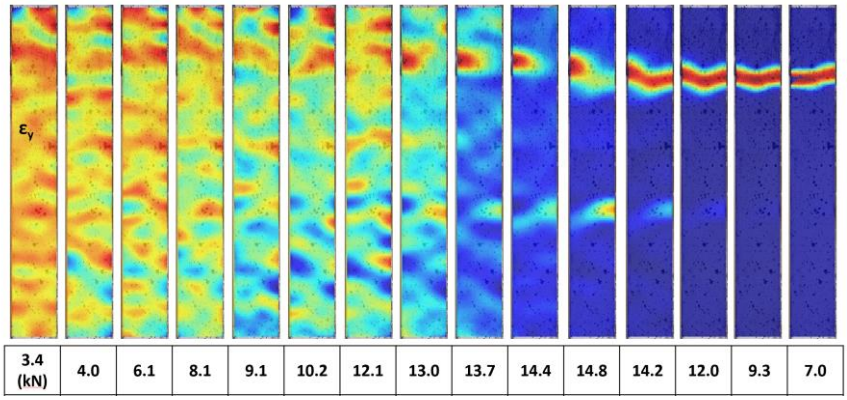

Figure B- 8: DIC analysis result for Type P direct tension specimen (OW-3, Mix DE2)

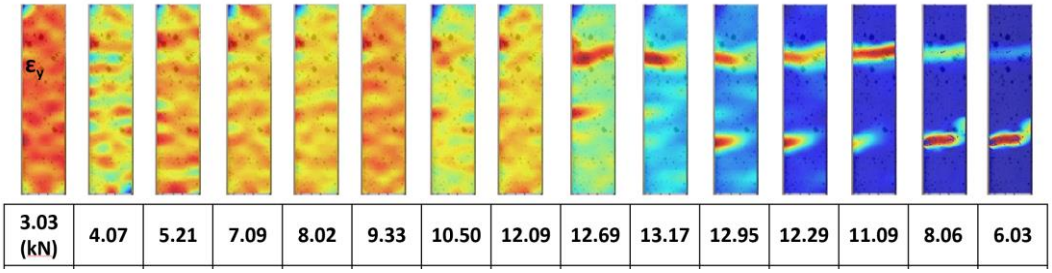

Figure B- 9: DIC analysis result for Type P direct tension specimen (R1, Mix DE2)

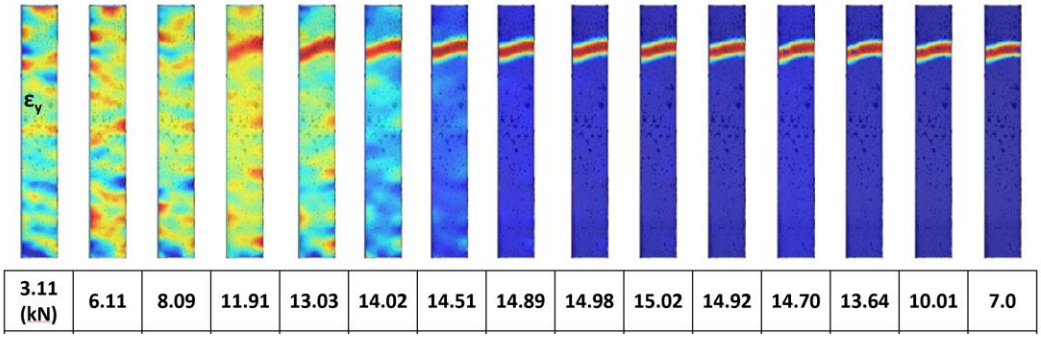

Figure B- 10: DIC analysis result for Type P direct tension specimen (R4, Mix DE2)

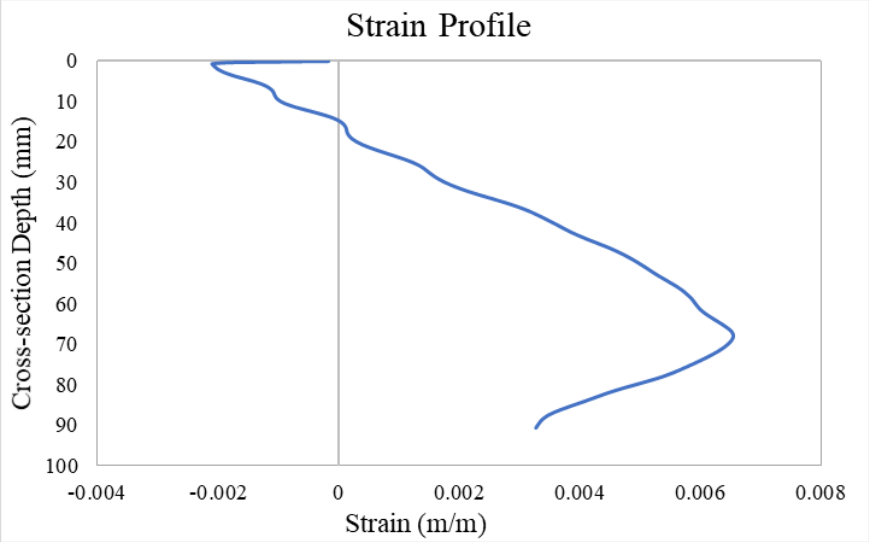

Figure B- 11: Typical strain profile in a flexural prism at peak moment

Figure B- 11 depicts the typical strain profile across the depth of flexural prism (100 mm x 100 mm) obtained using DIC post-processor. Profile shown corresponds to the maximum moment stage. Tensile strains are plotted on the positive axis and compressive strains on negative. Moreover, position of neutral axis can also be observed from the profile shown.

Figure B- 12 depicts the compressive strains observed in flexural prisms at peak load. DIC extensometer readings are obtained using a virtual extensometer whereas DIC strain profile readings are obtained using strain profiles from Ncorr post-processor program. Figure B- 13 shows the load vs tensile strain (bottom fiber) resistance curve for a flexural prism.

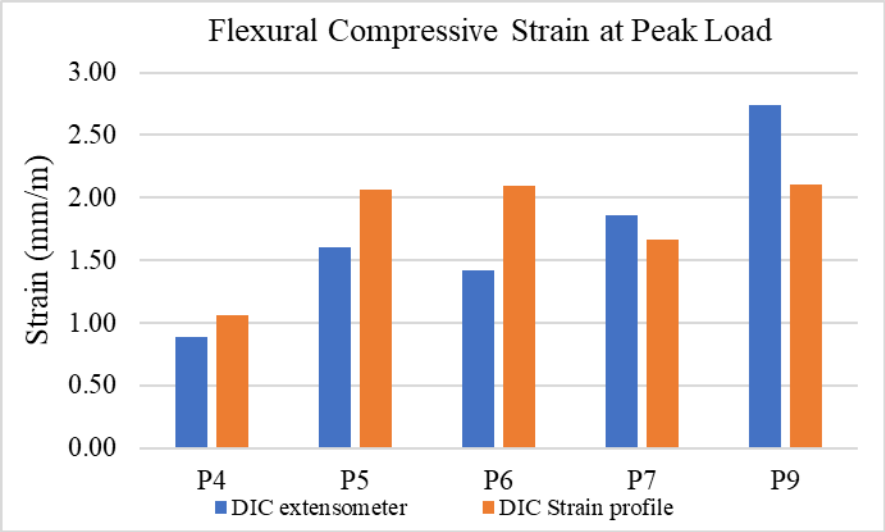

Figure B- 12: Maximum compressive strain at peak load in flexural prisms (Batch-1, Husain, 2021)

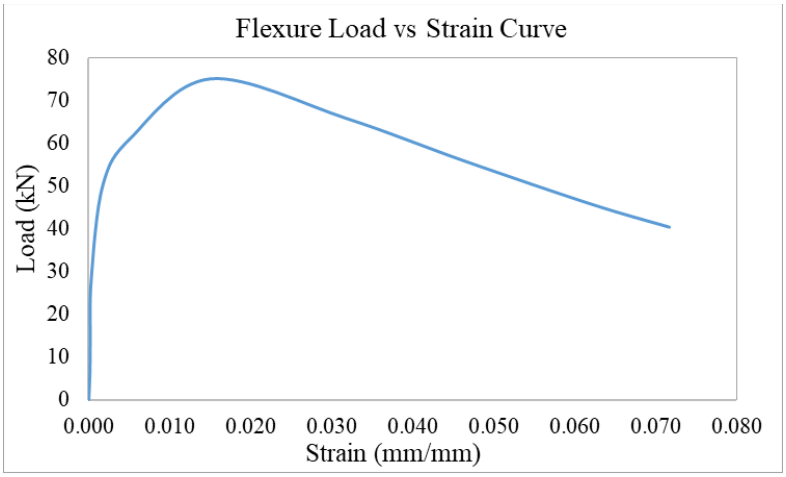

Figure B- 13: Typical load vs tensile strain curve for flexural prism

B.5 Fracture Energy Estimated for Flexural Tests

Figure B- 14 and Figure B- 15 show the fracture energy estimated for flexural prisms. Fracture energy was calculated by estimating the area under the flexural load vs deflection resistance curve up to a specific point in the response. Area (N-mm) under the load vs deflection curve was estimated by using a simple MATLAB script followed by dividing it with the cross-sectional area of the specimen (b x h) (mm^2) to arrive at fracture energy (N/mm). Fracture energy at 0.5% drift level was found to be more consistent amongst all specimens that were tested and may be used as a quality control criterion for UHPFRC materials. However, a wider dataset has to be established

considering different material mixes, specimen sizes, test configurations etc. before concluding on a specific drift level.

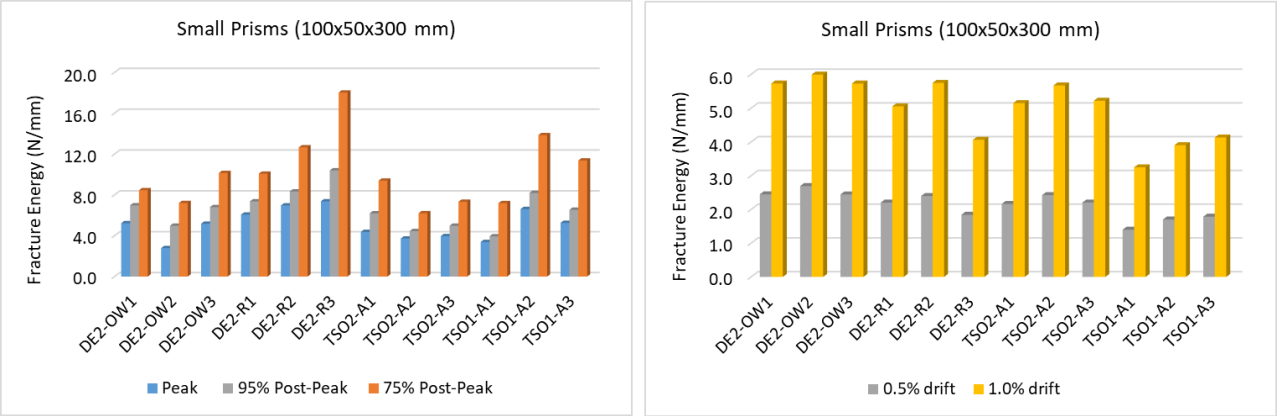

Figure B- 14: Fracture Energy for small flexural prisms at different levels

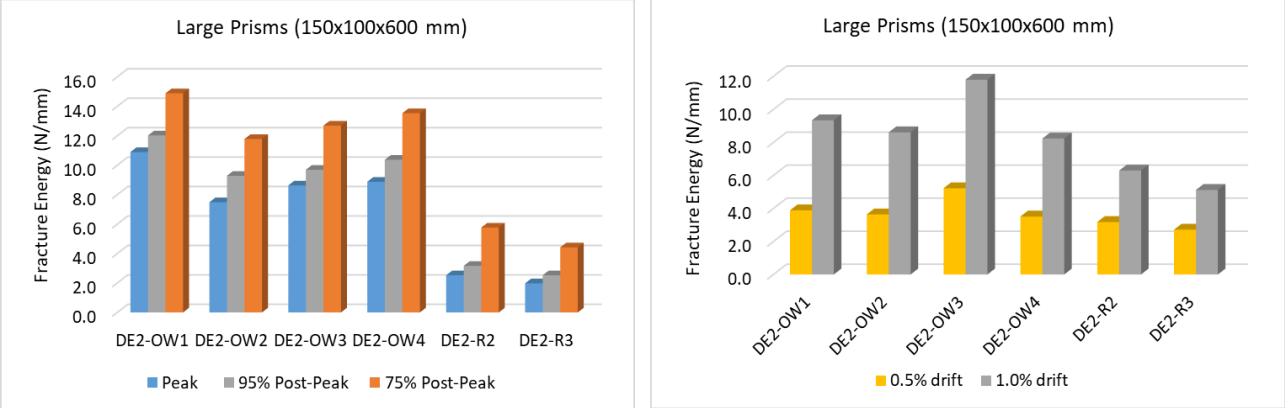

Figure B- 15: Fracture Energy for large flexural prisms at different levels